

High-accuracy Spectral Emissivity Measurement for Industrial and Remote Sensing Applications



Von der Fakultät Mathematik und Naturwissenschaften

Fachgruppe Physik

der Bergischen Universität Wuppertal

zur Erlangung des akademischen Grades

Dr. rer. nat.

genehmigte Dissertation

vorgelegt von

Albert Adibekyan

aus Moskau

Gutachter:

Univ.-Prof. Dr. Ralf Koppmann

Dr. Jörg Hollandt

Wuppertal 2016

Die Dissertation kann wie folgt zitiert werden:

urn:nbn:de:hbz:468-20160421-144304-2

[<http://nbn-resolving.de/urn/resolver.pl?urn=urn%3Anbn%3Ade%3Ahbz%3A468-20160421-144304-2>]

Abstract

The unique potential of radiation thermometry for temperature measurements ranging from non-contact temperature control of numerous industrial production processes to climate research by remote sensing of the Earth requires the accurate knowledge of the radiation properties of a material, i.e. its spectral emissivity. A variety of techniques for the emissivity measurements are available but in many cases they do not meet the wide range of requirements posed by modern science and industry and do not provide sufficiently accurate results with reliable uncertainty values. Therefore, a measurement setup and a validated method for highly accurate directional spectral emissivity, total directional emissivity and total hemispherical emissivity measurements under vacuum from 4 μm to 100 μm and from -40 °C to 600 °C with very low and validated uncertainties was developed and is presented in this work. The measurements, using the newly developed Reduced Background Calibration Facility (RBCF) of PTB, are traceable to the International Temperature Scale of 1990 (ITS-90).

The development and design of a dedicated vacuum sample holder for emissivity measurements, the highly accurate metrological characterization of the vacuum reference blackbodies and the developed method for calculation, which considers the complete radiation budget, are described in detail and allow the performance of very demanding measurement tasks. The setup has been successfully applied in the European Metrology Research Program (EMRP) within the projects MetEOC and MetEOC2, providing the traceability of atmospheric measurements with the instrument GLORIA with the required low uncertainty of less than 100 mK. The thermal emissivity of absorber coatings for solar thermal electricity generation could be measured at the RBCF at the operating temperature of 600 °C with a standard uncertainty of less than 0.005. These results can be used to systematically improve the efficiency of high temperature solar thermal absorbers in the future. Other examples of emissivity measurements for various materials presented in this work illustrate the broad capability of the developed method and facility.

List of symbols

a, b	fraction of radiation process	-
A	surface area	m^2
\mathbf{B}	magnetic induction	$V\ s\ m^{-2}$
d	thickness	m
\mathbf{D}	electric displacement	$C\ m^{-2}$
D	thickness of thin film	m
D^*	detectivity	$cm\ Hz^{1/2}\ W^{-1}$
D_{diff}	diffusivity	-
\mathbf{E}	electric field intensity	$V\ m^{-1}$
F	view factor	-
\mathbf{H}	magnetic field intensity	$A\ m^{-1}$
i	trajectory	-
i, j	integers	-
I	radiant intensity	$W\ sr^{-1}$
\mathbf{j}	flowing electric current	$A\ m^{-2}$
k	extinction coefficient	-
K_a	emissivity coefficient	-
K_ϵ	scaling factor for emissivity	-
L	radiance	$W\ m^{-2}\ sr^{-1}$
m_i	number of ray reflection	-
M	radiant exitance	$W\ m^{-2}$
M_{tr}	number of Monte Carlo trials	-
n	refractive index	-
n_{rays}	number of rays	-
q	heat flux	$W\ m^{-2}$
Q	quotient of measured	-
r	reflectivity coefficient	-
R	electrical resistance	Ohm
s	spectral responsivity	$A\ W^{-1}$
\mathbf{S}	Poynting vector	-
t	time	s
t_1	transmissivity coefficient	-
T, t_s	temperature	K, C
u, U	uncertainty	-
W	energy	J
x, y, z	rectangular coordinates	m
y	estimated output quantity	-

Greek symbols

α	absorptivity	-
$\alpha, \vartheta, \varphi$	angular coordinates	rad, °
ϵ	emissivity	-
ϵ_p	permittivity	$F\ m^{-1}$

κ	thermal conductivity	$\text{W m}^{-1} \text{K}^{-1}$
λ	wavelength	μm
μ	magnetic permeability	H m^{-1}
ν	radiation frequency	s^{-1}
$\tilde{\nu}$	wavenumber	cm^{-1}
ρ	reflectivity	-
ρ_{free}	free electronic charge density	A s m^{-3}
σ_c	specific conductance	$\text{A V}^{-1} \text{m}^{-1}$
τ	transmissivity	-
ϕ	phase difference	
Φ	radiant flux	$\text{J s}^{-1}, \text{W}$
χ	angle of refraction	$\text{rad}, ^\circ$
ω_e	energy density	J m^{-3}
ω	angular frequency	Rad s^{-1}
Ω	solid angle	sr

Physical constants

c_0	speed of light in vacuum	$299792458 \text{ m s}^{-1}$
c_1	first radiation constant	$3.741771 \cdot 10^{-16} \text{ W m}^2$
c_2	second radiation constant	$1.438777 \cdot 10^{-2} \text{ m K}$
h	Planck constant	$6.62607123 \cdot 10^{-34} \text{ J s}$
k_B	Boltzmann constant	$1.3806488 \cdot 10^{-23} \text{ J K}^{-1}$
σ	Stefan-Boltzmann constant	$5.670373 \cdot 10^{-8} \text{ W m}^{-2} \text{K}^{-4}$

Subscripts and abbreviations

a.....	amplitude, absorbed
Amb.....	ambience
b.....	blackbody
Back.....	thermal background
BB1.....	“main” reference blackbody
BNM-LNE.....	Bureau National de Metrologie-Laboratoire National d’Essais
C.....	conductivity
Cal.....	calibration
CCT.....	Consultative Committee for Thermometry
Ch.....	chopper
Compar.....	comparison
d.....	diffuse
Det.....	detector
DLaTGS.....	deuterated L-alanine doped triglycine sulfate
Emiss.....	emissivity
EMRP.....	European Metrology Research Program
Encl.....	enclosure
FDTGS.....	FIR deuterated triglycine sulfate
FFT.....	fast Fourier-transformation
FIR.....	far-infrared wavelength range
FT.....	Fourier-transformation
FTIR.....	Fourier-transform infrared spectrometer

GBB-C..... GLORIA Blackbody “Cold”
 GBB-H GLORIA Blackbody “Hot”
 GLORIA..... Gimballed Limb Observer for Radiance Imaging of the Atmosphere
 GUM Guide to Uncertainty of Measurement
 H..... heating plate
 hem.....hemispherical
 i..... incident
 IR..... infrared range
 isoth..... isothermal
 ITS-90..... International Temperature Scale of 1990
 K..... contact layer
 LBB..... liquid-operated variable temperature blackbody
 LN₂liquid nitrogen
 MCTliquid nitrogen-cooled mercury cadmium telluride detector
 MetEOC European Metrology for Earth Observation and Climate
 MIR mid-infrared wavelength range
 NEP noise-equivalent power
 NIRnear-infrared range
 NIST National Institute of Standards and Technology
 Non non-isothermal
 PRT.....platinum resistance thermometer
 PTB..... Physikalisch-Technische Bundesanstalt
 PTR..... Physikalisch-Technische Reichsanstalt
 r..... reflected
 RBCF..... Reduced Background Calibration Facility
 refreference
 Refl..... reflection
 s..... specular
 SNR signal-to-noise ratio
 SPRT..... Standard Platinum Resistance Thermometer
 STEEP3 Blackbody Emissivity Modeling Software
 Sub..... substrate
 t..... transmitted
 TF..... thin film
 UTLS..... Upper Troposphere/Lower Stratosphere
 VIRST..... vacuum infrared standard radiation thermometer
 VLTBB.....vacuum low-temperature blackbody
 VMTBB.....vacuum medium-temperature blackbody
 ZFF zero-filling factor

Contents

1 Introduction	1
2 Physical basis	4
2.1 Basic definitions	4
2.2 Radiation from a blackbody	5
2.3 Planck's law	6
2.4 Wien's displacement law	7
2.5 Lambert's cosine law	7
2.6 Technical application of blackbody radiation	8
2.7 Properties of surface.....	9
2.8 Kirchhoff's Law.....	15
2.9 Relation among surface properties	15
2.10 Classical electromagnetic theory	16
3 A brief review of methods for emissivity measurement	21
3.1 Indirect methods.....	21
3.2 Direct calorimetric methods	23
3.3 Direct radiometric methods.....	24
4 Setup for emissivity measurement under vacuum at PTB	26
4.1 General layout of the Reduced Background Calibration Facility	26
4.2 Vacuum reference blackbodies	29
4.3 Opto-mechanical unit and LN ₂ -cooled blackbody	32
4.4 Vacuum Infrared Standard Radiation Thermometer (VIRST)	34
4.5 Vacuum Fourier-Transform Infrared spectrometer (FTIR)	34
4.6 Vacuum sample holder for emissivity measurements	40
5 Metrological characterizations of FTIR-spectrometer and reference blackbodies	48
5.1 Performance of the facility and measurement of radiance temperature of VLTBB	48
5.2 Effective emissivity and uncertainty budget of reference blackbodies	55
5.3 Validation and traceability of emissivity measurements	75
6 Evaluation of emissivity measurements under vacuum	78

6.1 Calculation of emissivity and generalized radiation budget	78
6.2 Uncertainty budget.....	89
6.3 Evaluation of emissivity measurement under vacuum	93
7 Emissivity of high absorbing and low absorbing materials.....	94
7.1 Nextel Velvet Black 811-21.....	95
7.2 Silicon carbide.....	100
7.3 Polished gold.....	105
7.4 Theory of thin films with wave interference effect and validity of Kirchhoff's law discussed based on the emissivity results of Aeroglaze Z306	108
8 In-flight blackbody calibration system of the GLORIA Interferometer.....	129
8.1 GLORIA Blackbodies.....	130
8.2 Spectral radiance of GBBs.....	132
8.3 Emittance of GBBs	135
9 Conclusion	138
References.....	142
Acknowledgements	148

1 Introduction

Radiation thermometry is an important field of physics that covers measuring the temperature of a body via its emitted electromagnetic temperature radiation. As a fast and remote technique for temperature determination it has unique potential ranging from non-contact temperature control of numerous industrial production processes to climate research by remote sensing of the Earth. Accurate knowledge of the radiation properties of a material, i.e. its spectral emissivity, is always essential in performing a quantitative temperature measurement and determining a precise calculation of heat balance. The use of solar energy, the application of high-temperature ceramics in high-temperature engines, modern furnace technologies, improved thermal insulation of buildings, cryogenic insulations and remote sensing of the Earth require a sound metrological knowledge of the emissivity of the involved materials.

Radiation thermometry is now routinely performed over a temperature range from $-170\text{ }^{\circ}\text{C}$ to $3000\text{ }^{\circ}\text{C}$ in science and industry. When quantitative measurements are needed, emissivity is a key parameter and often limits the achieved uncertainty of the experiment. As emissivity is a material property that depends on temperature, wavelengths, angle of emission and the chemistry and surface structure of the sample, its precise measurement is complex. Often the emissivity must be determined for each individual sample as reliable literature data is not available or significantly depends on the individual surface structure. Currently there are a large number of methods for measuring emissivity but so far no technique completely meets the wide range of challenges posed by modern science and industry. Practical methods, as given e.g. in the technical specification VDI/VDE 3511-4 [1], often only provide a good approximation but give no accurate result with a reliable uncertainty value. To meet this need the main objective of this work is the development and application of a method for highly accurate directional spectral emissivity, total directional emissivity and total hemispherical emissivity measurements in a broad wavelength and temperature range with extremely low uncertainties. The experiment is performed under vacuum conditions in order to reduce heat losses by convection and, furthermore, to meet the specific needs of high-temperature solar energy production and remote sensing applications.

An important application that requires very low uncertainties of emissivity is the characterization of absorbers for high-temperature solar thermal energy generation [2]. Solar energy has the potential to become one of the major sources of renewable energy and the development of solar energy technologies has great advantages for economic growth and

better environmental protection. Solar absorptivity and thermal emissivity of absorber coatings are key parameters for the determination of efficiency solar thermal systems. Modern developments in high-temperature solar energy production are aiming to apply molten salts for heat storage and seek to operate the temperatures of the absorber pipes up to 600 °C. However, a major difficulty in the measuring process is that the emissivity of these absorber coatings is very low in the mid-infrared wavelength range (MIR), about 0.01 to 0.02. The reduction of the measurement uncertainty can provide support for industry by enabling systematic investigations of improved absorber coatings that lead to higher thermal efficiency and consequently, significant economic benefits. A major aim of this work is to measure the emissivity of solar absorber coatings with an, until now, unrivaled absolute uncertainty in the MIR of less than 0.005. An additional advantage is the possibility to measure the emissivity close to operating conditions, as the absorber is generally placed inside of an evacuated glass tube.

Another important area of application of precise emissivity measurements is the characterization of coatings of onboard reference blackbodies for air and space-borne remote sensing missions. Not only the number of current international projects, missions and initiatives underline the importance of the remote observation of the Earth, atmosphere and climate [3-5], but there is also a foreseeable increasing impact of possible climate change on society, ecology and economy. The state-of-the-art experimental techniques conducted in remote sensing experiments require sophisticated and traceable radiometric calibration procedures that lead to the lowest possible uncertainties. In general the expansion of the wavelength range and the reduction of the uncertainty of emissivity measurements of the coatings of the reference blackbodies will result in lower radiometric uncertainties of the reference blackbodies. This will directly lead to lower uncertainties of the data derived from the remote sensing experiments and should improve the existing climate models and deepen our understanding of the climate of the Earth. To significantly reduce the achieved uncertainties, an emissivity measurement of the coatings and an accurate radiometric and thermometric characterization of the complete reference blackbodies in the wavelength ranging from 4 μm to 100 μm is required, as well as a characterization under application conditions i.e. under similar conditions to space or the stratosphere.

Calibration and measurement procedures based on reference sources can be found in many quantitative spectroscopic applications. A better general knowledge about the reference source allows to improve the quality of the quantitative optical experiments and applications. This work might serve as a good example for this statement. With the newly developed emissivity measurement facility the emissivity measurements are based on two vacuum reference blackbodies. Precise metrological characterization of blackbodies in the MIR

and FIR (THz) spectral ranges requires the calculation of the effective emissivity of the applied cavities [6]. However, there are two difficulties: firstly, the lack of precise emissivity information about the wall coatings especially in the FIR, as there are no direct emissivity measurements of coatings up to 100 μm . Secondly, the increase of transparency of some coatings towards longer wavelengths. Consequently, another objective of this work is to develop a method that could also provide accurate measurements and calculations of the emissivity of semi-transparent materials.

This work is organized as follows:

In Chapter 2 the theoretical background of radiation properties of materials (blackbody, electromagnetic theory and measured properties) is briefly introduced.

Chapter 3 shortly summarizes current methods of emissivity measurement.

Chapter 4 gives a detailed technical description of the experimental set up for precision emissivity measurement under vacuum conditions achieved in this work.

Chapter 5 describes the complete metrological characterization of all relevant components of this set up.

Chapter 6 gives the detailed procedure of the data evaluation for the emissivity calculation yielding a full uncertainty budget in accordance with the Guide to Uncertainty of Measurement (GUM) [7].

In Chapter 7 representative experimental results are listed. A theory of the emissivity behavior of thin films is developed and compared with the experimental results.

Chapter 8 gives an example of special application, high-metrological characterization of the reference blackbodies in the European Metrology Research Program (EMRP) MetEOC and MetEOC2.

Chapter 9 is a conclusion, summarizing the major achievements of this work and providing an outlook on future applications of the new facility.

2 Physical basis

The study of the interaction of electromagnetic radiation with matter is of great importance as any two emitting objects in the “visual field” of each other interact through the exchange of radiant energy.

Radiation incident on a homogeneous object is partially reflected and partially penetrates the object. If the thickness of the material and its ability to internally absorb radiation, i.e. the absorption coefficient, are sufficiently high for complete absorption, all of the penetrating radiation is absorbed into the material and converted into internal energy. Conversely, if the thickness and the absorption coefficient are insufficiently high, the radiation can be partially transmitted through the material and is only partially absorbed. In the latter case the object is called optical thin. The product of the thickness and the absorption coefficient is a dimensionless quantity and is called absorbance or historically, the optical thickness.

In nature, there is no material that completely absorbs or fully reflects incident radiation, as materials usually pronounce one or the other ability. Typical materials with high reflectivity are metals, especially those with a polished surface. Even in this case, a small portion of the energy is absorbed by the surface of the metal. Good absorbers, for example, special black coatings (carbon black or gold black), which are designed for high absorbance, absorb most of the incident radiation, but still a small part of it is reflected at the surface.

The basic optical properties of materials as well as the concept of the blackbody, which has complete internal absorption, will be discussed in this chapter.

2.1 Basic definitions

It is necessary to provide the radiometric definitions of which optical energy transfer is based. All basic concepts discussed below can be found in detail in the [8]. To describe the basic definitions such as radiant power, intensity, exitance or radiance, the dependence of the energy of radiation on geometrics (area, solid angle) and time characteristics are used.

Radiant power or radiant flux Φ is the energy W per unit of time t which is carried by electromagnetic radiation:

$$\Phi = \frac{dW}{dt} \quad (2.1)$$

Radiant exitance M is the radiation power, leaving a surface per unit area:

$$M = \frac{d\Phi}{\cos \vartheta dA} \quad (2.2)$$

where ϑ is the angle between the normal of area dA and the direction of radiation.

Radiant intensity I is the radiant power leaving a source (undefined area) into an element of solid angle $d\Omega$:

$$I = \frac{d\Phi}{d\Omega} \quad (2.3)$$

Finally, radiance L can be described as the radiant flux emitted by a surface per unit element projected onto the direction of the radiation and into a unit of solid angle around this direction:

$$L = \frac{d^2\Phi}{\cos\vartheta dA d\Omega} \quad (2.4)$$

2.2 Radiation from a blackbody

An object that absorbs all incident radiation without reflecting and transmitting it is called a blackbody [9]. This idealized physical object, which serves as a standard in radiation thermometry has the following important properties:

- A blackbody is a perfect emitter for radiation in the visible and infrared region.
- A blackbody is a perfect absorber regardless of wavelength in the above-named spectral ranges and independent of angle of incidence.
- A blackbody is a perfect Lambert emitter, meaning that the directional spectral flux or power observed from the blackbody is directly related to the cosine of the angle between the observed line of sight and the surface normal for the emitting surface of the blackbody. Using the definition of radiance, this means the radiance emitted by the blackbody shows no angular dependence.
- The peak wavelength of the blackbody radiation can be calculated according to Wien's displacement law.
- The total spectrally integrated radiant power emitted from a blackbody can be calculated according to the Stefan-Boltzmann law.

This allows the use of a blackbody as a primary radiometric standard in metrology as the electromagnetic radiation of a blackbody is described by Planck's law as a function of the absolute temperature and wavelength.

2.3 Planck's law

The spectral distribution of blackbody radiation is a very important fundamental property for most applications in radiation thermometry. The mathematical description of this spectral distribution was derived by Planck [10], where $L_{\lambda b}(\lambda, T)$ denotes the spectral radiance at the wavelength λ and at the temperature of the blackbody T in Kelvin:

$$L_{\lambda b}(\lambda, T) = \frac{2\pi hc_0^2}{\pi\lambda^5 [\exp(hc_0 / \lambda T k_B) - 1]} = \frac{c_1}{\pi\lambda^5 [\exp(c_2 / \lambda T) - 1]} \quad (2.5)$$

Here h is the Planck constant, k_B is the Boltzmann constant, c_0 denotes the speed of electromagnetic radiation in a vacuum and the values of c_1 and c_2 are known as the first and second radiation constants [11]:

$$c_1 = 2\pi hc_0^2 = 3,741771 \times 10^{-16} \text{ W m}^2$$

$$c_2 = h \frac{c_0}{k_B} = 1,438777 \times 10^{-2} \text{ m K}$$

The functional dependence of the spectral radiance of a blackbody on the temperature and wavelength is plotted in Fig. 2.1. Here the spectral radiance is shown on the vertical axis; the horizontal axis shows the wavelengths. Both are shown on logarithmic scales.

The total radiance of the blackbody can be found by integrating the Planck's law over all wavelengths, which is known as the Stephan-Boltzmann law:

$$L_b = \int_0^{\infty} L_{\lambda b}(\lambda) d\lambda = \frac{\sigma}{\pi} T^4 \quad (2.6)$$

where σ denotes the Stephan-Boltzmann constant [11]:

$$\sigma = \frac{2c_1\pi^5}{15c_2^4} = 5.670373 \times 10^{-8} \text{ W m}^{-2}\text{K}^{-4}$$

The dependence between the total radiant exitance emitted by the blackbody in all directions and the total radiance gives:

$$M_b(T) = \pi L_b(T) = \sigma T^4 \quad (2.7)$$

2.4 Wien's displacement law

All of the curves in Fig. 2.1 have a maximum that shifts to shorter wavelengths as the temperature increases. The wavelength position of the maximum can be calculated by differentiating Planck's equation and subsequent root finding.

$$\lambda_{\max} T = \frac{c_2}{5} \frac{1}{1 - e^{-c_2/(\lambda_{\max} T)}} \quad (2.8)$$

Solving for λ_{\max} yields Wien's displacement law [12]:

$$\lambda_{\max} = \frac{2897.8}{T} \mu\text{m} \quad (2.9)$$

In words: Wien's displacement law states that the wavelength of peak radiance and peak exitance is inversely proportional to the temperature T (in Kelvin).

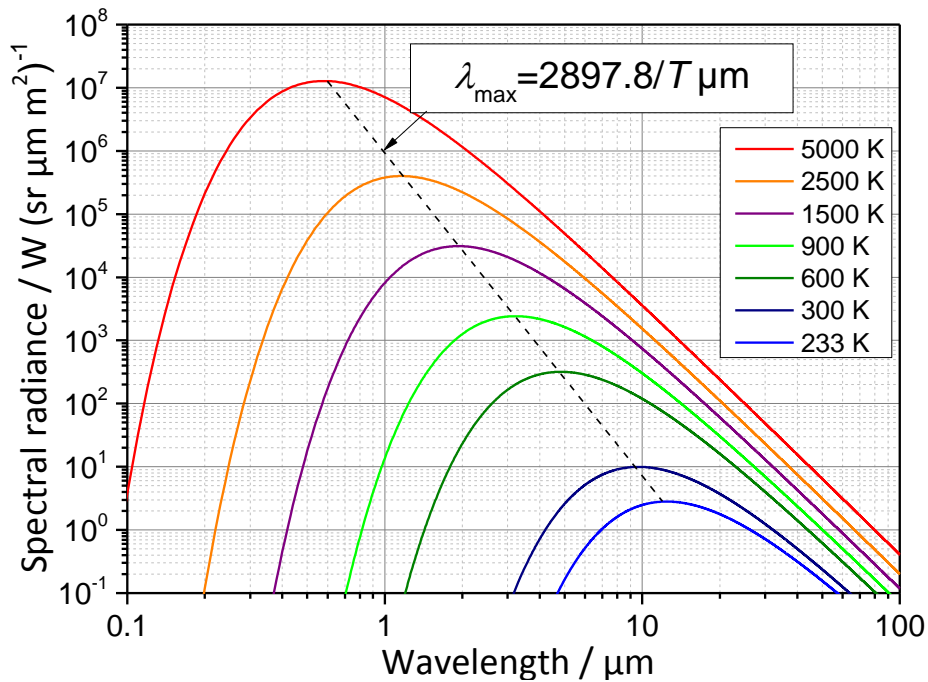


Fig. 2.1: The spectral radiance of a blackbody according to Planck's law plotted for various temperatures ranging from 233 K to 5000 K (the temperature range from 233.15 K to 873.15 K is relevant for this work)

2.5 Lambert's cosine law

Lambert's cosine law states that the radiant intensity is directly proportional to the cosine of the angle between surface normal and the direction of observation ϑ :

$$I(\vartheta) = I_0 \cos \vartheta \quad (2.10)$$

Hence, according to their definitions (Equations 2.2 and 2.4), the radiant exitance and the radiance of surfaces obeying this condition do not depend on the angle ϑ . These surfaces are known as diffuse or Lambertian.

2.6 Technical application of blackbody radiation

As stated previously, a blackbody has a number of key properties that make it a radiation standard. Ideally, it can be stated that for use of a blackbody as a primary standard of radiance or radiation temperature it must be isothermal and have an emissivity of 1 (reflectivity of 0) (Fig. 2.2). In reality an ideal blackbody is not achievable, however a practical blackbody should follow the ideal theoretical concept as closely as possible in order to be an absolute radiator with its radiance only depending on its temperature, but not on the optical properties of the surface or on the material.

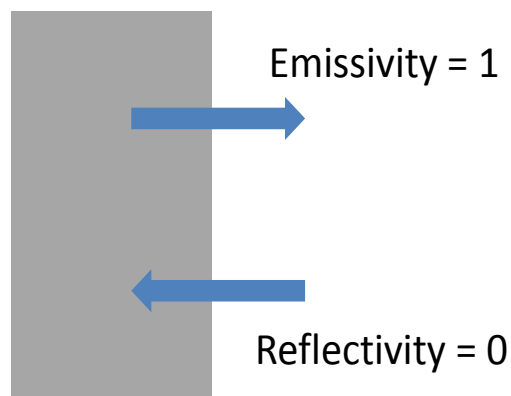


Fig. 2.2: The relation between the emissivity and reflectivity of a blackbody

The ideal black surface does not exist, but by careful design the conditions shown in Fig. 2.2 can be created with very good approximation to the ideal blackbody. A high-quality practical blackbody is often built as an isothermal cavity with a small opening. The first blackbodies built as a cavity radiator were used at the end of 19th century at the Physikalisch-Technische Reichsanstalt (PTR) [13-16]. Due to a very small opening and multiple reflections inside the cavity (Fig. 2.3), essentially all the radiation that falls into the blackbody is absorbed. The nature of a blackbody is based on thermal equilibrium, where the absorptivity of a black surface equals its emissivity (Chapter 2.8, Kirchhoff's law). Therefore the cavity is made with special insulation, radiation screens and often a sophisticated temperature control system, sometimes consisting of several zones, to achieve isothermal conditions. If the temperature of the cavity of the blackbody is higher than the environment, radiation emerges continuously from the cavity. The quality of construction determines how well isothermal conditions and high emissivity can be achieved and consequently, how close the radiation escaping from a

small hole in the cavity is equal to the blackbody radiation. For the emissivity calculation of the blackbodies applied in this work it will later be discussed which consequences a non-ideal isothermicity along the wall of the cavity has on the blackbody radiation of the cavity.

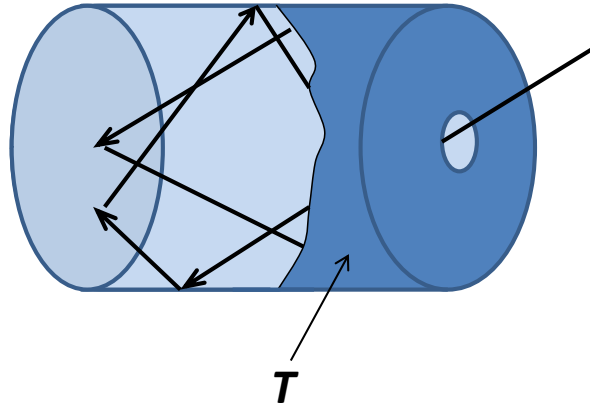


Fig. 2.3: Schematic representation of a blackbody cavity illustrating the concept of multiple internal reflections and a small opening reducing reflectance of radiation entering the opening

2.7 Properties of surface

As described previously, the radiance of an ideal blackbody depends only on its wall temperature, is independent of the wall material and has a Lambertian behavior. The optical properties of real objects are angular-dependent and determined by their composition and surface finish. The quantities describing the optical properties of materials are: emissivity, reflectivity and absorptivity.

Terminology

In this work, the following terminology will be used according to [8]: here the -ivity ending (emissivity, reflectivity or absorptivity) is used as a physical quantity or to describe properties of a material. The -ance ending (emittance, reflectance or absorptance) is associated with the experimental determination of the properties of a specific sample.

2.7.1 Emissivity

Emissivity ε describes the relative ability of a material's surface to emit radiation. It is a dimensionless quantity defined as the ratio of radiance emitted by the material to the radiance of a blackbody at the same temperature T . Therefore, the emissivity is a physical quantity whose value is less than or equal to 1. As mentioned in the introduction, emissivity is the most important characteristic of a material in the calculation of the heat balance and for calibration

and measurement procedures based on reference sources, therefore more specific definitions of emissivity are required.

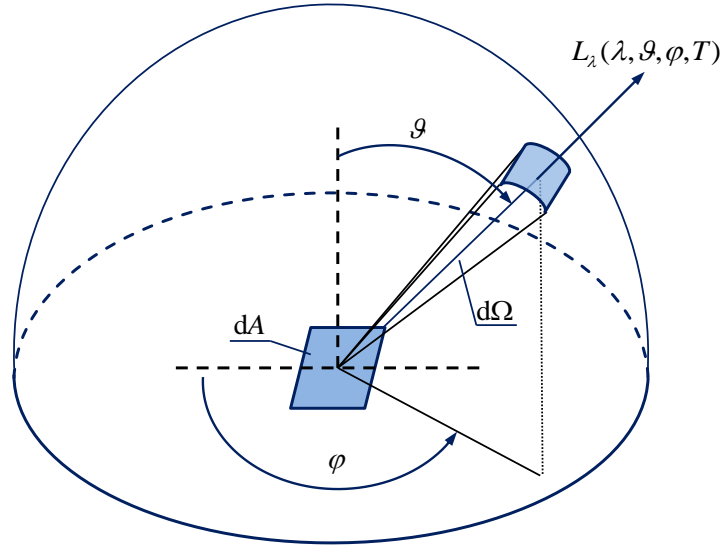


Fig. 2.4: Geometry of directional and hemispherical quantities of emissivity

Directional spectral emissivity

The directional spectral emissivity includes all information concerning the dependence on wavelength λ , direction (θ, φ) and temperature T . This comprehensively defined emissivity is calculated as the ratio of the spectral radiance, radiated by a real surface dA at the wavelength λ and within the solid angle $d\Omega$ to that of a blackbody at the same temperature with an equal emitting surface dA at the same wavelength λ and within the same solid angle $d\Omega$ (see Fig. 2.4):

$$\varepsilon_{\lambda}(\lambda, \theta, \varphi, T) = \frac{L_{\lambda}(\lambda, \theta, \varphi, T)}{L_{\lambda b}(\lambda, T)} \quad (2.11)$$

Directional total emissivity

The directional total emissivity is the ratio of the directional spectral radiance of the real surface integrated over all wavelengths to the wavelength-integrated radiance emitted by a blackbody (Eq. 2.6) at the same temperature. Using Equation 2.11, directional total emissivity can be represented in terms of directional spectral emissivity:

$$\varepsilon(\theta, \varphi, T) = \frac{\pi \int_0^{\infty} \varepsilon_{\lambda}(\lambda, \theta, \varphi, T) L_{\lambda b}(\lambda, T) d\lambda}{\sigma T^4} \quad (2.12)$$

Hemispherical spectral emissivity

The integration over all directions of the hemisphere gives the hemispherical spectral emissivity:

$$\varepsilon_{\lambda}(\lambda, T) = \frac{1}{\pi} \int_{\Omega} \varepsilon_{\lambda}(\lambda, \vartheta, \varphi, T) \cos \vartheta d\Omega \quad (2.13)$$

Hemispherical total emissivity

The hemispherical total emissivity is found by integrating the directional spectral quantities from a real surface and a blackbody over all wavelengths and solid angles:

$$\varepsilon(T) = \frac{\int_0^{\infty} \int_{\Omega} \varepsilon_{\lambda}(\lambda, \vartheta, \varphi, T) L_{\lambda b}(\lambda, T) d\lambda \cos \vartheta d\Omega}{\sigma T^4} \quad (2.14)$$

This quantity is often used in applications where total radiative heat losses are calculated.

2.7.2 Absorptivity

The ratio of the radiation absorbed by a material to the incident radiation is called absorptivity. The absorption depends on the incident radiation and on its characteristics such as wavelength or incident angle. Four quantities of absorptivity are commonly distinguished.

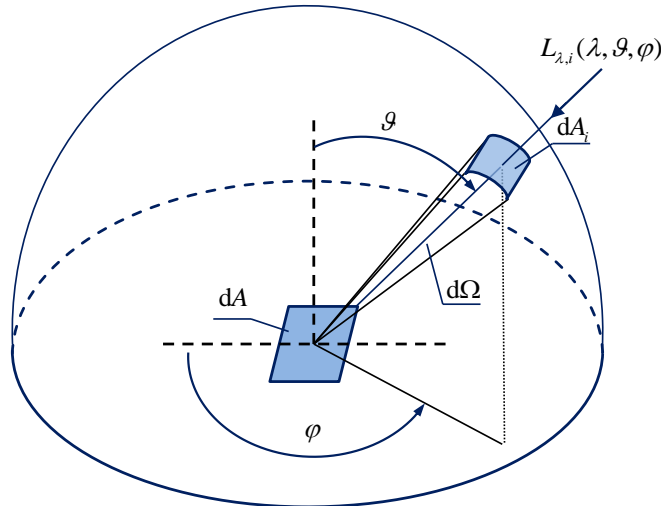


Fig. 2.5: Geometry of directional and hemispherical quantities of absorptivity

Directional spectral absorptivity

The radiant flux incident on a material can be written in terms of the spectral radiance as:

$$d^3\Phi_{\lambda,i}(\lambda, \vartheta, \varphi) = L_{\lambda,i}(\lambda, \vartheta, \varphi) d\Omega dA \cos \vartheta d\lambda \quad (2.15)$$

This equation describes the incident radiant flux from the source dA_i on the area dA of the material per unit time, wavelength and solid angle (see Fig. 2.5). Then the fraction $d^3\Phi_{\lambda,a}(\lambda, \vartheta, \varphi, T)$ that is absorbed by the material defines the directional spectral absorptivity:

$$\alpha_\lambda(\lambda, \vartheta, \varphi, T) = \frac{d^3\Phi_{\lambda,a}(\lambda, \vartheta, \varphi, T)}{d^3\Phi_{\lambda,i}(\lambda, \vartheta, \varphi)} = \frac{d^3\Phi_{\lambda,a}(\lambda, \vartheta, \varphi, T)}{L_{\lambda,i}(\lambda, \vartheta, \varphi) dA \cos \vartheta d\Omega d\lambda} \quad (2.16)$$

Directional total absorptivity

The ratio of the absorbed radiant flux to the incident radiant flux, where both quantities are integrated over the entire wavelength range, is the directional total absorptivity:

$$\alpha(\vartheta, \varphi, T) = \frac{d^2\Phi_a(\vartheta, \varphi, T)}{d^2\Phi_i(\vartheta, \varphi)} = \frac{\int_0^\infty \alpha_\lambda(\lambda, \vartheta, \varphi, T) L_{\lambda,i}(\lambda, \vartheta, \varphi) d\lambda}{\int_0^\infty L_{\lambda,i}(\lambda, \vartheta, \varphi) d\lambda} \quad (2.17)$$

Hemispherical spectral absorptivity

The hemispherical spectral absorptivity can be written in the following form, integrating the incident and absorbed radiation on the material over all directions of the hemisphere (Fig. 2.5):

$$\alpha(\lambda, T) = \frac{d^2\Phi_{\lambda,a}(\lambda, T)}{d^2\Phi_{\lambda,i}(\lambda)} = \frac{\int_{\cap} \alpha_\lambda(\lambda, \vartheta, \varphi, T) L_{\lambda,i}(\lambda, \vartheta, \varphi) \cos \vartheta d\Omega}{\int_{\cap} L_{\lambda,i}(\lambda, \vartheta, \varphi) \cos \vartheta d\Omega} \quad (2.18)$$

Hemispherical total absorptivity

Finally a combination of both integrations is determined. The absorbed radiation integrated over all wavelengths λ and angles (ϑ, φ) divided by the radiation incident from all directions and over all wavelengths gives the hemispherical total absorptivity:

$$\alpha(T) = \frac{d\Phi_a(T)}{d\Phi_i} = \frac{\int_0^\infty \int_{\Omega} \alpha_\lambda(\lambda, \vartheta, \varphi, T) L_{\lambda,i}(\lambda, \vartheta, \varphi) \cos \vartheta d\Omega d\lambda}{\int_0^\infty \int_{\Omega} L_{\lambda,i}(\lambda, \vartheta, \varphi) \cos \vartheta d\Omega d\lambda} \quad (2.19)$$

2.7.3 Reflectivity

To describe reflection it is important to consider not only the geometrical properties of the incident radiation, but also the geometrical properties of the reflected radiation (see Fig. 2.6). With this consideration, two times the number of types of reflectivity compared to emissivity and absorptivity can be distinguished. In this section only the most relevant types used in further calculation will be considered.

Similar to emissivity or absorptivity, the reflectivity depends on the temperature of the surface, but the “parameter T ” will be omitted here for clarity. In addition, there are two important types of reflecting surfaces: specularly reflecting surfaces which fulfill the law of reflection (the equality of the angles of the incident and reflected radiation) and diffusely reflecting surfaces, where an incident ray is reflected and scattered at many angles (Lambertian reflectance, see Chapter 2.5). The reflectivity of real surfaces is found somewhere between these two extremes.

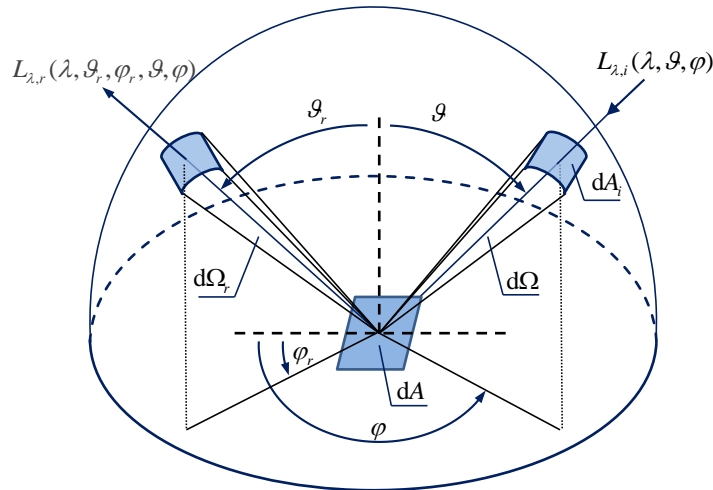


Fig. 2.6: Geometry of directional and hemispherical quantities of reflectivity

Bidirectional spectral reflectivity

Bidirectional spectral reflectivity is the ratio describing how much radiation from direction (ϑ, φ) per unit area and wavelength is reflected in the direction (ϑ_r, φ_r) :

$$\rho_{\lambda}(\lambda, \vartheta_r, \varphi_r, \vartheta, \varphi) = \frac{L_{\lambda,r}(\lambda, \vartheta_r, \varphi_r, \vartheta, \varphi)}{L_{\lambda,i}(\lambda, \vartheta, \varphi) \cos \vartheta} \quad (2.20)$$

Directional-hemispherical spectral reflectivity

The integrated spectral quantities are based on the principle of reflection into the entire hemisphere or the radiation incident from the hemisphere, or both. Thus the ratio 2.21 gives the directional-hemispherical reflectivity and shows how much radiation from one direction is reflected into the complete hemisphere:

$$\rho_{\lambda}(\lambda, \vartheta, \varphi) = \frac{d^3 \Phi_{\lambda,r}(\lambda, \vartheta, \varphi)}{d^3 \Phi_{\lambda,i}(\lambda, \vartheta, \varphi)} = \int_{\Omega} \rho_{\lambda}(\lambda, \vartheta_r, \varphi_r, \vartheta, \varphi) \cos \vartheta_r d\Omega_r \quad (2.21)$$

Hemispherical-directional spectral reflectivity

Similarly, it is possible to calculate the quantity of radiation reflected in one direction from the energy coming from the hemisphere. By integrating over all incident directions, the hemispherical-directional spectral reflectivity can be found as:

$$\rho_{\lambda}(\lambda, \vartheta_r, \varphi_r) = \frac{\int \rho_{\lambda}(\lambda, \vartheta_r, \varphi_r, \vartheta, \varphi) L_{\lambda,i}(\lambda, \vartheta, \varphi) \cos \vartheta d\Omega}{1/\pi \int L_{\lambda,i}(\lambda, \vartheta, \varphi) \cos \vartheta d\Omega} \quad (2.22)$$

Hemispherical spectral reflectivity

If the reflectivity is independent of the direction and integrated over the entire hemisphere in both cases, the hemispherical spectral reflectivity is defined as ratio:

$$\rho_{\lambda}(\lambda) = \frac{d^2 \Phi_{\lambda,r}(\lambda)}{d^2 \Phi_{\lambda,i}(\lambda)} = \frac{\int \rho_{\lambda,i}(\lambda, \vartheta, \varphi) L_{\lambda,i}(\lambda, \vartheta, \varphi) \cos \vartheta d\Omega}{\int L_{\lambda,i}(\lambda, \vartheta, \varphi) \cos \vartheta d\Omega} \quad (2.23)$$

Total reflectivity

Total reflectivities are obtained by integrating over all wavelengths and have a similar structure to types of quantity depending on the directional properties of incident and reflected radiation. A complete description of reflectivity can be found in detail in [17].

2.8 Kirchhoff's Law

This law describes the relation between the emission and absorption of a body in thermodynamic equilibrium. If a body is in an isothermal black enclosure of the same temperature, the emitted and absorbed thermal radiation of this body at every wavelength and in every direction must be equal, otherwise the thermodynamic equilibrium is violated. Hence:

$$\varepsilon_{\lambda}(\lambda, \vartheta, \varphi, T) = \alpha_{\lambda}(\lambda, \vartheta, \varphi, T) \quad (2.24)$$

This is the most specific form of Kirchhoff's law that includes wavelength, directional and surface temperature dependence. It can be generalized to the spectral and/or directional integrated forms similar to directional spectral quantities on both sides: emissivity and absorptivity [9]. An important limitation of the Kirchhoff's law will be considered in relation to thin films in (Chapter 7.4).

2.9 Relation among surface properties

A basic relation connects the previously described optical properties of materials. By also taking the transmissivity into account the relation derived on the energy balance is:

$$W_a + W_r + W_t = W_i \quad (2.25)$$

Where W_i is the incident energy and W_a , W_r and W_t are energies by absorptivity, reflectivity and transmissivity accordingly. In the form of the directional spectral quantities this equation can be written as:

$$\alpha_{\lambda}(\lambda, \vartheta, \varphi, T) + \rho_{\lambda}(\lambda, \vartheta, \varphi, T) + \tau_{\lambda}(\lambda, \vartheta, \varphi, T) = 1 \quad (2.26)$$

According to Kirchhoff's law the directional spectral emissivity and directional spectral absorptivity are equal and the equation can be transformed to:

$$\varepsilon_{\lambda}(\lambda, \vartheta, \varphi, T) + \rho_{\lambda}(\lambda, \vartheta, \varphi, T) + \tau_{\lambda}(\lambda, \vartheta, \varphi, T) = 1 \quad (2.27)$$

For an opaque body without transmitted energy the relation becomes:

$$\varepsilon_{\lambda}(\lambda, \vartheta, \varphi, T) + \rho_{\lambda}(\lambda, \vartheta, \varphi, T) = 1 \quad (2.28)$$

2.10 Classical electromagnetic theory

Classical electromagnetic theory is one of the main basic principles in understanding the optical processes in a material [18]. The calculation of heat balance with the energy transfer in scattering, absorbing and radiating a medium or calculation of thin films with wave interference effects are good examples based on this theory.

2.10.1 Fundamental equations of electromagnetic theory

The electromagnetic theory is based on the four fundamental Maxwell's equations. They can be written in two forms, a differential form and an integral form. These equations express, in a condensed form, the entire set of characteristics of an electromagnetic field.

The first equation is obtained by Gauss's law, which describes the electric field being generated by electric charge. This differential equation is shown in terms of the electric displacement \mathbf{D} and the free electronic charge density ρ_{free} :

$$\text{div}\mathbf{D}=\rho_{\text{free}} \quad (2.29)$$

Gauss's law for magnetism determines that the magnetic monopoles do not exist. The divergence of the magnetic induction \mathbf{B} is zero as the magnetic flux through a closed surface:

$$\text{div}\mathbf{B}=0 \quad (2.30)$$

The 3rd of Maxwell's equations, Faraday's Law, appears in Equation 2.31 and shows that the variation in time of the magnetic induction \mathbf{B} gives rise to a non-conservative electric field \mathbf{E} circulating around it, and vice-versa:

$$\text{rot}\mathbf{E}=-\frac{\partial\mathbf{B}}{\partial t} \quad (2.31)$$

The Maxwell-Ampère equation relates the magnetic field intensity \mathbf{H} to the flowing electric current \mathbf{j} and to the variation in time of the electric flux density $\partial\mathbf{D}/\partial t$:

$$\text{rot}\mathbf{H}=\mathbf{j}+\frac{\partial\mathbf{D}}{\partial t} \quad (2.32)$$

Maxwell's equations in integral form have more generality than the differential form because they are valid in cases where there is a surface rupture, on which the properties of the medium change in discrete steps. Equations in differential form require that all of the quantities in space and time vary continuously.

2.10.2 Material equations

The fundamental equations do not constitute a complete system of equations for the electromagnetic field. These equations are not sufficient for a determination of fields from a given distribution of charges and currents. Maxwell's equations must be supplemented by relations, which include quantities that characterize the individual properties of a medium. These relations are called material equations. The constitutive equations are relatively simple (i.e. linear and scalar) for isotropic media and also in cases of a sufficiently weak electromagnetic field, which is slowly varying in space and time. In this case the constitutive equations are as follows:

$$\mathbf{j} = \sigma_c \mathbf{E} \quad (2.33)$$

$$\mathbf{D} = \varepsilon_p \mathbf{E} \quad (2.34)$$

$$\mathbf{B} = \mu \mathbf{H} \quad (2.35)$$

where σ_c is the specific conductance, ε_p is the permittivity and μ is the magnetic permeability.

2.10.3 Poynting vector

In this work the energy carried by an electromagnetic wave per unit area and per unit time will be discussed. Therefore, it is necessary to consider the law of electromagnetic energy because the light intensity is the energy flux of the field. The total energy of an electromagnetic field in a given volume will vary by the flux of electromagnetic energy through its surface (out of the volume), and by interacting with the matter inside of the volume (e.g. energy loss by charging particles). To describe this law it is necessary to use not only the energy density ω_c in this area, but also the vector \mathbf{S} that characterizes the energy flux density:

$$\mathbf{j} \cdot \mathbf{E} + \text{div} \mathbf{S} + \frac{\partial \omega_c}{\partial t} = 0 \quad (2.36)$$

here \mathbf{j} is the current density, \mathbf{E} is electric field, and total energy contained within the volume can be found using energy density $W = \int \omega_c dV$.

This differential equation expresses the Poynting theorem: energy loss per unit time in a given volume is equal to the energy flux through the surface of the volume plus the work per unit time done by the field on the charges in that volume.

The energy flux density vector for electromagnetic energy is the Poynting vector which represents the amount of energy flux density perpendicular to both oscillations of \mathbf{E} and \mathbf{H} :

$$\mathbf{S} \equiv \mathbf{E} \times \mathbf{H} \quad (2.37)$$

In scalar form the energy flux density transmitted by the wave can be written as:

$$|\mathbf{S}| \equiv \frac{\bar{n}}{\mu c_0} |\mathbf{E}|^2 \quad (2.38)$$

here $\bar{n} = n - ik$ is the complex refractive index, and k is the extinction coefficient.

Detailed information on the basic properties of electromagnetic fields can be found in [18].

2.10.4 Radiative wave propagation within a medium and Fresnel's equation

The previously described Maxwell's equations will be of importance for the theory of electromagnetic waves. Understanding the nature of the propagation of electromagnetic waves in a material and the solution of Maxwell's equations allows one to calculate the optical properties of a material: reflectivity, emissivity and absorptivity.

A plane electromagnetic wave propagating in one direction can be described as the linear combination of two linear polarized waves with perpendicular polarization directions (Fig. 2.7). Furthermore it must be taken into account that the directions of the electric and magnetic fields are perpendicular to each other.

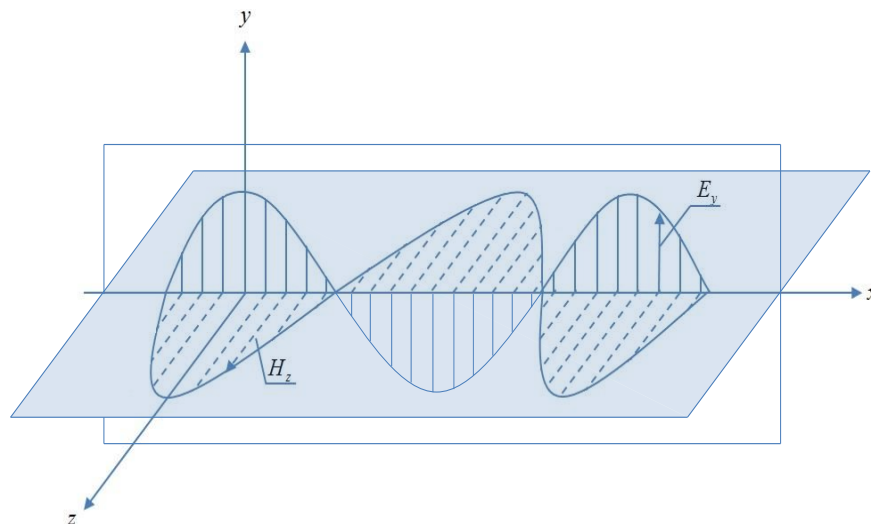


Fig. 2.7: The plane linearly polarized wave propagating in x direction with the electric and magnetic fields

In the following section, the propagation of an electromagnetic wave in a real dielectric i.e. within an absorbing medium, is discussed. This is necessary because the difference between emissivity and reflectivity in absorbing thin films with wave interference effects will

later be investigated. The transition from an imperfect to a perfect dielectric by setting the attenuation to zero ($k = 0$) will also be discussed in further sections of this work.

The equation describing a plane wave polarized in x - y plane with the electric field component E_y and propagating in the positive x -direction of an isotropic media of finite conductivity is shown as:

$$E_y = E_{y,0} \exp \left\{ i\omega \left[t - (n - ik) \frac{x}{c_0} \right] \right\} \quad (2.39)$$

This equation will be used for materials where the wave passes through a medium and some part of the energy will be absorbed. The angular frequency can be expressed by wavelengths in a medium or vacuum: $\omega = 2\pi\nu = 2\pi c / \lambda = 2\pi c_0 / \lambda_0$.

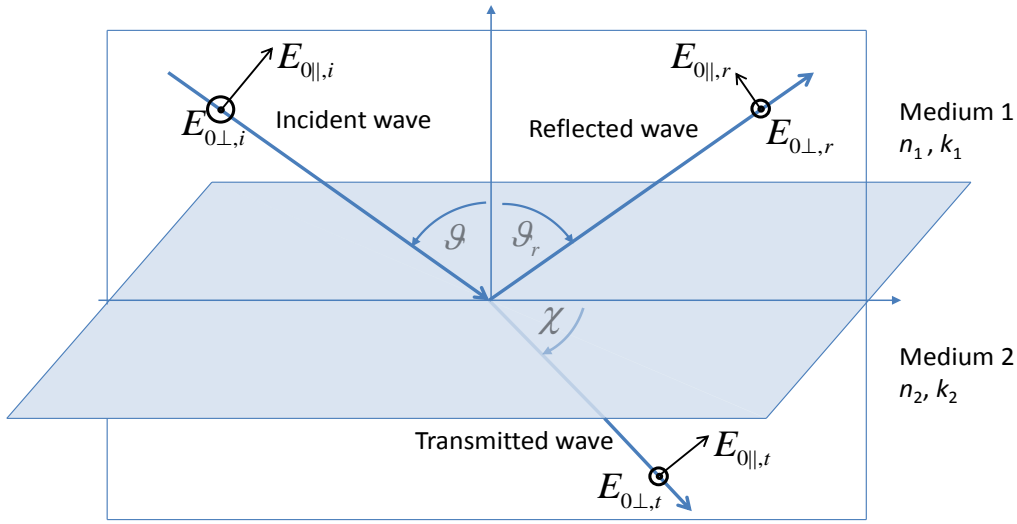


Fig. 2.8: Illustration of the reflection and transmission of an electric field, polarized in two planes on the boundary between two media

The relations between the angles of incident ϑ , reflection ϑ_r , and refraction χ that are in one plane (Fig. 2.8) are described by Snell's law:

$$\bar{n}_1 \sin \vartheta = \bar{n}_1 \sin \vartheta_r = \bar{n}_2 \sin \chi \quad (2.40)$$

This equation proves equality of angles of incidence and reflection for a perfect surface $\vartheta = \vartheta_r$, and also provides an important relation for the angles of incidence and refraction:

$$\frac{\sin \chi}{\sin \vartheta} = \frac{\bar{n}_1}{\bar{n}_2} = \frac{n_1 - ik_1}{n_2 - ik_2} \quad (2.41)$$

The specular reflectivity for an unpolarized ray can be founded by Fresnel's equation considering the parallel and perpendicular components of them:

$$\rho_{\lambda\parallel,s}(\lambda, \vartheta, \varphi) = \left(\frac{E_{0\parallel,r}}{E_{0\parallel,i}} \right)^2 = \left(\frac{\tan(\vartheta - \chi)}{\tan(\vartheta + \chi)} \right)^2 \quad (2.42)$$

$$\rho_{\lambda\perp,s}(\lambda, \vartheta, \varphi) = \left(\frac{E_{0\perp,r}}{E_{0\perp,i}} \right)^2 = \left(\frac{\sin(\vartheta - \chi)}{\sin(\vartheta + \chi)} \right)^2 \quad (2.43)$$

For an absorbing medium the interpretation of the angle of refraction as a simple angle is not possible because $\sin \chi$ is a complex number. However, the two perpendicular polarized parts of the specular reflectivity of an electromagnetic wave propagated from vacuum incident on the material (Fig. 2.8) can be calculated:

$$\rho_{\lambda\parallel,s}(\lambda, \vartheta, \varphi) = \frac{a^2 + b^2 - 2a \sin \vartheta \tan \vartheta + \sin^2 \vartheta \tan^2 \vartheta}{a^2 + b^2 + 2a \sin \vartheta \tan \vartheta + \sin^2 \vartheta \tan^2 \vartheta} \rho_{\lambda\perp}(\lambda, \vartheta) \quad (2.44)$$

$$\rho_{\lambda\perp,s}(\lambda, \vartheta, \varphi) = \frac{a^2 + b^2 - 2a \cos \vartheta + \cos^2 \vartheta}{a^2 + b^2 + 2a \cos \vartheta + \cos^2 \vartheta} \quad (2.45)$$

where a and b are given by:

$$2a^2 = \left[(n^2 - k^2 - \sin^2 \vartheta)^2 + 4n^2 k^2 \right]^{1/2} + n^2 - k^2 - \sin^2 \vartheta \quad (2.46)$$

$$2b^2 = \left[(n^2 - k^2 - \sin^2 \vartheta)^2 + 4n^2 k^2 \right]^{1/2} - (n^2 - k^2 - \sin^2 \vartheta) \quad (2.47)$$

For unpolarized incident radiation the specular reflectivity is calculated as the sum of both polarized components:

$$\rho_{\lambda}(\lambda, \vartheta) = \frac{\rho_{\lambda\parallel}(\lambda, \vartheta) + \rho_{\lambda\perp}(\lambda, \vartheta)}{2} \quad (2.48)$$

Other examples of calculation of reflectivity, transmissivity and emissivity, using electromagnetic theory, are given in detail in [17, 19].

3 A brief review of methods for emissivity measurement

A wide range of methods to determine emissivity are published in literature. These methods cover various temperature and wavelength ranges as well as varied physical conditions and properties of the material being investigated. Some examples of properties include the phase of the sample, its smoothness, roughness, transparency, presence of oxide films or coatings and different dimensions of the macrostructure. In addition, the methods differ by the measured type of quantity: directional-, hemispherical-, spectral- and total emissivity. However only very few methods and instrumentations published in literature state a traceable uncertainty for the measurement. A short overview of different methods will be presented here in order to better evaluate and understand the reasons and motivation for the chosen method described in this work.

The scheme shown in Fig. 3.1 is used here as a possible classification for methods of emissivity measurements. Initially, the methods are divided into two groups: direct and indirect. For direct methods it is characteristic that the emissivity is the directly measured quantity, while for indirect methods the desired emissivity value is obtained by means of other measured quantities using relations among the surface properties described in Chapter 2.9 or optical constants described in Chapter 2.10.4.

3.1 Indirect methods

The most commonly used indirect method for determining emissivity is to calculate the emissivity from the measured directional hemispherical reflectivity of opaque samples using Equation 2.28. The diffuse and specular component of the directional hemispherical reflectivity is detected by applying an integrating sphere [20]. The integrating sphere is either used to hemispherically illuminate a sample while directional reflected radiation is detected, or to detect hemispherically reflected radiation while the sample is directionally illuminated. Another possible way to obtain emissivity without the use of an integrating sphere is by applying a goniometer and measuring the directionally and diffusely reflected radiation at all angles. In approximation it is possible to use the reflection unit described in Chapter 4.5.4 for $12^\circ/12^\circ$ -geometry if the sample has a pronounced specular component and the diffuse component can be neglected. This is the case at very long wavelengths when the surfaces' roughness becomes small compared to the wavelength [20].

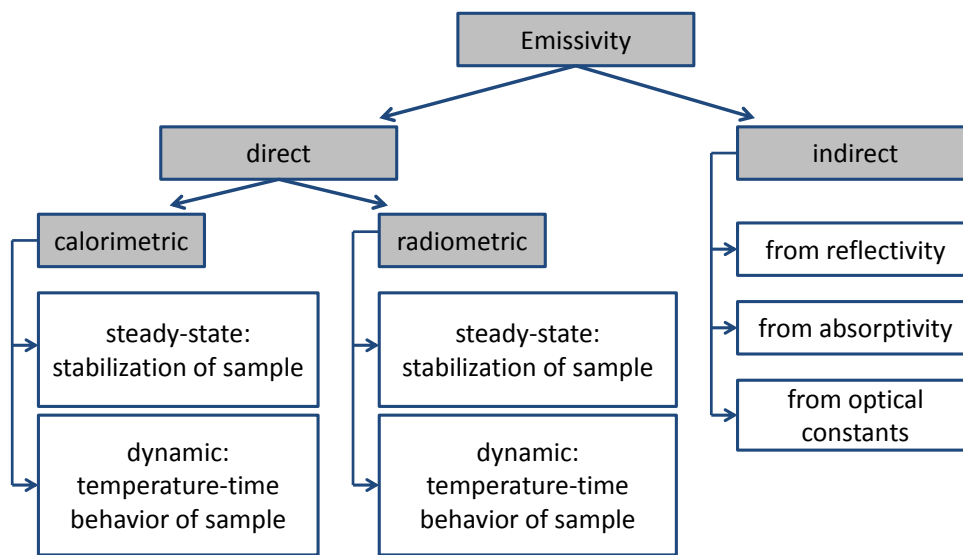


Fig. 3.1: A possible classification scheme for methods of emissivity measurements based on [21]

The indirect method has an important advantage as it allows the possibility to determine the reflectivity (and consequently the emissivity) in the near infrared and visible spectral range at moderate sample temperatures while a direct emissivity measurement requires the sample to be measured at very high temperatures to achieve a sufficient signal-to-noise ratio at short wavelengths. There are disadvantages of the indirect method, as measurements in an integrating sphere are technically difficult if the measurements must be performed at high sample temperatures. Furthermore, at longer wavelengths the wall reflectivity of integrating spheres becomes more and more specular and the integrating sphere becomes less suitable for this application.

L. Hanssen designed a complete hemispherical infrared laser-based reflectometer to determine total reflectivity. Using a gold-coated integrating sphere with the capability of angular dependence measurements and multiple wavelength laser sources, the specular and diffuse components of reflectivity can be measured. The cavity of a blackbody can be investigated on its reflectance properties using this facility [22]. A high-temperature Integrating sphere reflectometer with a sample heating mechanism in temperatures ranging from 150 °C to 1000 °C was designed also by National Institute of Standards and Technology (NIST) [23]. An infrared reflectometer for five angles in the range of 12° to 60° was proposed by Bureau National de Metrologie-Laboratoire National d'Essais (BNM-LNE) [24].

The equality of directional spectral absorptivity and directional spectral emissivity, which is known as Kirchhoff's law, is also used to determine emissivity. Based on the principles of calorimetry, the absorptivity is determined through the measurement of the heating time of a sample when illuminated by a laser beam [25].

The optical constants published in literature were used in [26] for calculating the directional radiative properties of glass as well as the hemispherical quantities obtained from them. The disadvantage of this method is the difficulty of measuring and calculating optical constants. Because sample roughness and surface films significantly affect the result, a complex surface preparation is required and a significant variation in experimental data is reported in literature [17].

3.2 Direct calorimetric methods

The direct calorimetric methods for the determination of emissivity are based on the heat transfer between the sample and the environment and are classified into two groups: the steady-state and the dynamic (transient) techniques. The first method is characterized by a thermal equilibrium of the sample with its environment. Knowing the temperature of the latter as well as the electrical power required for maintaining a constant temperature of the sample, the hemispherical total emissivity can be calculated. The application of the dynamic method involves the solution of the heat balance equation which describes the temperature-time behavior of a sample during its heating and cooling. These methods use different types of heat-transfer mechanisms, different environmental conditions (vacuum or air) and different assumptions, which are discussed in detail in [27]. Calorimetric methods only allow to obtain the hemispherical total emissivity. It is a significant disadvantage in terms of state-of-the-art requirements for the complete optical characterization of a material.

An example of determining the hemispherical total emissivity via steady-state calorimetry using the thermal equilibrium between a sample and a liquid nitrogen-cooled black receiver surface is described in [28].

A facility using two samples and a gadget to reduce heat-loss corrections was proposed by B. Hay [29]. Here the heat flow between two samples, which are surrounded by thermal guard rings of the same temperature, can be calculated. Using this method, the emissivity of solid opaque materials is obtained in the temperature range from $-20\text{ }^{\circ}\text{C}$ to $200\text{ }^{\circ}\text{C}$.

A technique to analyze the heating and cooling curves of a sample located in a vacuum chamber with a small window while being heated by a tungsten-halogen lamp was presented in [30].

A method which applies multi-frequency sine wave thermal modulation by electrical heating of the sample is presented in [31].

3.3 Direct radiometric methods

The most common method for determining emissivity is the direct radiometric method, which is a direct comparison of the radiation from a sample at a homogenous and stable temperature with the radiation from a blackbody of known temperature, according to the definition of emissivity in Chapter 2.7.1. Direct radiometric methods are accomplished by a wide variety of techniques which depend on the type of sample and the spectral and temperature range of interest. The methods differ in the practical realization of the reference blackbodies and the sample heating, the sample surrounding, and the instrumentation to achieve a spectral and, if applicable, angular and lateral resolution. Typically, the blackbody is stabilized at the same temperature as the sample. The sample and the blackbody can also be compared at different temperatures in order to achieve, for example, approximately equal total radiation levels.

The PTB has extensive experience in emissivity measurements using the direct radiometric method. J. Lohrengel [32] created a facility for total emissivity measurement in a vacuum chamber comprised of a sample heater, a reference blackbody and a broadband thermal detector with a flat spectral responsivity curve (“grey” detector). PTB routinely measures spectral and total emissivity from 20 °C up to 500 °C in the spectral range from 2.5 μm to 25 μm in air by comparing the sample radiation with a reference blackbody via a FTIR-spectrometer [33]. The experience with this instrumentation was the starting point for the achievement of emissivity measurement under vacuum conditions as described in this work.

An apparatus for the angular dependent spectral emissivity measurement at temperatures up to 1400 °C was presented by J. Manara [34]. A vessel which can be evacuated or filled with different gases serves as a temperature-stable surrounding for a sample mounted on a cylindrical tube furnace. For the determination of the sample surface temperature either two thermocouples are fixed on the front and back side of the sample by use of a sealing trip. Alternatively they are placed in two holes drilled in the sample.

Some other techniques for direct radiometric emissivity measurements were presented in [35-37].

Emissivity can also be measured by the absence of a reference, such as proposed in [38], where directional emissivity can be calculated by solving the system of equations obtained using two IR cameras for different wavelength bands.

Another method to determine the hemispherical total emissivity of coatings is proposed in [39], in which hemispherical total emissivity is measured using one or more heat flux sensors directly painted with the coating being investigated. Positioned in a cooled vacuum chamber,

the sensors installed on the high conductivity substrate directly measure the heat flux. Depending on the temperature and provided the thermal conductivity of the substrate and the emissivity of the chamber are known, the emissivity of the coating can be determined.

The laser flash technique is applied in a new facility for dynamic (transient) emissivity measurements within a temperature range from 750 °C to 2000 °C at PTB [40, 41]. In a vacuum furnace the sample is brought to the temperature of interest and a time-resolved absolute measurement of an additional temperature rise originating from a laser pulse with known energy irradiating the sample, allows calculating the emissivity of the sample at high temperatures. The heat capacity of the sample must be known and elaborated techniques are necessary to correct both the non-adiabatic temperature rise and the radiation background.

More examples of radiometric measurement techniques are described in detail in [37].

In conclusion, in this work the direct radiometric method was selected for the achievement of emissivity measurements under vacuum conditions. This method meets the objectives and goals described in introduction to this work, to perform measurements with the lowest possible uncertainty in the relevant temperature range for the remote sensing of the Earth and solar thermal energy conversion. Moreover, another argument in favor of this method is the experience of the PTB in radiometric emissivity measurements and the availability of a facility for radiation thermometry, which operates under vacuum conditions and has two high-precision references blackbodies.

4 Setup for emissivity measurement under vacuum at PTB

Within this work a new instrumentation for precise emissivity measurement has been developed as part of the experimental facility for radiation thermometry under vacuum at PTB [42]. This facility, the Reduced Background Calibration Facility (RBCF), is a unique metrology facility within Europe. It has been designed for several purposes: the RBCF allows radiation temperature and spectral radiance measurements strictly traceable to the International Temperature Scale of 1990 (ITS-90) [43] over a broad spectral and wide temperature range for remote sensing experiments as well as for industrial applications. With this work its capabilities have been extended to perform emissivity measurements with very low uncertainty.

In the first step the careful metrological characterization of all relevant parts of the RBCF as well as the development of a vacuum sample holder for emissivity measurements has been accomplished. In this chapter the general layout of the RBCF will be presented.

4.1 General layout of the Reduced Background Calibration Facility

The RBCF consists of several major units (Fig. 4.1): the source chamber, the detector chamber, the liquid nitrogen-cooled (LN_2) beamline, the opto-mechanical unit and the Fourier-transform infrared (FTIR) spectrometer. All parts of the instrumentation can be operated under vacuum conditions. Source and detector chambers are located at a distance of 2500 mm from each other, directly connected via the liquid nitrogen-cooled beamline. Use of linear translation units in both chambers allows calibration and comparison of the different sources and detectors simultaneously by positioning them on the optical axis defined by the cooled beamline (Fig. 4.2).

Several reference sources are operated at the RBCF: two vacuum variable-temperature blackbodies located in the source chamber (VLTBB and VMTBB) and a cold-reference source, the LN_2 -cooled blackbody, which is mounted on top of the opto-mechanical unit. The vacuum low-temperature blackbody (VLTBB) for the temperature range from -173 °C to 170 °C and the vacuum medium-temperature blackbody (VMTBB) for the temperature range from 80 °C to 430 °C are described in detail in Chapters 4.2 and 5.2. There is also the possibility of using additional blackbodies, an indium fixed-point blackbody and a liquid-operated variable temperature blackbody (LBB), but in this work they will be not considered.

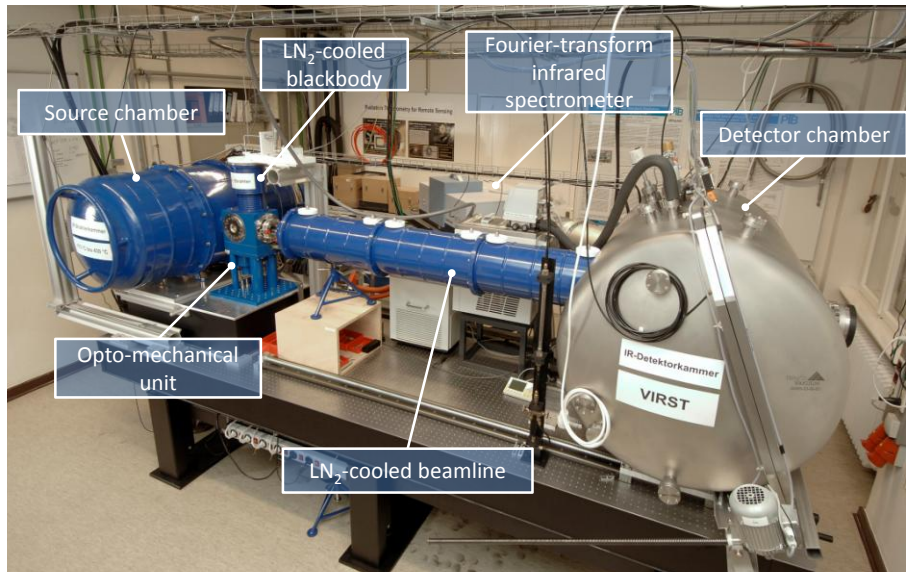


Fig. 4.1: Photo of the reduced background calibration facility (RBCF) illustrating the general concept: source and detector chambers, LN₂-cooled beamline, opto-mechanical unit, spectrometer and LN₂-cooled blackbody

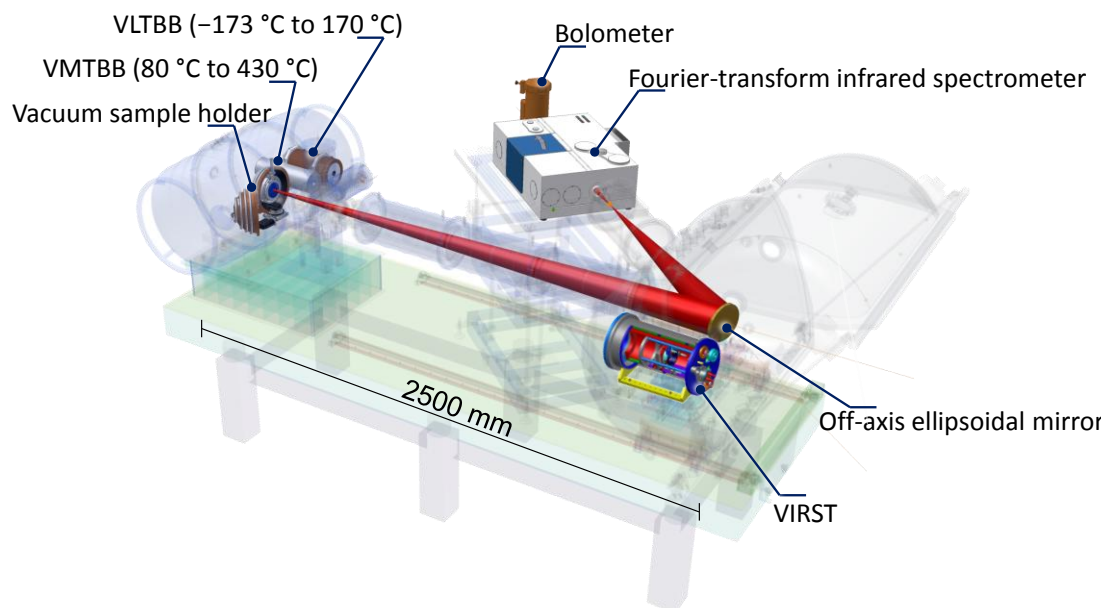


Fig. 4.2: Transparent view of the reduced background calibration facility (RBCF) to illustrate the positions of the blackbodies VLTBB and VMTBB, the vacuum sample holder for emissivity measurements, the vacuum infrared standard radiation thermometer (VIRST) and the optical path of the radiation in the LN₂-cooled beamline

The source chamber provides additional space, that either a radiation source under test or the sample holder with the sample enclosure for spectral emissivity measurement can be placed in the chamber next to the reference blackbodies. Optionally an additional vertical translation stage can be mounted in the source chamber. It allows a full 2-dimensional scan of

the surface of a source under test along the optical axis. This is especially important for the characterization of large aperture sources used as, for example, reference sources of hyperspectral imagers (i.e. limb sounding).

Two schemes for recording radiation are currently used at the RBCF:

- With the vacuum FTIR-spectrometer in terms of spectral radiance, in the wavelengths range from 1 μm to 1400 μm . Via an off-axis ellipsoidal mirror, mounted on the translation stage in the detector chamber, the radiation from the blackbodies or the sample under test is imaged onto the entrance port of the FTIR-spectrometer (Fig. 4.2).
- With the vacuum infrared standard radiation thermometer (VIRST) [44] in terms of radiation temperature from -170 $^{\circ}\text{C}$ to 170 $^{\circ}\text{C}$, in the spectral band from 8 μm to 14 μm .

One of the main features of the RBCF is operation under vacuum conditions and reduction of the background radiation by the cooling of all critical parts - the opto-mechanical unit, all apertures and optical components in the optical path - with liquid nitrogen. This significantly reduces the uncertainty of emissivity measurements. Furthermore, the uncertainty derived from changing atmospheric absorptions caused by change of partial pressures of H_2O and CO_2 is also omitted. Operation under vacuum conditions allows a more accurate determination of the surface temperature of the sample (Chapter 6) resulting from the absence of heat conductance through the air and especially avoiding convective heat loss from the sample surface (necessary for calculation of the surface temperature in air [33]).

Vacuum

The source and detector chambers are equipped with several vacuum pumps: each chamber is evacuated by a combination of an oil-free roots-backing pump and a turbomolecular pump to establish a vacuum of typically 10^{-6} hPa. A valve located between the opto-mechanical unit and the LN_2 -cooled beamline provides a possible separation of the two chambers and simplifies the process of evacuating and venting. Between the detector chamber and the FTIR-spectrometer is a diamond window. This is necessary because the vacuum inside of the spectrometer is typically 10^{-2} hPa and not as low as in the RBCF, so the two vacuum regimes must be separated. In addition, this simplifies the venting of the spectrometer which is necessary when detectors and beamsplitters must be changed. Due to the use of nitrogen gas for ventilation, as well as the utilization of pressure sensors, it is possible to control the pressure inside the facility. It allows performing the experiments not only under a high vacuum but also at well-defined pressure levels, while still avoiding water absorption. This is important for remote sensing experiments, when measurements are taken

at different heights in the atmosphere, requiring calibration of reference source under similar conditions (Chapter 8).

Optical Alignment

The optical alignment of the facility is achieved with the help of several components. One laser is located behind the source chamber and is aligned onto the optical axis through a vacuum window on the back of the source chamber; a portable bidirectional laser is placed in the source chamber on the translation stage, allowing to trace and adjust the pathway of the optical radiation in both directions. The internal laser of the spectrometer allows an additional verification of the alignment.

The radiation emitted by the sources is imaged onto the FTIR-spectrometer by using an off-axis ellipsoidal mirror and a mechanism for tilting and swivelling the mirror is installed. It is mounted on the translation stage in the detector chamber and allows the precise adjustment of the mirror in three directions. This is facilitated by the adjustment lasers.

Lastly, using two bellows, which connect the spectrometer to the source chamber and the opto-mechanical unit to the beamline (Fig. 4.7), the ability to vary the length of the optical path at a distance of ± 50 mm is provided for adjustment of the focusing.

4.2 Vacuum reference blackbodies

The resulting overall accuracy of measurements and calibration procedures in radiation thermometry is significantly based on the accuracy of the applied radiation standard. The primary radiation standard in metrology is the blackbody, which plays the central role through the direct method of emissivity measurements. Two dedicated vacuum variable-temperature blackbodies, VLTBB and VMTBB, were developed for the RBCF. Their design and characterization will be described below and in Chapter 5.2.

4.2.1 Vacuum Variable Low-Temperature Blackbody (VLTBB)

The VLTBB is the radiation standard in the temperature range from -173 °C to 170 °C. The concept of the VLTBB is shown in Figures 4.3 and 4.4. It consists of three basic components: a long cylindrical radiation cavity with a conical bottom, a three-zone heater of the cavity for fine temperature regulation and an outer thermostat providing the coarse temperature regulation. The cavity made of oxygen-free copper is 40 mm in diameter, 250.6 mm in length and has an aperture of 22 mm diameter. It was coated with the space-qualified black paint Aeroglaze Z306 [45] which is investigated in detail in this work.

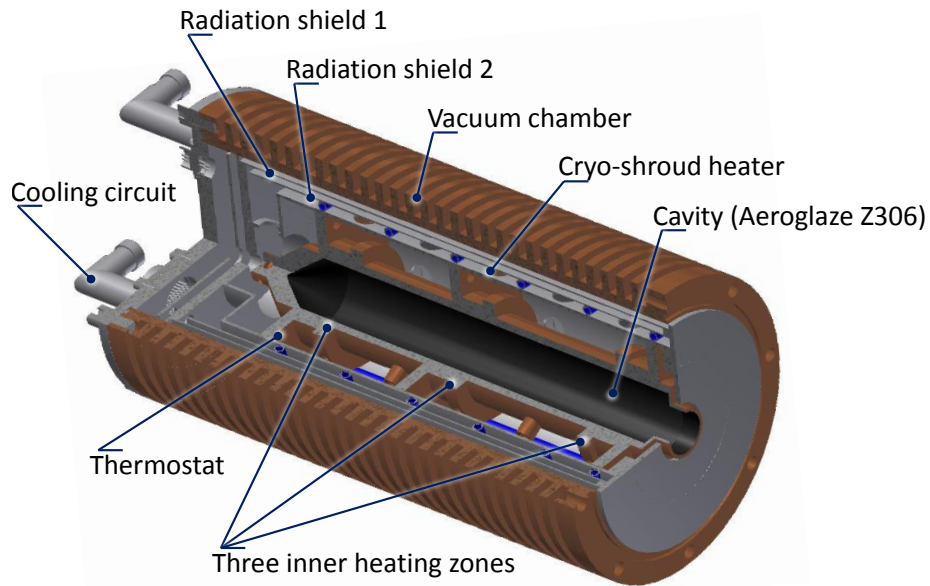


Fig. 4.3: The construction of VLTBB in a cross section

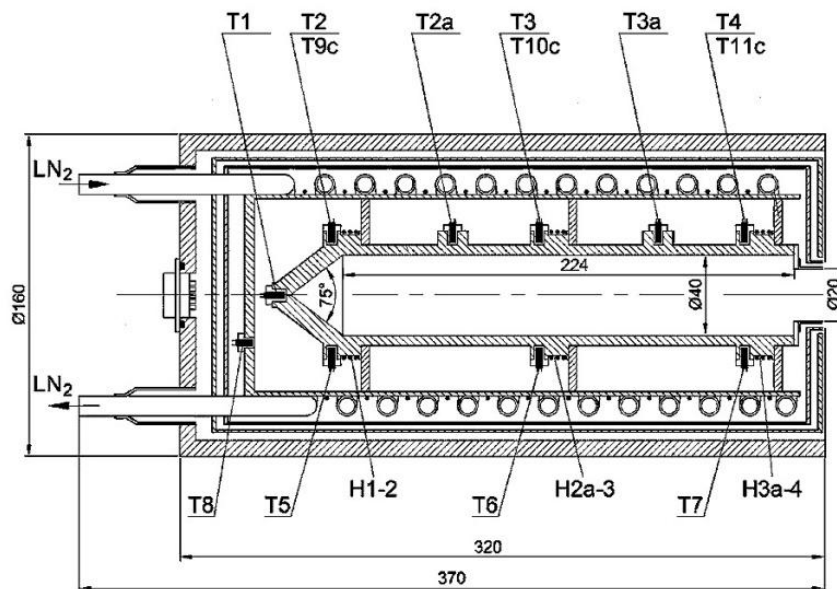


Fig. 4.4: Schematic drawing of the VLTBB from [48]: the cavity dimensions and all thermometers are shown

Six platinum resistance thermometers (PRTs, [46]) (T1, T2, T2a, T3, T3a, T4) are located along the cavity for monitoring of the blackbody temperature via a Hart Super-Thermometer model 1590. Six more PRTs are used for precision temperature regulation, of them, T9c, T10c and T11c, located respectively in the first H1-2, second H2a-3, and third H3a-4 zones, are used with the microcontroller Eurotherm 2604 for the respective temperature control. The three other PRTs, T5, T6 and T7, are read out by a Keithley Multimeter and allow the correction of

the set-point of the microcontroller via the control program. The outer thermostat has a reservoir for liquid nitrogen cooling and a cryo-shroud heater. The regulation of the outer thermostat is done with the thermometer T8 used in the screen temperature controller. Two radiation screens and all above-mentioned components are contained within a vacuum housing. A more detailed description of the VLTBB is given in [47].

4.2.2 Vacuum Variable Medium-Temperature Blackbody (VMTBB)

The VMTBB is of similar design as the VLTBB and operates in the temperature range from 80 °C to 430 °C (Figs. 4.5 and 4.6). Three inner heating zones provide a temperature fine regulation via direct contact with the cavity. The diameter of the cavity of VMTBB is made of oxygen-free copper and measures 26 mm. The length is 243.3 mm and the diameter of the aperture is 20 mm. The cavity is coated with the black paint Duplicolor tested by PTB for high temperature application, up to 430 °C.

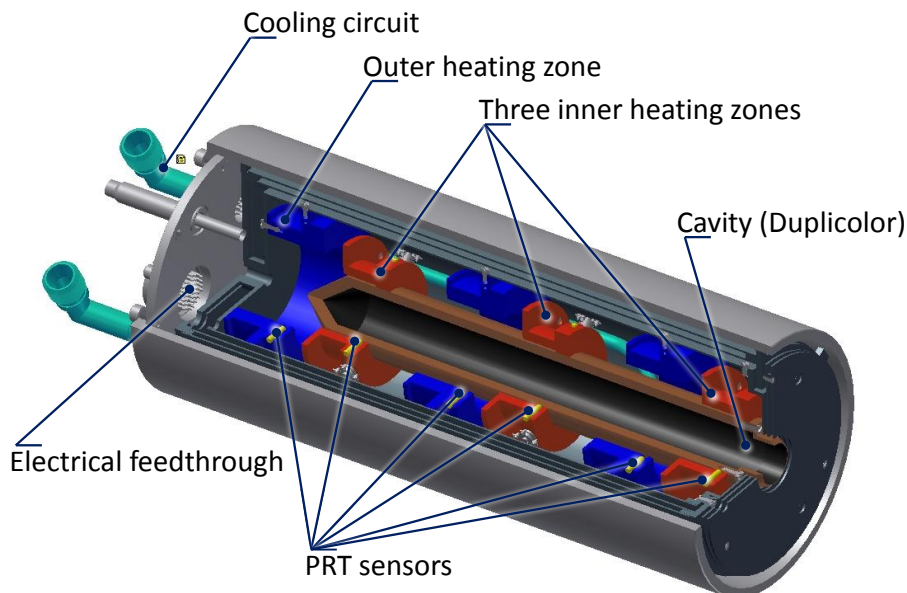


Fig. 4.5: The construction of VMTBB in cross section

The VMTBB also has an electrically-heated thermostat with three heating zones for a coarse temperature regulation and an additional gas-cooling inlet for a quick change of temperature. Six PRTs (T1, T2, T2a, T3, T3a, T4) are located along the cavity and dedicated to monitoring the cavity temperature via the Hart Super-Thermometer model 1590. T8 provides the regulation of the thermostat, TS-1, TS-2 and TS-3 serve for individual regulation of three heating zones via the microcontroller Eurotherm 2604 and TC-1a, TC-2a and TC-3a- are again used for the correction the set-point of the microcontroller with the digital precision

multimeter Keithely 2000 and the control-software. A more detailed description of the VMTBB is given in [49].

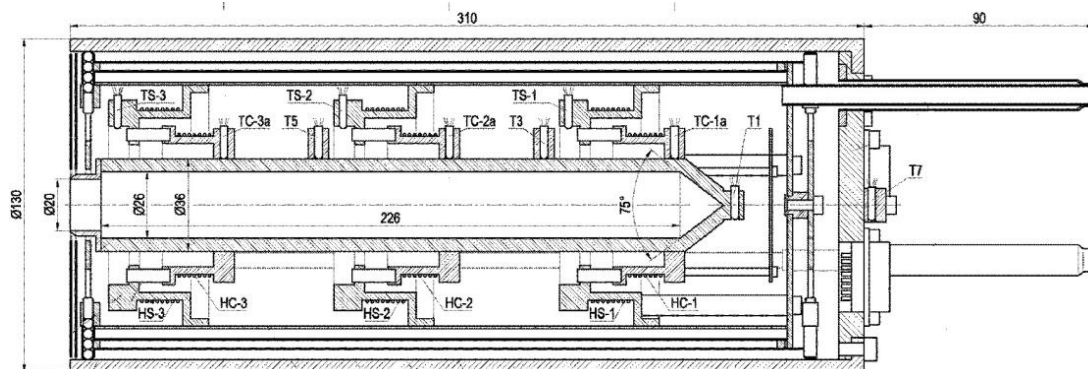


Fig. 4.6: Schematic drawing of the VMTBB from [50]: the cavity dimensions and all thermometers are shown

4.3 Opto-mechanical unit and LN₂-cooled blackbody

The opto-mechanical unit is the part of the facility which connects the source chamber with the beamline and via the beamline with the detector chamber. In the case of emissivity measurements it consists of the following components: an LN₂-cooled reference blackbody, an apertures system, a reflective chopper wheel and a valve. In Fig. 4.7 the layout of the opto-mechanical unit is shown with the LN₂-cooled blackbody mounted headover on top. In Fig. 4.8 the cross section of the LN₂-cooled blackbody is depicted without outer housing.

The LN₂-cooled blackbody is a radiation standard at the temperature of liquid nitrogen at -196 °C. It has an outer housing, a reservoir for liquid nitrogen and a cylindrical radiation cavity with a conical bottom (Figs. 4.7 and 4.8). The cavity is placed inside a reservoir of liquid nitrogen so that cooling occurs over the entire area of the cavity from the outside, including the bottom. There is a space for evacuation between the reservoir wall and the housing. The housing of the blackbody has a connection flange with an o-ring groove and, thus, after connection to the opto-mechanical unit, the inner surface of the cavity as well as the space between the reservoir wall and the housing are under vacuum conditions. The reservoir filled with liquid nitrogen remains at ambient pressure constantly. A protective screen, provided in the upper part of the reservoir, is used to reduce the direct heat exchange between the environment and the walls of the blackbody. Thus, there is only one possibility for direct heat exchange between the cavity and the outside: by conduction via the welding joint of the housing with the reservoir. The latter, in turn, has direct contact to the cavity. Thermometer (T1) located at the wall of the reservoir at the same level with the bottom not only allows current temperature determination, but also ensures that the level of the liquid is above a

threshold defined by the mount position of the thermometer. The inner surface of the cavity is made of steel and coated with Aeroglaze Z302. The optical axis of the LN₂-cooled blackbody is perpendicular to the main optical axis of the facility and a reflective chopper wheel is used for imaging radiation from the LN₂-cooled blackbody onto the beamline.

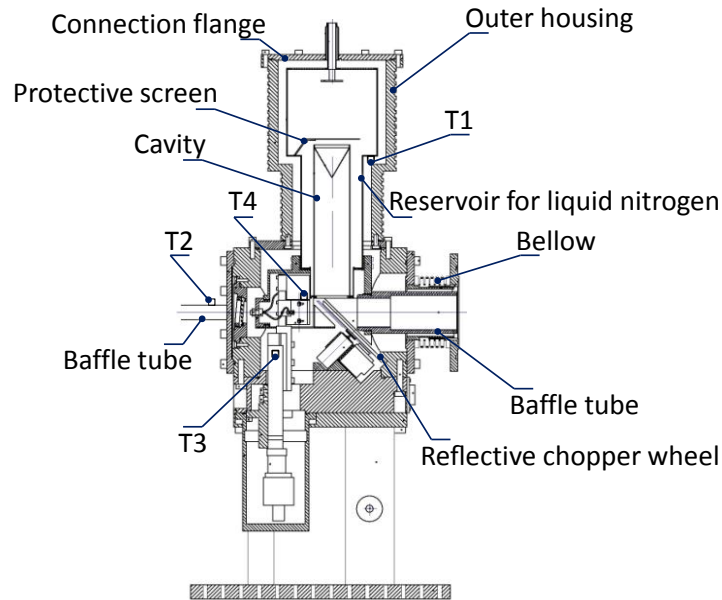


Fig. 4.7: Construction of the opto-mechanical unit with an LN₂-cooled blackbody mounted on top. Indicated parts are explained in the text

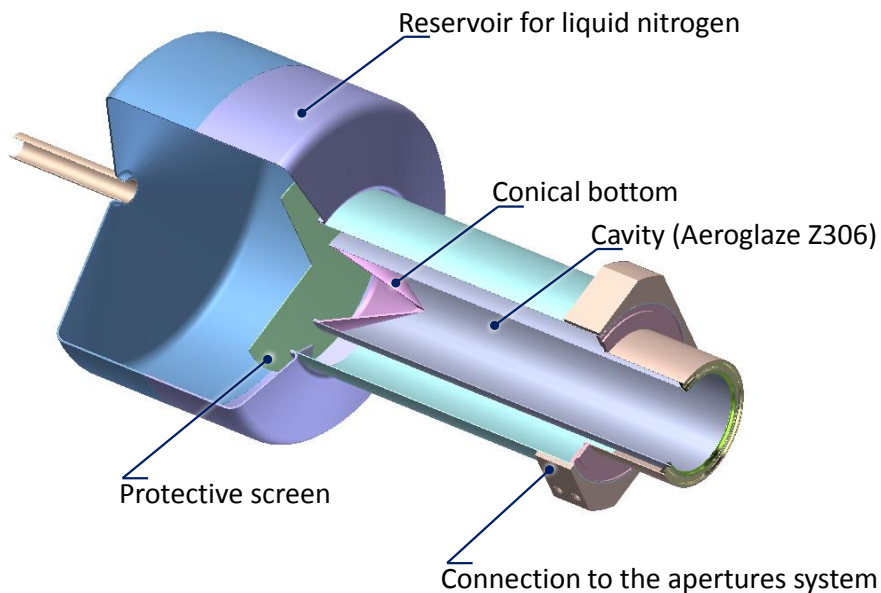


Fig. 4.8: Cross section of an LN₂-cooled blackbody without outer housing. Several parts are highlighted: cylindrical radiation cavity with a conical bottom, reservoir for liquid nitrogen, protective screen and connection to the apertures system of opto-mechanical unit

This blackbody is also used as a cooler for the chopper wheel, the baffle tubes and the apertures located in the opto-mechanical unit. Two black-coated baffle tubes are fixed directly to the reservoir with liquid nitrogen and are located on the optical axis. One of the tubes extends to the aperture of blackbodies or the sample and ends directly in front of them. Cooling of the chopper wheel is provided via a copper braid. Three thermometers located on the aperture in front of the source (T2), on the rotation stage (T3) and on the fixing block (T4) allow the temperature monitoring. The typical temperature of these components is below $-100\text{ }^{\circ}\text{C}$.

4.4 Vacuum Infrared Standard Radiation Thermometer (VIRST)

VIRST was specially developed for operation at the reduced background calibration facility and can measure radiation temperatures in the temperature range from $-170\text{ }^{\circ}\text{C}$ to $170\text{ }^{\circ}\text{C}$ and in a spectral bandpass from $8\text{ }\mu\text{m}$ to $14\text{ }\mu\text{m}$. VIRST is located inside the detector chamber on a linear translation unit and is able to move in three directions for high-precision adjustment. The design of VIRST allows using it as an instrument for the comparison and calibration of blackbodies and radiation sources as well as a transfer radiation thermometer for operation outside of the RBCF in air. More details of VIRST are given in [44].

4.5 Vacuum Fourier-Transform Infrared spectrometer (FTIR)

The nature of light based on electric and magnetic sine waves was discussed in Chapter 2.10. One of the most common and powerful methods of analyzing an infrared spectrum of light is the Fourier-transform infrared spectroscopy. Almost all measurements described in this work that are used to determine physical quantities are done by using the FTIR-spectrometer.

4.5.1 Theory of IR spectroscopy

The basic part of the FTIR-spectrometer is an interferometer. The Michelson interferometer is based on the effect of interference and consists of a beamsplitter, a fixed mirror and a movable mirror (Fig. 4.9).

The infrared radiation is incident on the beamsplitter, which splits the beam of light into two parts (ideally into two equal parts). The first part is reflected towards the fixed mirror M1, and there it is reflected back and travels the distance $2L$ before it reaches the beamsplitter again. The transmitted part of the beam is reflected from the moving mirror M2, also back towards the beamsplitter. Each of the components is split again and now two components in

each case travel back towards both the light source and the detector. By focusing on the detector plane, an interference pattern which depends on the position x of the moveable mirror, is generated. The detector detects part of this pattern. The moving mirror translates back and forth, very precisely, thus the path length becomes $2(L+x)$. The optical retardation between two halves of the beams can be obtained from the difference in optical path length and equals $2x$.

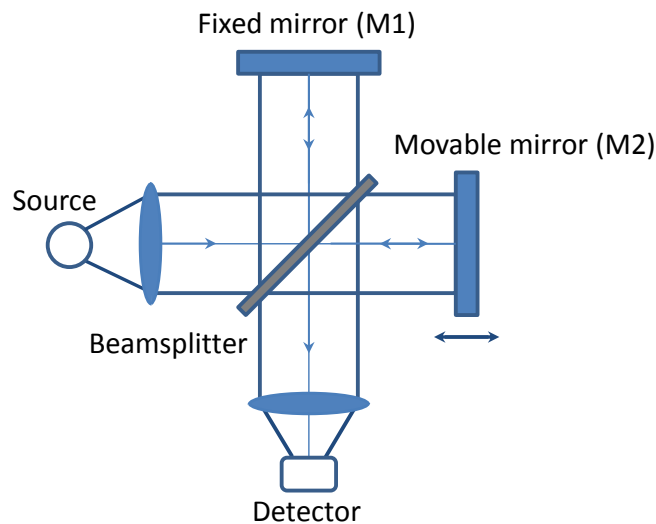


Fig. 4.9: Schematic presentation of a Michelson interferometer

The interferogram $I(x)$ showed in Fig. 4.10 is obtained by observing the interference pattern, which changes according to the relative phase difference, depending on the mirror displacement. The amplitude of the interferogram is proportional to the radiant energy incident on the detector. In the case of a non-monochromatic source with the broad emitted radiation spectrum, the interferogram can be represented as integral:

$$I(x) = \int_0^{\infty} I(\tilde{\nu}) \cos(2\pi\tilde{\nu}x) d\tilde{\nu} \quad (4.1)$$

where $\tilde{\nu}$ is the wavenumber, and $I(\tilde{\nu})$ is the intensity of the combined IR beams at wavenumber.

Equation 4.1 is one half of a cosine Fourier-transform pair. The other (Eq. 4.2) gives the result in terms of the measured quantity $I(x)$ and shows the variation in intensity depending on the wavenumbers:

$$I(\tilde{\nu}) = \int_{-\infty}^{\infty} I(x) \cos(2\pi\tilde{\nu}x) dx \quad (4.2)$$

These two interconvertible equations can be solved using the mathematical method (or algorithm) of Fourier-transformation (FT). The measurement process described in this work consists of the measurement of the interferograms from three sources- the sample and two reference blackbodies transforming into their spectra, as shown in Fig. 4.10, and comparing them.

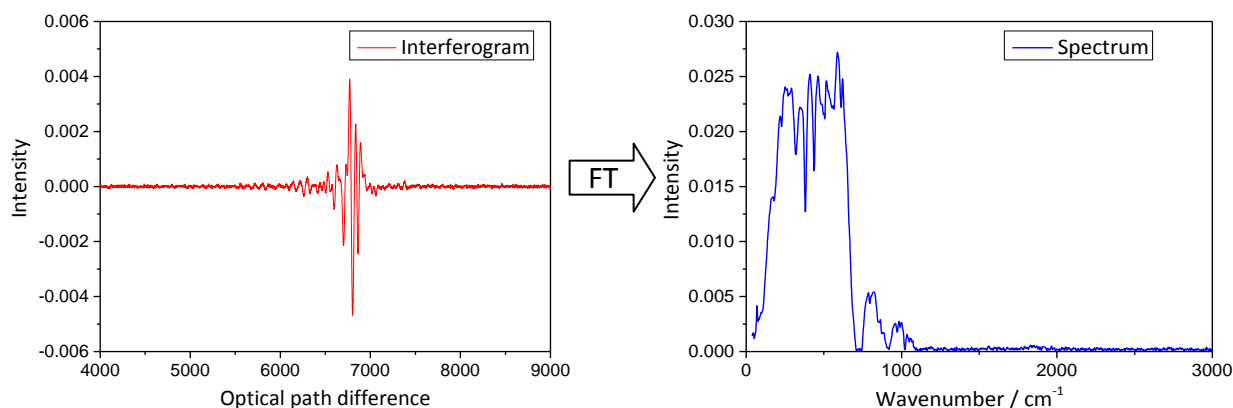


Fig. 4.10: Interferogram and spectrum as a result of Fourier-transformation

4.5.2 Advantages and disadvantages of FTIR-spectrometers

The FTIR-spectrometer has several important features that stand as advantages over a typical dispersive infrared spectrometer [51]. An integral part of a Fourier transform spectrometer is a He-Ne laser which is used to control the change in optical path difference via the zero crossings of the laser interferogram recorded in parallel. This is an internal automatic reference system which provides a wavenumber accuracy of better than 0.01 cm^{-1} . This high precision wavelength calibration is known as Connes advantage.

Another advantage of the spectrometer is related to the fact that each point of interferogram contains information about each wavenumber and the detector registers all frequencies emitted from the source simultaneously. This significantly reduces the time of measurement and is called the multiplex- or Fellgett advantage.

Also the circular apertures used in FTIR-spectrometers, with areas much larger than the linear slits of a grating or prism spectrometer, allow higher optical throughput towards the detector. The higher signal improves the signal-to-noise ratio (SNR), allowing measurements to be conducted in a much shorter period of time. This Jacquinot advantage leads to the high sensitivity of the instrument, proved to be significant for the measurement of, for example, samples at low temperatures or with low emittance.

Measuring time and resolution in Fourier transform spectroscopy are directly related to the mirror M2 and the extent of its scanning distance. The resolution of measurement is proportional to the distance which mirror M2 moves and by the choice of the apodization function. For this type of spectrometer the resolution is constant at all wavenumbers. The typical high velocity of the mirror gains a full spectrum of radiation in a fraction of a second.

The point-wise recording of the interferogram and its subsequent fast Fourier-transformation (FFT) leads to a point-wise discretized spectrum. This means the spectral information is given at accurate, specific and regular intervals that are determined by the analysis parameters. In this case the Picket Fence Effect occurs because a frequency component may lie between or even exactly halfway between frequency lines of the FFT analysis and would therefore be significantly damped. To avoid significant errors in the signal, a zero-filling factor (ZFF) can be used, which adds zeros to the end of the interferogram. The resulting higher density of frequency points of the spectrum after the FFT can be seen as a kind of interpolation [51, 52].

Another effect of discretisation is the aliasing, which causes distortion or artifacts due to high frequency components above the Nyquist frequency when reconstructing the spectrum. By proper filtering of the signal adapted to the sampling rate these effects can be avoided.

The finiteness of the recorded optical path difference leads to a truncation of the “ideal” interferogram. The FFT of such a truncated interferogram yields to a “leaking out” of spectral intensity into side lobes, which is best seen when looked at through narrow signals. This effect is called leakage. Leakage can be avoided by damping the outermost ends of the interferogram by an appropriate (boxcar, triangular or bell-shaped) function. The use of this “damping” or “cutoff” function is known as apodization. The different kinds of apodization and their individual drawbacks can be found in the review by [51].

4.5.3 Experimental setup: FTIR-spectrometer

The proper use of the spectrometer depends on the combination of three components: the source, beamsplitter and detector. The vacuum FTIR-spectrometer used at the RBCF is the VERTEX 80 Series research spectrometer of the manufacturer Bruker. It has several detectors and several available beamsplitter options which can cover a wavelength range from 0.2 μm to 1400 μm with spectral resolution of better than 0.2 cm^{-1} (this work is focused on the range from 4 μm to 100 μm). The following detectors are employed:

- A liquid nitrogen-cooled Mercury Cadmium Telluride (MCT) detector with a ZnSe window for the range from 0.8 μm to 20 μm [53]. The photoconductive MCT detector is

a semiconductor used for infrared detection. The various alloys of CdTe as semiconductor and HgTe as semimetal provide the optical absorption of the material to the required infrared wavelength. High detectivity D^* [54] and high scan velocity are the main advantages of this detector.

- A pyroelectric deuterated L-alanine doped triglycine sulfate (DLaTGS) detector with a KBr window for the MIR range from 0.8 μm to 40 μm [55]. The working principle of a standard DLaTGS detector is based on the change in the polarization of a crystal due to the change of temperature.
- A pyroelectric DTGS detector with PE-window for the FIR range from 14 μm to 200 μm is similar in the principle of operation, but has somewhat different characteristics, for example, a slower scan velocity and different window material [55].
- A Si-composite bolometer for the FIR range from 10 μm to 1400 μm [56]. The bolometer offers a higher detectivity in the FIR range but the requirement for liquid helium cooling leads to a more complicated operation and an increase in the cost of the measurements.

These detectors in combination with a set of different beamsplitters will be used for the measurements: the KBr beamsplitter covers the range from 1 μm to 28 μm , the 6 μm Multilayer Mylar beamsplitter is applied from 14.7 μm to 333 μm and the 50 μm Mylar beamsplitter for the range from 166 μm to 1000 μm .

Several internal sources are available for the VERTEX 80V model. However, taking into account the above-mentioned wavelength range, the Globar is used as the most suitable source of radiation for the performed reflectivity measurements.

The spectrometer is a highly accurate and sensitive instrument for the recording of infrared radiation. This also means that the spectrometer is very sensitive to thermal radiation from all parts and all apertures in the optical path, especially in the case of low signals from the sample. The basic components of an FTIR-spectrometer (beamsplitter, mirrors and detector) also have a certain temperature and contribute to the measured signal. The problem of this thermal radiation can be reduced by a measurement scheme based on a comparison of the signals of several reference sources and the sample, as the background radiation is equal for all measurements and can be eliminated. However, the spectrometer must maintain sufficient temperature stability over the entire measuring period required for one sequence (blackbodies vs. sample). In certain cases this can be critical because the measuring period, depending on the detector, sample and required accuracies, can reach several hours. Thus the long-term temperature stability of the spectrometer is very important in achieving the low uncertainty. This was discovered by using special aluminum blocks (cooling elements) along

the outer perimeter of the housing of the spectrometer, a thermostat and two thermometers for monitoring and stabilizing the spectrometer. Fig. 4.11 shows the achieved stability of the spectrometer to be better than 5 mK over a period of 5 hours.

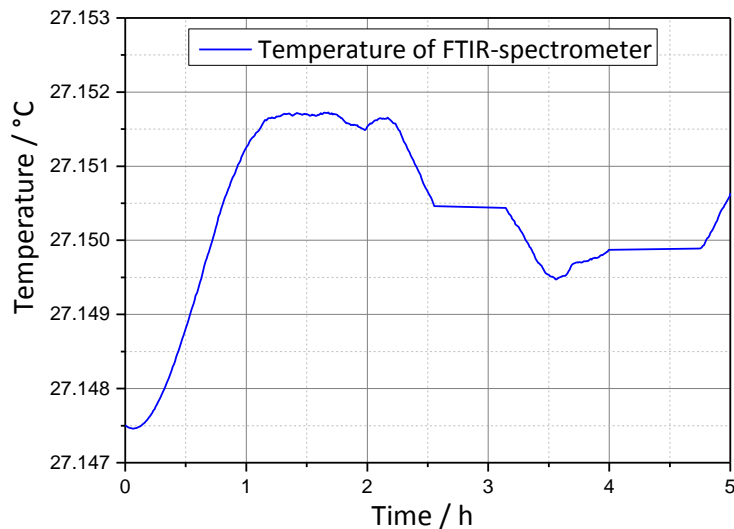


Fig. 4.11: Temperature stability of the FTIR-spectrometer using special aluminum blocks (cooling elements) along the outer perimeter of the housing of the spectrometer, temperature controlled by a liquid thermostat

4.5.4 Setup for directional reflectivity measurement

The reflectivity measurements are performed with the reflection unit “A 519-A” of Bruker, which allows the absolute directional spectral reflectivity of the sample with an angle of incidence of 12° to be measured. A schematic representation of the measurement is shown in Fig. 4.12. A detailed description of the reflection unit as well as a depiction of the optical path using a reference mirror and a double reflection from a sample can be found here [57].

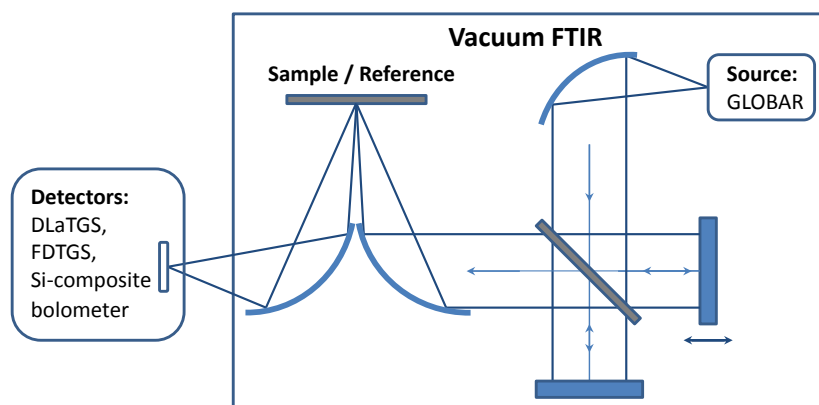


Fig. 4.12: Schematic representation of the measurement of the directional spectral reflectivity with the FTIR-spectrometer

4.6 Vacuum sample holder for emissivity measurements

Measurements under vacuum conditions are not affected by the convection heat loss and atmospheric absorptions. This reduces the uncertainty of measurements, i.e. it simplifies the calculation of the surface temperature [33]. Nevertheless, the thermal radiation, reflections as well as the temperature non-homogeneity of the surrounding source chamber will affect the measured radiation signal of the sample. Incidentally for a precise measurement and calculation of emissivity, a well-known stabilized surrounding of the sample is required. Furthermore, a highly accurate temperature stabilization of the sample is essential for the determination of the surface temperature, which, in turn, is of great importance for the determination of emissivity. The design of the heater should also provide measurements at different angles as well as high-precision positioning of the sample for focusing of the FTIR-spectrometer. Finally, the sample enclosure should be suitable for the mathematical calculation of the radiation budget to separate the radiation emitted directly by the sample from all other contributions to the detected overall radiation.

The dedicated sample holder for emissivity measurements under vacuum conditions has been developed based on two components: two halves of a spherical enclosure made of copper and a sample heater inside this enclosure (Figs. 4.13 and 4.14). The spherical enclosure can be temperature controlled by a liquid circulating in tubular channels soldered onto the surface of the sphere. Its temperature can vary from $-80\text{ }^{\circ}\text{C}$ to $80\text{ }^{\circ}\text{C}$ using the liquid Novec HFE-7500 and a thermostat. In combination with the good thermal conductivity of copper it provides perfect temperature homogeneity and the ability to accurately measure the temperature of the inner surface of the sphere via temperature sensors located inside blocks soldered on the outside of the sphere. The sample is mounted on the heater made of Inconel 600. The heating plate with the mounted sample is heated from the back side by a resistive, bifilar-wound heating wire. The sample can be controlled in the temperature range from $-40\text{ }^{\circ}\text{C}$ to $600\text{ }^{\circ}\text{C}$. The temperatures below room temperature are achieved by countercurrent thermal radiation from the sphere (radiative cooling), which then must be stabilized for a certain time at $-80\text{ }^{\circ}\text{C}$. To improve the thermal contact between the sample and the surface of the heater, which is especially important under vacuum conditions, a special thermal grease must be used. The heater with the sample can be rotated by a DC-motor-driven rotation stage. This allows to perform emissivity measurements under different angles in the range of $\pm 75^{\circ}$ with respect to the sample surface normal. By the use of an additional linear stage, samples of varied thickness can be positioned in the focus of the optical system which is also the rotational axis of the sample holder. To reduce the heat transfer between the heater and the DC-motor-driven rotation stage, a ceramic insert is added. Radiation from the sample is observed through the opening in the sample enclosure.

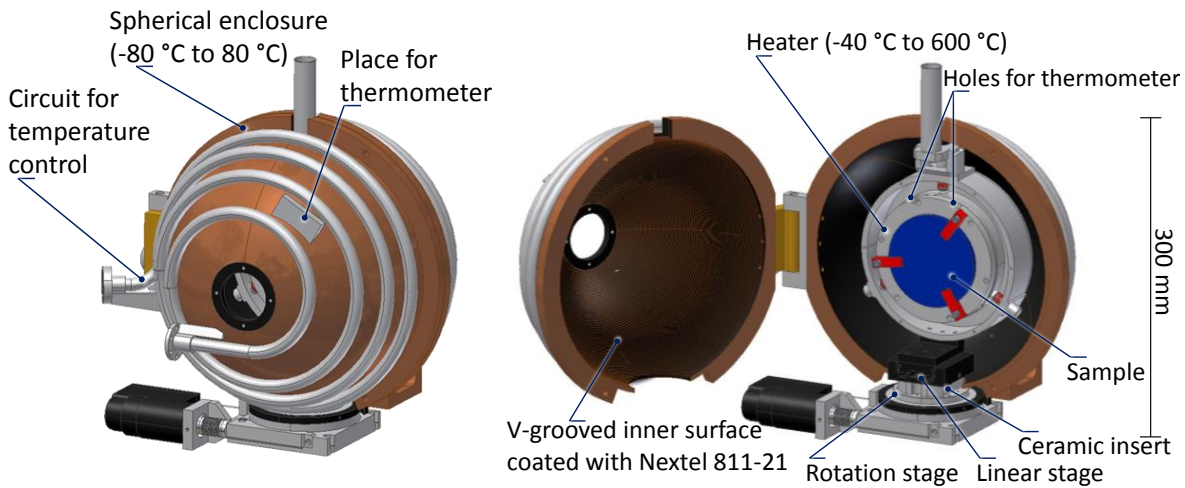


Fig. 4.13: Setup of the vacuum sample holder for spectral emissivity measurement. On the left-hand side the sample enclosure is shown in a closed “working” position, on the right-hand side, in an open position. The sample is mounted on a heater. The sample temperature can be controlled in the range from -40 °C to 600 °C . The heater with the sample can be rotated by a DC-motor-driven rotation stage. Emissivity measurements can be performed under angles in the range of $\pm 75^\circ$ with respect to the sample surface normal. The temperature of the sample enclosure can be controlled in the range from -80 °C to 80 °C . The inside of the sample enclosure is V-grooved and coated with Nextel Velvet Black 811-21. Radiation from the sample is observed through the opening in the sample enclosure

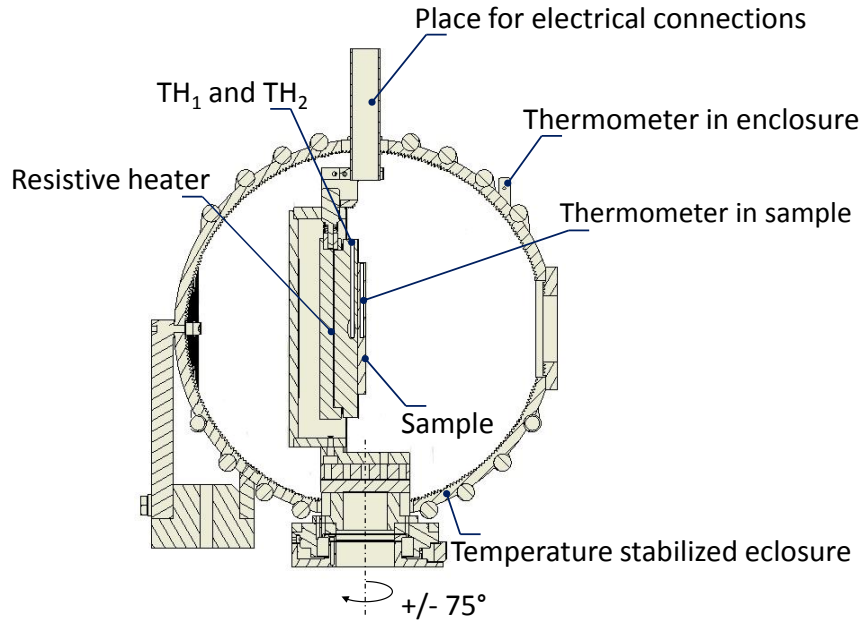


Fig. 4.14: Construction of the setup of the vacuum sample holder for spectral emissivity measurement. Positions of thermometers in the heating plate and in the sample are shown

The spherical enclosure has three temperature sensors for the measurement of the temperature of the inner surface and one for temperature regulation via a thermostat: two are located on the front of the sphere and two on the back.

The temperature of the heating plate is controlled by a microcontroller Eurotherm 2704 which monitors the temperature sensor TH_1 . The temperature sensor TH_2 is used for monitoring the heating plate temperature via an additional independent instrument. A digital precision multimeter Keithley 2010 is used here.

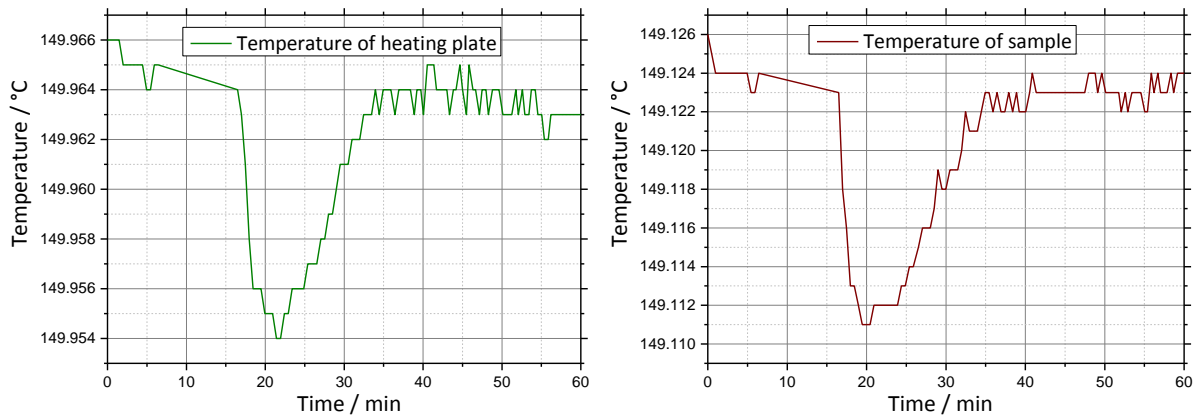


Fig. 4.15: Example of the achieved temperature stability of the heater and the sample under vacuum conditions. At a temperature of 150 °C the stability is better than 20 mK over a period of one hour

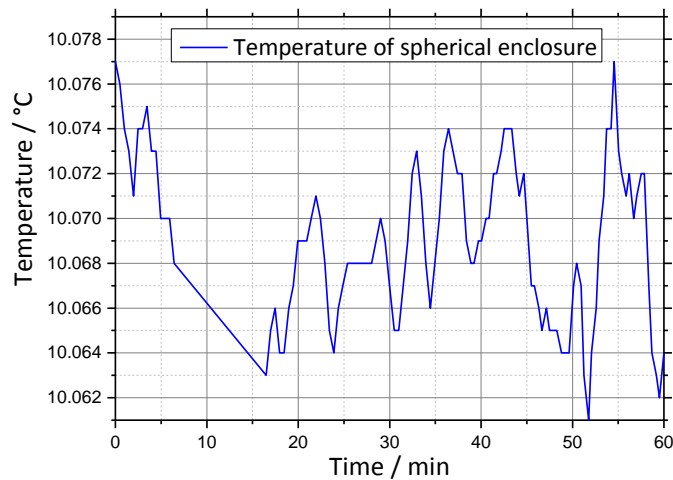


Fig. 4.16: Example of the temperature stability of the sphere stabilized at 10 °C under vacuum conditions. The stability is better than 15 mK over a period of one hour. A sample at a temperature of 150 °C is located inside the sphere

An example of the achieved temperature stability of the heating plate and the sample under vacuum conditions is shown in the Fig. 4.15; the temperature stability of the spherical enclosure in Fig. 4.16, respectively. The calibrated at the PTB platinum resistance thermometer of type PT100 are used for measuring temperatures in heating plate and sample. Stabilities of

the heater at 150 °C and a sample mounted on it are better than 20 mK over a period of one hour. The stability of the spherical enclosure operated at 10 °C at the same time is better than 15 mK. The difference in temperatures shown in Fig. 4.15 ($T_{\text{Heater}}=149.96$ °C and $T_{\text{Sample}}=149.12$ °C) is due to the thermal gradient over the distance between the “controlling” thermometer of the heater and the monitoring thermometer inside the sample (Chapter 6.1.2).

Typical samples have a diameter in the range from 30 mm to 120 mm and a width of 1.8 mm to 10 mm (Fig. 4.17). The sample substrates with or without coating usually have one or two holes to accommodate temperature sensors for monitoring the temperature and the size of the hole depends on the diameter of the thermometers. If the sample is of sufficient thickness, two thermometers can be placed in the middle of the sample at varied distances from the heating plate, allowing an extrapolation of the measured temperature gradient to the sample surface (Chapter 6.1.2). In most cases this isn't possible because of the finite thickness of the sample.

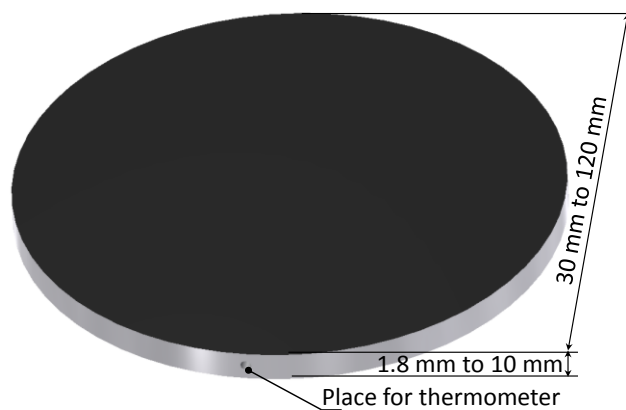


Fig. 4.17: Typical sample: the sample substrate with or without coating has one or two holes for thermometers

4.6.1 Selection of coating for the sample enclosure

The directional spectral emissivity of a sample is calculated according to the radiation budget, including multiple reflections between the enclosure and the sample (Chapter 6.1.1). Thus, the exact knowledge of not only the surface temperature of the enclosure is necessary, but also its emissivity. Moreover, this value should be as high as possible for two reasons:

- To reduce multiple reflections between sample and enclosure.
- To reduce the influence of a possible temperature dependence of the emissivity of the enclosure.

Therefore the inner surface of the sphere was structured by circular grooves (60°). Additionally, it was coated with Nextel Velvet Black 811-21 as a suitable black coating to provide an emissivity of greater than 0.9. For the characterization of this coating, two identical samples were made with the same surface structure as the sphere. They had identical groove geometry and, as the enclosure, were made of copper and also chemically plated with nickel. Finally they were sandblasted and coated with Nextel Velvet Black 811-21, one sample with and one without primer. The two final samples are shown in Fig. 4.18.

To test the possible coating with respect of its suitability for emissivity measurements in the MIR and FIR-range as well as compatibility with vacuum and low temperature conditions, the directional spectral emissivity of the two samples was determined before and after a series of cooling cycles in liquid nitrogen [58]. Additionally, the directional spectral reflectivity of the two samples was determined before and after the cooling test. The sample without primer showed an insufficient mechanical stability of the coating. In the following, only the results of the sample with applied primer are shown. In the next section the evaluation of emissivity measurements under vacuum conditions developed in this work will already be taken into account, although the method of calculation as well as the uncertainty budget will be presented later.

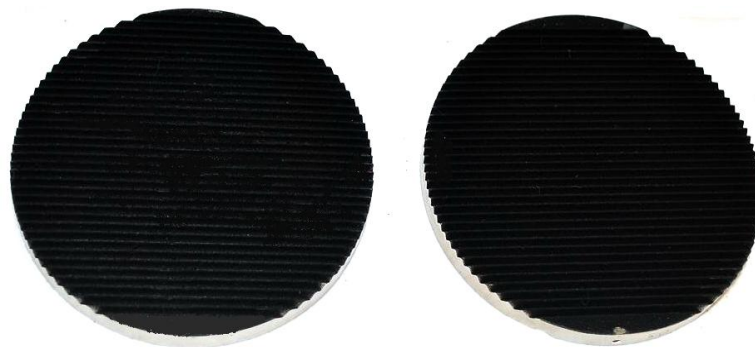


Fig. 4.18: Two samples with the same surface structure as the spherical enclosure of the emissivity sample holder. They are made of copper, plated with nickel, sandblasted and coated with Nextel Velvet Black 811-21, one sample with and one without primer [58]

4.6.2 Directional spectral emittance of the coating of the enclosure

The directional spectral emittance of the samples coated similarly to the spherical enclosure of the sample holder were determined during the setup for emissivity measurement in air of PTB [33] at a temperature of 120°C in the wavelength range from $4\ \mu\text{m}$ to $25\ \mu\text{m}$ (Fig. 4.19), and in the wavelength range from $25\ \mu\text{m}$ to $100\ \mu\text{m}$ during the setup for emissivity measurement under vacuum conditions (Fig. 4.20). The range of uncertainties, calculated according to [33] and Chapter 6.2, are also shown.

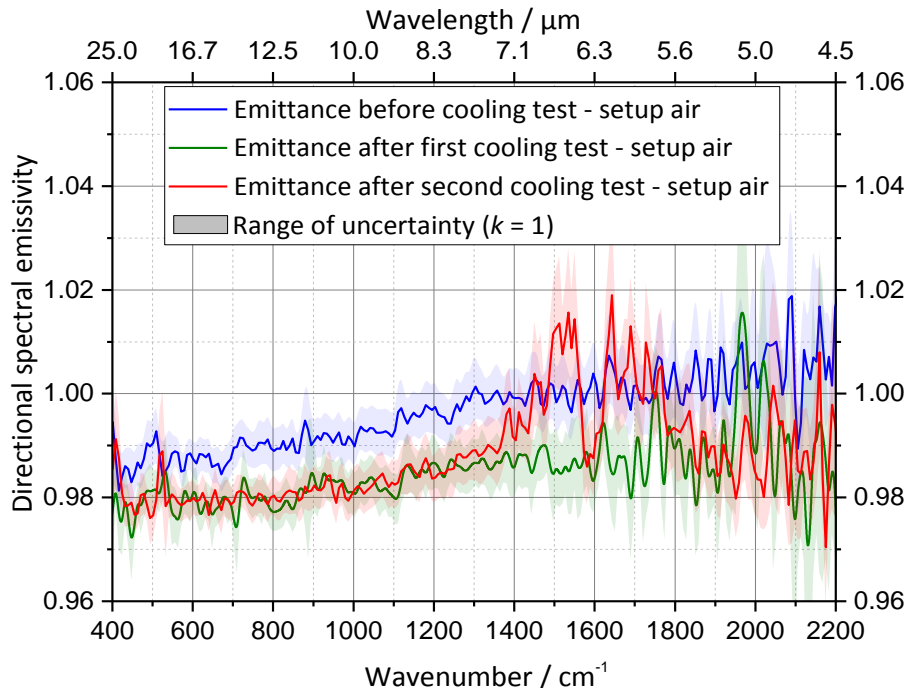


Fig. 4.19: The directional spectral emissivity of one sample from Fig. 4.18 at a temperature of $120\text{ }^{\circ}\text{C}$ observed under an angle of 5° before and after the cooling test in liquid nitrogen. The shaded area around the curve is the range of standard uncertainty. The sample was grooved, plated with nickel, sandblasted and coated with Nextel Velvet Black 811-21

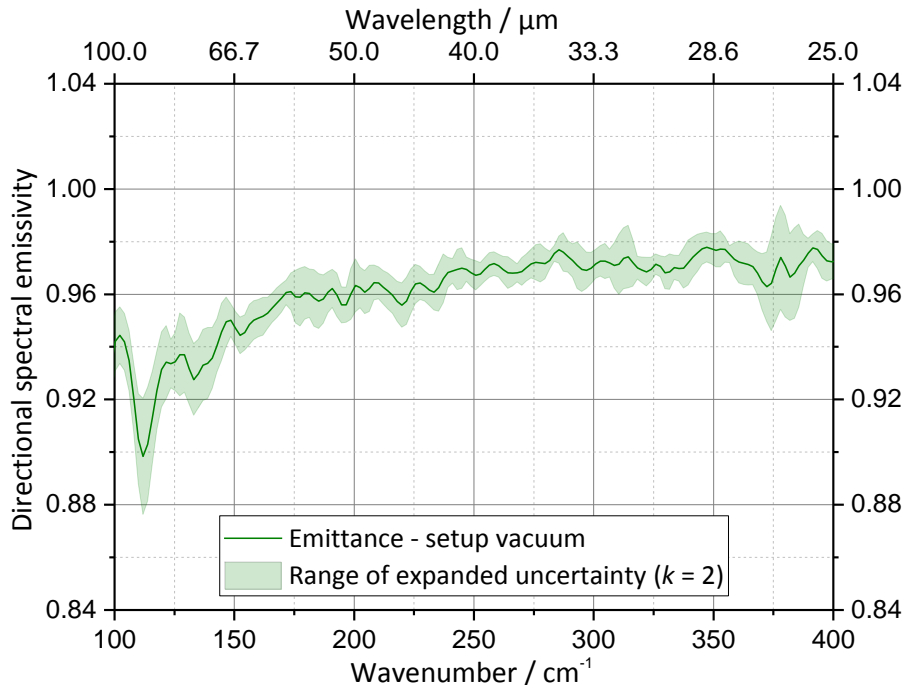


Fig. 4.20: The directional spectral emissivity of a sample coated with Nextel Velvet Black 811-21 at a temperature of $120\text{ }^{\circ}\text{C}$ observed at an angle of 10° . The shaded area around the curve is the range of expanded uncertainty

Apparently, the directional spectral emittance in Fig. 4.19 is reduced by about 0.01 after the first cooling test but afterwards the emittance remains constant with respect to the standard uncertainty of the measurement, and is at the desired level of 0.98. A slight increase in emissivity around 1600 cm^{-1} is related to the increased presence of water in the rough surface structure of the black coating after a longer, second cooling.

4.6.3 Directional spectral reflectance of the coating of the enclosure

The spectral directional reflectivity measurements ($12^\circ/12^\circ$) of the surface sample of the spherical enclosure have been performed during the setup, described in Chapter 4.5.4, with the Si-composite bolometer and the $6\text{ }\mu\text{m}$ Multilayer Mylar beamsplitter. The results after the cooling test in liquid nitrogen are shown in Fig. 4.21 for the wavelength range from $12.5\text{ }\mu\text{m}$ to $100\text{ }\mu\text{m}$. For clarity, the measurement before the cooling series is shown only in the expanded view in Fig. 4.22.

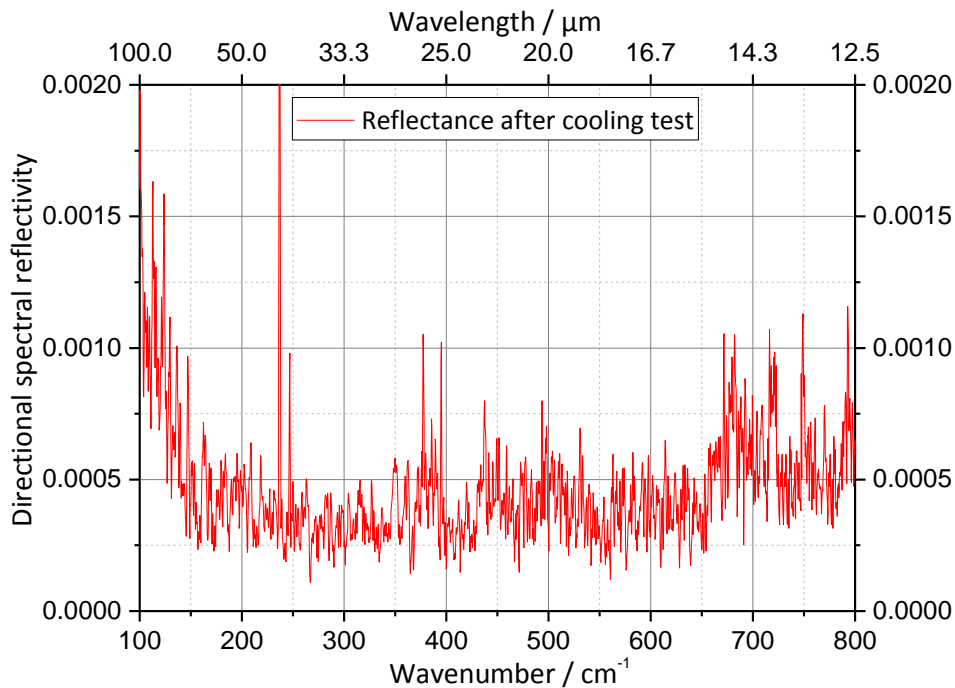


Fig. 4.21: The directional spectral reflectance ($12^\circ/12^\circ$) of the surface sample of the spherical enclosure (Fig. 4.18) after the cooling test

Obviously the directional spectral reflectance of the sample has not changed after the cooling test and remains below 0.001. Thus the directional spectral reflectance and the directional spectral emittance of this coating meet the demands for the inner surface of the sample enclosure with respect to its suitability for MIR and FIR emissivity measurements and compatibility with vacuum and low temperature conditions. A slight reduction in the emissivity of Nextel at long wavelengths (Fig. 4.20) does not contradict this conclusion. The difference

between the angles of observation of emissivity and reflectivity measurements is not essential due to only slight changes in the characteristics of this material in this angular range.

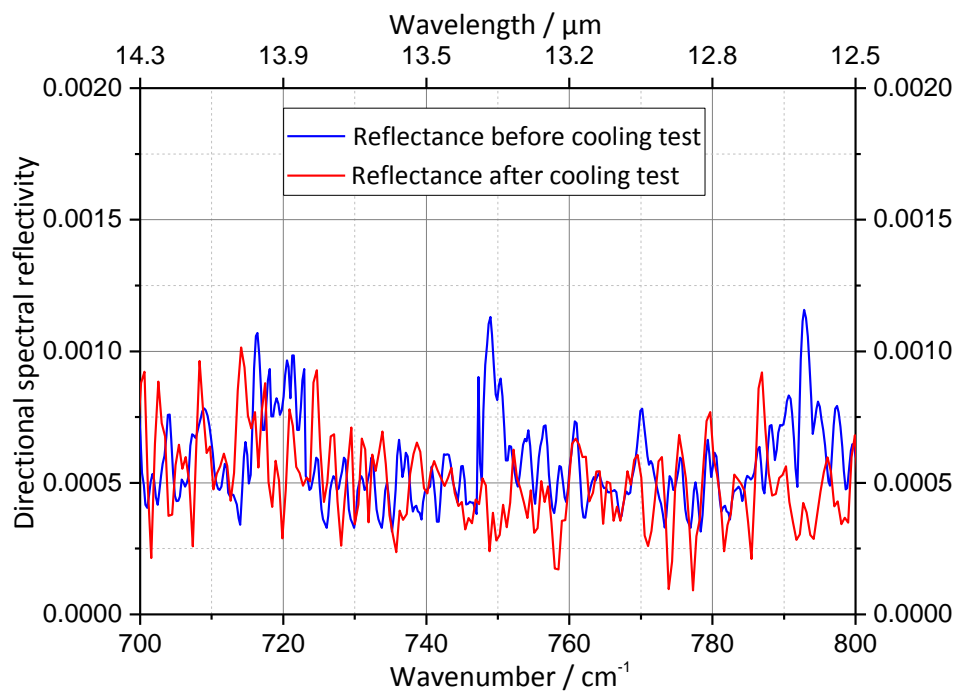


Fig. 4.22: The directional spectral reflectance ($12^\circ/12^\circ$) of the surface sample of the spherical enclosure (Fig. 4.18) before and after the cooling test in the wavenumber range from $12.5 \mu\text{m}$ to $14.3 \mu\text{m}$ (expanded view of Fig. 4.21)

5 Metrological characterizations of FTIR-spectrometer and reference blackbodies

In the previous chapter the new facility and its hardware were discussed in detail. The next step is the metrological characterization of the most important elements. The characterization of the FTIR-spectrometer as a central part of the RBCF was done using three different detectors to measure the radiation temperature from -100 °C to 140 °C . An effective emissivity, as the most important characteristic of blackbodies, was calculated with the program STEEP3 [59], taking into account the real coating and geometry of the cavity. Finally, the uncertainty budget of each blackbody, which will be used for the calculation of overall uncertainty budget of emissivity measurements under vacuum, will be presented depending on the temperature and wavelength.

5.1 Performance of the facility and measurement of radiance temperature of VLTBB

The following measurements have been performed to show that the spectral radiance of the VLTBB can be measured consistently at the RBCF in a wavelength range from $4\text{ }\mu\text{m}$ to $100\text{ }\mu\text{m}$ down to a radiance temperature of -100 °C [58]. For these measurements the temperature-stabilized FTIR-spectrometer was operated as a stable instrument with a constant spectral responsivity over a time span of five days. In contrast to the comparison method for determination of emissivity measurement (Chapter 6), where the spectral responsivity can be eliminated, the direct measurement of radiation from one source requires a calibration of the spectrometer. For this purpose the spectrometer was calibrated at the beginning of measurements at two additional temperatures of the VLTBB: at 0 °C and at -170 °C in the wavelength range from $4\text{ }\mu\text{m}$ to $20\text{ }\mu\text{m}$ as well as at 80 °C and at 0 °C for the measurements in the wavelength range from $20\text{ }\mu\text{m}$ to $100\text{ }\mu\text{m}$.

5.1.1 Radiation budget at RBCF

Signal of the “main” reference blackbody

To calculate the spectral radiance, a radiation budget from each blackbody is required. The measured signal of the “main” reference blackbody, VLTBB or VMTBB, is given according to [60] by:

$$\tilde{L}_{\text{BB1}}(T_{\text{BB1}}) = s \cdot (L_{\text{BB1}}(T_{\text{BB1}}) + L_{\text{Back}} - L_{\text{Det}}) \quad (5.1)$$

Here s is the spectral responsivity of the spectrometer; the spectral radiance of the blackbody is $L_{\text{BB1}}(T_{\text{BB1}}) = \varepsilon_{\text{BB1}}(\lambda, 0^\circ, T_{\text{BB1}}) L_{\text{Planck}}(T_{\text{BB1}})$, given by the spectral radiance according to Planck's law $L_{\text{Planck}}(T_{\text{BB1}})$ and the effective directional spectral emissivity of the blackbody $\varepsilon_{\text{BB1}}(\lambda, 0^\circ, T_{\text{BB1}})$ (Chapter 5.2). L_{Back} represents the spectral radiance of the thermal background of the RBCF and L_{Det} is the self-radiation of the detector. Hereinafter, the azimuthal angle φ at emissivity and reflectivity (definition of radiation characteristics in Chapter 2) will be omitted for clarity, just as the dependence of the spectral radiance and the spectral responsivity on the wavelength. Furthermore, it is necessary to consider a view factor. Hereinafter, the view factors denote the transfer of radiation between two surfaces and can be calculated, as a rule, based on the geometrical characteristics such as diameter of two surfaces (by use of FTIR-spectrometer only round surfaces are considered) and the distance between them [17]. So, $F_{\text{BB1-Det}}$ characterizes the fraction of radiation transferred from the surface of blackbody with area A_{BB1} to the detector, located some distance away. In the case of background and detector radiations the view factors and areas will be omitted, because in the following these radiation components will be eliminated. Thus, the measured signal of the "main" blackbody can be written as:

$$\tilde{L}_{\text{BB1}}(T_{\text{BB1}}) = s \cdot (\varepsilon_{\text{BB1}}(\lambda, 0^\circ, T_{\text{BB1}}) L_{\text{Planck}}(T_{\text{BB1}}) A_{\text{BB1}} F_{\text{BB1-Det}} + L_{\text{Back}} - L_{\text{Det}}) \quad (5.2)$$

Signal of the LN₂-cooled blackbody

Similarly, the measured signal from the LN₂-cooled blackbody can be written taking into account the design of the RBCF, namely, the use of the highly reflective chopper in the optical path:

$$\tilde{L}_{\text{BB-LN}_2}(T_{\text{BB-LN}_2}) = s \cdot (\rho_{\text{Ch}}(\lambda, 45^\circ, 45^\circ) L_{\text{BB-LN}_2}(T_{\text{BB-LN}_2}) + L_{\text{Ch}}(T_{\text{Ch}}) + L_{\text{Back}} - L_{\text{Det}}) \quad (5.3)$$

where $L_{\text{Ch}}(T_{\text{Ch}}) = \varepsilon_{\text{Ch}}(\lambda, 45^\circ, T_{\text{Ch}}) L_{\text{Planck}}(T_{\text{Ch}})$ is the radiance of the highly reflective chopper with directional spectral emittance under an angle of observation of 45°: $\varepsilon_{\text{Ch}}(\lambda, 45^\circ, T_{\text{Ch}})$; $\rho_{\text{Ch}}(\lambda, 45^\circ, 45^\circ) = 1 - \varepsilon_{\text{Ch}}(\lambda, 45^\circ, T_{\text{Ch}})$ its bidirectional spectral reflectance and $L_{\text{BB-LN}_2}(T_{\text{BB-LN}_2}) = \varepsilon_{\text{BB-LN}_2}(\lambda, 0^\circ, T_{\text{BB-LN}_2}) L_{\text{Planck}}(T_{\text{BB-LN}_2})$ represents the spectral radiance of the LN₂-cooled blackbody with its effective directional spectral emissivity $\varepsilon_{\text{BB-LN}_2}(\lambda, 0^\circ, T_{\text{BB-LN}_2})$. Substituting these expressions in Equation 5.3 and considering view factors between the LN₂-cooled blackbody and the detector as well as between the chopper and the detector, the measured signal gives:

$$\begin{aligned} \tilde{L}_{\text{BB-LN}_2}(T_{\text{BB-LN}_2}) = & \\ & s \cdot \left([1 - \varepsilon_{\text{Ch}}(\lambda, 45^\circ, T_{\text{Ch}})] \varepsilon_{\text{BB-LN}_2}(\lambda, 0^\circ, T_{\text{BB-LN}_2}) L_{\text{Planck}}(T_{\text{BB-LN}_2}) A_{\text{BB-LN}_2} F_{\text{BB-LN}_2-\text{Det}} + \right. \\ & \left. + \varepsilon_{\text{Ch}}(\lambda, 45^\circ, T_{\text{Ch}}) L_{\text{Planck}}(T_{\text{Ch}}) A_{\text{Ch}} F_{\text{Ch-Det}} + L_{\text{Back}} - L_{\text{Det}} \right) \end{aligned} \quad (5.4)$$

Thus, the Equations 5.2 and 5.4 can be solved for the fraction of radiation of the reference blackbody, in our case for $L_{\text{VLTBB}}(T_{\text{VLTBB}})$:

$$\begin{aligned} L_{\text{VLTBB}}(T_{\text{VLTBB}}) = & \\ = & \frac{\tilde{L}_{\text{VLTBB}}(T_{\text{VLTBB}}) - \tilde{L}_{\text{BB-LN}_2}(T_{\text{BB-LN}_2})}{s \cdot F_{\text{VLTBB-Det}} A_{\text{VLTBB}}} + \varepsilon_{\text{Ch}}(\lambda, 45^\circ, T_{\text{Ch}}) L_{\text{Planck}}(T_{\text{Ch}}) + \\ & + [1 - \varepsilon_{\text{Ch}}(\lambda, 45^\circ, T_{\text{Ch}})] \varepsilon_{\text{BB-LN}_2}(\lambda, 0^\circ, T_{\text{BB-LN}_2}) L_{\text{Planck}}(T_{\text{BB-LN}_2}) \end{aligned} \quad (5.5)$$

This equation has been simplified assuming that:

$$F_{\text{VLTBB-Det}} = F_{\text{BB-LN}_2-\text{Det}} = F_{\text{Ch-Det}} \quad \text{and} \quad A_{\text{VLTBB}} = A_{\text{BB-LN}_2} = A_{\text{Ch}}$$

The still unknown spectral responsivity s can be calculated from an independent set of measurements and operating the VLTBB at two well separated temperatures T_1 and T_2 (calibration of spectrometer). The difference of Equations 5.2 and 5.4 for two different temperatures gives for the spectral responsivity:

$$s = \frac{\tilde{L}_{\text{VLTBB}}(T_{1,\text{VLTBB}}) - \tilde{L}_{\text{VLTBB}}(T_{2,\text{VLTBB}})}{F_{\text{VLTBB-Det}} A_{\text{VLTBB}} \left(\varepsilon_{\text{VLTBB}}(\lambda, 0^\circ, T_{1,\text{VLTBB}}) L_{\text{Planck}}(T_{1,\text{VLTBB}}) - \varepsilon_{\text{VLTBB}}(\lambda, 0^\circ, T_{2,\text{VLTBB}}) L_{\text{Planck}}(T_{2,\text{VLTBB}}) \right)} \quad (5.6)$$

The measurements, which are processed using Equations 5.5 and 5.6, are described in the following sections.

5.1.2 Performance of FTIR-spectrometer with MCT detector

The first set of measurements has been performed with the vacuum FTIR-spectrometer applying the KBr broadband beamsplitter and the liquid nitrogen-cooled MCT detector [58]. The results of the experimentally determined spectral radiances of the VLTBB and the theoretical radiances calculated from Planck's law (Chapter 2.3) at temperatures in the range from -100°C to 80°C are shown in Fig. 5.1. Additionally, the noise level of these measurements is depicted, which was determined from the standard deviation of the series of measurements at 0°C . The MCT detector has been corrected for its non-linearity.

For a different visualization of these results the radiation temperature was calculated from the obtained radiances by using the inverted form of Planck's law. The resulting radiance

temperature over wavelength for the various measured blackbody temperatures is plotted in Fig. 5.2.

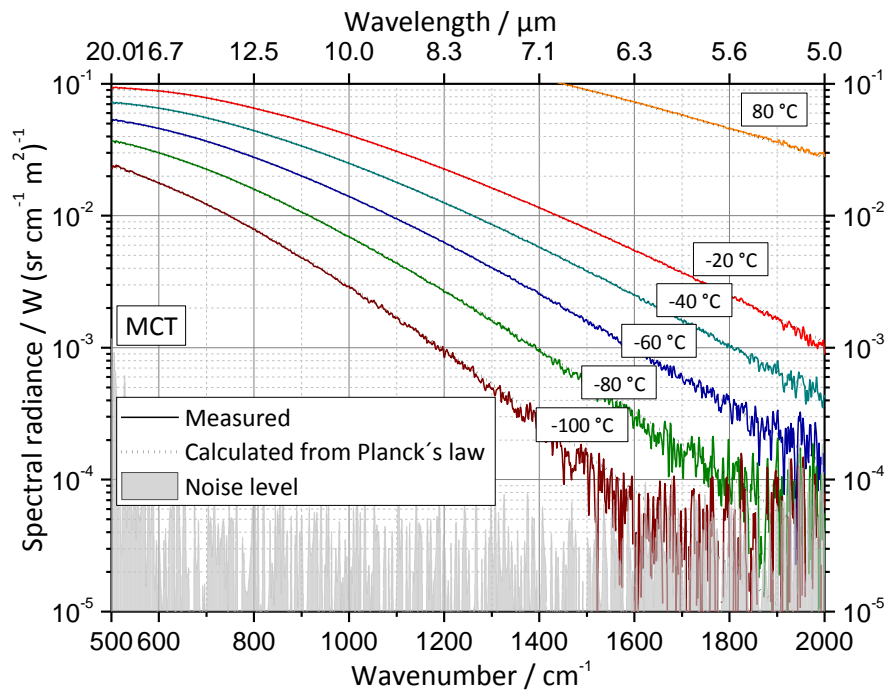


Fig. 5.1: The measured spectral radiances of the blackbody VLTBB operated in the range from $-100\text{ }^{\circ}\text{C}$ to $80\text{ }^{\circ}\text{C}$ in comparison with the corresponding theoretical radiances calculated from Planck's law. Also the noise level is shown, calculated from the standard deviation of these measurements

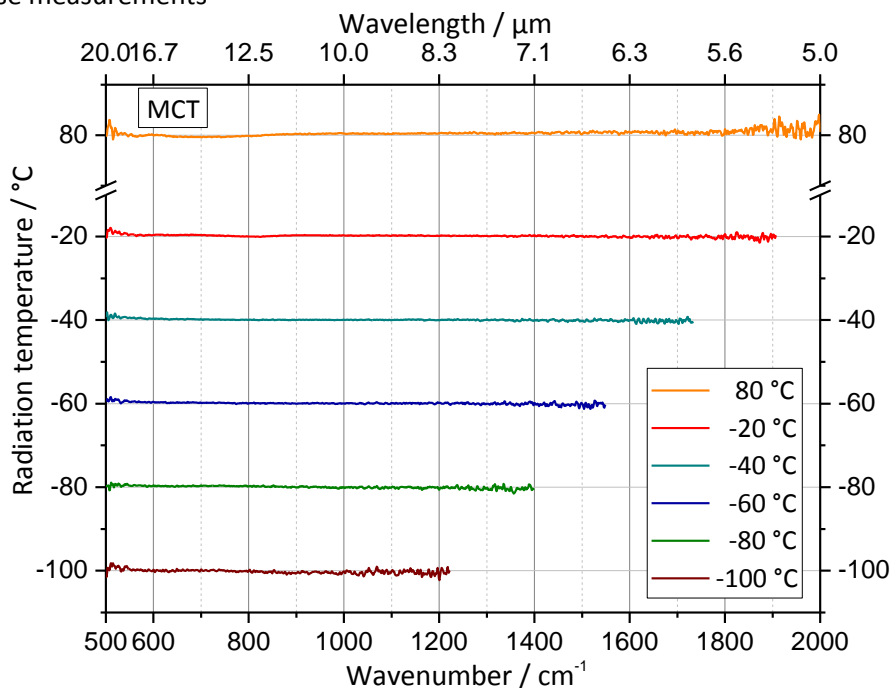


Fig. 5.2: The spectral distribution of radiation temperatures of the VLTBB in the range from $-100\text{ }^{\circ}\text{C}$ to $80\text{ }^{\circ}\text{C}$ calculated from the radiances shown in Fig. 5.1 from the inverted Planck's law

The results show that the measured radiation temperatures deviate from its nominal values, which are calculated according to Planck's formula, in the range of ± 0.5 K for measurements at -60 °C, -80 °C and -100 °C, and less than ± 0.2 K at -20 °C and -40 °C. The here observed deviations are mainly caused by a drift of the responsivity of FTIR-spectrometer over the time period of several days (the responsivity of FTIR-spectrometer can be changed with its temperature, therefore the FTIR-spectrometer has to be calibrated for each measurement). As explained above, the purpose of this series of measurements was to test the performance of the RBCF over a broad temperature and spectral range and not to perform a high quality comparison of the blackbodies with Planck's law. In summary, radiances down to radiation temperature of -100 °C can be measured consistently with the vacuum FTIR-spectrometer applying the KBr broadband beamsplitter and the liquid nitrogen-cooled MCT detector.

5.1.3 Performance of FTIR-spectrometer with DLaTGS detector

The second set of measurements has been performed with the FTIR-spectrometer applying the KBr broadband beamsplitter and the pyroelectric DLaTGS detector. The results of the experimentally determined spectral radiances of the VLTBB and the theoretical radiances calculated by Planck's law at temperatures in the range from -100 °C to 140 °C are compared in Fig. 5.3. Again the noise level is also shown. Here the spectral radiance of the LN_2 -cooled blackbody could be neglected due to the higher noise level of the DLaTGS detector. In analogy to the previews section the spectral radiation temperatures of the VLTBB was calculated from the radiances shown in Fig. 5.3 by applying the inverted form of Planck's law. These results are given in Fig. 5.4.

The results show a deviation of the radiation temperature with wavelength from Planck's law in the range of ± 0.4 K for measurements at -100 °C, -80 °C and -60 °C and within ± 0.15 K for all other temperatures. Again, it is necessary to point out that this deviation is mainly caused by a drift of the spectral responsivity of the FTIR-spectrometer over the time period of several days. As explained above, the purpose of this series of measurements was to test the performance of the RBCF over a broad temperature and spectral range and not to perform a high precision comparison of the blackbodies with Planck's law.

The measurements with the DLaTGS at lower temperatures exhibit a significantly higher noise level than with the MCT but show also a consistent radiance temperature. In summary, radiances in a temperature range from -100 °C to 140 °C can be measured consistently at RBCF with the vacuum FTIR-spectrometer applying the KBr broadband beamsplitter and the pyroelectric DLaTGS detector.

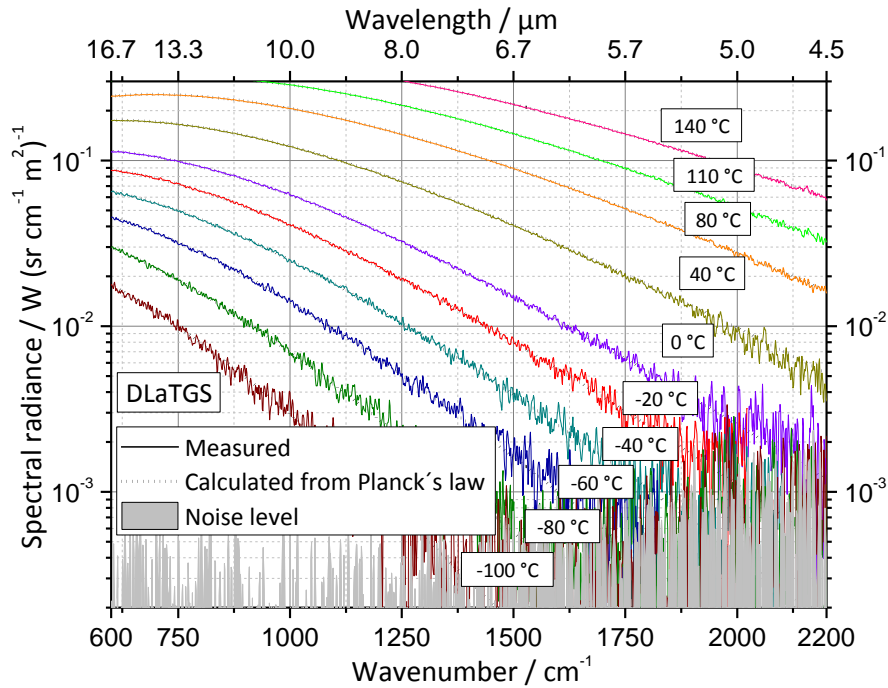


Fig. 5.3: The measured spectral radiances of the blackbody VLTBB operated at temperatures in the range from $-100\text{ }^{\circ}\text{C}$ to $140\text{ }^{\circ}\text{C}$ detected by the DLaTGS detector in comparison with the corresponding theoretical radiances calculated from Planck's law. Also the noise level is shown, calculated from the standard deviation of these measurements

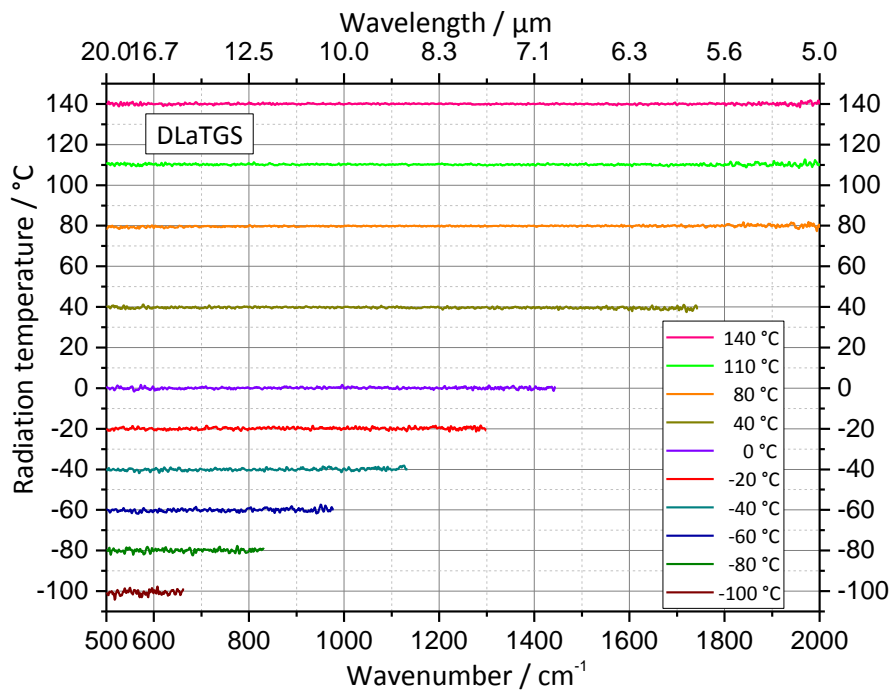


Fig. 5.4: The spectral distribution of radiation temperature of the VLTBB in the range from $-100\text{ }^{\circ}\text{C}$ to $140\text{ }^{\circ}\text{C}$ calculated from the radiances shown in Fig. 5.3 from the inverted Planck's law

5.1.4 Performance of FTIR-spectrometer with Si-composite bolometer

Finally, the measurements in the wavelength range from 20 μm to 100 μm have been performed with the vacuum FTIR-spectrometer applying the 6 μm Multilayer Mylar beamsplitter and the Si-composite bolometer. Considering time-consuming measurements, the analysis in this spectral region was performed only in a limited temperature range to show the capability of the facility at the most critical low temperatures. Again, the results are presented in two forms: the experimentally determined spectral radiances, compared with the theoretical values calculated by Planck's law, and, additionally, the radiation temperatures of the VLTBB. The measurements at -20 $^{\circ}\text{C}$, -60 $^{\circ}\text{C}$ and -100 $^{\circ}\text{C}$ are shown in Figs. 5.5 and 5.6.

It was shown that spectral radiances down to a radiation temperature of -100 $^{\circ}\text{C}$ can be measured consistently in the wavelength range from 20 μm to 100 μm with the Si-composite bolometer. The low noise-equivalent power ($NEP = 2.86 \cdot 10^{-13} \text{ W Hz}^{-1/2}$) of Si-composite bolometer, which provides the higher detectivity, is a strong argument in favor of this detector when measuring at low temperatures in the FIR range.

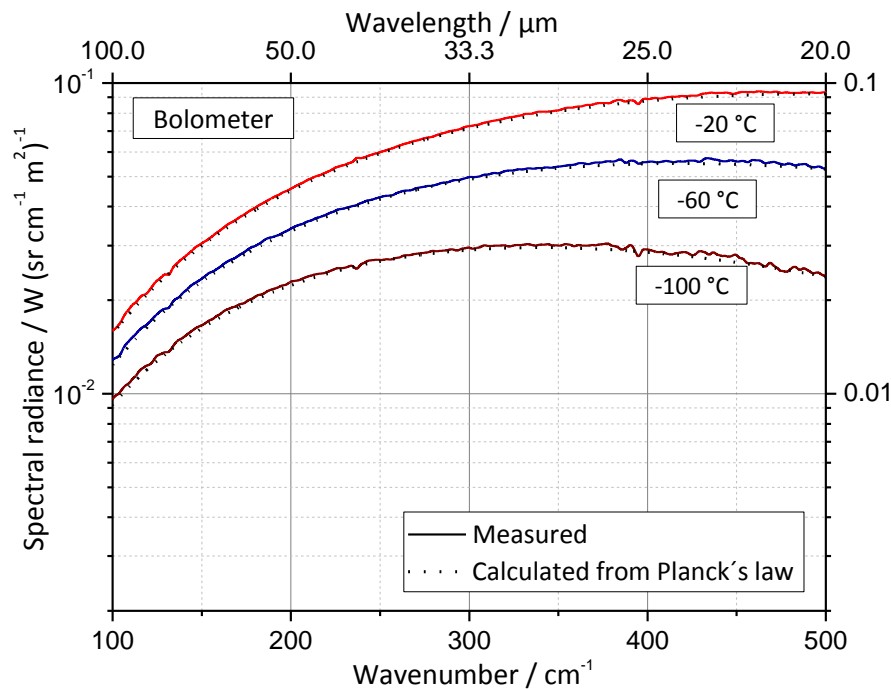


Fig. 5.5: The measured spectral radiances of the blackbody VLTBB operated at temperatures in the range from -100 $^{\circ}\text{C}$ to -20 $^{\circ}\text{C}$ detected by the Si-composite bolometer in comparison with the corresponding theoretical radiances calculated from Planck's law

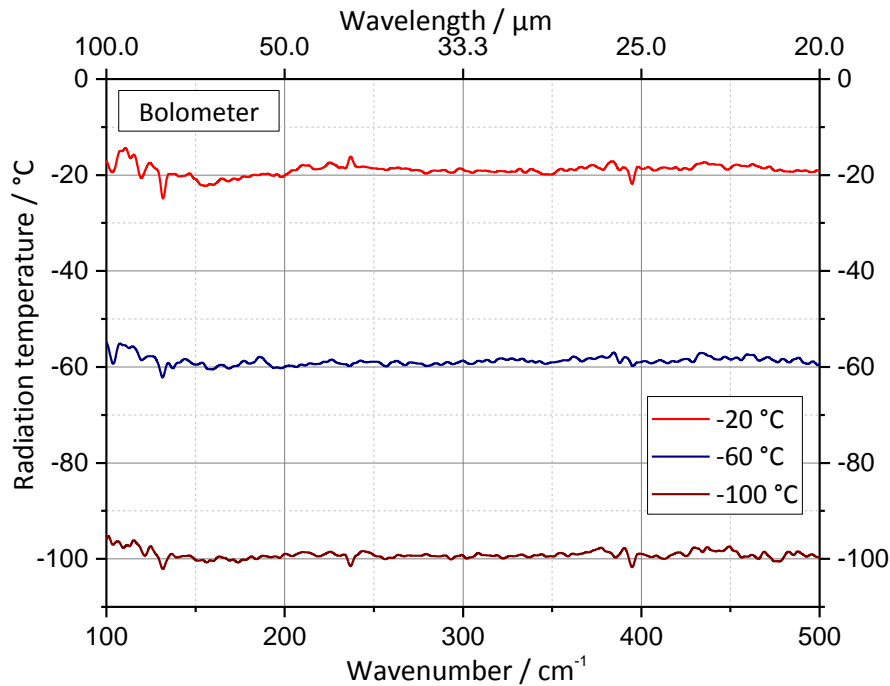


Fig. 5.6: The spectral distribution of radiation temperature of the VLTBB in the range from $-100\text{ }^{\circ}\text{C}$ to $-20\text{ }^{\circ}\text{C}$ calculated from the radiances shown in Fig. 5.5 from the inverted Planck's law

5.2 Effective emissivity and uncertainty budget of reference blackbodies

As mentioned before, the resulting overall accuracy of measurements and calibration procedures in radiating thermometry is significantly based on the accuracy of the radiation standards employed. Because of its precisely calculable properties one preferred radiation standard in metrology is a blackbody. Two dedicated vacuum variable-temperature blackbodies were developed for the RBCF. The designs of the VLTBB and the VMTBB were already presented in Chapter 4.2. Their characterization and uncertainty budgets are given here. In this section the results obtained by emissivity measurements under vacuum will be used, although the method of calculation as well as the overall uncertainty budget will be presented later.

5.2.1 Effective emissivity

The effective emissivity determines how close a real blackbody resembles an ideal blackbody and is therefore, in addition to the temperature range of operation, the main characteristic of a blackbody. The cavity geometry, the temperature homogeneity and the coating of the cavity wall determine the effective emissivity.

The calculation of the effective emissivity can be performed based on a Monte-Carlo ray tracing simulation by using the emissivity modeling program STEEP3 [59]. This simulation program follows an approach which considers rays entering the blackbody, instead of rays, which the blackbody emits. A schematic representation of a blackbody cavity where the radiation that enters the cavity is after multiple reflections either completely absorbed or escapes outside can be seen in the Fig. 2.3. Similarly, blackbody radiation generated at the cavity walls at a particular temperature can be considered as a ray emitted from the last point of reflection of the incoming radiation from the outside, but in the opposite direction. A random number generator is used for the determination of the directions of the contributing rays, which are used for the calculation of the effective emissivity of the cavity. Finally, all contributing rays are summed up and the ratio of the rays entering the cavity and escaping from the cavity within the geometry of observation determines the effective emissivity as a function of the cavity geometry and the reflective properties of the wall coating. A non-ideal or realistic cavity has a non-isothermal temperature distribution along the cavity, which influences the effective emissivity, too. This inhomogeneity results often from the size of the aperture which sometimes has to be large. Some examples of temperature distributions of the VMTBB along their cavities are shown in the Fig. 5.10. The Monte-Carlo ray tracing simulation also allows determining the emissivity of cavity with non-isothermal temperature distributions. In this case the emissivity of the wall cavity is weighted with the temperature of the particular location. If ε_j , ρ_k and T_j denote the emissivity, reflectivity and temperature in the j^{th} point of reflection, respectively, then the spectral effective cavity emissivity by reference temperature T_{ref} can be calculated from the equation:

$$\varepsilon(\lambda, T_{ref}) = \frac{1}{n_{\text{rays}}} \left[\exp\left(\frac{c_2}{\lambda T_{ref}}\right) - 1 \right] \sum_{i=1}^{n_{\text{rays}}} \sum_{j=1}^{m_i} \varepsilon_j(\lambda) \left[\exp\left(\frac{c_2}{\lambda T_j}\right) - 1 \right]^{-1} \prod_{k=1}^{j-1} \rho_k(\lambda) \quad (5.7)$$

where n_{rays} is the number of rays, is m_i the number of ray reflection in the i^{th} trajectory.

A more detailed description of this calculation approach for the effective emissivity of a cavity can be found in [61-64].

5.2.2 Effective emissivity of VMTBB

As written above the effective emissivity is calculated depending on the optical characteristics of the wall coating and the geometric features of the cavity. As a prerequisite the wall coating has to be characterized by angularly resolved directional spectral emissivity and

reflectivity measurements. To investigate the cavity of the VMTBB further test samples of the cavity coating were made. The black paint Duplicolor, used in the cavity of the VMTBB, was coated on a disc made of copper and measured in the wavelength range from 4 μm to 100 μm for directional spectral emittance and reflectance. The coating has a mean thickness of 77 μm .

The measurements of the directional spectral emissivity have been performed in two steps depending on the spectral range: in the MIR the measurement was determined at the setup for emissivity measurement in air with FTIR-spectrometer equipped with the pyroelectric detector of type DLATGS and the KBr beamsplitter; and the setup under vacuum was used for measurement in the FIR with the pyroelectric detector of type FDTGS and the 6 μm Multilayer Mylar beamsplitter (Fig. 5.7).

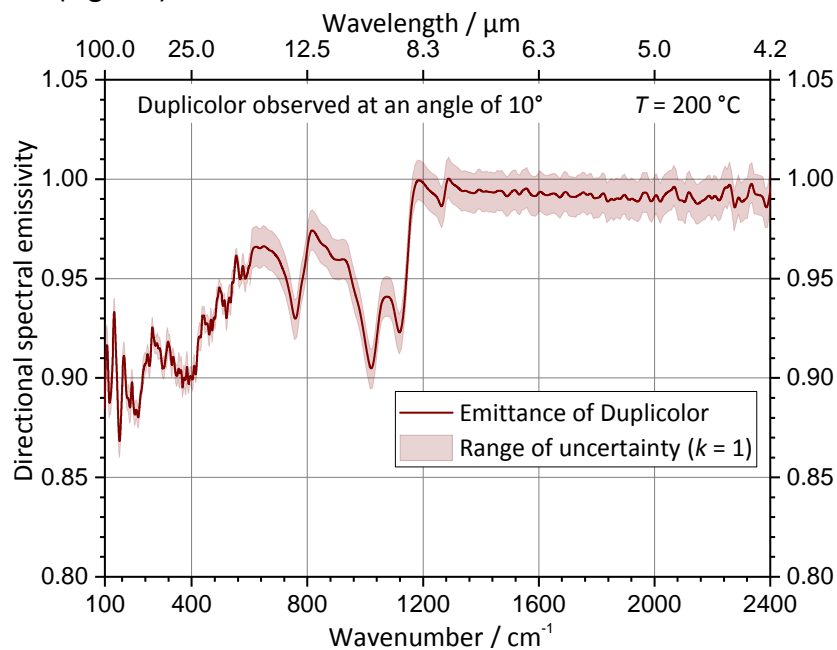


Fig. 5.7: Directional spectral emittance of a copper test substrate coated with Duplicolor recorded under an angle of observation of 10° with respect to the surface normal. This data is used as input parameter to STEEP3 for the effective emissivity calculation of the VMTBB. The sample was coated with a mean thickness of 77 μm . A shaded area shows the standard uncertainty

The reflectivity measurements were performed at the setup, described in Chapter 4.5.4, with the same combination of detectors and beamsplitters depending on the spectral range (Fig. 5.8). Both results show relatively stable characteristics up to 100 μm with a directional spectral emittance higher than 0.9 and a specular reflectance lower than 0.1. A slight decrease of emittance and an increase of reflectance can be seen at wavelengths longer than 8 μm . Consequently slight degradations of the effective emissivity can also be expected in that wavelength range.

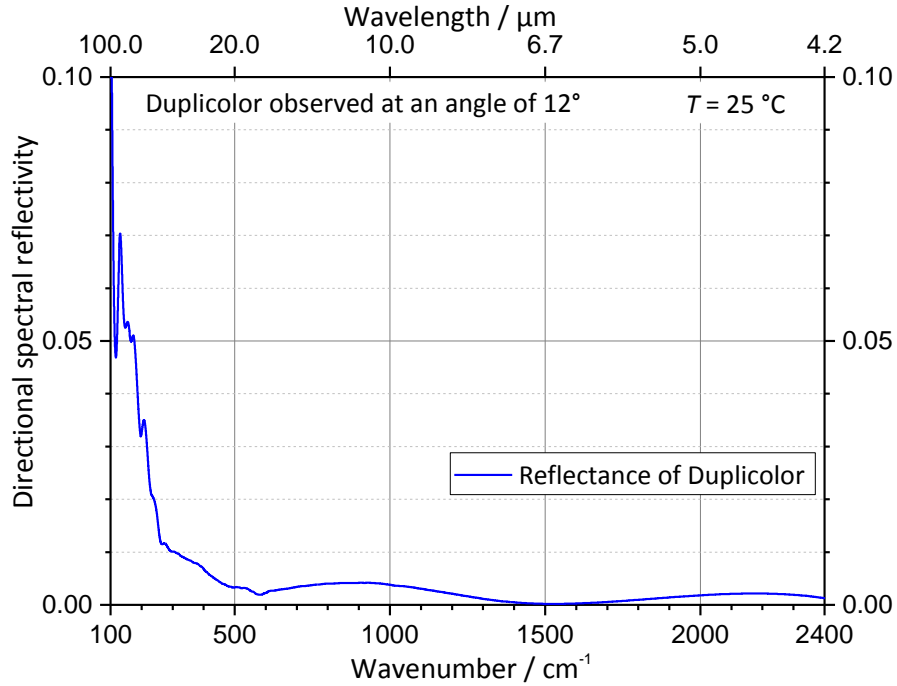


Fig. 5.8: Directional spectral reflectance in a 12°/12°-geometry of the copper test substrate coated with Duplicolor. This data is also used as input parameter to STEEP3 for the effective emissivity calculation of the VMTBB. The sample was coated with a mean thickness of 77 μm

As mentioned earlier, the Monte-Carlo calculation is based on the emissivity and reflectivity measurements of the coating. For the use by STEEP3 the quantities have to be expressed in terms of the specular reflectivity and a diffusivity [59]. According to the specular-diffuse model the reflection is represented as a sum of the Lambertian (diffuse) ρ_d and specular components ρ_s :

$$\rho = \rho_d + \rho_s \quad (5.8)$$

The diffusivity is a quantity that determines share of diffuse component in the total hemispherical reflectance and is calculated as:

$$D_{\text{diff}} = \frac{\rho_d}{\rho} \quad (5.9)$$

According to the relation $\rho = 1 - \varepsilon$ the diffusivity can be exactly calculated using the measured quantities- directional spectral emissivity under an angle of 10° and the spectral reflectivity under an angle of 12° (the difference between 12° and 10° can be neglected due to the very low angular dependence of the quantities at these angles):

$$D_{\text{diff}} = \frac{1 - \varepsilon - \rho_s}{1 - \varepsilon} \quad (5.10)$$

The lack of the measurements of the specular reflectivity, under other angles, can be compensated using a Fresnelian-Lambertian model [65]. In this model the spectral directional-hemispherical reflectance is the sum of a specular component depending on the angle and an angle-independent diffuse component. Based on it, the diffusivity of Duplicolor was calculated and is presented in Fig. 5.9 as function of wavelengths and angles. Fig. 5.9 shows that the diffusivity decreases towards longer wavelengths and larger angles.

The calculation of the effective spectral emittance of the VMTBB has been performed with the real geometry of the cavity and under the typical observation conditions at the RBCF. The diameter of the observed spot size in the cavity is 12.7 mm, the divergence of the detected bundle of ray is 2.8°. Three cases were investigated: an isothermal cavity (T constant) and non-isothermal cavity at 200 °C and 80 °C. The temperature distribution of the non-isothermal cavity of the VMTBB was measured for several temperatures and is plotted in Fig. 5.10 with respect to the bottom temperature.

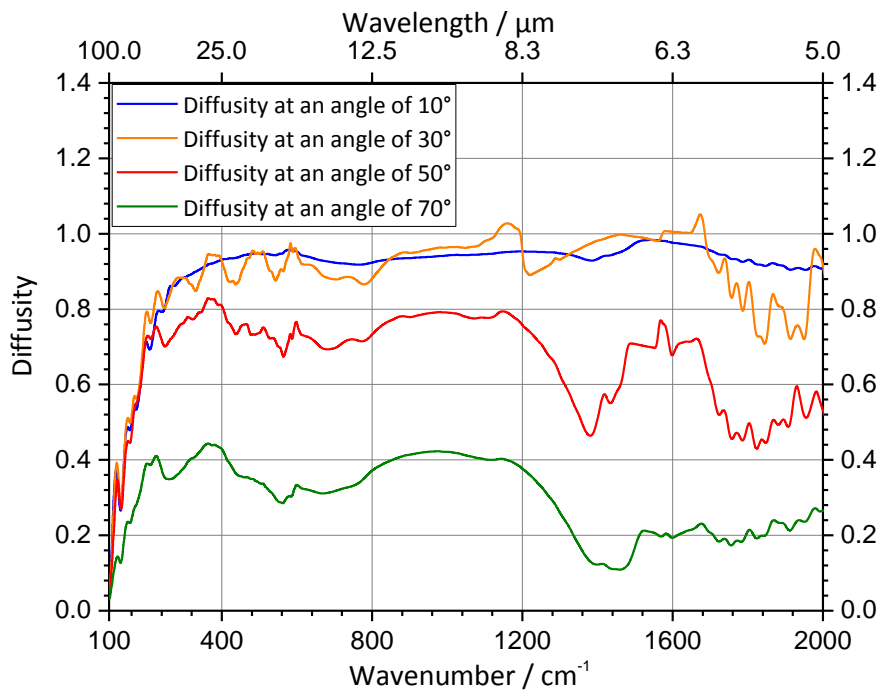


Fig. 5.9: Diffusivity calculated from measured directional spectral emittance and directional spectral reflectance of a copper substrate coated with Duplicolor under angles of observation of 10°, 30°, 50°, 70°

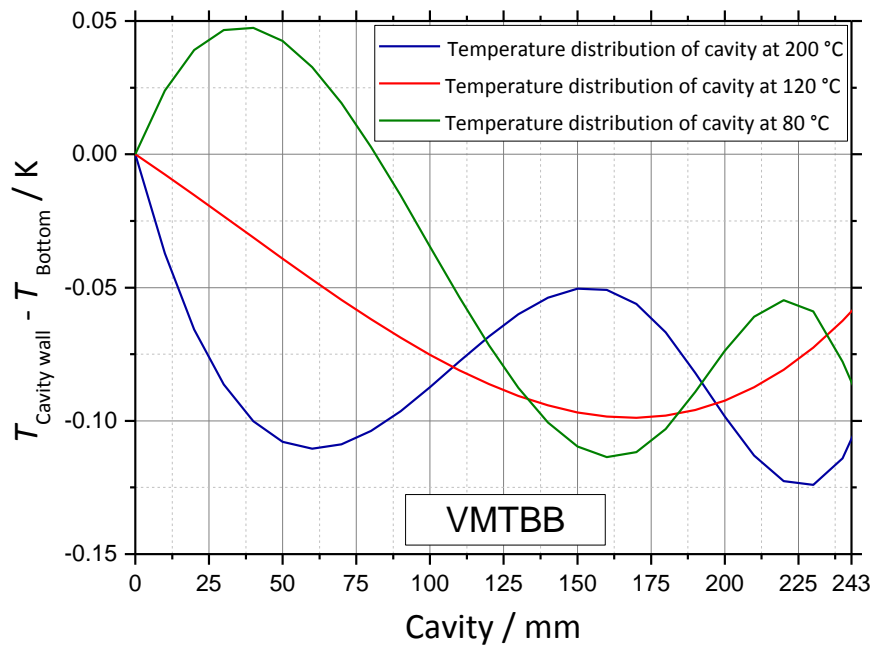


Fig. 5.10: Measured temperature distribution of cavity of the VMTBB at 200 °C, 120 °C and 80 °C with respect to the bottom temperature

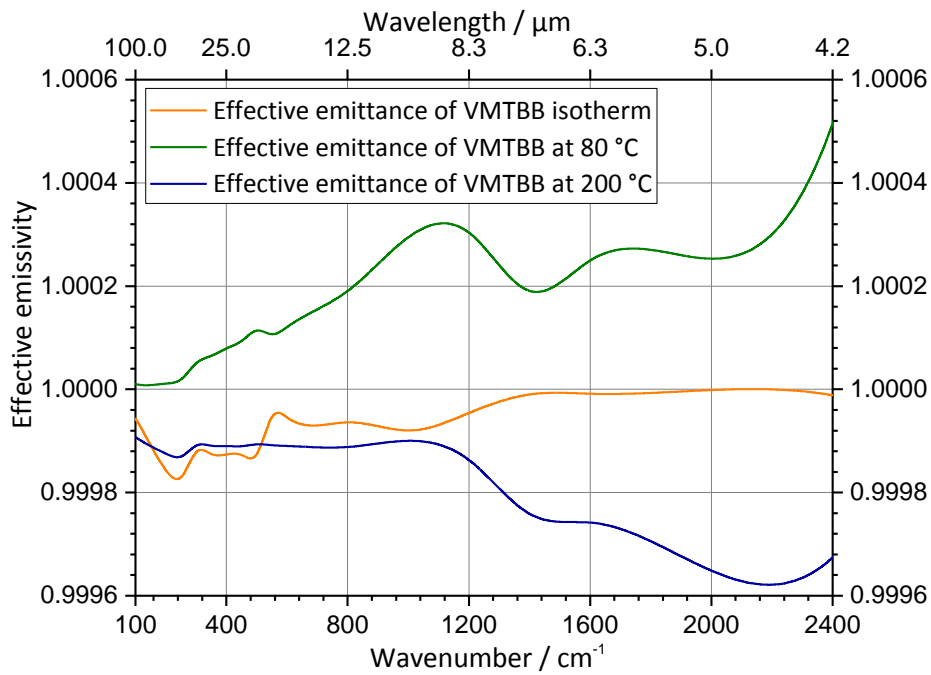


Fig. 5.11: The calculated effective spectral emittance of the VMTBB for isothermal distribution along the cavity and for non-uniform case at two reference temperatures: 200 °C and 80 °C

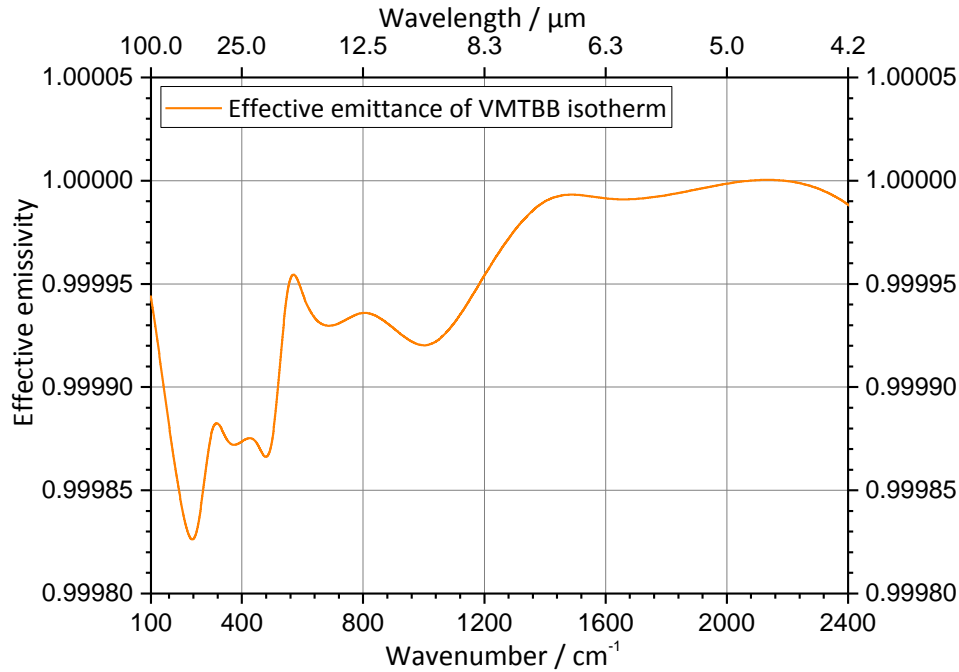


Fig. 5.12: Detailed view of effective spectral emittance of the VMTBB calculated in STEEP3 for isothermal cavity. The cavity radiator is brush coated with Duplicolor. For the calculation the emittance and reflectance of Duplicolor was used as input parameters to STEEP3

Table 5.1: Effective spectral emittance of the VMTBB for isothermal cavity and for two non-uniform temperature distribution along the cavity at $T_1=200\text{ °C}$ and $T_2=80\text{ °C}$

$T, \text{ °C}$	ε at								
	4.16 μm	5.55 μm	6.24 μm	7.14 μm	8.33 μm	9.91 μm	12.49 μm	16.64 μm	18.16 μm
Iso	0.99999	0.99999	0.99999	0.99999	0.99995	0.99992	0.99994	0.99994	0.99995
80	1.00052	1.00027	1.00025	1.00019	1.00031	1.00031	1.00019	1.00012	1.00011
200	0.99967	0.99971	0.99974	0.99976	0.99986	0.9999	0.99989	0.99989	0.99989
$T, \text{ °C}$	ε at								
	19.98 μm	22.25 μm	24.92 μm	28.48 μm	33.23 μm	39.88 μm	49.85 μm	66.47 μm	101.66 μm
Iso	0.99988	0.99987	0.99987	0.99987	0.99988	0.99983	0.99984	0.99989	0.99995
80	1.00011	1.00009	1.00008	1.00007	1.00005	1.00002	1.00001	1.00001	1.00001
200	0.99989	0.99989	0.99989	0.99989	0.99989	0.99987	0.99988	0.99989	0.99991

The effective spectral emittances of the VMTBB are calculated with STEEP3 for the three above-mentioned cases at 18 selected wavelengths in the range from 4 μm to 100 μm . The results are summarized in Table 5.1. The interpolated spectral curves are shown in Fig. 5.11. The resulting isothermal effective spectral emittance of the cavity radiator of the VMTBB coated with Duplicolor is better than 0.9999 in the wavelength range from 4 μm to 20 μm , and better than 0.9998 from 20 μm to 100 μm (Fig. 5.12). The small decrease in effective emittance towards longer wavelengths is due to the corresponding decrease in emittance of the wall coating (Fig. 5.7). The effect, that the effective emittance of a non-isothermal cavity is greater than 1 for the case of 80 °C , is explained by the fact that the

reference temperature is taken at the bottom of the cavity, and the temperature distribution along the cavity can rise above the bottom temperature (Fig. 5.10).

5.2.3 Uncertainty budget of VMTBB

The uncertainty of the VMTBB depends of four components with corresponding type evaluations of standard uncertainty [7] and is due to the spectral dependence of the effective emissivity also spectrally dependent (Table 5.2). Because of the very time-consuming calculation in STEEP3, the determination of effective emissivity for the non-isothermal cavity at each temperature in the desired range from 80 °C to 430 °C is not possible. Therefore the required calculations of the effective emissivity under vacuum for the uncertainty budget were done by the isothermal approximation of the blackbody. However, the final uncertainty budget will take into account the contribution associated with the difference between the isothermal and non-isothermal cases. In the following subsections the individual uncertainty components and their sub components are discussed in detail.

Table 5.2: Uncertainty contributions to the overall uncertainty of the VMTBB

Uncertainty contributions	Sub components	Symbol	Type
Effective emissivity	Reflection of background	u_{Refl}	B
	Emissivity of wall coating	u_{Emiss}	B
	Non-isothermal cavity	u_{Non}	B
Calibration of temperature sensor		u_{Cal}	A
Noise (PRTs)		u_{Noise}	A
Stability (PRTs)		u_{PRT}	B

Uncertainty of effective emissivity

1) Reflection of background

Each of the two reference blackbodies at the RBCF is located in the source chamber, thus the background radiation from the chamber and all components on the optical path is reflected from the nonideal cavities of the blackbodies and contributes to the resulting radiation temperatures. As mentioned before, in the following the approximation of the isothermal cavity of the VMTBB is used with the effective emissivity shown in Fig. 5.12. The radiance of a nonideal blackbody has to be considered as the sum of the radiance emitted by the cavity and the reflected background radiance:

$$L_{\text{nonideal}} = \varepsilon_{\text{BB-isoth}} L_{\text{Planck}}(T_{\text{BB}}) + (1 - \varepsilon_{\text{BB-isoth}}) L_{\text{Background}}(T_{\text{Amb}}) \quad (5.11)$$

Here the spectral radiance of the blackbody is given by Planck's function $L_{\text{Planck}}(T_{\text{BB}})$ at the respective temperature multiplied by $\varepsilon_{\text{BB-isoth}}$ - the spectral effective emissivity of the blackbody

calculated in STEEP3 for the isothermal case (the dependence of effective emissivity on the wavelength, temperature and polar angle are here omitted for clarity). The background radiance is given by the Planck function $L_{\text{Background}}(T_{\text{Amb}})$ at room temperature. It is reflected by the reflectivity of the blackbody $\rho_{\text{BB-isoth}} = 1 - \varepsilon_{\text{BB-isoth}}$. So the influence of a non-ideal emissivity is twofold: it reduces the amount of radiation emitted directly by the cavity and increases the amount of ambient or background radiation reflected by the cavity.

The respective radiation temperature of the nonideal blackbody can be calculated by applying the inverted form of Planck's law on Equation 5.11. The deviation in radiation temperature is then given as the difference to the radiation temperature of ideal blackbody ($\varepsilon_{\text{BB-ideal}} = 1$) at the same temperature:

$$\Delta T_{\text{Refl}} = T \left(\varepsilon_{\text{BB-isoth}} L_{\text{Planck}}(T_{\text{BB}}) + (1 - \varepsilon_{\text{BB-isoth}}) L_{\text{Background}}(T_{\text{Amb}}) \right) - T \left(L_{\text{Planck}}(T_{\text{BB}}) \right) \quad (5.12)$$

The corresponding uncertainty is given as the deviation divided by the square root of 3 [7]. The uncertainty values for this subcomponent are shown in Table 5.3.

$$u_{\text{Refl}} = \frac{\Delta T_{\text{Refl}}}{\sqrt{3}} \quad (5.13)$$

Table 5.3: Uncertainty of reflection of background of the VMTBB

$T, ^\circ\text{C}$	$u_{\text{Refl}}, \text{K}$								
	4.16 μm	5.55 μm	6.24 μm	7.14 μm	8.33 μm	9.91 μm	12.49 μm	16.64 μm	18.16 μm
80	0.001	0.001	0.001	0.001	-0.002	-0.003	-0.002	-0.002	-0.002
100	-0.001	0.001	0.001	0.001	-0.002	-0.004	-0.003	-0.002	-0.002
120	-0.001	0.001	0.001	0.001	-0.003	-0.004	-0.004	-0.003	-0.003
150	-0.001	0.001	-0.001	0.001	-0.003	-0.006	-0.005	-0.004	-0.004
170	-0.001	0.001	-0.001	0.001	-0.004	-0.007	-0.005	-0.005	-0.005
200	-0.001	-0.001	-0.001	0.001	-0.005	-0.008	-0.007	-0.006	-0.005
250	-0.002	-0.001	-0.001	-0.001	-0.006	-0.010	-0.008	-0.007	-0.007
350	-0.002	-0.001	-0.002	-0.001	-0.009	-0.015	-0.012	-0.010	-0.010
430	-0.003	-0.001	-0.002	-0.001	-0.011	-0.019	-0.015	-0.013	-0.013
$T, ^\circ\text{C}$	$u_{\text{Refl}}, \text{K}$								
	19.98 μm	22.25 μm	24.92 μm	28.48 μm	33.23 μm	39.88 μm	49.85 μm	66.47 μm	101.66 μm
80	-0.004	-0.004	-0.004	-0.004	-0.004	-0.006	-0.005	-0.004	-0.002
100	-0.006	-0.006	-0.006	-0.006	-0.005	-0.008	-0.007	-0.005	-0.002
120	-0.007	-0.007	-0.007	-0.007	-0.007	-0.010	-0.009	-0.006	-0.003
150	-0.009	-0.009	-0.009	-0.009	-0.009	-0.012	-0.012	-0.008	-0.004
170	-0.011	-0.011	-0.011	-0.011	-0.010	-0.014	-0.013	-0.009	-0.005
200	-0.013	-0.013	-0.013	-0.013	-0.012	-0.017	-0.016	-0.011	-0.006
250	-0.016	-0.017	-0.017	-0.016	-0.016	-0.022	-0.021	-0.014	-0.007
350	-0.024	-0.024	-0.024	-0.024	-0.023	-0.032	-0.030	-0.021	-0.010
430	-0.029	-0.030	-0.030	-0.030	-0.029	-0.040	-0.037	-0.026	-0.013

2) Emissivity of wall coating

The calculation of the next uncertainty component u_{Emiss} follows the calculation of the previously discussed sub component u_{Refl} , but takes into account the uncertainty of the emissivity measurements of the wall coating (measurement of test substrate coated with Duplicolor). The effective emissivity of the cavity was calculated in STEEP3 for two cases. According to the uncertainty of the directional spectral emittance of Duplicolor (Fig. 5.7) this was done for a lower and a higher course of directional spectral emittance. Correspondingly two effective emissivities were obtained $\varepsilon_{\text{BB-isoth}}^{+u}$ and $\varepsilon_{\text{BB-isoth}}^{-u}$ which influence the amount of radiation emitted directly from the cavity and of the ambient radiation reflected from the cavity. Then the radiation temperatures of the blackbody considering the amount of the reflected radiance from the background are calculated via Equation 5.12 for the two effective emissivities $\varepsilon_{\text{BB-isoth}}^{+u}$ and $\varepsilon_{\text{BB-isoth}}^{-u}$. The difference of the two cases is given in Equations 5.14. It gives the variation of the radiation temperature due to uncertainty of the spectral emissivity. The resulting uncertainty is again obtained by division by the square root of 3 and given in Equation 5.15 as well as in Table 5.4.

Table 5.4: Uncertainty of emissivity of wall coating of the VMTBB

$T, ^\circ\text{C}$	$u_{\text{Emiss}}, \text{K}$ 4.16 μm	$u_{\text{Emiss}}, \text{K}$ 5.55 μm	$u_{\text{Emiss}}, \text{K}$ 6.24 μm	$u_{\text{Emiss}}, \text{K}$ 7.14 μm	$u_{\text{Emiss}}, \text{K}$ 8.33 μm	$u_{\text{Emiss}}, \text{K}$ 9.91 μm	$u_{\text{Emiss}}, \text{K}$ 12.49 μm	$u_{\text{Emiss}}, \text{K}$ 16.64 μm	$u_{\text{Emiss}}, \text{K}$ 18.16 μm
80	0.001	0.001	0.001	0.002	0.003	0.002	0.002	0.001	0.001
100	0.002	0.001	0.002	0.002	0.004	0.003	0.003	0.001	0.001
120	0.002	0.001	0.002	0.003	0.005	0.004	0.003	0.002	0.002
150	0.003	0.001	0.002	0.004	0.006	0.005	0.004	0.002	0.002
170	0.003	0.001	0.003	0.005	0.007	0.006	0.005	0.003	0.003
200	0.004	0.002	0.003	0.006	0.009	0.008	0.006	0.003	0.003
250	0.005	0.002	0.004	0.007	0.011	0.010	0.008	0.004	0.004
350	0.007	0.003	0.006	0.011	0.016	0.014	0.011	0.006	0.006
430	0.009	0.004	0.008	0.013	0.020	0.018	0.014	0.007	0.007
$T, ^\circ\text{C}$	$u_{\text{Emiss}}, \text{K}$ 19.98 μm	$u_{\text{Emiss}}, \text{K}$ 22.25 μm	$u_{\text{Emiss}}, \text{K}$ 24.92 μm	$u_{\text{Emiss}}, \text{K}$ 28.48 μm	$u_{\text{Emiss}}, \text{K}$ 33.23 μm	$u_{\text{Emiss}}, \text{K}$ 39.88 μm	$u_{\text{Emiss}}, \text{K}$ 49.85 μm	$u_{\text{Emiss}}, \text{K}$ 66.47 μm	$u_{\text{Emiss}}, \text{K}$ 101.66 μm
80	0.001	0.001	0.001	0.001	0.001	0.001	0.001	0.001	0.002
100	0.001	0.001	0.001	0.001	0.001	0.002	0.002	0.002	0.003
120	0.002	0.002	0.002	0.002	0.002	0.002	0.002	0.003	0.004
150	0.002	0.002	0.002	0.002	0.002	0.002	0.003	0.003	0.005
170	0.003	0.003	0.003	0.003	0.003	0.003	0.003	0.004	0.006
200	0.003	0.003	0.003	0.003	0.003	0.003	0.004	0.005	0.007
250	0.004	0.004	0.004	0.004	0.004	0.004	0.005	0.006	0.009
350	0.006	0.006	0.006	0.006	0.006	0.006	0.007	0.008	0.012
430	0.007	0.007	0.008	0.008	0.008	0.008	0.008	0.010	0.015

$$\begin{aligned} \Delta T_{\text{Emiss}} &= T_{\text{BB-isoth}}^{+u} - T_{\text{BB-isoth}}^{-u} = \\ &= T \left(\varepsilon_{\text{BB-isoth}}^{+u} L_{\text{Planck}}(T_{\text{BB}}) + (1 - \varepsilon_{\text{BB-isoth}}^{+u}) L_{\text{Background}}(T_{\text{Amb}}) \right) - \\ &- T \left(\varepsilon_{\text{BB-isoth}}^{-u} L_{\text{Planck}}(T_{\text{BB}}) + (1 - \varepsilon_{\text{BB-isoth}}^{-u}) L_{\text{Background}}(T_{\text{Amb}}) \right) \end{aligned} \quad (5.14)$$

$$u_{\text{Emiss}} = \frac{\Delta T_{\text{Emiss}}}{\sqrt{3}} \quad (5.15)$$

3) Uncertainty of non-isothermal cavity

As mentioned above, the uncertainty due the difference between the effective emissivity of the isothermal and non-isothermal cavity has to be considered as well. The difference in the effective emissivities yield again to a different amount of radiation emitted from the cavity and a different amount of ambient radiation reflected from the cavity.

The non-isothermal case was calculated in STEEP3 with the temperature distribution at 80 °C as a worst case scenario. The difference of the radiation temperatures of the isothermal and the non-isothermal cases ΔT_{Non} is calculated by Equation 5.16 always using the worst case $\varepsilon_{\text{BB-noniso}}$. So the real radiation temperature will be between $T(L_{\text{BB-noniso}})$ and $T(L_{\text{BB-isoth}})$. Assuming a rectangular distribution the corresponding uncertainty u_{Non} is given by Equation 5.17 and in Table 5.5.

Table 5.5: Uncertainty of non-isothermal cavity

$T, ^\circ\text{C}$	u_{Non}, K								
	4.16 μm	5.55 μm	6.24 μm	7.14 μm	8.33 μm	9.91 μm	12.49 μm	16.64 μm	18.16 μm
80	-0.018	-0.009	-0.009	-0.007	-0.013	-0.014	-0.010	-0.007	-0.007
100	-0.024	-0.012	-0.012	-0.009	-0.017	-0.019	-0.013	-0.010	-0.009
120	-0.030	-0.016	-0.015	-0.011	-0.021	-0.024	-0.017	-0.012	-0.011
150	-0.039	-0.021	-0.019	-0.015	-0.028	-0.032	-0.022	-0.016	-0.015
170	-0.046	-0.024	-0.023	-0.017	-0.032	-0.037	-0.026	-0.018	-0.017
200	-0.055	-0.029	-0.027	-0.020	-0.039	-0.045	-0.031	-0.022	-0.020
250	-0.070	-0.037	-0.035	-0.026	-0.050	-0.057	-0.040	-0.028	-0.026
350	-0.101	-0.053	-0.050	-0.038	-0.072	-0.082	-0.057	-0.041	-0.038
430	-0.126	-0.066	-0.062	-0.047	-0.090	-0.103	-0.071	-0.051	-0.047
$T, ^\circ\text{C}$	u_{Non}, K								
	19.98 μm	22.25 μm	24.92 μm	28.48 μm	33.23 μm	39.88 μm	49.85 μm	66.47 μm	101.66 μm
80	-0.011	-0.010	-0.010	-0.009	-0.009	-0.010	-0.009	-0.006	-0.003
100	-0.015	-0.014	-0.013	-0.013	-0.012	-0.014	-0.013	-0.009	-0.005
120	-0.018	-0.018	-0.017	-0.016	-0.015	-0.018	-0.016	-0.011	-0.006
150	-0.024	-0.023	-0.022	-0.021	-0.019	-0.023	-0.021	-0.014	-0.008
170	-0.028	-0.027	-0.025	-0.024	-0.022	-0.027	-0.024	-0.017	-0.009
200	-0.034	-0.032	-0.030	-0.029	-0.027	-0.032	-0.029	-0.020	-0.011
250	-0.043	-0.041	-0.039	-0.037	-0.034	-0.041	-0.037	-0.026	-0.014
350	-0.062	-0.059	-0.056	-0.053	-0.049	-0.059	-0.053	-0.037	-0.020
430	-0.078	-0.074	-0.070	-0.066	-0.061	-0.074	-0.066	-0.046	-0.025

$$\begin{aligned}\Delta T_{\text{Non}} &= T(L_{\text{BB-noniso}}) - T(L_{\text{BB-iso}}) = \\ &= T\left(\varepsilon_{\text{BB-noniso}} L_{\text{Planck}}(T_{\text{BB}}) + (1 - \varepsilon_{\text{BB-noniso}}) L_{\text{Background}}(T_{\text{Amb}})\right) - \\ &- T\left(\varepsilon_{\text{BB-iso}} L_{\text{Planck}}(T_{\text{BB}}) + (1 - \varepsilon_{\text{BB-iso}}) L_{\text{Background}}(T_{\text{Amb}})\right)\end{aligned}\quad (5.16)$$

$$u_{\text{Non}} = \frac{\Delta T_{\text{Non}}}{\sqrt{3}} \quad (5.17)$$

Uncertainty of PRTs

The four calibrated temperature sensors in the VMTBB age slightly during their period of operation yielding to an additional uncertainty component. This aging can be calculated from the, over the time, increasing spread of the temperature values measured by the sensors when the cavity is stable and at a given temperature. It is calculated for three operating temperatures and interpolated for the temperatures given in Table 5.6. The uncertainty of the other component u_{Cal} (see Table 5.2) is given by the certificate of calibration [66], and the noise of PRT measurement is directly determined from the data recorded with the temperature monitor the Hart Super-Thermometer.

Table 5.6: Stability of PRTs of VMTBB

$T, ^\circ\text{C}$	80	100	120	150	170	200	250	350	430
u_{PRT}, K	0.015	0.014	0.013	0.012	0.011	0.010	0.008	0.005	0.006

Table 5.7: Uncertainty of calibration of PRTs and uncertainty of Noise of PRTs

Uncertainty contributions (component)	Uncertainty, K	Type
Calibration of temperature sensor, u_{Cal}	0.025	A
Noise (PRTs), u_{Noise}	0.001	A

Uncertainty budget of the VMTBB

Finally the combined uncertainty is calculated at chosen wavelengths in the range from 4 μm to 100 μm and from 80 $^\circ\text{C}$ to 430 $^\circ\text{C}$. The resulting overall uncertainty budget of VMTBB is given in Table 5.8.

Table 5.8: Overall uncertainty budget of the VMTBB

$T, ^\circ\text{C}$	u, K 4.16 μm	u, K 5.55 μm	u, K 6.24 μm	u, K 7.14 μm	u, K 8.33 μm	u, K 9.91 μm	u, K 12.49 μm	u, K 16.64 μm	u, K 18.16 μm
80	0.034	0.031	0.030	0.030	0.032	0.033	0.031	0.030	0.030
100	0.037	0.031	0.031	0.030	0.034	0.035	0.032	0.030	0.030
120	0.041	0.032	0.032	0.031	0.036	0.038	0.033	0.031	0.031
150	0.048	0.035	0.034	0.032	0.040	0.043	0.036	0.032	0.032
170	0.053	0.036	0.036	0.033	0.043	0.047	0.038	0.033	0.033
200	0.061	0.039	0.038	0.034	0.049	0.053	0.042	0.035	0.034
250	0.075	0.045	0.044	0.038	0.058	0.064	0.049	0.039	0.038
350	0.105	0.059	0.057	0.047	0.079	0.089	0.065	0.050	0.047
430	0.129	0.071	0.068	0.055	0.096	0.109	0.078	0.059	0.055

$T, ^\circ\text{C}$	u, K 19.98 μm	u, K 22.25 μm	u, K 24.92 μm	u, K 28.48 μm	u, K 33.23 μm	u, K 39.88 μm	u, K 49.85 μm	u, K 66.47 μm	u, K 101.66 μm
80	0.031	0.031	0.031	0.031	0.031	0.031	0.031	0.030	0.029
100	0.033	0.032	0.032	0.032	0.032	0.033	0.032	0.031	0.029
120	0.035	0.034	0.034	0.033	0.033	0.035	0.034	0.031	0.029
150	0.038	0.037	0.037	0.036	0.035	0.038	0.037	0.033	0.030
170	0.041	0.040	0.039	0.038	0.037	0.041	0.039	0.034	0.030
200	0.045	0.044	0.043	0.042	0.040	0.045	0.043	0.036	0.030
250	0.053	0.052	0.050	0.048	0.046	0.054	0.050	0.040	0.032
350	0.072	0.069	0.067	0.064	0.060	0.072	0.066	0.050	0.036
430	0.087	0.084	0.081	0.078	0.073	0.088	0.081	0.060	0.041

5.2.4 Effective emissivity and uncertainty budget of VLTBB from 4 μm to 20 μm

In the case of the VLTBB the main difficulty for the calculation of the effective emissivity results from the coating of the cavity which becomes transparent towards longer wavelengths (Chapter 7.4). When this is the case the influence of the thickness of the coating and of possible thickness variations on the effective emissivity increase significantly. This is not only due to the decrease of the emissivity towards longer wavelengths, but also due to the multiple beam interference, which is discussed in Chapter 7.4. Because the cavity of the VLTBB was brush coated with Aeroglaze Z306 and this method of application does not allow obtaining a uniform layer, thickness variations are likely and one has to deal with a distribution of thicknesses.

Thus, the study of effective emissivity of the VLTBB is divided into two steps: from 4 μm to 20 μm , where the variation of the coating thickness, considering its opacity, does not have a significant influence; and from 20 μm to 100 μm , where the correct calculation using STEEP3 is not possible without exact knowledge of the thickness of the coating.

Four samples, copper substrates coated with Aeroglaze Z306, were prepared for the investigation of the effective emissivity of the VLTBB. For a better resemblance of the situation in the cavity, the Aeroglaze Z306 was brush coated on the first substrate of copper with a mean thickness of 88 μm . This sample is most suitable for the calculation of effective emissivity in the first wavelength range from 4 μm to 20 μm . The other three samples were obtained by applying of Aeroglaze Z306 according to the instructions given in the European Cooperation for Space Standardization document ECSS-Q-70-25A [45] to obtain uniform thicknesses of 44 μm , 99 μm and 236 μm , respectively. For that purpose different numbers of crossed layers were sprayed on a set of three copper substrates according to the desired final thickness. This method provides a high homogeneity of the surfaces. These three samples were not only used to estimate the experimentally obtained effective emissivity of the VLTBB in the range from 20 μm to 100 μm and to indirectly determine the coating thickness of the

cavity (see below), but also used to study the interference effect in thin films during of emissivity and reflectivity measurements (Chapter 7.4).

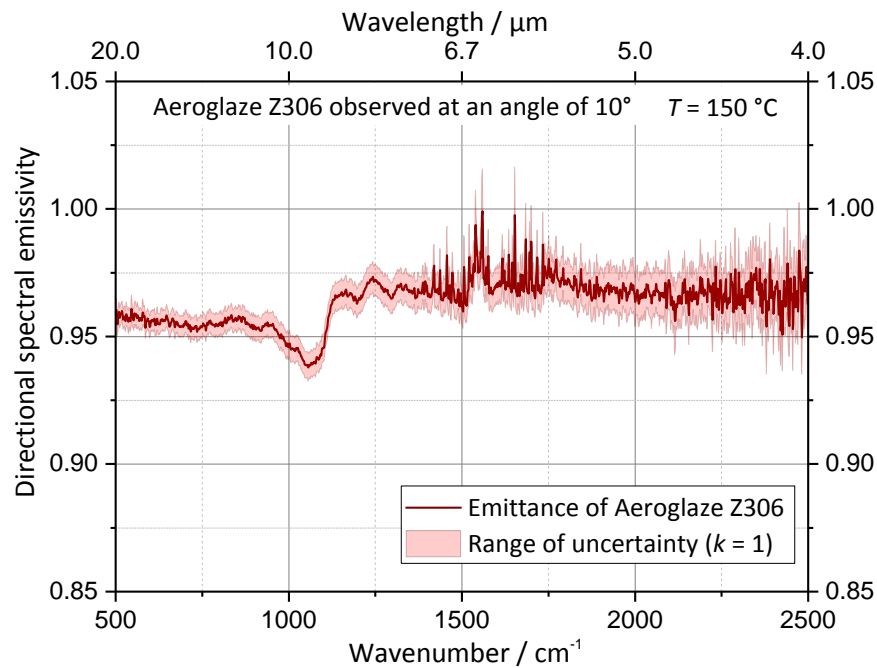


Fig. 5.13: Directional spectral emittance of a copper plate coated with Aeroglaze Z306 under an angle of observation of 10° to the surface normal. The sample was brush coated with a mean thickness of $88\ \mu\text{m}$. The shaded area shows the range of the standard uncertainty

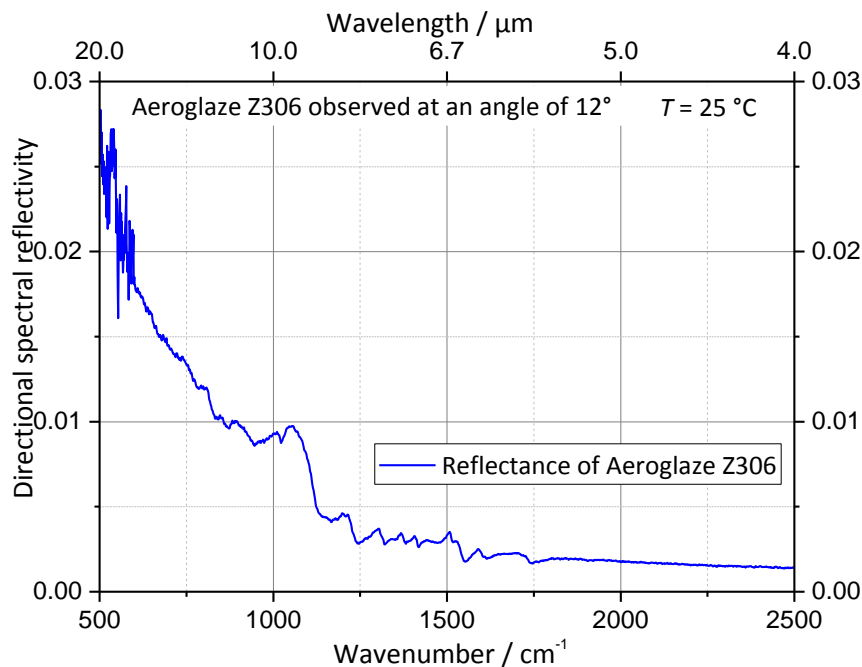


Fig. 5.14: Directional spectral reflectance in a $12^\circ/12^\circ$ -geometry of a copper plate coated with Aeroglaze Z306. The sample was brush coated with a mean thickness of $88\ \mu\text{m}$. It is the same sample as shown in Fig. 5.13

The effective emissivity of the VLTBB has been calculated from 4 μm to 20 μm by a Monte-Carlo simulation using emissivity and reflectivity measurements of the wall coating as input parameters (Figs. 5.13 and 5.14), similar as it was done for the VMTBB. The brush coated sample was investigated at the emissivity setup in air with the spectrometer equipped with a similar combination of detector and beamsplitter as in Chapter 5.2.2. The uncertainty budget of the VLTBB was calculated similar to the scheme described above for the VMTBB. Here the effective spectral emittance of the VLTBB, calculated in STEEP3 for the isothermal cavity, and the uncertainty budget from 4 μm to 20 μm are shown in Fig. 5.15 and Table 5.9, respectively.

Table 5.9: Overall uncertainty budget of the VLTBB from 4 μm to 20 μm

$T, ^\circ\text{C}$	u, K	u, K	u, K	u, K						
	4.16 μm	5.55 μm	6.24 μm	7.14 μm	8.33 μm	9.91 μm	12.49 μm	16.64 μm	18.16 μm	19.9 μm
-50	0.334	0.116	0.086	0.067	0.054	0.040	0.043	0.040	0.040	0.040
-40	0.185	0.081	0.066	0.056	0.049	0.042	0.043	0.042	0.042	0.042
-30	0.111	0.063	0.056	0.051	0.048	0.044	0.045	0.044	0.044	0.044
-20	0.075	0.054	0.051	0.049	0.048	0.046	0.047	0.046	0.046	0.046
0	0.051	0.049	0.049	0.049	0.048	0.048	0.048	0.048	0.048	0.048
80	0.031	0.029	0.029	0.028	0.028	0.026	0.027	0.027	0.027	0.027
140	0.029	0.026	0.025	0.024	0.023	0.016	0.021	0.019	0.018	0.018
150	0.030	0.027	0.026	0.025	0.024	0.016	0.022	0.019	0.019	0.018
170	0.033	0.030	0.029	0.029	0.027	0.018	0.025	0.022	0.021	0.020

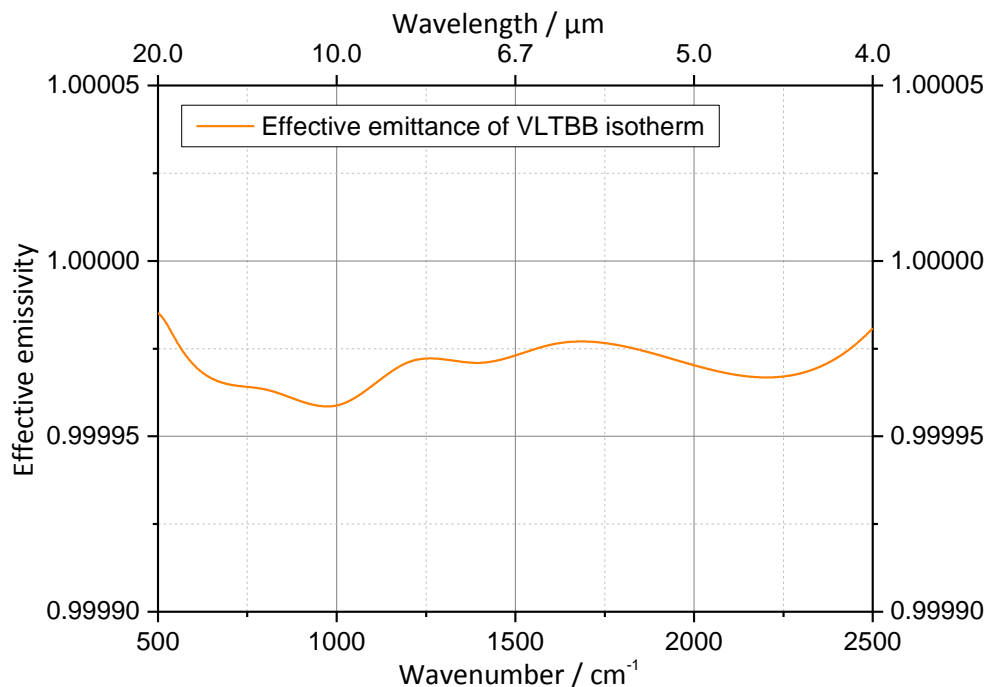


Fig. 5.15: Effective spectral emittance of the VLTBB calculated in STEEP3 for isothermal cavity. The cavity radiator is brush coated with Aeroglaze Z306. For the calculation the emittance and reflectance of Aeroglaze Z306 with a mean thickness of 88 μm was used

5.2.5 Comparison of two reference vacuum blackbodies VLTBB and VMTBB

A direct comparison of the VLTBB and the VMTBB has been performed to validate the two blackbodies and the determined uncertainties of their radiation temperatures. For the comparison a sequence of measurements according to Equations 5.4 and 5.6 has been done for each blackbody. It is assumed that the radiance of one blackbody (VLTBB in this case) is given by its effective emissivity and Planck's law from its operating temperature. A deviation of the radiation temperature of the other blackbody from its operating temperature is an estimation of the consistency of both blackbodies. By dividing two independent equations (difference of Equations 5.4 and 5.6) for the VLTBB and the VMTBB, the radiance of the VMTBB can be calculated as:

$$L_{\text{VMTBB}}(T) = \frac{(\tilde{L}_{\text{VMTBB}}(T_{\text{VMTBB}}) - \tilde{L}_{\text{BB-LN}_2}(T_{\text{BB-LN}_2})) (L_{\text{VLTBB}}(T_{\text{VLTBB}}) - [1 - \varepsilon_{\text{Ch}}(\lambda, 45^\circ, T_{\text{Ch}})] \varepsilon_{\text{BB-LN}_2}(\lambda, 0^\circ, T_{\text{BB-LN}_2}) L_{\text{Planck}}(T_{\text{BB-LN}_2}) - \varepsilon_{\text{Ch}}(\lambda, 45^\circ, T_{\text{Ch}}) L_{\text{Planck}}(T_{\text{Ch}}))}{(\tilde{L}_{\text{VLTBB}}(T) - \tilde{L}_{\text{BB-LN}_2}(T_{\text{BB-LN}_2}))} + \varepsilon_{\text{Ch}}(\lambda, 45^\circ, T_{\text{Ch}}) L_{\text{Planck}}(T_{\text{Ch}}) + [1 - \varepsilon_{\text{Ch}}(\lambda, 45^\circ, T_{\text{Ch}})] \varepsilon_{\text{BB-LN}_2}(\lambda, 0^\circ, T_{\text{BB-LN}_2}) L_{\text{Planck}}(T_{\text{BB-LN}_2}) \quad (5.18)$$

where $L_{\text{Ch}}(T_{\text{Ch}})$ and $L_{\text{BB-LN}_2}(T_{\text{BB-LN}_2})$ are the spectral radiance of the chopper and the LN₂-cooled blackbody according to Chapter 5.1.

At first step the comparison between VLTBB and VMTBB was performed from 4 μm to 20 μm with the vacuum FTIR-spectrometer equipped with the liquid nitrogen-cooled MCT detector and the KBr broadband beamsplitter. The result is shown in Fig. 5.16 for a temperature of 80 °C. It is plotted as a difference of radiation temperatures over wavelength (wavenumber) calculated from the determined radiance according to Equation 5.18, application of the inverted Planck function and final subtraction of the nominal temperature. The grey area illustrates the range of the combined expanded uncertainty ($k=2$) of the radiance temperature calculated from the uncertainty budgets of both blackbodies (Tables 5.8 and 5.9). The vacuum radiation thermometer VIRST was used to perform an additional comparison between VLTBB and VMTBB in the wavelength band from 8 μm to 14 μm.

The radiance temperatures of the two reference blackbodies, VLTBB and VMTBB, agree well within their combined uncertainty in the spectral range from 4 μm to 20 μm. The difference of 30 mK measured with VIRST shows a good agreement with the FTIR measurements. Other examples of spectral comparison of the blackbodies of the RBCF are given in [67].

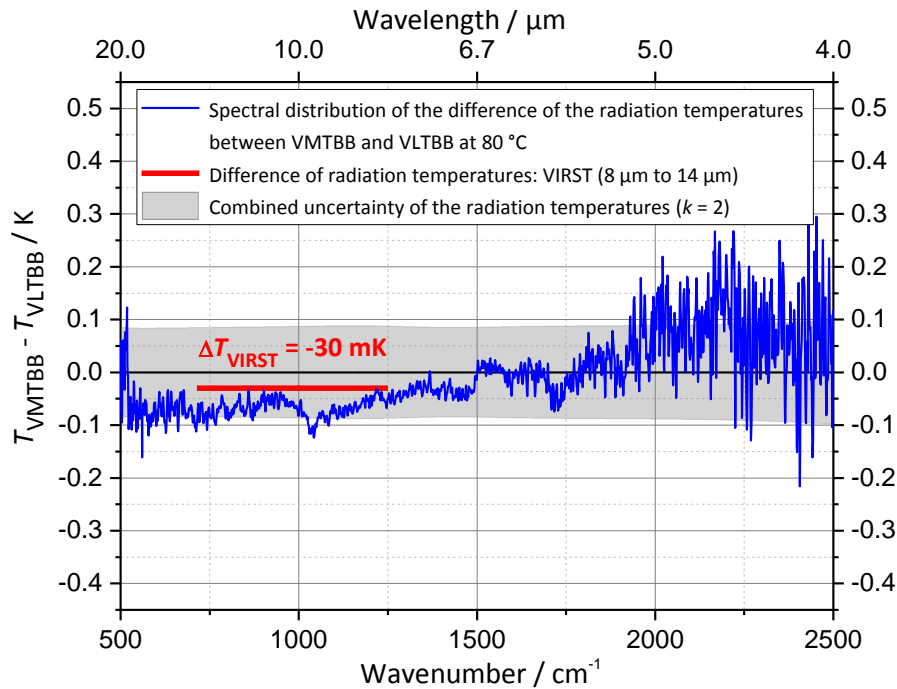


Fig. 5.16: Spectral distribution of difference of the radiation temperatures between VLTBB and VMTBB at 80 °C measured with FTIR-spectrometer. The range of the combined expanded uncertainty of the radiance temperatures of both blackbodies is shown as grey area. The horizontal bar ranging from 8 μm to 14 μm shows the comparison performed with the radiation thermometer VIRST

5.2.6 Effective emissivity and uncertainty budget of VLTBB from 20 μm to 100 μm

In the previous sections the two blackbodies VMTBB and VLTBB were characterized in terms of their effective emissivity using characteristics of the wall coating, and then the both were successfully compared in the range from 4 μm to 20 μm . As mentioned above, due to the increasing transparency of the Aergolaze Z306 in the wavelength range from 20 μm to 100 μm , the direct calculation of the effective emissivity of the VLTBB based on the Monte-Carlo ray-tracing simulation is not possible. Thus, an “inverse” scheme will be followed, using as a basis the comparison of the two blackbodies in the desired wavelength range. Assuming the VMTBB as a reference with well known characteristics, the effective emissivity of the VLTBB can be calculated using Equation 5.18, which is solved for spectral radiance of the VLTBB, and then for its effective emissivity. The comparison shown in Fig. 5.17 was done using the FTIR-spectrometer with the FDTGS detector and the 6 μm beamsplitter. The relatively large deviation at wavelengths longer than 50 μm is associated with changes in the effective emissivities of both blackbodies for longer wavelengths. While in the case of the VMTBB the change is not significant (Fig. 5.12), it is quite critical for the VLTBB. The effective emissivity of the VLTBB can be calculated from this comparison and is shown in Fig. 5.18. Since the

comparative measurements are noisy in particular in the FIR, the resulting calculated effective emissivity shows an unrealistically strong structuring especially in FIR. Therefore, the values shown in Fig. 5.18 were spectrally smoothed. The represented values decrease continuously towards longer wavelengths down to a value 0.9955.

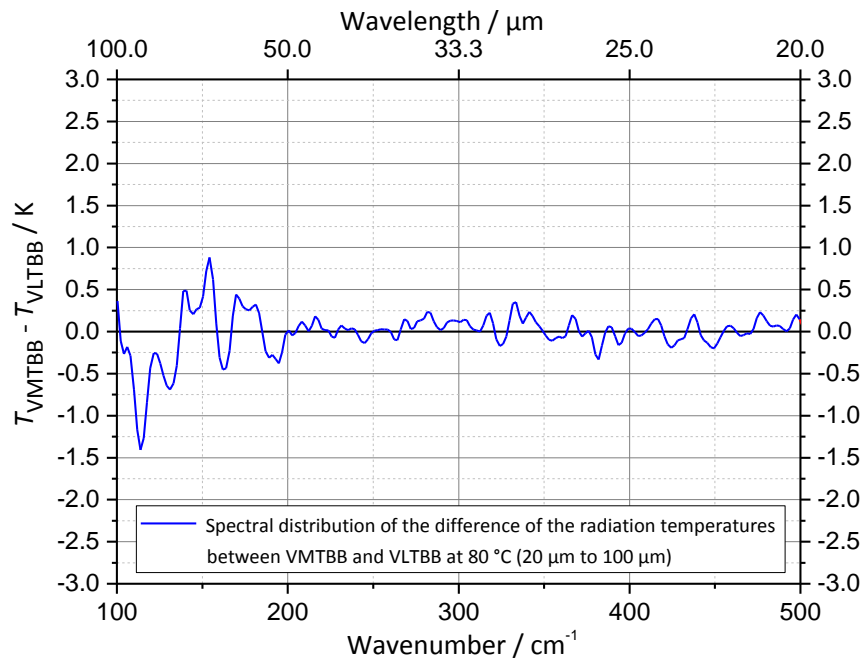


Fig. 5.17: Spectral distribution of the difference of the radiation temperatures between VLTBB and VMTBB at 80 °C measured with an FTIR-spectrometer from 20 μm to 100 μm

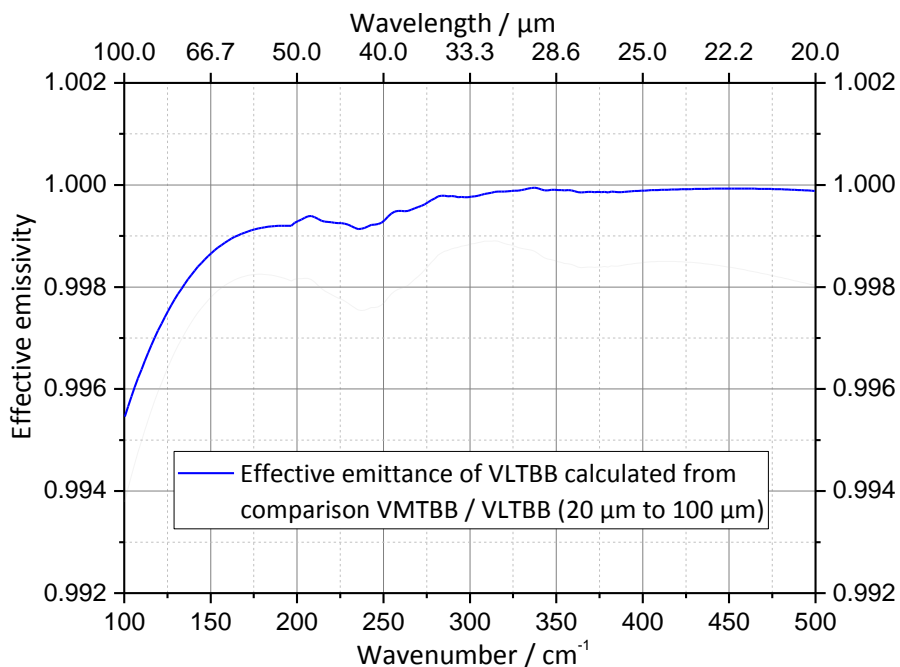


Fig. 5.18: The effective spectral emittance of the VLTBB calculated from the comparison with the VMTBB shown in Fig. 5.17

For an independent test of the obtained result the previously manufactured samples of the Aeroglaze Z306 of different thicknesses have been used. The directional spectral emittances of the samples with thicknesses of 44 μm and 99 μm were determined and used as input quantities for the STEEP3 calculations assuming that the thickness of the wall coating of the VLTBB varies within this range. This assumption is based on the experience that the coating thickness of the brush coated VLTBB cavity should not differ too much from the brush coated test sample with a thickness of 88 μm investigated in the previous section.

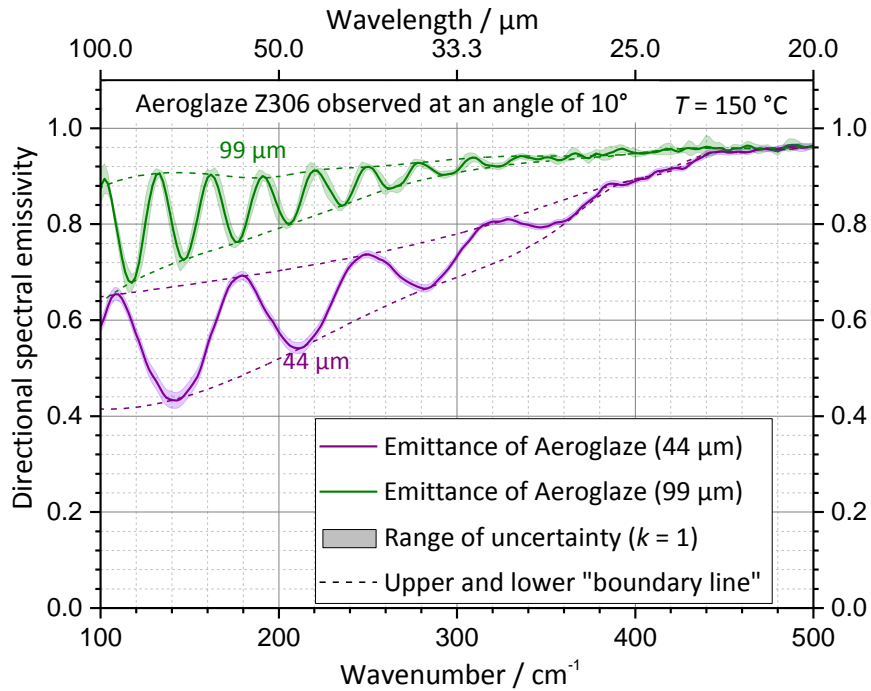


Fig. 5.19: Directional spectral emittance of Aeroglaze Z306 coated on copper plates with thicknesses of 44 μm and 99 μm under an angle of observation of 10° with respect to the surface normal. The standard measurement uncertainties are shown as shaded areas. The dotted lines represent the upper and lower "boundary line" of the modulations

The directional spectral emittances of the two samples, 44 μm and 99 μm , under an angle of observation of 10° are shown in Fig. 5.19; the shaded areas illustrate the standard uncertainty of each measurement (other results of Aeroglaze Z306 are shown in Chapter 7.4). As mentioned earlier, both samples, becoming transparent, show a reduction of emittance towards longer wavelengths. This also leads to the well visible modulations caused by multiple beam interference. So the calculation of the effective emissivity of the cavity from these measurements would only be possible with a precise knowledge of the thickness and uniformity of the coating.

Nevertheless, an estimative analysis was done in STEEP3 using the dotted lines (see Fig. 5.19) - the upper and lower “boundary line” of each modulation - as possible emissivities of the wall coating. The effective emissivity of the cavity of the VLTBB was calculated for four possible cases to estimate the influence of the modulation and the thickness variation on the effective emissivity. The results are shown in Fig. 5.20 as dashed lines.

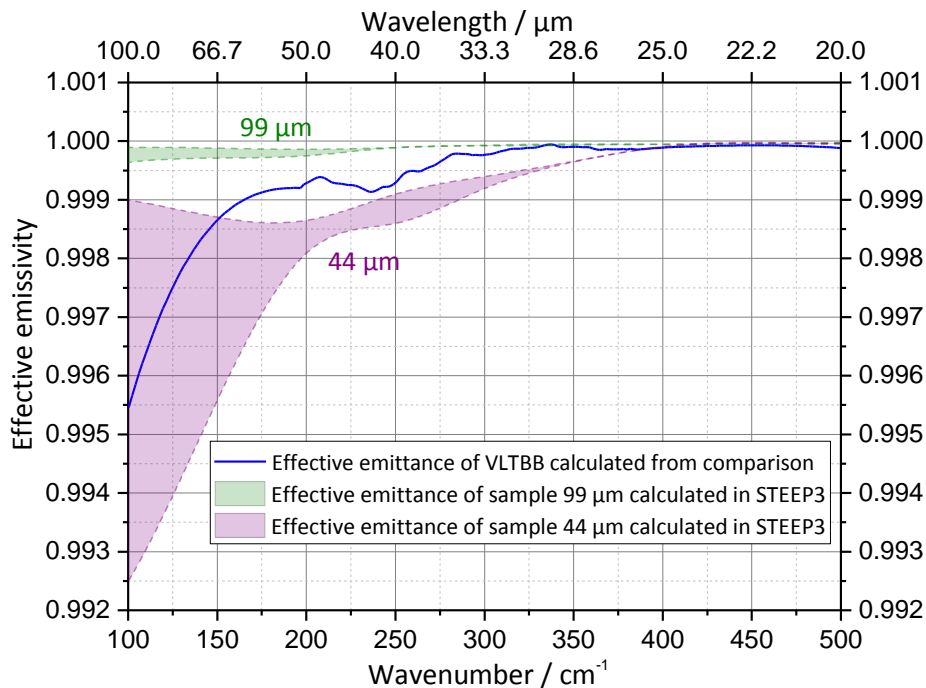


Fig. 5.20: Effective spectral emittance of VLTBB calculated for the four “boundary curves” from Fig. 5.19 corresponding to two possible thicknesses, of the wall coatings 44 μm and 99 μm , and modulation maxima and minima in their directional spectral emittances. The dashed areas correspond to possible values of the effective emissivity of the cavity. Additionally, the experimentally derived effective emissivity from the comparison with the VMTBB is shown as blue line

The two shaded areas in Fig. 5.20 for both thicknesses between the respective dashed lines represent the possible values of the effective emissivity of the cavity of the VLTBB, resulting from modulations in the emissivity of the wall coatings. The usage of the boundary curves is also justified by the fact that the positions of the maxima and minima in the modulation of the directional spectral emittances change according to the angle of incidence (Chapter 7.4). So due to the multiple reflections within a cavity and the large amount of beams with different directions an average of the emissivities for different angles of incidence/observation has to be considered for which the boundaries give an upper and lower estimate.

The calculations in STEEP3 (especially of the sample with a coating thickness of 44 μm , lower “boundary line”) confirm a sharp decrease in effective emittance, which can be also seen by the blue line obtained from the comparison with the VMTBB. It can be also noted, that

the change in thickness is not critical up to wavelengths of 25 μm , which confirms the validity of the calculations in first wavelengths range from 4 μm to 20 μm . At wavelengths above 25 μm , the difference in thickness and uniformity of the coatings leads to a significant difference of effective emissivity and consequently, of radiation temperature.

Based on the good comparability of the results from the calculations and the experimental values of the effective emittance obtained by the comparison with the VMTBB, it can be safely assumed, that the thickness of the wall coating of the VLTBB is within the range limited by the two samples with thicknesses of 44 μm and 99 μm .

The results from Figures 5.17 and 5.18 are used for the calculation of the uncertainty budget of the VLTBB from 20 μm to 100 μm (Table 5.10). It consists of two components: the uncertainty of the VMTBB at 80 $^{\circ}\text{C}$ (Table 5.8) and the standard deviation of 12 measurement sequences VLTBB/VMTBB (Table 5.11). The resulting uncertainty budget in the range from 20 μm to 100 μm is given in Table 5.12. In connection with the calculation based on the comparison at 80 $^{\circ}\text{C}$, the resulting uncertainty budget of the VLTBB in this wavelength range does not depend on the temperature.

Table 5.10: Uncertainty contributions to the overall uncertainty of the VLTBB

Uncertainty contributions	Symbol	Type
Uncertainty of VMTBB	u_{VMTBB}	B
Standard deviation of 12 comparisons VLTBB/VMTBB	u_{Compar}	A

Table 5.11: Standard deviation of 12 comparisons VLTBB/VMTBB at 80 $^{\circ}\text{C}$

$u_{\text{Compar, K}}$ 22.25 μm	$u_{\text{Compar, K}}$ 24.92 μm	$u_{\text{Compar, K}}$ 28.48 μm	$u_{\text{Compar, K}}$ 33.23 μm	$u_{\text{Compar, K}}$ 39.88 μm	$u_{\text{Compar, K}}$ 49.85 μm	$u_{\text{Compar, K}}$ 66.47 μm	$u_{\text{Compar, K}}$ 101.66 μm
0.247	0.243	0.262	0.186	0.355	0.272	0.224	0.502

Table 5.12: Overall uncertainty budget of VLTBB from 20 μm to 100 μm

u, K 22.25 μm	u, K 24.92 μm	u, K 28.48 μm	u, K 33.23 μm	u, K 39.88 μm	u, K 49.85 μm	u, K 66.47 μm	u, K 101.66 μm
0.248	0.245	0.264	0.189	0.356	0.273	0.226	0.503

5.3 Validation and traceability of emissivity measurements

The emissivity measurements under vacuum at the RBCF are traceable to the VLTBB and the VMTBB, which are the standards of radiation temperature and spectral radiance. Using calibrated PRTs, the both blackbodies are linked to the ITS-90 [43].

A comparison between the VLTBB and an ammonia heat-pipe blackbody (NH₃-BB) was performed to validate the traceability of the VLTBB, and therefore- all measurements at the RBCF. The ammonia heat-pipe blackbody is the primary national standard of radiation

temperature from $-60\text{ }^{\circ}\text{C}$ to $50\text{ }^{\circ}\text{C}$ in air at PTB [68]. It has successfully been used in international comparisons with other national metrology institutes [69].

The comparison was performed using a compact industrial radiation thermometer of the type OPTRIS CSLaser LT hs SPEZIAL as a transfer instrument. This comparison was described in detail in [70].

The results of the comparison between the two blackbodies in the temperature range from $-50\text{ }^{\circ}\text{C}$ to $50\text{ }^{\circ}\text{C}$ are shown in Fig. 5.21. Here the differences between the radiation temperatures of the ammonia heat-pipe blackbody and the VLTBB, both regarding to the measured temperature of their bottom (of standard platinum resistance thermometer (SPRT) [46] and PRT accordingly), are presented with the combined expanded uncertainty of the comparison. For the calculation of the results several corrections related to the different conditions of measurements were applied. In particular the VLTBB was operated under vacuum in a cold environment (at RBCF) and the ammonia heat-pipe blackbody in air at standard environment (room temperature).

The results demonstrate the good agreement of the two blackbodies within the expanded uncertainty of the comparison and confirm the uncertainty budget and traceability of the VLTBB.

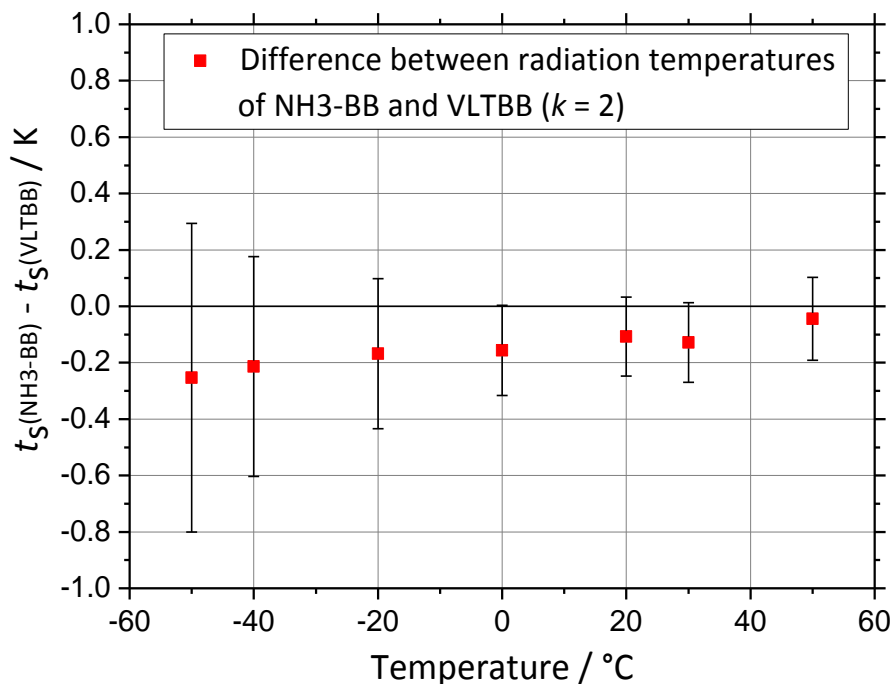


Fig. 5.21: The differences between the radiation temperatures of the ammonia heat-pipe blackbody and the VLTBB, regarding to the measured temperatures of the SPRT and PRT in the bottoms of their cavities, measured by radiation thermometer of the type OPTRIS CSLaser LT hs SPEZIAL. The comparison is shown with the combined expanded uncertainty of the comparison calculated for each temperature

More comparisons among the used blackbodies were performed. Details to these validation and traceability measurements are given in [70]. Fig. 5.22 shows a scheme of the comparisons performed with the two blackbodies, VLTBB and VMTBB, with the ammonia heat-pipe and an additional liquid-operated variable temperature blackbody (LBB) [70]. The consistent results obtained in all these comparisons validate the traceability of the blackbodies their uncertainty budgets and consequently the emissivity measurements at the RBCF.

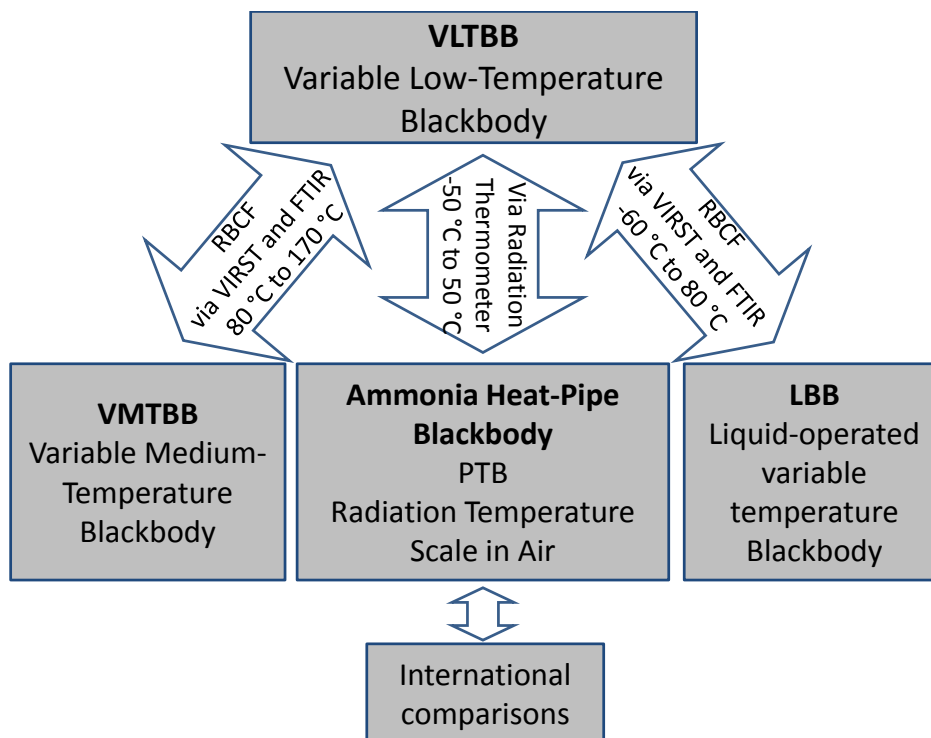


Fig. 5.22: Comparisons of the VLTBB with other radiation temperature standards in PTB validating the traceability of the blackbodies their uncertainty budget based on [70]

6 Evaluation of emissivity measurements under vacuum

In this chapter the evaluation of the emissivity measurements is presented and the radiation balance of the sample is discussed in detail, based on the theoretical foundations provided in Chapter 2 and according to the characteristics and design of the facility described in Chapters 4 and 5. The important aspect of the evaluation scheme is a multiple reflections method for the calculation of the signal of the sample located inside of the spherical enclosure. The uncertainty budget of emissivity measurements based on all contributions is also presented.

6.1 Calculation of emissivity and generalized radiation budget

The basis of the measurement scheme for determination of emissivity and for the calculation of the generalized radiation budget is the comparison of the spectral radiance of the sample inside of the temperature-stabilized spherical enclosure against the spectral radiances of the two reference blackbodies at different temperatures (Fig. 6.1 and Fig. 6.2). The “main” blackbody, which is usually operated at a temperature close to the radiation temperature of the sample, will be either the VLTBB or the VMTBB, depending on the temperature range. The second reference source is the LN₂-cooled blackbody, which is used for the elimination of the background radiation (Chapter 4.1). This scheme may be represented as follows:

$$Q = \frac{\tilde{L}_{\text{Sample}}(T_{\text{Sample}}) - \tilde{L}_{\text{BB-LN}_2}(T_{\text{BB-LN}_2})}{\tilde{L}_{\text{BB1}}(T_{\text{BB1}}) - \tilde{L}_{\text{BB-LN}_2}(T_{\text{BB-LN}_2})} \quad (6.1)$$

where $\tilde{L}_{\text{Sample}}(T_{\text{Sample}})$ is the signal measured from the sample and T_{Sample} is the temperature of the sample surface, $\tilde{L}_{\text{BB1}}(T_{\text{BB1}})$ denotes the signal from the first (main) reference blackbody at temperature T_{BB1} , and $\tilde{L}_{\text{BB-LN}_2}(T_{\text{BB-LN}_2})$ is the signal from the second reference LN₂-cooled blackbody at temperature $T_{\text{BB-LN}_2}$ (Chapter 5.1.1). According to the classical definition this ratio would directly give the value of emissivity, but the complexity of the facility and the large number of elements leads to a difference between the “true” emitted radiation from each of the sources and the detected signal, and therefore requires the detailed consideration of the radiation budget, which results in a complex calculation process with an iterative solution.

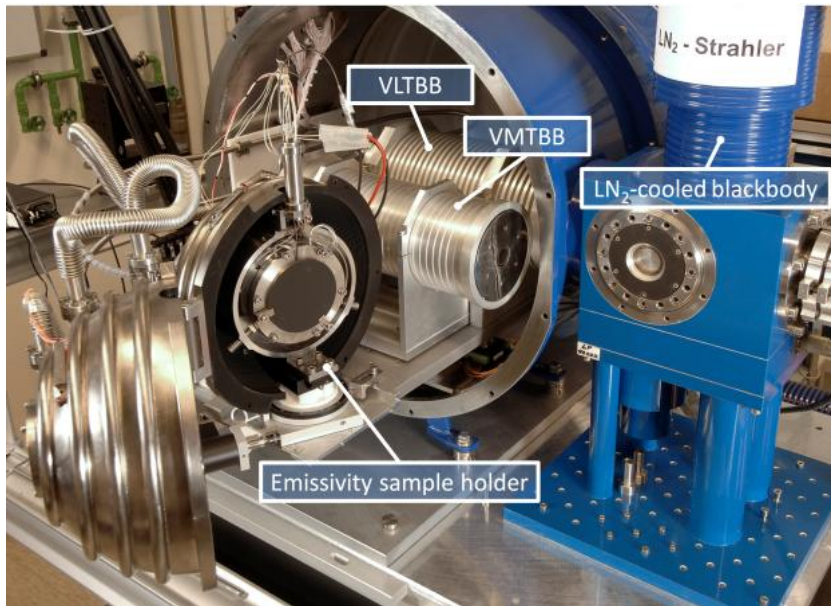


Fig. 6.1: Photo of the opened source chamber illustrating the measurement scheme: comparison of the spectral radiance of the sample inside of the temperature-stabilized spherical enclosure (also opened) with the spectral radiances of the two reference blackbodies

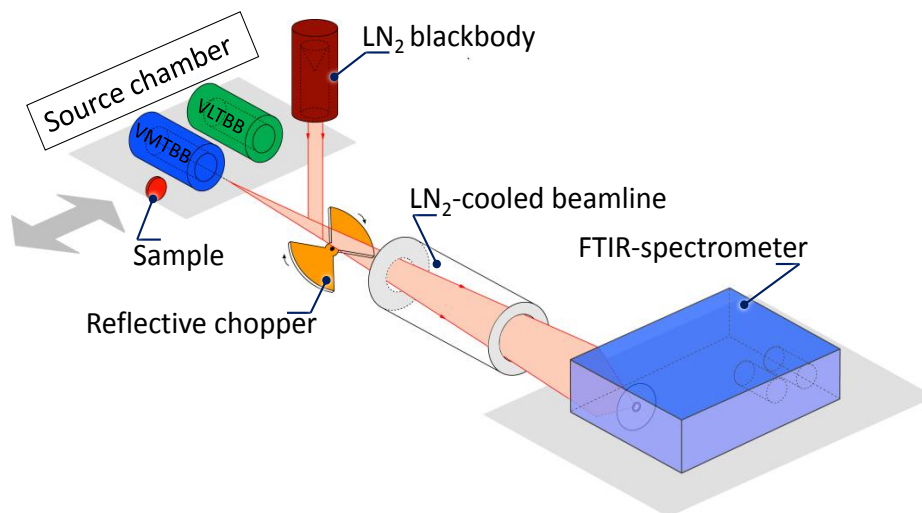


Fig. 6.2: Schematic representation of measurement scheme

6.1.1 Multiple reflections method

One of the main features of the developed facility is versatility and the ability to accurately measure various types of samples on a high metrological level, including samples with highly reflective characteristics. As will be shown in Chapter 7, the signal level of the samples may vary greatly depending not only upon their characteristics but also on experimental conditions (sample surface temperature, temperature of the sphere, type of detector and wavelength). Thus, the radiation exchange between the sample and the enclosure, as well as

the influence of the latter on the final signal should be considered (Chapter 7.3). This is done using the multiple reflections method for the calculation of emissivity of different samples in various experimental conditions.

There are several models allowing the calculation of the “true” radiation from a sample located inside of any enclosure. The methods and systematic errors associated with each method are reviewed in detail in [71], in which the multiple reflection method was presented as the most accurate and suitable for all possible characteristics of the sample and sphere.

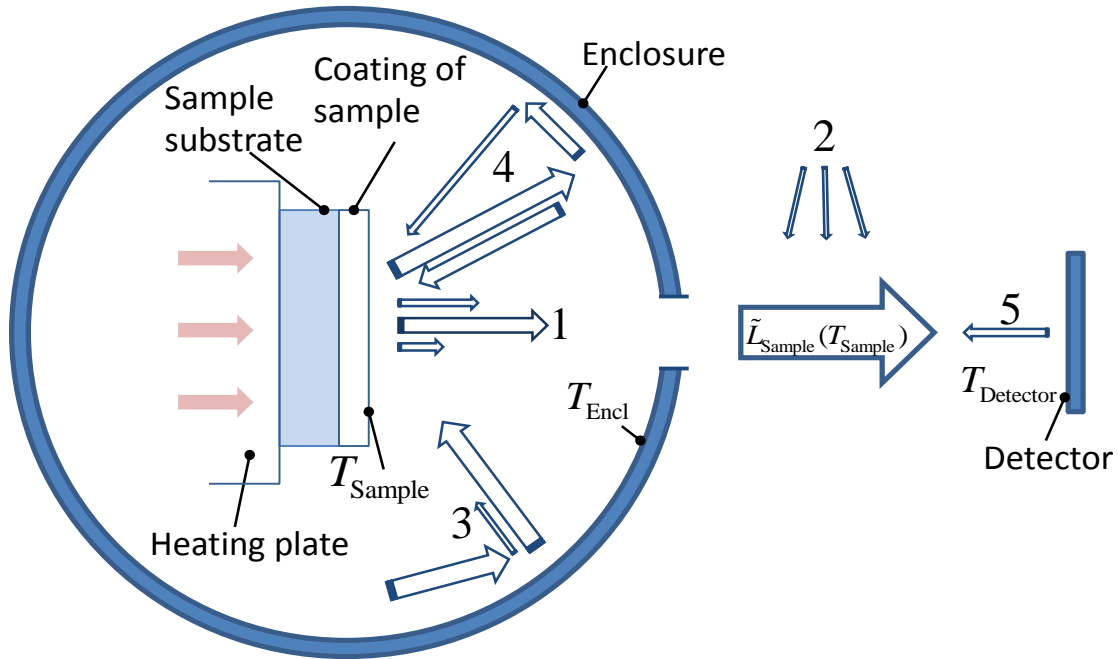


Fig. 6.3: Schematic representation of radiation budget of the sample inside of the temperature stabilized enclosure

The recorded signal of the sample $\tilde{L}_{\text{Sample}}(T_{\text{Sample}})$ results not only from the radiation $\varepsilon_{\text{Sample}}(\lambda, \vartheta, T_{\text{Sample}})L_{\text{Planck}}(T_{\text{Sample}})$ emitted directly by the sample (“1” in the Fig. 6.3; self-radiance of detector L_{Det} is considered) and the background radiance L_{Back} (“2”) but consists of several additional components. A schematic representation of the radiation budget of the sample inside of the temperature-stabilized enclosure is shown in Fig. 6.3. The sphere, which is temperature stabilized at a specific constant temperature, is also a source of radiation and acts as a reflector of radiation. Its contribution to the overall signal can be divided into two components: the radiation (“3”), originating from the inner walls of the enclosure, which is reflected by the sample in the direction of the detector; and the radiation from the sample (“4”), which is reflected back by the enclosure and, in the same way, reaches the

detector. Finally, the radiation of the detector (“5”) can reach the sample and be reflected back (not the self-radiation of the detector L_{Det} , which influences the signal processing).

Radiation of spherical enclosure

If the radiation “3” represents the contribution of the spherical enclosure as a source of radiation in the resulting signal, then each element on the inner surface of the hemisphere dA_{Encl} , excluding the opening, radiates towards the sample, given by the directional spectral emissivity under an angle of 0 (Chapter 2.7.1) and multiplied by Planck’s law. This spectral radiance $\varepsilon_{\text{Encl}}(\lambda, 0^\circ, T_{\text{Encl}})L_{\text{Planck}}(T_{\text{Encl}})$ is reflected in the direction of the detector via the diffuse bidirectional reflectance of the sample $\rho_{\text{Sample}}(\lambda, \vartheta, \vartheta_r)$ (Fig. 6.4, a), where ϑ and ϑ_r are the polar angles of incidence and the reflection corresponding to the angle of rotation of the sample (azimuthal angles are here omitted). Because the radiation characteristics of the sample are initially unknown, the resulting, after-integration hemispherical-directional reflectivity must be expressed in terms of emissivity, namely, through the directional spectral emissivity of the sample: $1 - \varepsilon_{\text{Sample}}(\lambda, \vartheta, T_{\text{Sample}})$. Thus, the fraction of the radiation of the enclosure going towards the detector can be written as:

$$L_{3.a} = \varepsilon_{\text{Encl}}(\lambda, 0^\circ, T_{\text{Encl}})L_{\text{Planck}}(T_{\text{Encl}})A_{\text{Encl}}F_{\text{Encl-Sample}} \left[1 - \varepsilon_{\text{Sample}}(\lambda, \vartheta, T_{\text{Sample}}) \right] F_{\text{Sample-Det}} \quad (6.2)$$

$F_{\text{Encl-Sample}}$ and $F_{\text{Sample-Encl}}$ denote the radiation exchange between the area of the sample A_{Sample} , which is determined by the field-of-view of the detector, and the hemisphere of the enclosure A_{Encl} except the opening, with view factors $F_{\text{Sample-Det}}$ and $F_{\text{Det-Sample}}$ between the area of the detector A_{Det} and the area of the sample A_{Sample} depending on the directions, respectively.

Obviously, the radiation from the hemisphere is diffusely-directionally reflected not only towards the detector, but also back into the sphere. This part of radiation from the hemisphere will be reflected in all directions except the solid angle, which is equivalent to the opening area on the sphere (see Fig. 6.4, b). With some approximation the bihemispherical reflectivity, in turn, can be expressed in terms of the hemispherical emissivity: $1 - \varepsilon_{\text{Sample}}(\lambda, T_{\text{Sample}})$. Hence, the fraction of radiation from the sphere, which is reflected by the entire area of sample (not only by the area of field-of-view) and returns back, can be written as:

$$L_{3.b} = \varepsilon_{\text{Encl}}(\lambda, 0^\circ, T_{\text{Encl}})L_{\text{Planck}}(T_{\text{Encl}})A_{\text{Encl}}F_{\text{Encl-Entire sample}} \left[1 - \varepsilon_{\text{Sample}}(\lambda, T_{\text{Sample}}) \right] F_{\text{Entire sample-Encl}} \quad (6.3)$$

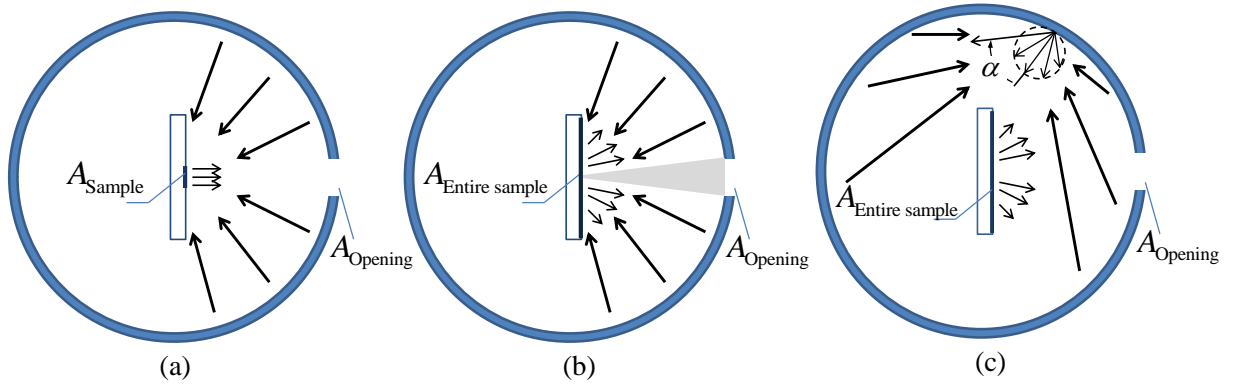


Fig. 6.4: Schematic representation of radiation between sample and enclosure. a) Radiation from hemisphere, which is reflected by sample towards detector; b) Radiation from hemisphere, which is reflected back by sample into the spherical enclosure; c) Reflection of self-radiation of enclosure and of sample by the inner wall of the spherical enclosure

To describe the internal reflection, which includes the multiple reflections inside of the sphere, the sphere must be considered as a diffuse sphere because the diffuse component dominates the specular reflectivity in the radiation characteristics of the wall coating, as described in Chapter 4.6. Thus, the diffuse directional-hemispherical spectral reflectivity can be assumed independent of the incident angle. This also provides that the incident radiation reflects via $\rho_{\text{Encl}}(\lambda)\cos\alpha/\pi$ [17], where $\rho_{\text{Encl}}(\lambda)$ is the hemispherical reflectivity and α represents the angle between the surface normal of area element $dA_{\text{Entire encl}}$ and the direction of reflection (Fig. 6.4, c). Some part of the radiation, reaching the inner surface of the sphere, is reflected back to the sample and another part is reflected towards sphere, undergoing multiple reflections inside and some part also hits the sample. If a is the fraction of the radiation process, which represents one reflection by the sample and one reflection back towards the sample by the enclosure (here $\cos\alpha=1$, since this reflection occurs in direction of normal to $dA_{\text{Entire encl}}$):

$$a = [1 - \varepsilon_{\text{Sample}}(\lambda, T_{\text{Sample}})] F_{\text{Entire sample-Encl}} [\rho_{\text{Encl}}(\lambda)/\pi] F_{\text{Encl-Entire sample}} \quad (6.4)$$

then b is the fraction describing the reflected by the enclosure radiation towards itself:

$$b = F_{\text{Entire encl-Entire encl}} 2 \int_0^{\pi/2} \rho_{\text{Encl}}(\lambda)\cos\alpha/\pi d\alpha = 2F_{\text{Entire encl-Entire encl}} \rho_{\text{Encl}}(\lambda)/\pi \quad (6.5)$$

Here $F_{\text{Entire sample-Encl}}$ and $F_{\text{Encl-Entire sample}}$ represent the view factors between the area of the entire sample $A_{\text{Entire sample}}$ and the hemisphere of the enclosure, depending on direction. $F_{\text{Entire encl-Entire encl}}$ is the view factor of the entire enclosure $A_{\text{Entire encl}}$ with itself.

As follows, the fraction of radiation emitted by the half-sphere of the enclosure to the sample, which is partly reflected towards the detector and partly reflected back, undergoing multiple reflections between the sphere and the sample as well as multiple reflections inside of the sphere with itself, and then finally reaching the detector as well, can be calculated as:

$$\begin{aligned}
 L_{3,1} &= \varepsilon_{\text{Encl}}(\lambda, 0^\circ, T_{\text{Encl}}) L_{\text{Planck}}(T_{\text{Encl}}) A_{\text{Encl}} F_{\text{Encl-Sample}} \left[1 - \varepsilon_{\text{Sample}}(\lambda, \vartheta, T_{\text{Sample}}) \right] F_{\text{Sample-Det}} \\
 &\left[1 + a(1 + b + b^2 + \dots) + a^2(1 + b + b^2 + \dots) + \dots \right] = \\
 &= \varepsilon_{\text{Encl}}(\lambda, 0^\circ, T_{\text{Encl}}) L_{\text{Planck}}(T_{\text{Encl}}) A_{\text{Encl}} F_{\text{Encl-Sample}} \left[1 - \varepsilon_{\text{Sample}}(\lambda, \vartheta, T_{\text{Sample}}) \right] F_{\text{Sample-Det}} \\
 &\left[1 + (a + a^2 + \dots)(1 + b + b^2 + \dots) \right] = \\
 &= \varepsilon_{\text{Encl}}(\lambda, 0^\circ, T_{\text{Encl}}) L_{\text{Planck}}(T_{\text{Encl}}) A_{\text{Encl}} F_{\text{Encl-Sample}} \left[1 - \varepsilon_{\text{Sample}}(\lambda, \vartheta, T_{\text{Sample}}) \right] F_{\text{Sample-Det}} \left[1 + \sum_{i=1}^{\infty} \sum_{j=0}^{\infty} a^i b^j \right]
 \end{aligned} \tag{6.6}$$

where i and j are integers ($i \geq 1, j \geq 0$).

Similarly the self-radiation of the enclosure, which after multiple reflections with itself can reach the sample and is reflected towards the detector, should be considered (Fig. 6.4, c). Depending on the sample properties, this reflection can be significant and must be taken into account for highly accurate emissivity measurements.

If $\int \varepsilon_{\text{Encl}}(\lambda, \vartheta, \varphi, T_{\text{Encl}}) d\Omega L_{\text{Planck}}(T_{\text{Encl}}) = 2\varepsilon_{\text{Encl}}(\lambda, T_{\text{Encl}}) L_{\text{Planck}}(T_{\text{Encl}})$ is the spectral radiance from the entire sphere towards itself to one area element $dA_{\text{Entire encl}}$, where $\varepsilon_{\text{Encl}}(\lambda, T_{\text{Encl}})$ is the hemispherical spectral emissivity of the wall, then the fraction of self-radiation of the enclosure after multiple reflections with itself as well as with sample is:

$$\begin{aligned}
 L_{3,2} &= 2\varepsilon_{\text{Encl}}(\lambda, T_{\text{Encl}}) L_{\text{Planck}}(T_{\text{Encl}}) A_{\text{Entire encl}} F_{\text{Entire encl-Encl}} \left[\rho_{\text{Encl}}(\lambda)/\pi \right] F_{\text{Encl-Sample}} \left[1 - \varepsilon_{\text{Sample}}(\lambda, \vartheta, T_{\text{Sample}}) \right] F_{\text{Sample-Det}} \\
 &\left[(1 + b + b^2 + \dots) + a(1 + b + b^2 + \dots) + a^2(1 + b + b^2 + \dots) + \dots \right] = \\
 &= 2\varepsilon_{\text{Encl}}(\lambda, T_{\text{Encl}}) L_{\text{Planck}}(T_{\text{Encl}}) A_{\text{Entire encl}} F_{\text{Entire encl-Encl}} \left[\rho_{\text{Encl}}(\lambda)/\pi \right] F_{\text{Encl-Sample}} \left[1 - \varepsilon_{\text{Sample}}(\lambda, \vartheta, T_{\text{Sample}}) \right] F_{\text{Sample-Det}} \\
 &\left[(1 + a + a^2 + \dots)(1 + b + b^2 + \dots) \right] = \\
 &= 2\varepsilon_{\text{Encl}}(\lambda, T_{\text{Encl}}) L_{\text{Planck}}(T_{\text{Encl}}) A_{\text{Entire encl}} F_{\text{Entire encl-Encl}} \left[\rho_{\text{Encl}}(\lambda)/\pi \right] F_{\text{Encl-Sample}} \left[1 - \varepsilon_{\text{Sample}}(\lambda, \vartheta, T_{\text{Sample}}) \right] F_{\text{Sample-Det}} \left[\sum_{i=0}^{\infty} \sum_{j=0}^{\infty} a^i b^j \right]
 \end{aligned} \tag{6.7}$$

where i and j are integers ($i \geq 0, j \geq 0$).

Radiation of sample reflected by spherical enclosure

The radiation emitted by the sample into the enclosure ("4" on Fig. 6.3) via the hemispherical spectral emissivity of the sample $\varepsilon_{\text{Sample}}(\lambda, T_{\text{Sample}})L_{\text{Planck}}(T_{\text{Sample}})$ excluding the solid angle equivalent to the opening area on the sphere, can also be considered in the same way. Part of the radiation is reflected back by the enclosure and another part will be reflected towards itself and then reflected back (Fig. 6.4, c). Thus, there are also two methods of calculating the multiple reflections of the original radiation, described with coefficients a and b :

$$\begin{aligned}
 L_4 &= \varepsilon_{\text{Sample}}(\lambda, T_{\text{Sample}})L_{\text{Planck}}(T_{\text{Sample}})A_{\text{Entire sample}}F_{\text{Entire sample-Encl}}[\rho_{\text{Encl}}(\lambda)/\pi]F_{\text{Encl-Sample}}[1 - \varepsilon_{\text{Sample}}(\lambda, \vartheta, T_{\text{Sample}})]F_{\text{Sample-Det}} \\
 &\left[(1 + b + b^2 + \dots) + a(1 + b + b^2 + \dots) + a^2(1 + b + b^2 + \dots) + a^3(1 + b + b^2 + \dots) + \dots \right] = \\
 &= \varepsilon_{\text{Sample}}(\lambda, T_{\text{Sample}})L_{\text{Planck}}(T_{\text{Sample}})A_{\text{Entire sample}}F_{\text{Entire sample-Encl}}[\rho_{\text{Encl}}(\lambda)/\pi]F_{\text{Encl-Sample}}[1 - \varepsilon_{\text{Sample}}(\lambda, \vartheta, T_{\text{Sample}})]F_{\text{Sample-Det}} \\
 &\left[(1 + a + a^2 + a^3 + \dots)(1 + b + b^2 + b^3 + \dots) \right] = \\
 &= \varepsilon_{\text{Sample}}(\lambda, T_{\text{Sample}})L_{\text{Planck}}(T_{\text{Sample}})A_{\text{Entire Sample}}F_{\text{Entire sample-Encl}}[\rho_{\text{Encl}}(\lambda)/\pi]F_{\text{Encl-Sample}}[1 - \varepsilon_{\text{Sample}}(\lambda, \vartheta, T_{\text{Sample}})]F_{\text{Sample-Det}} \left[\sum_{i=0}^{\infty} \sum_{j=0}^{\infty} a^i b^j \right]
 \end{aligned} \tag{6.8}$$

where i and j are integers ($i \geq 0, j \geq 0$).

Signal of sample

Considering these sums (Equations 6.7 and 6.8) as infinite geometric series, the measured signal of the sample can be written as:

$$\begin{aligned}
 \tilde{L}_{\text{Sample}}(T_{\text{Sample}}) &= s \cdot \left(\varepsilon_{\text{Sample}}(\lambda, \vartheta, T_{\text{Sample}})L_{\text{Planck}}(T_{\text{Sample}})A_{\text{Sample}}F_{\text{Sample-Det}} + L_{\text{Back}} - L_{\text{Det}} + \right. \\
 &+ \varepsilon_{\text{Encl}}(\lambda, 0^\circ, T_{\text{Encl}})L_{\text{Planck}}(T_{\text{Encl}})A_{\text{Encl}}F_{\text{Encl-Sample}}[1 - \varepsilon_{\text{Sample}}(\lambda, \vartheta, T_{\text{Sample}})]F_{\text{Sample-Det}} \left[1 + \frac{a}{1-a} \frac{1}{1-b} \right] + \\
 &+ 2\varepsilon_{\text{Encl}}(\lambda, T_{\text{Encl}})L_{\text{Planck}}(T_{\text{Encl}})A_{\text{Entire encl}}F_{\text{Entire encl-Encl}}[\rho_{\text{Encl}}(\lambda)/\pi]F_{\text{Encl-Sample}}[1 - \varepsilon_{\text{Sample}}(\lambda, \vartheta, T_{\text{Sample}})]F_{\text{Sample-Det}} \left[\frac{1}{1-a} \frac{1}{1-b} \right] + \\
 &+ \varepsilon_{\text{Sample}}(\lambda, T_{\text{Sample}})L_{\text{Planck}}(T_{\text{Sample}})A_{\text{Entire Sample}}F_{\text{Entire sample-Encl}}[\rho_{\text{Encl}}(\lambda)/\pi]F_{\text{Encl-Sample}}[1 - \varepsilon_{\text{Sample}}(\lambda, \vartheta, T_{\text{Sample}})]F_{\text{Sample-Det}} \left[\frac{1}{1-a} \frac{1}{1-b} \right] + \\
 &+ \varepsilon_{\text{Detector}}(\lambda, 0^\circ, T_{\text{Detector}})L_{\text{Planck}}(T_{\text{Detector}})A_{\text{Det}}F_{\text{Det-Sample}}[1 - \varepsilon_{\text{Sample}}(\lambda, \vartheta, T_{\text{Sample}})]F_{\text{Sample-Det}} \left. \right)
 \end{aligned} \tag{6.9}$$

where $\varepsilon_{\text{Detector}}(\lambda, 0^\circ, T_{\text{Detector}})L_{\text{Planck}}(T_{\text{Detector}})$ is the spectral radiance of detector ("5" on Fig. 6.3).

The self-radiation of detector L_{Det} , the spectral responsivity of spectrometer s as well as the thermal background L_{Back} can be eliminated by substituting Equation 6.9 and the Equations 5.2 and 5.4, which describe radiation budgets of the signals from the “main” reference blackbody and the LN₂-cooled blackbody, in the Equation 6.1. This is possible because the spectrometer and the RBCF are stable over the period of time it takes for one sequence of measurements. Furthermore, using the reciprocity theorem for view factors, which states that: $F_{\text{Encl-Sample}} A_{\text{Encl}} = F_{\text{Sample-Encl}} A_{\text{Sample}}$, $F_{\text{Encl-Entire sample}} A_{\text{Encl}} = F_{\text{Entire sample-Encl}} A_{\text{Entire sample}}$ as well as $F_{\text{Det-Sample}} A_{\text{Det}} = F_{\text{Sample-Det}} A_{\text{Sample}}$; and assuming that the following emitted areas and view factors (due to the removal of sources from the detector) are equal: $F_{\text{Sample-Det}} = F_{\text{BB1-Det}} = F_{\text{LN}_2\text{-Det}} = F_{\text{Ch-Det}}$ and $A_{\text{Sample}} = A_{\text{BB1}} = A_{\text{LN}_2} = A_{\text{Ch}}$, Equation 6.1 can be transformed to:

$$\begin{aligned}
& \left(\varepsilon_{\text{Sample}}(\lambda, \vartheta, T_{\text{Sample}}) L_{\text{Planck}}(T_{\text{Sample}}) + \varepsilon_{\text{Encl}}(\lambda, 0^\circ, T_{\text{Encl}}) L_{\text{Planck}}(T_{\text{Encl}}) F_{\text{Sample-Encl}} [1 - \varepsilon_{\text{Sample}}(\lambda, \vartheta, T_{\text{Sample}})] \left[1 + \frac{a}{1-a} \frac{1}{1-b} \right] + \right. \\
& + 4 \varepsilon_{\text{Encl}}(\lambda, T_{\text{Encl}}) L_{\text{Planck}}(T_{\text{Encl}}) F_{\text{Entire encl-Encl}} [\rho_{\text{Encl}}(\lambda)/\pi] F_{\text{Sample-Encl}} [1 - \varepsilon_{\text{Sample}}(\lambda, \vartheta, T_{\text{Sample}})] \left[\frac{1}{1-a} \frac{1}{1-b} \right] + \\
& + \varepsilon_{\text{Sample}}(\lambda, T_{\text{Sample}}) L_{\text{Planck}}(T_{\text{Sample}}) F_{\text{Encl-Entire sample}} [\rho_{\text{Encl}}(\lambda)/\pi] F_{\text{Sample-Encl}} [1 - \varepsilon_{\text{Sample}}(\lambda, \vartheta, T_{\text{Sample}})] \left[\frac{1}{1-a} \frac{1}{1-b} \right] + \\
& + \varepsilon_{\text{Detector}}(\lambda, 0^\circ, T_{\text{Detector}}) L_{\text{Planck}}(T_{\text{Detector}}) F_{\text{Sample-Det}} [1 - \varepsilon_{\text{Sample}}(\lambda, \vartheta, T_{\text{Sample}})] - \\
& \left. - \rho_{\text{Ch}}(\lambda, 45^\circ, 45^\circ) \varepsilon_{\text{BB-LN}_2}(\lambda, 0^\circ, T_{\text{BB-LN}_2}) L_{\text{Planck}}(T_{\text{BB-LN}_2}) - \varepsilon_{\text{Ch}}(\lambda, 45^\circ, T_{\text{Ch}}) L_{\text{Planck}}(T_{\text{Ch}}) \right) = \\
& = Q \left(\varepsilon_{\text{BB1}}(\lambda, 0^\circ, T_{\text{BB1}}) L_{\text{Planck}}(T_{\text{BB1}}) - [1 - \varepsilon_{\text{Ch}}(\lambda, 45^\circ, T_{\text{Ch}})] \varepsilon_{\text{BB-LN}_2}(\lambda, 0^\circ, T_{\text{BB-LN}_2}) L_{\text{Planck}}(T_{\text{BB-LN}_2}) - \varepsilon_{\text{Ch}}(\lambda, 45^\circ, T_{\text{Ch}}) L_{\text{Planck}}(T_{\text{Ch}}) \right)
\end{aligned} \tag{6.10}$$

where Q is calculated as quotient of measured quantities.

Some approximations can be made to the coefficients a and b . As $A_{\text{Sample}} \ll A_{\text{Encl}}$, then $\frac{1}{1-a} \approx 1+a$. According to the closeness theorem of view factors, the b can be written as:

$$b = 2 \left(1 - \frac{A_{\text{Entire sample}}}{A_{\text{Entire encl}}} F_{\text{Entire sample-Entire encl}} \right) \rho_{\text{Encl}}(\lambda) / \pi \tag{6.11}$$

The problem of the presence of the hemispherical spectral emissivity of the sample $\varepsilon_{\text{Sample}}(\lambda, T_{\text{Sample}})$ is solved by the iterative method. Thus, Equation 6.10 is a simple equation, which is solved for the directional spectral emissivity of the sample $\varepsilon_{\text{Sample}}(\lambda, \vartheta, T_{\text{Sample}})$, since all temperatures (for determination of the sample surface temperature see the next

Chapter 6.1.2), and all other relevant quantities are recorded during the experiment or are previously established with their uncertainty. The directional spectral emissivity of the sample is:

$$\varepsilon_{\text{Sample}}(\lambda, \vartheta, T_{\text{Sample}}) = \frac{p}{t} \quad (6.12)$$

where p and t are following coefficients:

$$\begin{aligned} p = & Q \left(\varepsilon_{\text{BB1}}(\lambda, 0^\circ, T_{\text{BB1}}) L_{\text{Planck}}(T_{\text{BB1}}) - [1 - \varepsilon_{\text{Ch}}(\lambda, 45^\circ, T_{\text{Ch}})] \varepsilon_{\text{BB-LN}_2}(\lambda, 0^\circ, T_{\text{BB-LN}_2}) L_{\text{Planck}}(T_{\text{BB-LN}_2}) - \varepsilon_{\text{Ch}}(\lambda, 45^\circ, T_{\text{Ch}}) L_{\text{Planck}}(T_{\text{Ch}}) \right) + \\ & + \rho_{\text{Ch}}(\lambda, 45^\circ, 45^\circ) \varepsilon_{\text{BB-LN}_2}(\lambda, 0^\circ, T_{\text{BB-LN}_2}) L_{\text{Planck}}(T_{\text{BB-LN}_2}) + \varepsilon_{\text{Ch}}(\lambda, 45^\circ, T_{\text{Ch}}) L_{\text{Planck}}(T_{\text{Ch}}) - \\ & - \varepsilon_{\text{Encl}}(\lambda, 0^\circ, T_{\text{Encl}}) L_{\text{Planck}}(T_{\text{Encl}}) F_{\text{Sample-Encl}} \left[1 + \frac{a+a^2}{1-b} \right] - 4 \varepsilon_{\text{Encl}}(\lambda, T_{\text{Encl}}) L_{\text{Planck}}(T_{\text{Encl}}) F_{\text{Entire encl-Encl}} \left[\rho_{\text{Encl}}(\lambda)/\pi \right] F_{\text{Sample-Encl}} \left[\frac{1+a}{1-b} \right] - \\ & - \varepsilon_{\text{Sample}}(\lambda, T_{\text{Sample}}) L_{\text{Planck}}(T_{\text{Sample}}) F_{\text{Encl-Entire sample}} \left[\rho_{\text{Encl}}(\lambda)/\pi \right] F_{\text{Sample-Encl}} \left[\frac{1+a}{1-b} \right] - \varepsilon_{\text{Detector}}(\lambda, 0^\circ, T_{\text{Detector}}) L_{\text{Planck}}(T_{\text{Detector}}) F_{\text{Sample-Det}} \end{aligned} \quad (6.13)$$

$$t = L_{\text{Planck}}(T_{\text{Sample}}) - \varepsilon_{\text{Encl}}(\lambda, 0^\circ, T_{\text{Encl}}) L_{\text{Planck}}(T_{\text{Encl}}) F_{\text{Sample-Encl}} \left[1 + \frac{a+a^2}{1-b} \right] -$$

$$- 4 \varepsilon_{\text{Encl}}(\lambda, T_{\text{Encl}}) L_{\text{Planck}}(T_{\text{Encl}}) F_{\text{Entire encl-Encl}} \left[\rho_{\text{Encl}}(\lambda)/\pi \right] F_{\text{Sample-Encl}} \left[\frac{1+a}{1-b} \right] - \quad (6.14)$$

$$- \varepsilon_{\text{Sample}}(\lambda, T_{\text{Sample}}) L_{\text{Planck}}(T_{\text{Sample}}) F_{\text{Encl-Entire sample}} \left[\rho_{\text{Encl}}(\lambda)/\pi \right] F_{\text{Sample-Encl}} \left[\frac{1+a}{1-b} \right] -$$

$$- \varepsilon_{\text{Detector}}(\lambda, 0^\circ, T_{\text{Detector}}) L_{\text{Planck}}(T_{\text{Detector}}) F_{\text{Sample-Det}}$$

6.1.2 Determination of sample surface temperature

As previously mentioned, the direct radiometric static method with the comparison of radiation from the sample and the two reference blackbodies is used at the RBCF to determine the emissivity of various samples. In this case, the accurate knowledge concerning the sample surface temperature is of great importance. In Chapter 3 the various methods to determine the emissivity were reviewed, including several ways to determine the sample surface temperature. For example, use of an additional infrared thermo-camera or a computer simulation is a time-consuming process where problems can occur and can also raise uncertainties depending on several factors. Another possible method of fixing thermocouples on the surface of the sample is also associated with a certain uncertainty because of the possible non-uniformity of the temperature distribution of the sample between the edge and

the middle as well as the heat exchange between the sensor and the environment. Thus, a non-direct method for determination of the surface temperature, based on the calculation of the heat balance of heat fluxes at the sample surface, was chosen as the most optimal in this work.

The heat balance for a stationary system, shown in Fig. 6.5, is:

$$q''_{\text{in,Conduction}} = q''_{\text{out,Radiation}} \quad (6.15)$$

Here $q''_{\text{in,Conduction}}$ is the heat flux by conduction from the heating plate to the sample surface, and $q''_{\text{out,Radiation}}$ is the heat flux from the sample surface to the spherical enclosure by radiation. The obtained pressure in the facility is about 10^{-6} hPa, and therefore the heat flux by conduction and convection of residual gas in vacuum is negligible.

The Fig. 6.5 also shows the parameters required to solve this equation: the sample, which consists of a substrate with thickness d_{Sub} and thermal conductivity κ_{Sub} and a coating (thin film) with thickness d_{C} and thermal conductivity κ_{C} . It is fixed on the heating plate, where $d_{\text{H}}, \kappa_{\text{H}}$ and $d_{\text{K}}, \kappa_{\text{K}}$ are the thickness and thermal conductivity of the heating plate (here the distance from the temperature sensor to the heating surface is considered) and the contact layer between heating plate and sample, respectively.

According to Fourier's law the heat flux by conduction [17] is given by:

$$q''_{\text{in,Conduction}} = (T_{\text{H}} - T_{\text{Sample}}) / \left(\frac{d_{\text{H}}}{\kappa_{\text{H}}} + \frac{d_{\text{K}}}{\kappa_{\text{K}}} + \frac{d_{\text{Sub}}}{\kappa_{\text{Sub}}} + \frac{d_{\text{C}}}{\kappa_{\text{C}}} \right) \quad (6.16)$$

Here T_{H} is the temperature of sensor in heating plate.

The heat flux by radiation can be written as:

$$q''_{\text{out,Radiation}} = \varepsilon_{\text{Sample}} (T_{\text{Sample}}) \sigma (T_{\text{Sample}}^4 - T_{\text{Encl}}^4) \quad (6.17)$$

where σ is the Stefan-Boltzmann constant (Chapter 2.3).

Substitution of Equations 6.16 and 6.17 in 6.15 gives:

$$(T_{\text{H}} - T_{\text{Sample}}) / \left(\frac{d_{\text{H}}}{\kappa_{\text{H}}} + \frac{d_{\text{K}}}{\kappa_{\text{K}}} + \frac{d_{\text{Sub}}}{\kappa_{\text{Sub}}} + \frac{d_{\text{C}}}{\kappa_{\text{C}}} \right) = \varepsilon_{\text{Sample}} (T_{\text{Sample}}) \sigma (T_{\text{Sample}}^4 - T_{\text{Encl}}^4) \quad (6.18)$$

This can be transform to the form:

$$T_{\text{Sample}}^4 + BT_{\text{Sample}} + C = 0 \quad (6.19)$$

with coefficients B and C :

$$B = \left(1 / \left(\frac{d_H}{\kappa_H} + \frac{d_K}{\kappa_K} + \frac{d_{Sub}}{\kappa_{Sub}} + \frac{d_C}{\kappa_C} \right) \right) \frac{1}{\varepsilon_{Sample}(T_{Sample})\sigma} \quad (6.20)$$

$$C = \left(-T_H / \left(\frac{d_H}{\kappa_H} + \frac{d_K}{\kappa_K} + \frac{d_{Sub}}{\kappa_{Sub}} + \frac{d_C}{\kappa_C} \right) \right) \frac{1}{\varepsilon_{Sample}(T_{Sample})\sigma} - T_{Encl}^4 \quad (6.21)$$

The solution of Equation 6.19 gives the sample surface temperature T_{Sample} . It is also an iterative process, because the calculated sample surface temperature allows the calculation of the directional spectral emissivity under various polar angles, and then hemispherical total emissivity can be calculated, which is necessary, in turn, for solving Equation 6.19. The stable solution is found, as a rule, after less than 4 iterations.

The readings from the temperature sensor located in the sample are used to verify the accuracy of the calculation. Usually, the thickness of the contact layer between the sample and heating plate (d_K) is unknown because the thermal grease, used to improve the conductivity, is applied manually each time. Therefore some variations in layer thickness are possible (usually, d_K is less than 0.1 mm). As follows, the sensor, located in the middle of the sample, allows the adjustment of the value of contact layer to achieve high-precision surface temperature calculation.

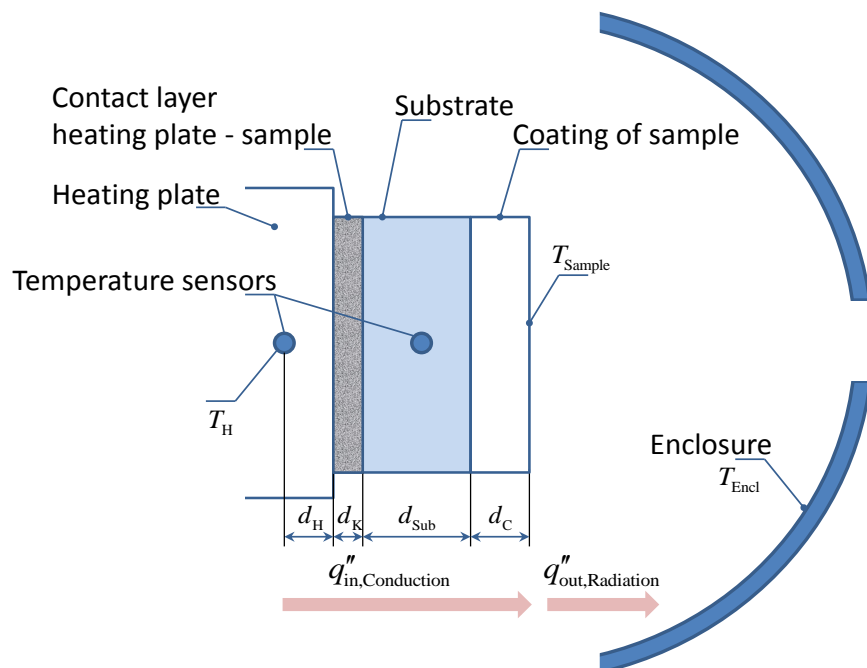


Fig. 6.5: Scheme of the layers for the heat balance for determination of sample surface temperature

6.2 Uncertainty budget

The uncertainty budget is necessary for the estimation and comparison of a measurement. According to the GUM [7] the combined standard uncertainty is given as:

$$u_c^2(y) = \sum_{i=1}^N \left(\frac{\partial f}{\partial x_i} \right)^2 u^2(x_i) \quad (6.22)$$

where $u(x_i)$ is the standard uncertainty and $\partial f / \partial x_i$ is the respective sensitivity coefficient.

The standard uncertainty $u(x_i)$ for each component is obtained from a distribution of possible values of the input quantity, depending on the type of uncertainty. The respective sensitivity coefficient is provided by the partial derivative $\partial f / \partial x_i$ and shows the variation in output estimate with changes in the values of the input estimates.

The uncertainty $u(\varepsilon_{\text{Sample}})$ of the directional spectral emissivity is calculated based on Equation 6.12 and is spectrally dependent via Planck's law. Furthermore, the uncertainty budget of emissivity measurements is calculated for each specific condition and for each individual measurement, since many components depend on the measurement conditions. All contributing uncertainty components are presented in Table 6.1.

Table 6.1: Uncertainty contributions to the uncertainty budget of the directional spectral emissivity

Uncertainty contributions	Sub components	Symbol	Type
Temperature of "main" blackbody	Non-isothermal cavity	T_{BB1}	B
	Emissivity of wall coating		B
	Calibration of temperature sensor		A
	Noise (PRT)		A
	Stability of PRT		B
Emissivity of main blackbody		$\varepsilon_{\text{BB1}}(\lambda, 0^\circ, T_{\text{BB1}})$	B
Temperature of LN ₂ blackbody	Non-isothermal cavity	$T_{\text{BB-LN2}}$	B
	Emissivity of wall coating		B
	Calibration of temperature sensor		A
	Noise (PRT)		A
	Stability of PRT		B
Emissivity of LN ₂ blackbody		$\varepsilon_{\text{BB-LN2}}(\lambda, 0^\circ, T_{\text{BB-LN2}})$	B
Temperature of enclosure	Calibration of temperature sensor	T_{Encl}	A
	Repeatability of temperature measurement		A
	Resistance measurement		A

Directional emissivity of enclosure		$\epsilon_{\text{Encl}}(\lambda, 0^\circ, T_{\text{Encl}})$	B
Hemispherical emissivity of enclosure		$\epsilon_{\text{Encl}}(\lambda, T_{\text{Encl}})$	B
Temperature of chopper	Calibration of temperature sensor Repeatability of temperature measurement Resistance measurement	T_{Ch}	A A A
Emissivity of chopper		$\epsilon_{\text{Ch}}(\lambda, 45^\circ, T_{\text{Ch}})$	B
Measured signal of spectrometer	Repeatability Nonlinearity	Q	A B
Temperature of detector	Calibration of temperature sensor Repeatability of temperature measurement Resistance measurement	T_{Detector}	A A A
Emissivity of detector		$\epsilon_{\text{Detector}}(\lambda, 0^\circ, T_{\text{Detector}})$	B
View factors	Diameter of sample (field-of-view) Diameter of entire sample Diameter of detector Diameter of enclosure Distance sample / enclosure Distance sample / detector	F d_{Sample} $d_{\text{Entire sample}}$ d_{Det} d_{Encl} $h_{\text{Sample / Encl}}$ $h_{\text{Sample / Det}}$	B B B B B B B
Temperature of sample surface	Thermal conductivity of sample substrat Thermal conductivity of sample coating Thermal conductivity of heating plate Thermal conductivity of contact layer Thickness of sample substrate Thickness of heating plate Thickness of sample coating Thickness of contact layer Temperature of heating plate Temperature of enclosure Hemispherical emissivity of sample	T_{Sample} κ_{Sub} κ_{C} κ_{H} κ_{K} d_{Sub} d_{H} d_{C} d_{K} T_{H} T_{Encl} $\epsilon_{\text{Sample}}(T_{\text{Sample}})$	B B B B B B B B A A B

The calculation of the uncertainty budget under vacuum is performed using a special software, written in LabVIEW, similar to the calculation given in detail in [42]. Here, the results of the complete equations for each sensitivity coefficient will be omitted due to the complex

form of the final Equation 6.12. However, a brief description of each uncertainty contribution and the final formula for overall uncertainty of directional spectral emissivity are given below.

Uncertainty of temperature and emissivity of reference blackbodies

The calculation as well as the uncertainty budget of the blackbodies are described in detail in Chapter 5.2. The value is selected depending on the type of blackbody, as well as the experimental conditions and wavelength range.

Uncertainty of temperature of sample enclosure and detector

The uncertainty is based on three sub-components indicated in Table 6.1, which are combined in quadrature to obtain the combined uncertainty $u(T_{\text{Encl}})$. In this case the repeatability of temperature measurement and the uncertainty of resistance measurement can be transformed into temperature via the calibration of the temperature sensor.

Uncertainty of emissivity of sample enclosure and detector

This uncertainty comes from the emissivity measurement of these surfaces.

Uncertainty of measured signal of spectrometer

The uncertainty of the measured signal of the spectrometer $u(Q)$ consists of more than two components shown in Table 6.1. However, due to the high stabilization of the spectrometer during the measurements described in Chapter 4.5.3, the uncertainty of the long-term stability can be neglected. The measurement scheme which is based on the comparison of the signal from the sample with the signal from the reference blackbody, eliminates the spectral responsivity of the spectrometer as well as its temperature drift. Thus, there are two main sub-components: the repeatability is obtained during an actual measurements and the non-linearity is determined for each detector from the measurements described in Chapter 5.1.

Uncertainty of view factors

This uncertainty is calculated according to the knowledge concerning geometrical characteristics of two surfaces with radiation exchange in between.

Uncertainty of temperature of sample surface

The calculation of the uncertainty of the temperature of the sample surface is based on the Monte Carlo method. This method choice is required by the large number of parameters involved in the calculation which are shown in the table. By the Monte Carlo method, each of the input quantities is associated with respective uncertainties as well as with a probability density function, based on the knowledge about those quantities. All quantities vary independently in these given intervals and provide a wide range of solutions depending on the selected number of Monte Carlo trials. Here, the solutions give a distribution of the sample surface temperature which is necessary to calculate a mean value and a standard deviation. This standard deviation is selected according to Supplement 1 of the GUM [7] as a standard uncertainty $u(y)$ associated with the estimate y of output quantity:

$$u^2(\tilde{y}) = \frac{1}{M_{tr} - 1} \sum_{r=1}^{M_{tr}} (y_r - \tilde{y})^2 \quad (6.23)$$

where M represents the number of Monte Carlo trials, y_r is the probability density function and \tilde{y} is the estimate output quantity, obtained as the average of the M model values y_r from a Monte Carlo run and given by:

$$\tilde{y} = \frac{1}{M_{tr}} \sum_{r=1}^{M_{tr}} y_r \quad (6.24)$$

The uncertainty of directional spectral emissivity

According to Equation 6.22, the overall uncertainty of the directional spectral emissivity is calculated as following:

$$\begin{aligned} u(\varepsilon_{\text{Sample}}) = & \left[\left(\frac{\partial \varepsilon_{\text{Sample}}}{\partial T_{\text{BB1}}} u(T_{\text{BB1}}) \right)^2 + \left(\frac{\partial \varepsilon_{\text{Sample}}}{\partial \varepsilon_{\text{BB1}}(\lambda, 0^\circ, T_{\text{BB1}})} u(\varepsilon_{\text{BB1}}(\lambda, 0^\circ, T_{\text{BB1}})) \right)^2 + \left(\frac{\partial \varepsilon_{\text{Sample}}}{\partial T_{\text{BB-LN}_2}} u(T_{\text{BB-LN}_2}) \right)^2 + \right. \\ & + \left(\frac{\partial \varepsilon_{\text{Sample}}}{\partial \varepsilon_{\text{BB-LN}_2}(\lambda, 0^\circ, T_{\text{BB-LN}_2})} u(\varepsilon_{\text{BB-LN}_2}(\lambda, 0^\circ, T_{\text{BB-LN}_2})) \right)^2 + \left(\frac{\partial \varepsilon_{\text{Sample}}}{\partial T_{\text{Encl}}} u(T_{\text{Encl}}) \right)^2 + \left(\frac{\partial \varepsilon_{\text{Sample}}}{\partial \varepsilon_{\text{Encl}}(\lambda, 0^\circ, T_{\text{Encl}})} u(\varepsilon_{\text{Encl}}(\lambda, 0^\circ, T_{\text{Encl}})) \right)^2 + \\ & + \left(\frac{\partial \varepsilon_{\text{Sample}}}{\partial \varepsilon_{\text{Encl}}(\lambda, T_{\text{Encl}})} u(\varepsilon_{\text{Encl}}(\lambda, T_{\text{Encl}})) \right)^2 + \left(\frac{\partial \varepsilon_{\text{Sample}}}{\partial T_{\text{Ch}}} u(T_{\text{Ch}}) \right)^2 + \left(\frac{\partial \varepsilon_{\text{Sample}}}{\partial \varepsilon_{\text{Ch}}(\lambda, 45^\circ, T_{\text{Ch}})} u(\varepsilon_{\text{Ch}}(\lambda, 45^\circ, T_{\text{Ch}})) \right)^2 + \\ & + \left(\frac{\partial \varepsilon_{\text{Sample}}}{\partial Q} u(Q) \right)^2 + \left(\frac{\partial \varepsilon_{\text{Sample}}}{\partial T_{\text{Det}}} u(T_{\text{Det}}) \right)^2 + \left(\frac{\partial \varepsilon_{\text{Sample}}}{\partial \varepsilon_{\text{Detector}}(\lambda, 0^\circ, T_{\text{Detector}})} u(\varepsilon_{\text{Detector}}(\lambda, 0^\circ, T_{\text{Detector}})) \right)^2 + \sum \left(\frac{\partial \varepsilon_{\text{Sample}}}{\partial F} u(F) \right)^2 + \\ & \left. \left(\frac{\partial \varepsilon_{\text{Sample}}}{\partial T_{\text{Sample}}} u(T_{\text{Sample}}) \right)^2 \right]^{1/2} \quad (6.25) \end{aligned}$$

6.3 Evaluation of emissivity measurement under vacuum

Summarizing this section, the evaluation process can be presented in the form of the following scheme (Fig. 6.6). To calculate the ratio of the measured signals of the sample and of the blackbody (Eq. 6.1), the raw-data, obtained with the FTIR-spectrometer, is processed using the Bruker OPUS FTIR software, which subtracts the interferograms and divides the resulting spectra. Special software, written in LabVIEW, allows the emissivity calculation using the obtained spectra as well as the incoming temperature data from two instruments: the Digital Precision Multimeter Keithley and the Hart Super-Thermometer. The emissivity of the sample with the corresponding uncertainty is calculated by an iterative solution using hemispherical spectral and total emissivities which is necessary for the determination of the directional spectral emissivity (Eq. 6.12) as well as the sample surface temperature (Eq. 6.19), respectively. The latter should be adjusted based on the readings of the temperature sensor inside of the sample (Chapter 6.1.2). The uncertainty of the sample surface temperature is calculated by the Monte-Carlo method in a separate program, written also in LabVIEW. By adding this uncertainty to the basic program all required data for calculation is obtained by the experiment or an analytical calculation. The directional spectral emissivity with its uncertainty and all integrated quantities can be calculated and will be presented in the next Chapter 7.

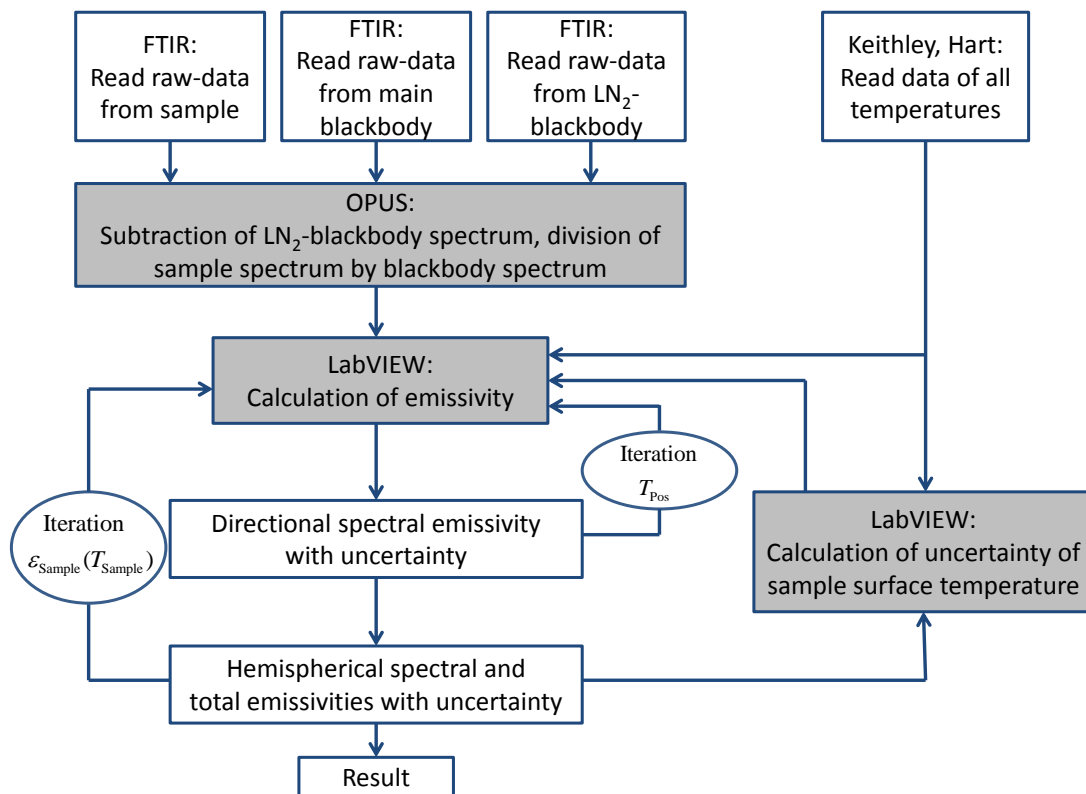


Fig. 6.6: Scheme of evaluation of emissivity measurements under vacuum

7 Emissivity of high absorbing and low absorbing materials

In Chapters 4 and 5 the setup for emissivity measurements under vacuum has been described in detail, including its technical characteristics and the characteristics of the reference blackbodies. In Chapter 6 the measurement scheme and the method for evaluation of the emissivity of a sample located inside of the temperature-stabilized enclosure are discussed. The experimental results obtained with the developed facility and the derived theoretical foundations for evaluation of the emissivity of thin films are presented in this chapter and [72].

Four samples made of different materials were selected to illustrate the capability and potential of the facility for determining the directional spectral emissivity, total directional emissivity and total hemispherical emissivity in a broad wavelength and temperature range. The black coating, Nextel Velvet Black 811-21, was chosen as an example of a well-known coating with high and stable emissivity in the MIR. A polished sample of silicon carbide, a very stable and inert material, with large variations of directional spectral emissivity over wavelengths was chosen to demonstrate the capability of the facility to determine emissivities in a temperature range from $-40\text{ }^{\circ}\text{C}$ to $450\text{ }^{\circ}\text{C}$. A polished gold sample is used here as an example of a high-reflecting material with a very low emissivity, hence producing a very low measurement signal. Lastly, a sample coated with Aeroglaze Z306 is utilized to demonstrate the variation of the directional spectral emissivity and the directional spectral reflectivity with varying optical thickness of semitransparent materials in wide spectral range up to $100\text{ }\mu\text{m}$. These variations will be explained using a theoretical model for multiple beam interferences in the semitransparent coatings which also explains the found differences for emissivity and reflectivity measurements. On the basis of this model it will be concluded that there are limitations in the application of Kirchhoff's law for semitransparent materials.

Some of the measurements obtained with this vacuum facility are compared with measurements obtained with the facility for emissivity measurement in air [42], which is successfully operated at PTB for several years and which successfully took part in an international comparison in the framework of the Consultative Committee for Thermometry (CCT) with other national metrology institutes [73]. Furthermore, the results are compared, when possible, with emissivity values, calculated indirectly from reflectivity measurements (Chapter 4.5.4). Thus, the results described in this work are validated in various ways.

7.1 Nextel Velvet Black 811-21

The Nextel Velvet Black 811-21 is a well known high-emitting coating with many applications ranging from coating the inner surfaces or cavity walls of blackbodies to interiors (furniture) or automotive instrumentation to avoid unwanted reflections. This coating has several important properties: a non-reflective surface and a high degree of absorption of scattered light, a resistance to scratching and abrasion and excellent anti-static properties. In the experiments discussed here the paint is used as coating for the inner surface of the spherical enclosure of the emissivity sample holder (Chapter 4.6) as well as for the GLORIA Blackbodies (Chapter 8). The results of the emissivity measurements of Nextel were obtained using two samples. One sample is a smooth plate of copper substrate sandblasted and spray-coated with Nextel Velvet Black 811-21. Its emissivity is discussed in this chapter. The other sample, resembling the inner surface of the sample holder and featuring additional grooves (60°), was characterized in a previous section of this work, in the wavelength range from $4\ \mu\text{m}$ to $100\ \mu\text{m}$.

Measurements were taken using two sets of detectors and beamsplitters, chosen in accordance with the specific wavelength range. For the range from $5\ \mu\text{m}$ to $20\ \mu\text{m}$ the DLaTGS detector and the KBr beamsplitter were used. To improve the thermal contact between the sample and the heating plate of the sample holder under vacuum conditions, special thermal vacuum grease Apiezon H suitable for the temperature range from $-10\ ^\circ\text{C}$ to $240\ ^\circ\text{C}$ was used to mount the sample on the heating plate. The VLTBB was used as the main reference blackbody for these measurements. Other parameters of this experiment are provided in Table 7.1.

Table 7.1: Experimental parameters for measurement of the Nextel Velvet Black 811-21 emissivity

Sample	Nextel Velvet Black 811-21
Wavelength range	$5\ \mu\text{m}$ to $20\ \mu\text{m}$
Wavenumber range	$2000\ \text{cm}^{-1}$ to $500\ \text{cm}^{-1}$
Detector and beamsplitter	DLaTGS, KBr
Field-of-view (diameter)	18 mm
Blackbody type and temperature	VLTBB, $120.0\ ^\circ\text{C}$
Temperature of LN_2 -blackbody	$-193.4\ ^\circ\text{C}$
Temperature of sample heating plate	$120.5\ ^\circ\text{C}$
Temperature of spherical enclosure	$10.3\ ^\circ\text{C}$
Temperature of spectrometer	$27.2\ ^\circ\text{C}$
Surface temperature of sample	$117.3\ ^\circ\text{C}$

The resulting emittance of the Nextel Velvet Black 811-21 measured at the setup under vacuum at temperature of $120\ ^\circ\text{C}$ is depicted in Fig. 7.1 and Fig. 7.2. In Fig. 7.1 the directional

spectral emittance observed at an angle of 10° is surrounded by a shaded area, which is the range of the standard uncertainty of the measurement, calculated according to Chapter 6. The brown curve and the corresponding right-hand ordinate axis separately show the spectral distribution of the uncertainty. With the exception of the borders the uncertainty does not exceed 0.01 in the depicted wavelength range and in some parts of the curve it is even less than 0.005.

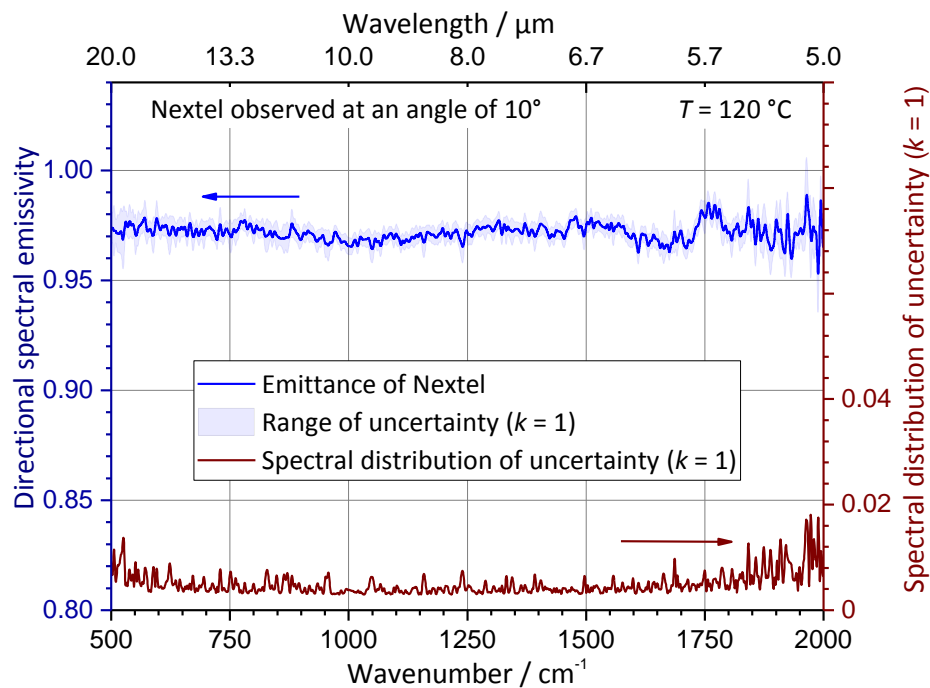


Fig. 7.1: Directional spectral emittance of Nextel Velvet Black 811-21 measured at a temperature of 120°C and under an angle of observation of 10° to the surface normal. In the lower half of the plot the spectral distribution of the standard uncertainty is shown. The respective scale is shown on the right-hand ordinate axis

Fig. 7.2 shows the angular distribution of directional spectral emittance, of which some of the typically measured angles (10° , 20° , 30° , 40° , 50° , 60° and 70°) are omitted for clarity of the picture. Typical of high-emitting samples is the decrease of the directional spectral emittance and total emittance towards larger angles.

Furthermore, the directional total emittances with their standard uncertainties are shown in the inset. The theoretical model, which is based on the sum of the Fresnel equations for two polarization directions as functions of the complex refractive index and an offset, is fitted to the experimental values (circles with standard uncertainty) and plotted as a solid line. As mentioned earlier, the indirect calculation of emissivity using optical constants is sometimes connected with a significant uncertainty. This can be also seen by the deviation of the experimental values from the fit at an angle of 70° . The directional total and hemispherical

total emittances of Nextel Velvet Black 811-21 in the wavelength range from 5 μm to 20 μm are also provided in Table 7.2.

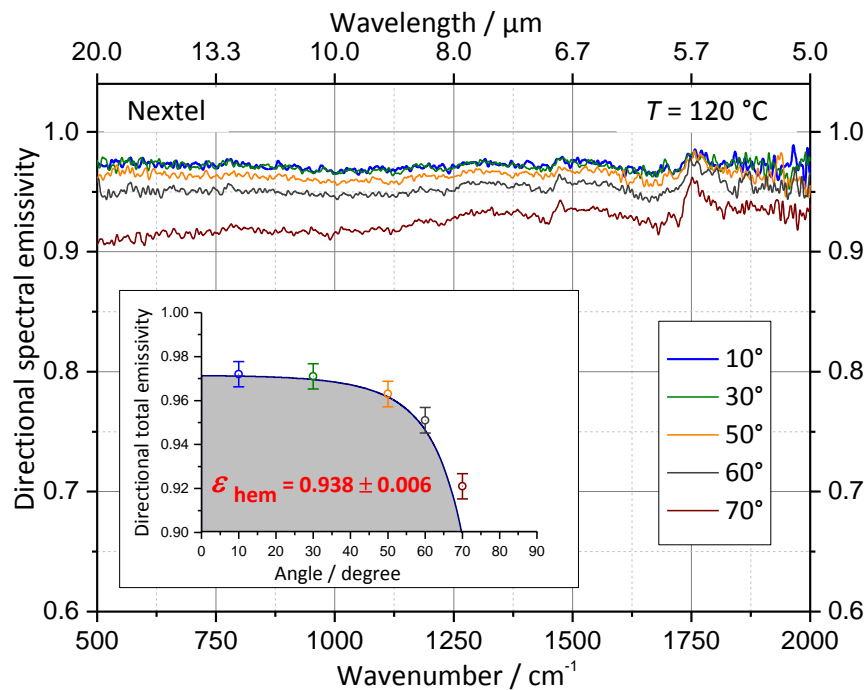


Fig. 7.2: Angular distribution of the directional spectral emittance of Nextel Velvet Black 811-21 measured at a temperature of 120 °C. The course of the resulting values of the directional total emittances with their standard uncertainties as well as the hemispherical total emittance are shown in the inset

Table 7.2: Directional total and hemispherical total emittances of Nextel Velvet Black 811-21 in the wavelength range from 5 μm to 20 μm with their respective standard uncertainties

Angle	Nextel	$u(\epsilon)$
10°	0.9717	0.0058
15°	0.9719	0.0057
30°	0.9685	0.0057
40°	0.9684	0.0057
50°	0.9609	0.0058
60°	0.9518	0.0058
70°	0.9138	0.0057
ϵ_{hem}	0.9381	0.0056

To validate the obtained results, the emittance measured under vacuum was compared to the results obtained in air (see Fig. 7.3). The measurement under vacuum is shown as in Fig. 7.1 as a blue curve, but with the expanded range of uncertainty. The red curve illustrates the directional emittance measurement in air, also with the expanded range of uncertainty. Both results agree very well within the range of the expanded uncertainty. Compared to the measurement in air the uncertainty under vacuum is

reduced. Also a reduction of artefacts caused by water absorption around 1600 cm^{-1} can clearly be seen on the blue curve. As described in Chapter 6.2, the uncertainty budget depends on several contributions. For measurement under air the uncertainty of the surface temperature dominates the measurement uncertainty due to the convective flow of the surrounding air. Under vacuum the type A or statistical uncertainties, i.e. the noise of the measurement, dominate the uncertainty budget. In this case, an increase in the measuring time would result in a further reduction of uncertainty.

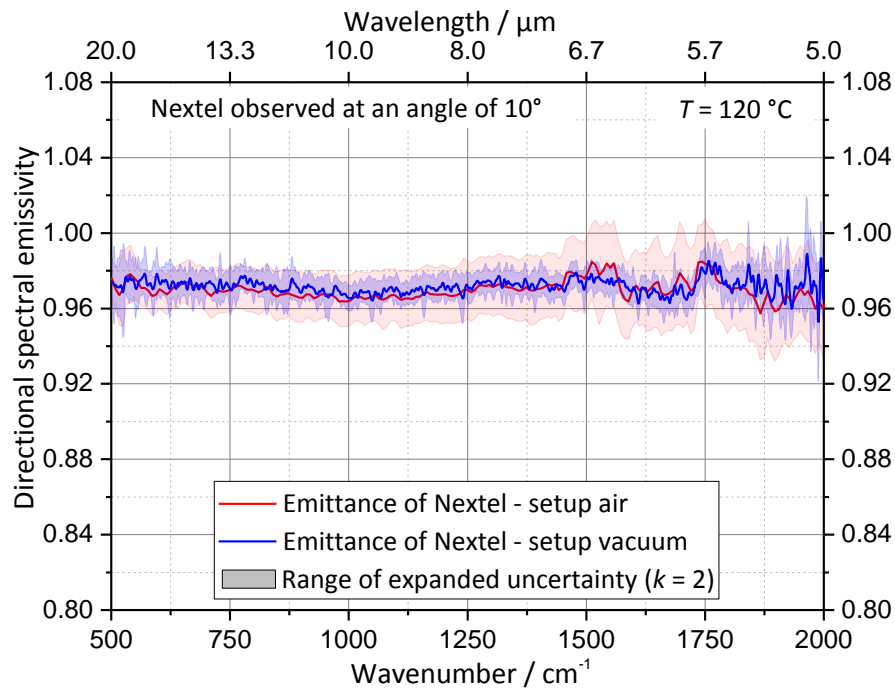
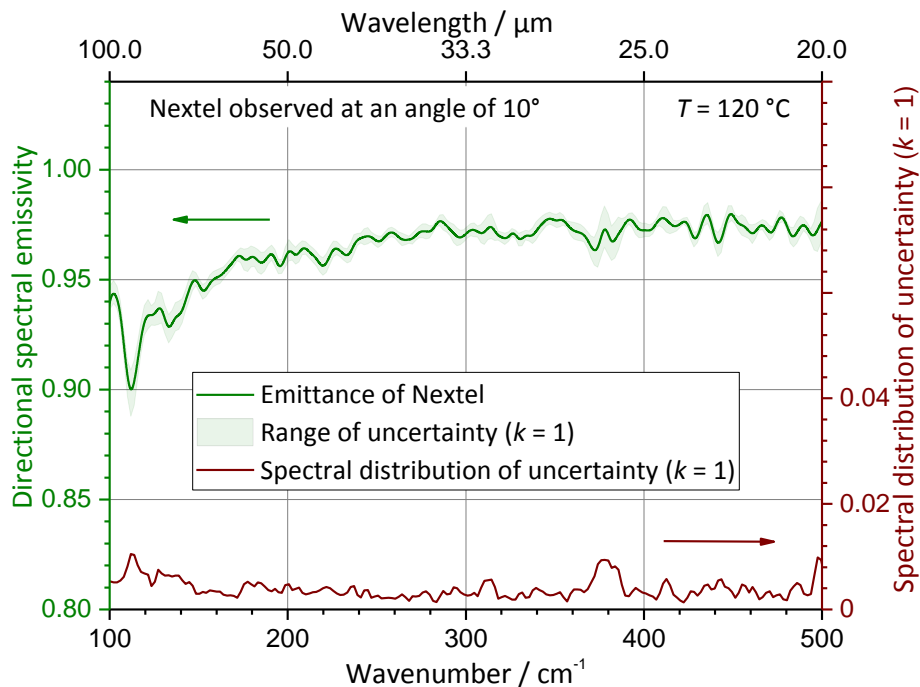


Fig. 7.3: Directional spectral emittance of Nextel Velvet Black 811-21 measured at a temperature of 120 °C and under an angle of observation of 10° to the surface normal is compared with emittance obtained at the setup in air. The shaded areas show the expanded uncertainties of both measurements

One of the important objectives of this work is to expand the wavelength range for emissivity measurements up to $100\text{ }\mu\text{m}$. The required investigation of the facility for suitability in this wavelength range was described in Chapter 5. The same sample of Nextel as described above was measured at a temperature of 120 °C in the range from $16.7\text{ }\mu\text{m}$ to $100\text{ }\mu\text{m}$ using the FDTGS detector in combination with the $6\text{ }\mu\text{m}$ Multilayer Mylar beamsplitter to show the capability of the facility. The experimental parameters are shown in Table 7.3 and the results are depicted in Fig. 7.4.

Table 7.3: Experimental parameters for the measurement of the Nextel Velvet Black 811-21 emissivity up to 100 μm

Sample	Nextel Velvet Black 811-21
Wavelength range	16.7 μm to 100 μm
Wavenumber range	598 cm^{-1} to 100 cm^{-1}
Detector and beamsplitter	FDTGS, 6 μm
Field-of-view (diameter)	18 mm
Blackbody type and temperature	VMTBB, 120.0 $^{\circ}\text{C}$
Temperature of LN_2 -blackbody	-193.4 $^{\circ}\text{C}$
Temperature of sample heating plate	120.5 $^{\circ}\text{C}$
Temperature of spherical enclosure	10.1 $^{\circ}\text{C}$
Temperature of spectrometer	27.2 $^{\circ}\text{C}$
Surface temperature of sample	118.4 $^{\circ}\text{C}$

**Fig. 7.4:** Directional spectral emittance of Nextel Velvet Black 811-21 up to 100 μm measured at a temperature of 120 $^{\circ}\text{C}$ and under an angle of observation of 10 $^{\circ}$ with respect to the surface normal. In the lower half of the plot the spectral distribution of the standard uncertainty is shown. The respective scale is shown on the right-hand ordinate axis

Note that the directional spectral emittance of Nextel stays constant up to 33 μm , and then a slight decrease can be seen at wavelengths longer than 33 μm . The spectral distribution of the uncertainty does not exceed 0.01. For most parts of the curve the uncertainty is below 0.005. The integrated quantities of emittance with their standard uncertainties are shown in Table 7.4. The detector requires a four times slower speed of the Michelson interferometer than the MCT or DLaTGS due to its limited frequency range, and thus the measurements are time consuming and calculated only at four angles of observation, shown in Table 7.4.

The comparison of the FIR-measurements with the previously discussed results in the MIR range is presented in the overlapping range from 16 μm to 44 μm in the Fig. 7.5. The results are consistent within the range of the expanded uncertainty of the measurements.

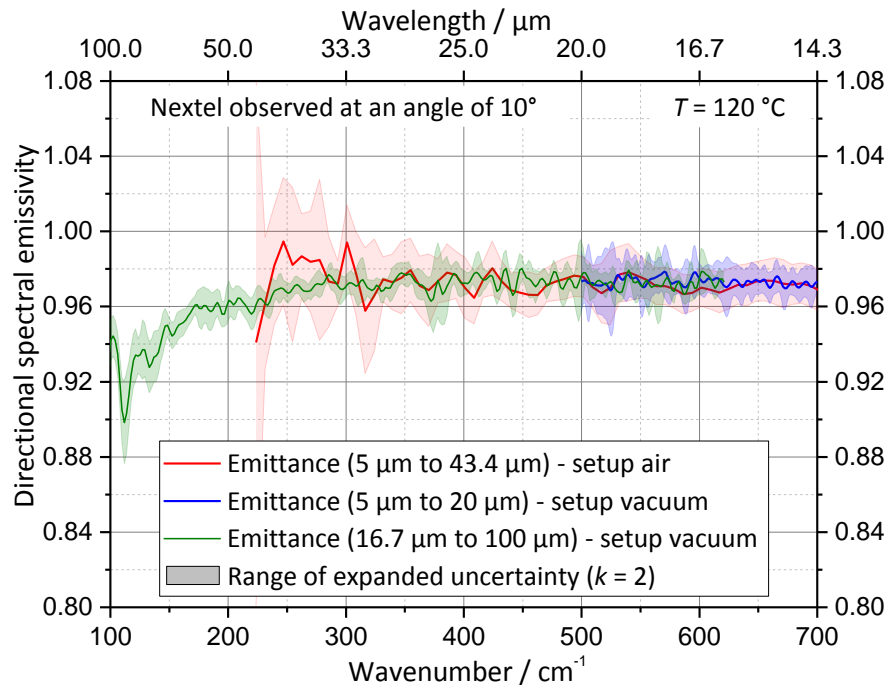


Fig. 7.5: Directional spectral emittance of Nextel Velvet Black 811-21 measured under vacuum up to 100 μm and compared in the overlapping wavelength range with measurements obtained earlier in the MIR range under vacuum and in air with a different detector and beamsplitter configuration of the spectrometer

Table 7.4: Directional total and hemispherical total emittances of Nextel Velvet Black 811-21 in the wavelength range from 16.7 μm to 100 μm with their respective standard uncertainties

Angle	Nextel	$u(\epsilon)$
10°	0.9712	0.0038
30°	0.9689	0.0036
50°	0.9579	0.0038
70°	0.8947	0.0048
ϵ_{hem}	0.9378	0.0039

7.2 Silicon carbide

The ability of the facility to determine the emissivity in the broad temperature range especially from lower temperatures below 0 °C is shown using measurements of a silicon carbide sample. The sample is polished and of pure siliconcarbide (SiC). It was clamped on the

heating plate with an intermediate substrate made of Inconel 600 to allow the positioning of two temperature sensors very close (2.5 mm and 7.5 mm) to the thin sample. The thermal contact between SiC and the intermediate substrate as well as between the substrate and the Inconel heating plate was improved by using varied thermal vacuum greases, depending on the temperatures - Apiezon N, Apiezon H and Mueller 20041 - for mounting.

Table 7.5: Experimental parameters for the measurement of the SiC emissivity

Sample	SiC	SiC	SiC
Temperature of sample	-40 °C	200 °C	450 °C
Wavelength range	7.1 μm to 18 μm	3.3 μm to 25 μm	3.3 μm to 25 μm
Wavenumber range	1400 cm^{-1} to 550 cm^{-1}	3030 cm^{-1} to 400 cm^{-1}	3030 cm^{-1} to 400 cm^{-1}
Detector and beamsplitter	MCT, KBr	DLaTGS, KBr	DLaTGS, KBr
Field-of-view (diameter)	18 mm		
Blackbody type and temperature	VLTBB, -40.0 °C	VLTBB, 120.0 °C	VMTBB, 250.1 °C
Temperature of LN ₂ -blackbody	-193.4 °C		
Temperature of sample heating plate	-42.0 °C	201.0 °C	454.0 °C
Temperature of spherical enclosure	-62.9 °C	10.1 °C	-17.3 °C
Temperature of spectrometer	27.2 °C		
Surface temperature of sample	-42.1 °C	199.1 °C	441.8 °C

The directional spectral emittance of the silicon carbide sample was measured under vacuum at three different temperatures: -40 °C, 200 °C and 450 °C (see Fig. 7.6). The measurement at a temperature of -40 °C is separately considered in the next Fig. 7.7 as it is the most critical temperature for the determination of emissivity. To cool the sample the spherical enclosure was operated at a temperature of -63 °C. Due to radiation cooling from one side and slight heating from the other, the required temperature of -40 °C was reached on the sample surface. For these measurements the spectrometer was equipped with a combination of the MCT detector and the KBr beamsplitter, considering the better sensitivity of the MCT for low temperatures (Chapter 5.1.2). Nevertheless, because of the very low signal, the measurement at -40 °C exhibits a higher noise level in comparison with measurements at 200 °C or 450 °C and was recorded in a limited wavelength range. The spectral distribution of the uncertainty is also significantly increased compared to the previous examples and is in the range between 0.02 and 0.04. The characteristic increase of the uncertainty in the range from 10 μm to 14.3 μm is directly related to the decrease of emittance and therefore related to the level of the recorded signal.

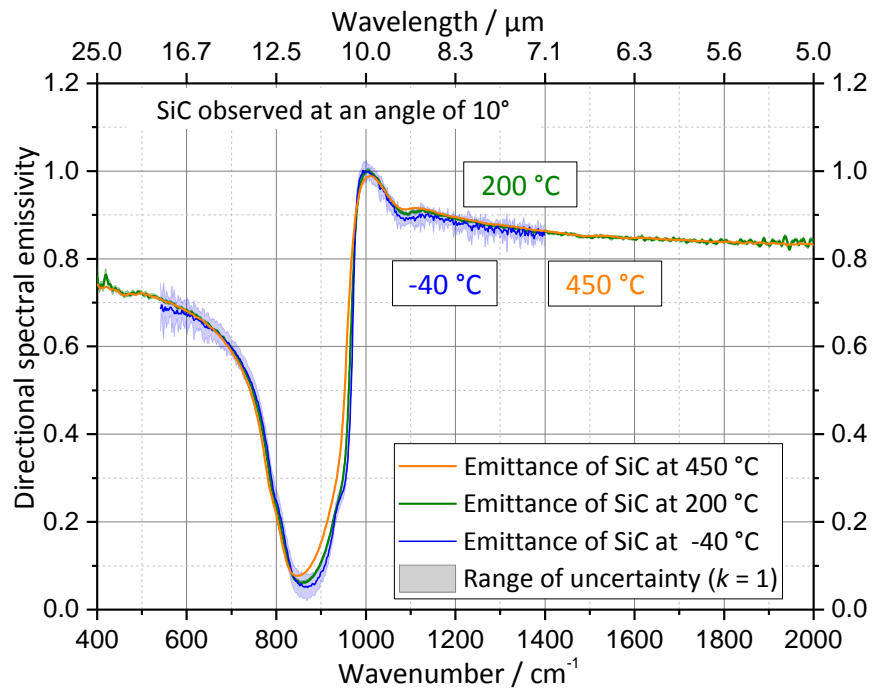


Fig. 7.6: The directional spectral emissance of a SiC sample measured under vacuum at temperatures of -40 °C, 200 °C and 450 °C. All measurements were observed at an angle of 10°

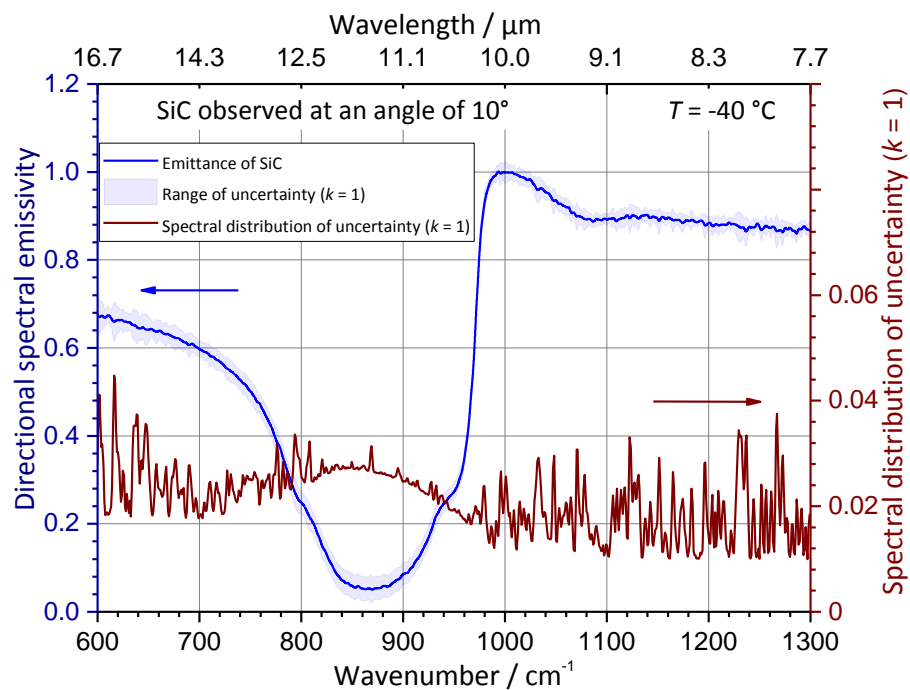


Fig. 7.7: Directional spectral emissance of SiC measured at a temperature of -40 °C and under an angle of observation of 10° with respect to the surface normal. Also shown is the spectral distribution of the standard uncertainty. The respective scale is shown on the right-hand ordinate axis

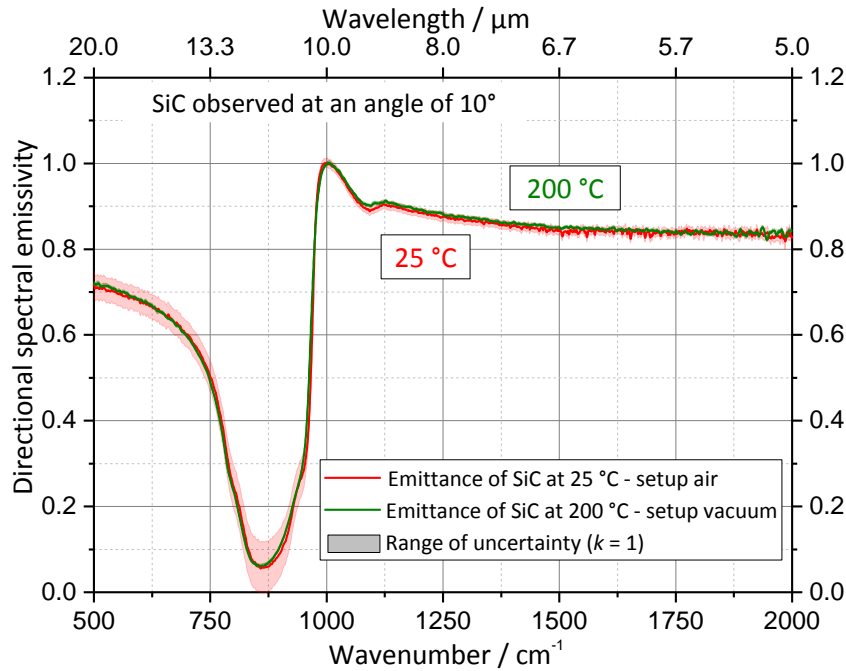


Fig. 7.8: The directional spectral emittance of a SiC sample measured under vacuum at a temperature of 200 °C shows agreement with the emittance determined by the setup in air at a temperature of 25 °C. Both measurements are observed at an angle of 10° with respect to the surface normal

Table 7.6: Directional total and hemispherical total emittances of SiC for temperatures of 200 °C and 450 °C in the wavelength range from 3.3 μm to 25 μm, and for a temperature of -40 °C from 7.1 μm to 18 μm

Angle	SiC	$u(\epsilon)$	SiC	$u(\epsilon)$	SiC	$u(\epsilon)$
10°	0.564	0.024	0.6997	0.0040	0.7323	0.0050
15°	0.566	0.024	0.7217	0.0039	0.7337	0.0050
30°	0.577	0.024	0.7223	0.0039	0.7321	0.0050
40°	0.564	0.024	0.7174	0.0039	0.7285	0.0050
50°	0.558	0.025	0.7084	0.0039	0.7194	0.0049
60°	0.558	0.024	0.6881	0.0038	0.6977	0.0047
70°	0.543	0.026	0.6399	0.0037	0.6506	0.0044
ϵ_{hem}	0.551	0.025	0.6851	0.0038	0.6981	0.0048

Neither the significantly different temperatures nor the different sets of detectors and reference blackbodies (see experimental parameters in Table 7.5) lead to significant deviations within the ranges of the standard uncertainties (see Fig. 7.6). An actual change in the emissivity of SiC at the sample temperature of 450 °C can be seen in the 10 - 12 μm range. This can be explained by a higher thermal excitation of the vibrations in the crystal structure of SiC.

The comparison between the two setups, under vacuum and in air (see Fig. 7.8), illustrates agreement as well as in the previous example and confirms, in combination with the other

results, the ability to correctly determine emissivities in a broad temperature range, in particular below 0 °C.

With a third set of detector and beamsplitter, the FDTGS and the 6 μm Multilayer Mylar beamsplitter (see Table 7.7), the emittance of SiC was obtained in the wavelength range up to 100 μm . The brown curve in Fig. 7.9 shows the consistency within the range of uncertainty of the measurements. Furthermore, it shows a notable decrease in emittance from 0.78 to about 0.60 at wavelengths longer than 33 μm . The integrated quantities in the wavelength range from 16.7 μm to 100 μm with their standard uncertainty are listed in Table 7.8.

Table 7.7: Experimental parameters for the measurement of the SiC emissivity up to 100 μm

Sample	SiC
Wavelength range	16.7 μm to 100 μm
Wavenumber range	598 cm^{-1} to 100 cm^{-1}
Detector and beamsplitter	FDTGS, 6 μm
Field-of-view (diameter)	18 mm
Blackbody type and temperature	VMTBB, 200.0 °C
Temperature of LN ₂ -blackbody	-193.4 °C
Temperature of sample heating plate	201.6 °C
Temperature of spherical enclosure	10.3 °C
Temperature of spectrometer	27.2 °C
Surface temperature of sample	198.3 °C

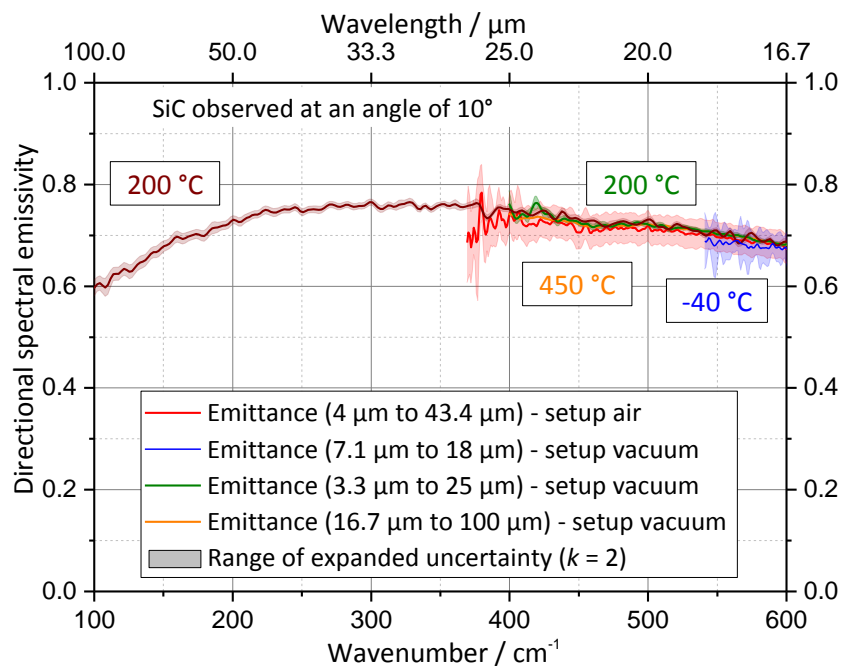


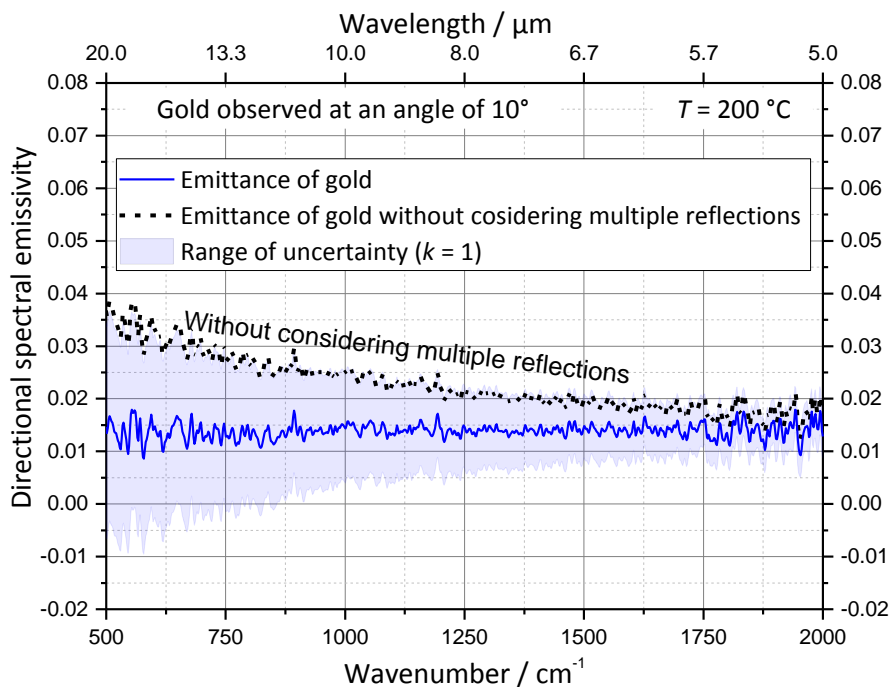
Fig. 7.9: The directional spectral emittance of a SiC sample measured under vacuum up to 100 μm and compared in the overlapping wavelength range from 16.7 μm to 25 μm with measurements obtained earlier in the MIR in both setups, under vacuum and in air. All measurements were performed at an angle of 10°

Table 7.8: Directional total and hemispherical total emittances of SiC in the wavelength range from 16.7 μm to 100 μm with their standard uncertainty

Angle	SiC	$u(\epsilon)$
10°	0.7119	0.0062
30°	0.7121	0.0063
50°	0.7079	0.0062
70°	0.6798	0.0067
ϵ_{hem}	0.6959	0.0061

7.3 Polished gold

With the polished gold sample it is exemplarily shown that samples with very low emissivity can be measured at the RBCF with sufficient accuracy. Gold is a material with a very high reflectance and therefore provides a very low signal due to its low emissivity. Thus, the measurement of gold allows a critical assessment of the capabilities of the RBCF and the applied evaluation method which includes the consideration of multiple reflections, discussed in Chapter 6.1.1. The consideration of multiple reflections is particularly important because the signal of the sample was increased by radiation from the spherical enclosure to improve the signal-to-noise ratio (Chapter 4.6). For that purpose the sphere is operated at a temperature of 80 °C. The radiation incident from the sphere onto the sample can be precisely evaluated because all characteristics of the spherical enclosure are well known.

**Fig. 7.10:** The directional spectral emittance of a Gold sample with and without considering the multiple reflection method in the evaluation

In Fig. 7.10 shows the directional spectral emittance of Gold measured under vacuum at a polar angle of 10° and at a temperature of 200°C . The calculated emittances with and without considering multiple reflections (dashed line) are compared. The difference to the blue solid line illustrates the calculation error by the simpler evaluation method, which is increased with increasing wavelength and reaches about 0.04 at $20\ \mu\text{m}$. This results from the temperature difference of sample and sphere and the accordingly shifted maxima of their respective emitted thermal radiation (the peak of blackbody radiation, Fig. 2.1).

In Fig. 7.11 the correct emissivity measurement of gold under vacuum, calculated using the multiple reflection method, shown as a blue curve, is compared with a measurement performed at the setup in air, shown as a green curve. For both measurements the spectrometer was equipped with a KBr broadband beamsplitter and a pyroelectric DLaTGS detector (other parameters for measurement under vacuum are provided in Table 7.9). The directional spectral emissivities of the same sample at the same temperature are shown in combination with their respective range of uncertainty. Both curves show a slight decrease with increasing wavelength, which is typical for metals, according to the Hagen-Rubens emissivity relation [17] derived for metals in the IR region from electromagnetic theory. The artefacts around $1600\ \text{cm}^{-1}$ are caused by residual water absorption and are only visible in the measurement in air and absent under vacuum. As the polished gold sample is a good reflector in which the diffuse part of the directional-hemispherical reflectivity can be practically neglected towards longer wavelengths, both results are compared to an emittance determined indirectly (Chapter 4.5.4) from a specular reflectivity measurement at room temperature (red curve). The different conditions of the two experiments are assumed to have no influence, because of the small temperature dependence of the emissivity of gold between 23°C and 200°C [17] and an also small angular dependence of the directional emissivity between 10° and 12° . The consistency of three independent measurements within the range of uncertainty confirms the correctness of the measurements.

Table 7.9: Experimental parameters for the measurement of the Gold emissivity

Sample	Polished gold
Wavelength range	$5\ \mu\text{m}$ to $20\ \mu\text{m}$
Wavenumber range	$2000\ \text{cm}^{-1}$ to $500\ \text{cm}^{-1}$
Detector and beamsplitter	DLaTGS, KBr
Field-of-view (diameter)	12 mm
Blackbody type and temperature	VLTBB, 80.0°C
Temperature of LN_2 -blackbody	-193.4°C
Temperature of sample heating plate	202.0°C
Temperature of spherical enclosure	79.9°C
Temperature of spectrometer	27.2°C
Surface temperature of sample	200.5°C

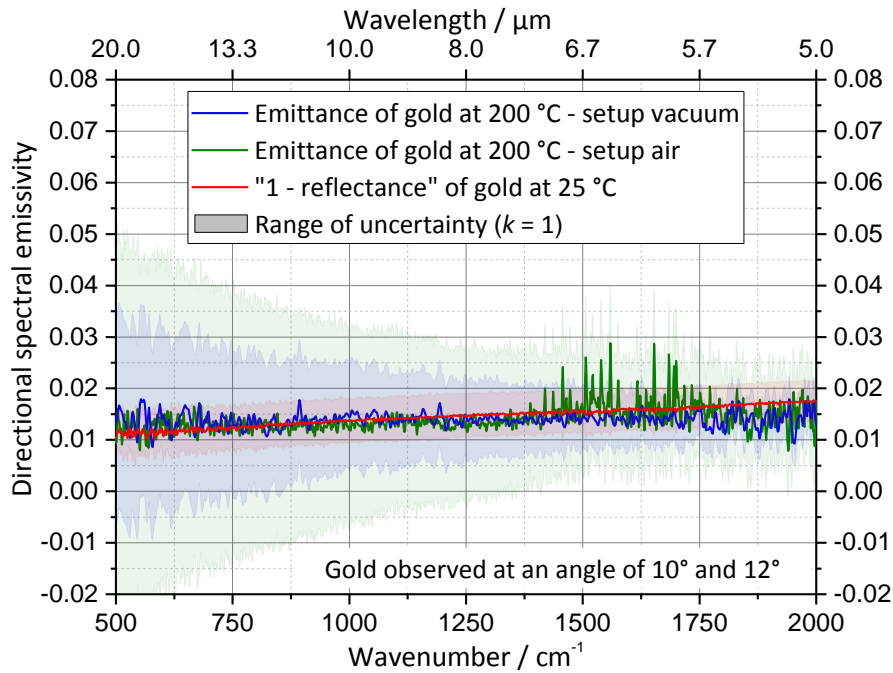


Fig. 7.11: The directional spectral emittance of a polished gold sample measured at the setup under vacuum at a temperature of 200 °C and observed at an angle of 10°. This measurement is compared with the emittance observed at the setup in air at the same temperature and with the indirectly determined emittance from a specular reflectance measurement (12°/12°- geometry)

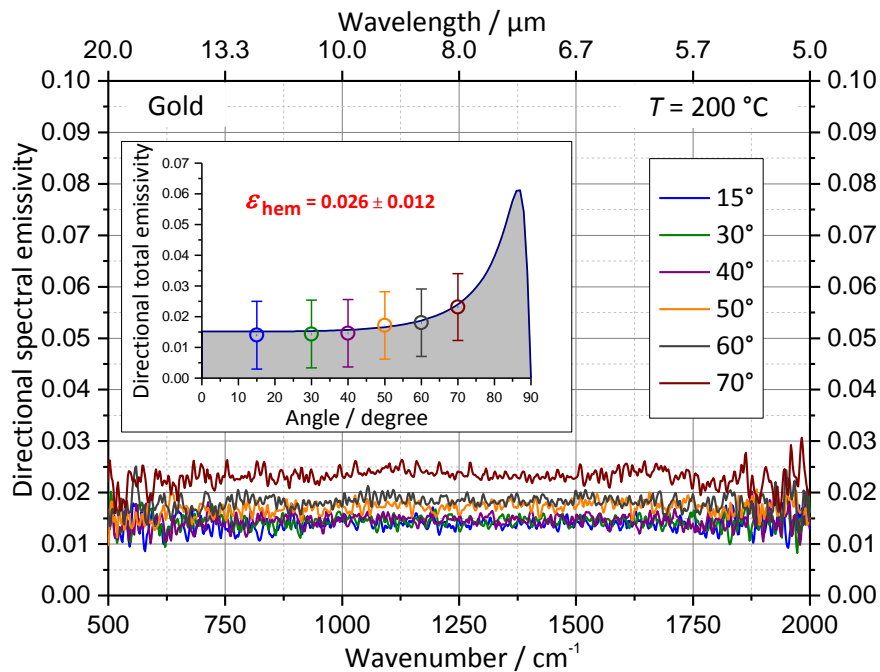


Fig. 7.12: The directional spectral emittance of a gold sample measured at different polar angles. The resulting values for the directional total emittances with their standard uncertainty, a Fresnel equation-based model fitted to these values as well as the hemispherical total emittance are shown in the inset

The directional spectral emittances at angles from 15° to 70° and the resulting integrated quantities are shown in Fig. 7.12. The directional total emittances of gold including their standard uncertainties (circles with point) are shown with values from a fitted model (solid line) based on the Fresnel equations. In contrast to materials with a relatively high emissivity (Nextel, or other dielectrics) the directional emissivity of metals remains low for smaller angles of observation and increases to a maximum towards larger angles with a sharp decrease to zero for 90°.

Table 7.10: Directional total and hemispherical total emittances of polished gold in the wavelength range from 5 μm to 20 μm with their standard uncertainty

Angle	Gold	$u(\epsilon)$
15°	0.023	0.011
30°	0.024	0.011
40°	0.024	0.011
50°	0.026	0.011
60°	0.027	0.011
70°	0.033	0.010
ϵ_{hem}	0.026	0.011

7.4 Theory of thin films with wave interference effect and validity of Kirchhoff's law discussed based on the emissivity results of Aeroglaze Z306

In practical applications one is often dealing with combinations of different materials. Substrates, coatings and covers with often different wavelength dependent characteristics are stacked or arranged in a particular order to provide the desired characteristics or functionality. An example is the solar energy collectors for energy conversion, where the surface of the absorber is coated with a special step-type coating to provide a high absorption of solar radiation and a low loss of thermal emission. The absorber is often mounted inside of a glass tube. In this case, one should consider such a device as a combination of substrate, coating and glass window.

The modification of surface characteristics can not only be achieved by a combination of different coatings or chemical or electro-chemical processing, but also by changing the parameters of the selected materials: the variation of thicknesses and number of layers of film can provide a significant modification to the ability to absorb, emit or reflect radiant energy. This effect is based on the changes of reflection and refraction at an interface as well as the propagation of electromagnetic radiation into an absorbing, emitting and scattering media, namely, into the thin film. Some of the layers or the whole film stack may be partially

transparent depending on the wavelength range. If the layer is thin i.e. its thickness is on the order of a wavelength, then the interference effects can occur between waves, which are reflected from the first, second and deeper surface. In the following only the case of one partially transparent layer is considered.

Today there are many software packages and models in use for the calculation and design of different types of optical interference coatings, including complex multilayer systems [74-76]. These models are based on the reflection, absorption and transmission characteristics of the individual material of the layers and describe the propagation of an incident wave according to the refraction and reflection theory, thin films theory, transfer-matrix method, etc. and enable the calculation of the reflectance and transmittance of the multilayer system. The emissivity is then calculated indirectly from these characteristics, using Kirchhoff's law, which states that a body emits as much radiation as it absorbs (Chapters 2.8 and 3.1). The first attempts to directly calculate the emissivity of a "partially transparent reflecting body" were made in 1950 by McMahon, who proposed a consideration of emissivity as energy generated within the coating [77]. Later publications have developed this theory further [78, 79]. The possible inconsistencies in the direct and indirect calculation of the emissivity as well as the validation of Kirchhoff's law in the case of thin films with the interference effect were investigated and discussed while considering the different mechanisms: an independent and incoherent Planckian radiation from the volume element of the real body (direct method) and incident radiation from an external source (indirect) [80-83]. However, a consistent explanation of the found effects is still pending. Thus the direct method utilized in this work to determine the emissivity of thin films with the consideration of wave interference effect and the validity of Kirchhoff's law in this case is an important area of research, because many of the coatings, used in modern technologies, become or must be transparent in certain spectral ranges. The development of the according theory provides the required basis for a reliable evaluation of the emissivity measurements of thin semitransparent samples with the facility described in this work and the discussions and conclusions are based on measurement results obtained with Aeroglaze Z306.

7.4.1 Aeroglaze Z306

Aeroglaze Z306 is an absorptive polyurethane coating which is often used in aerospace operations. It is well suited for vacuum conditions and has high emissivity properties. As already mentioned in the discussion of the VLTBB, three samples were prepared by spray coating a set of three copper substrates with Aeroglaze Z306 in thicknesses of 44 μm , 99 μm and 236 μm . Homogeneous surfaces were obtained by spraying according to the instructions given in the European Cooperation for Space Standardization document ECSS-Q-70-25A

[45]. The measurements were performed at the setup under vacuum at a temperature of 150 °C and at the setup for reflectivity at a temperature of 23 °C. For these measurements the pyroelectric FDTGS detector and the 6 μm Multilayer Mylar beamsplitter were used (see Table 7.11). The directional spectral emittances of the three samples under an angle of observation of 10° are shown in Fig. 7.13; the shaded areas illustrate the standard uncertainty for each measurement.

Table 7.11: Experimental parameters for the measurement of the Aeroglaze Z306 emissivity

Sample	Aeroglaze Z306	Aeroglaze Z306	Aeroglaze Z306
Coating thickness	44 μm	99 μm	236 μm
Wavelength range	14.7 μm to 100 μm		
Wavenumber range	680 cm^{-1} to 100 cm^{-1}		
Detector and beamsplitter	FDTGS, 6 μm		
Field-of-view (Diameter)	18 mm		
Blackbody type and temperature	VMTBB, 150.0 °C		
Temperature of LN ₂ -blackbody	-193.4 °C		
Temperature of sample heating plate	153.1 °C	150.5 °C	150.4 °C
Temperature of spherical enclosure	10.1 °C		
Temperature of spectrometer	27.2 °C		
Surface temperature of sample	146.8 °C	148.6 °C	148.5 °C

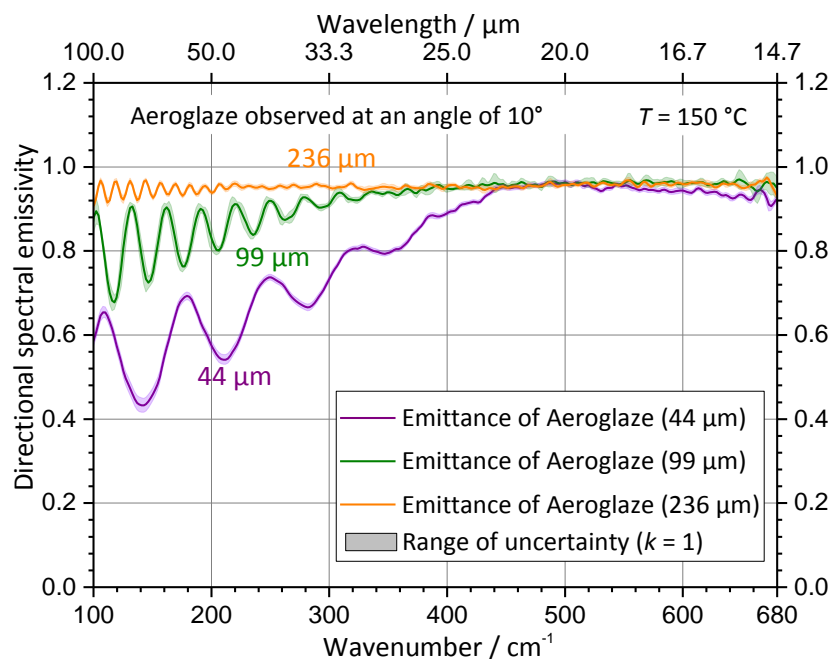


Fig. 7.13: Directional spectral emittances of three Aeroglaze Z306 samples with thicknesses of 44 μm , 99 μm and 236 μm on copper substrates under an angle of observation of 10° with respect to the surface normal. The standard measurement uncertainties are shown as shaded areas

The sample with the thickness of 44 μm shows a significant decrease in emittance at wavelengths longer than 22 μm , the sample with the thickness of 99 μm shows a slighter decrease whereas the thickest sample shows a nearly constant average emittance. All samples demonstrate a significant modulation towards longer wavelengths with a period inversely proportional to the coating thickness. This decrease can be explained by an onset of transparency of the coating towards longer wavelengths. Because it is applied on a reflective substrate, multiple beam interference should occur, which results in a modulation inversely proportional to the optical thickness of the coating.

Table 7.12: Directional total and hemispherical total emittances of Aeroglaze Z306 at three different thicknesses. All measurements were performed at a temperature of 150 °C and in the wavelength range from 14.7 μm to 100 μm

Angle	Aeroglaze Z306, 44	$u(\epsilon)$	Aeroglaze Z306, 99	$u(\epsilon)$	Aeroglaze Z306, 236	$u(\epsilon)$
10°	0.8793	0.0066	0.9434	0.0102	0.9553	0.0054
30°	0.8852	0.0065	0.9422	0.0094	0.9555	0.0054
50°	0.8823	0.0066	0.9288	0.0092	0.9402	0.0052
70°	0.7966	0.0067	0.8299	0.0082	0.8368	0.0047
ϵ_{hem}	0.8512	0.0064	0.8966	0.0102	0.9129	0.0052

For the sample with the 99 μm thick Aeroglaze Z306 coating, emissivity and reflectivity measurements were performed and the measured and derived emissivities are compared as follows. The emittance observed at an angle of 10° and obtained by the direct method is shown as a green line in Fig. 7.14 with its standard uncertainty range shown as a shaded area. The emittance derived as “1 - reflectance” from the specular reflectance measurement at an angle of 12° is shown as a red line in Fig. 7.14. The small angular differences of the two experiments can be neglected due to the small dependence of the emittance from these quantities.

Two independent measurements of the same sample show a relatively constant emittance from shorter wavelengths up to 22 μm and a decrease in emittance at the wavelengths longer than 22 μm . Furthermore, modulations whose amplitudes increase towards longer wavelengths become more visible. This can be explained by the increase of the transparency of the coating towards longer wavelength. More and more multiple reflected components built up towards longer wavelengths and consequently, the interference observed becomes stronger modulated.

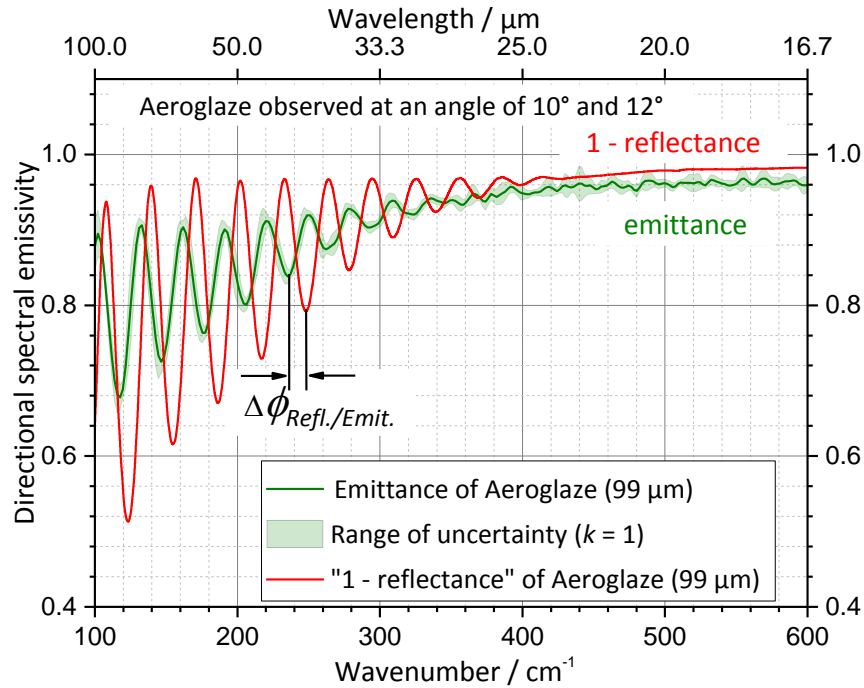


Fig. 7.14: The “phase difference” between directional spectral emittance and reflectance of the same sample of 99 μm thick Aeroglaze Z306 on copper. The directional spectral reflectance is shown as “1 - reflectance”

The small difference in magnitude between the directly measured emittance and the emittance calculated from the reflectance, which is clearly visible in Fig. 7.14 in the range from 16.7 μm to 22 μm , is caused by the diffuse part of the reflectivity, which is neglected in the calculation. The decrease in difference towards longer wavelengths is typical because the diffuse part becomes smaller towards longer wavelengths. Additionally a “phase difference” between emittance and reflectance modulations is clearly visible in Fig. 7.14. There are also ranges where the “1 - reflectance” curve is below the emittance curve. This is a contradiction with Kirchhoff’s law:

$$\varepsilon(\theta, \varphi, \lambda) + \rho_d(\lambda) + \rho_s(\theta, \varphi, \lambda) + \tau(\theta, \varphi, \lambda) \neq 1, \quad (7.1)$$

making its use for the measured quantities from 22 μm to 100 μm not applicable.

The directional spectral emittance was also measured with the direct method under angles of observation of 10°, 30°, 50° and 70°. The results are shown in Fig. 7.15. The modulations are clearly visible as is a shift of the maxima corresponding to the increase of the optical thickness of the coating at larger angles of observation. Nevertheless, regardless of these noticeable change it can be seen that the slight difference in viewing conditions - of 10° by emittance and 12° by reflectance measurements - cannot cause such a significant phase difference as found in Fig. 7.14.

To explain the observed phase difference between emittance and reflectance measurements, the two cases will be modeled as follows: for reflectivity the multiple beam interference in the semitransparent layer with an external source will be described, and for the emissivity the model will take into account the fact that the radiation source is the coating itself. Finally, a synopsis concerning the limitation of Kirchhoff's law for semitransparent materials will be concluded.

The reflectivity rather than absorptivity is considered for two reasons: the reflectivity has the same mechanism of interference with radiation from an external source as the absorptivity and secondly, the reflectivity is experimentally most commonly used for the indirect determination of the emissivity, even for semitransparent thin films [84].

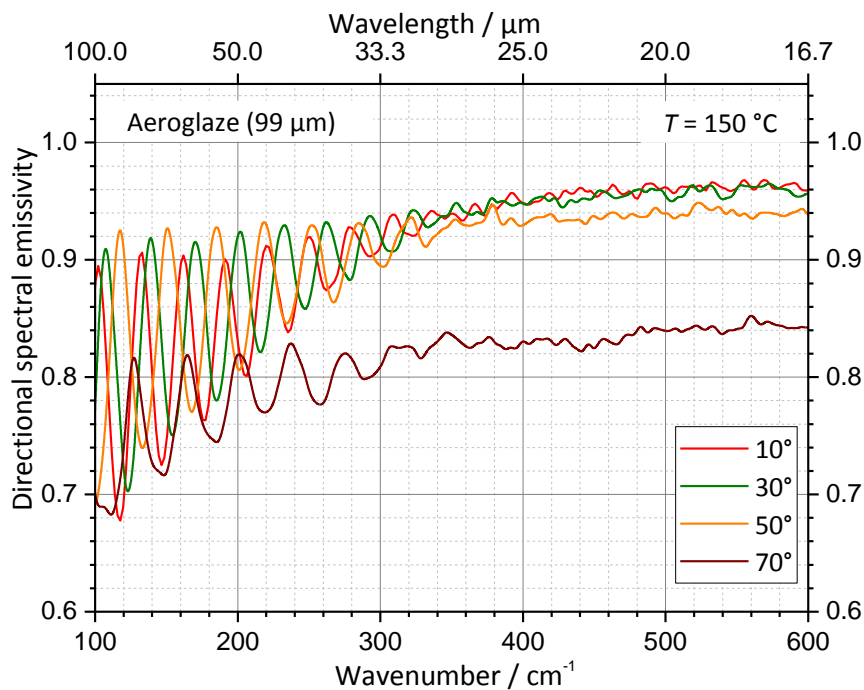


Fig. 7.15: Directional spectral emittances of Aeroglaze Z306 with a thickness of 99 μm on a copper substrate plate under angles of observation of 10°, 30°, 50° and 70° with respect to the surface normal

7.4.2 Reflectivity of a thin film considering wave interference effects

The calculation of the reflectivity of a semitransparent layer on a reflective substrate with the consideration of multiple beam interference is based on the classical thin film model with reflection and refraction of electromagnetic waves [17]. Consider the general case of a thin isotropic film of finite conductivity with thickness D on a metallic substrate (Fig. 7.16). The coating has a transmissivity coefficient t_1 , a complex index of refraction $n_1 - ik_1$ and a specular

reflectivity coefficient r_1 . The substrate has a reflectivity coefficient r_2 and a complex index of refraction $n_2 - ik_2$. It should be noted that the considered coating in the modeled cases for reflectivity as well as for emissivity is not completely transparent but attenuating ($\tau < 1$) and furthermore that n and k depend on wavelength. The substrate is a metal with high reflectivity and low absorptivity. For simplification, the surface of coating and substrate are assumed to be optically smooth. The medium is isotropic.

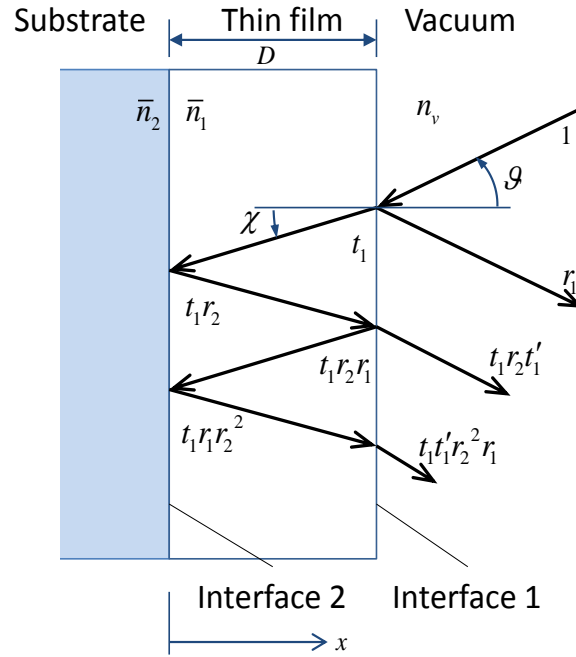


Fig. 7.16: Graphical representation of the theoretical model of the reflectivity of a semitransparent layer on a substrate showing the multiple reflections from the first and second interfaces

The radiation, propagated in vacuum, is incident from an external source onto the thin film with an angle of incidence ϑ . It can be written using Equation 2.39 as an electromagnetic wave propagating within an isotropic media of finite conductivity in the negative x -direction. The wave originates at the time $\tau = 0$, and according to the electromagnetic theory (Chapter 2.10), which states that the energy flux density is proportional to the square of the amplitude of the wave, the energy flux density of this wave can be written as:

$$|S_{r,0}| = \frac{\bar{n}}{\mu c_0} |E|^2 = \frac{\bar{n}}{\mu c_0} |E_{r,0} \exp(-i\omega t)|^2 \quad (7.2)$$

Where μ is the magnetic permeability, c_0 the speed of an electromagnetic wave in vacuum and $E_{r,0}$, the amplitude of the wave.

According to Snell's law [17], reflection and refraction of the radiation occur on a boundary between two isotropic media (interface 1). The reflected beam amplitude is proportional to the reflectivity coefficient of the coating: r_1' . The refracted beam is transmitted into the medium (t_1'), reflected from the second surface (interface 2, r_2) and divided again into two parts on interface 1: $t_1 r_2 t_1'$ and $t_1 r_2 r_1'$. The travelled distance of the beam within the thin film equals $2D/\cos(\chi)$, where χ is the angle of refraction. According to the equation of plane wave, the phase difference between the first reflected part of the original beam (r_1') and the beam after propagation once through the thin film ($t_1 r_2 t_1'$) can be written as:

$$\Delta\phi = \exp\left(\frac{-i4\pi(n_1 - ik_1)D}{\cos(\chi)\lambda_0}\right) \quad (7.3)$$

Applying this principle, for higher order reflections the overall reflectivity coefficient can be written as the infinite sum of beams reflected and refracted at these two interfaces (Fig. 7.16) and concatenated into the last term in Equation 7.4:

$$\begin{aligned} r_{a,TF} = & r_1' + t_1 t_1' r_2 \exp\left(-i\frac{4\pi(n_1 - ik_1)D}{\cos(\chi)\lambda_0}\right) + t_1 t_1' r_1 r_2^2 \exp\left(-i\frac{8\pi(n_1 - ik_1)D}{\cos(\chi)\lambda_0}\right) + \\ & + t_1 t_1' r_1^2 r_2^3 \exp\left(-i\frac{12\pi(n_1 - ik_1)D}{\cos(\chi)\lambda_0}\right) + \dots = r_1' + \frac{t_1 t_1' r_2 \exp\left(-i\frac{4\pi(n_1 - ik_1)D}{\cos(\chi)\lambda_0}\right)}{1 - r_1 r_2 \exp\left(-i\frac{4\pi(n_1 - ik_1)D}{\cos(\chi)\lambda_0}\right)} \end{aligned} \quad (7.4)$$

Thus, after multiple reflections the amplitude of the outgoing (reflected) wave is given by Equation 7.5 with corresponding energy flux density, shown in Equation 7.6 respectively:

$$E_r = E_{r,0} \exp(-i\omega t) \left[r_1' + \frac{t_1 t_1' r_2 \exp\left(-i\frac{4\pi(n_1 - ik_1)D}{\cos(\chi)\lambda_0}\right)}{1 - r_1 r_2 \exp\left(-i\frac{4\pi(n_1 - ik_1)D}{\cos(\chi)\lambda_0}\right)} \right] = E_{r,0} \exp(-i\omega t) [r_{a,TF}] \quad (7.5)$$

$$|S_r| = \frac{\bar{n}}{\mu c_0} |E_r|^2 = \frac{\bar{n}}{\mu c_0} \left| E_{r,0} \exp(-i\omega t) [r_{a,TF}] \right|^2 \quad (7.6)$$

According to the definition, the ratio of the energy flux density of the reflected wave (Eq. 7.6) to the energy flux density of the incident wave (Eq. 7.2) on the interface 1 gives the reflectivity of thin film:

$$\rho_{\text{TF}} = \frac{\frac{\bar{n}}{\mu c_0} \left| E_{r,0} \exp(-i\omega t) [r_{\text{a,TF}}] \right|^2}{\frac{\bar{n}}{\mu c_0} \left| E_{r,0} \exp(-i\omega t) \right|^2} = |r_{\text{a,TF}}|^2 = r_{\text{a,TF}} r_{\text{a,TF}}^* \quad (7.7)$$

with $r_{\text{a,TF}}^*$ the complex conjugate of $r_{\text{a,TF}}$.

Thus, the resulting reflectivity, which describes the interference effect within semitransparent coatings and depends on the optical material quantities r , t , n and k , the angle of refraction χ (relation between angle of incidence ϑ and angle of refraction is given in Equation 2.41), the wavelength and the thickness D , can be found as:

$$\rho_{\text{TF}} = |r_{\text{a,TF}}|^2 = \frac{r_1'^2 + 2r_1'(t_1 t_1' r_2 - r_1 r_1' r_2) \exp\left(\frac{-4\pi D k_1}{\cos(\chi) \lambda_0}\right) \cos\left(\frac{-4\pi D n_1}{\cos(\chi) \lambda_0}\right) + (t_1 t_1' r_2 - r_1 r_1' r_2)^2 \exp\left(\frac{-8\pi D k_1}{\cos(\chi) \lambda_0}\right)}{1 + r_1^2 r_2^2 \exp\left(\frac{-8\pi D k_1}{\cos(\chi) \lambda_0}\right) - 2r_1 r_2 \exp\left(\frac{-4\pi D k_1}{\cos(\chi) \lambda_0}\right) \cos\left(\frac{-4\pi D n_1}{\cos(\chi) \lambda_0}\right)} \quad (7.8)$$

7.4.3 Emissivity of a thin film considering wave interference effects

In the case of the emissivity of thin films we also consider the ratio of energy fluxes densities of electromagnetic waves: from the initial wave undisturbed by the thin film and the wave after propagation within the thin film. In contrast to the calculation of the reflectivity this ratio does not directly provide the emissivity. The introduced and calculated emissivity coefficients K_a and the following derived scaling factors for emissivity K_ε describe the change of the radiance of the wave in the case of an optically thin film with wave interference effect. The initial radiance is: $L_\lambda(\lambda, \vartheta, \varphi, T) = L_{\lambda b}(\lambda, T) \varepsilon_\lambda(\lambda, \vartheta, \varphi, T)$. Thus this scaling factor is added to the original definition of the emissivity (Eq. 2.11):

$$\varepsilon_\lambda(\lambda, \vartheta, \varphi, T) = \frac{L_\lambda(\lambda, \vartheta, \varphi, T)}{L_{\lambda b}(\lambda, T) \cdot K_\varepsilon} \quad (7.9)$$

On the other hand this allows the determination of the emissivity of the materials, the thin film or the substrate, and consists of separating the effects induced by the geometrical structure.

The second difference to the previous section is the consideration of the sample as a source of radiation in contrast to the model for reflectivity, which describes the propagation of

radiation from an external source. Here the radiation consists of two parts: the radiation originating within the thin film $L_{TF}(T_{TF})$ and the radiation emitted by the heated substrate $L_{Sub}(T_{Sub})$:

$$L_{Sample}(T_{Sample}) = L_{TF}(T_{TF}) + L_{Sub}(T_{Sub}) \quad (7.10)$$

The sum $L_{Sample}(T_{Sample})$ is the radiation emitted directly by the sample (the radiation component labeled "1" in the Fig. 6.3), which is used in Equation 6.9 and the resulting Equation 6.12 for the calculation of the emissivity in Chapter 6.

Thin film (TF)

Consider a wave originating from each volume element within the thin film (see Fig. 7.17). In the case of emissivity the electromagnetic wave must be considered as propagating in two directions: the positive and negative direction of the x-axis. As consequence the energy flux density that we consider as initial is doubled and thus after integration over the thickness D of the thin film, the energy flux density is given by:

$$|S_{TF,0}| = \int_0^D \frac{\bar{n}}{\mu c_0} |2E_{TF,0} \exp(-i\omega t)|^2 dx \quad (7.11)$$

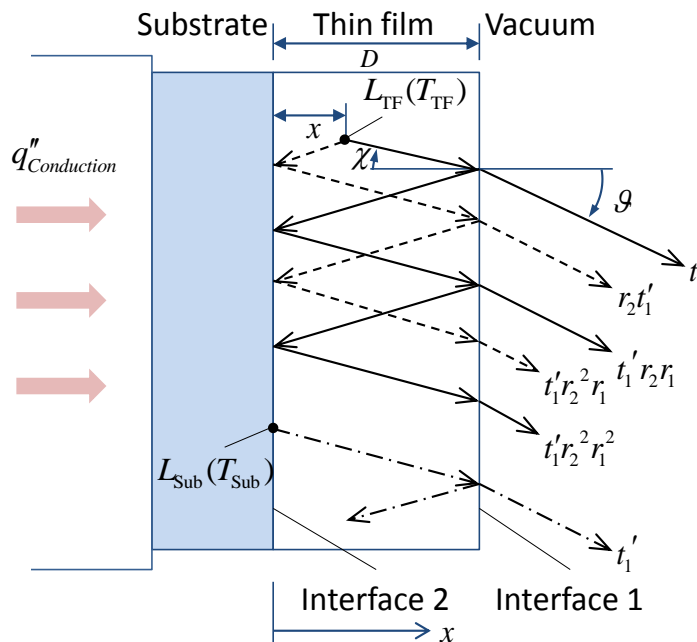


Fig. 7.17: A graphical representation of the theoretical model of the emissivity with wave interference effect. All contributions of radiation are shown: the two directions of propagating waves, originating from each volume element within the semitransparent thin film (solid and dashed line) and the radiation of the opaque substrate (dash-dot line)

Similarly, both propagation directions of the radiation along the x -axis must be taken into account to describe the energy flux density of the wave on the interface 1 after multiple reflections. The wave, propagating in the positive direction of the x -axis towards the interface 1, first travels a distance $(D-x)/\cos(\chi)$ (solid line in Fig. 7.17). Accordingly, the radiation propagating into the opposite direction will travel a distance $(x+D)/\cos(\chi)$ until it reaches interface 1 (dashed line in Fig. 7.17).

Similar to the discussion of reflectivity in the preceding chapter, when considering multiple beam interference and the phase relationship between reflected beams, the coefficients of emissivity can be written for the wave travelling in the positive direction ($K_{a,TF}^+$, solid line) and the wave travelling in negative direction ($K_{a,TF}^-$, dashed line) as:

$$K_{a,TF}^+ = t_1' \exp\left(-i \frac{2\pi(n_1 - ik_1)(D-x)}{\cos(\chi)\lambda_0}\right) + r_1 r_2 t_1' \exp\left(-i \frac{2\pi(n_1 - ik_1)(D-x)}{\cos(\chi)\lambda_0}\right) \exp\left(-i \frac{4\pi(n_1 - ik_1)D}{\cos(\chi)\lambda_0}\right) +$$

$$+ r_1^2 r_2^2 t_1' \exp\left(-i \frac{2\pi(n_1 - ik_1)(D-x)}{\cos(\chi)\lambda_0}\right) \exp\left(-i \frac{8\pi(n_1 - ik_1)D}{\cos(\chi)\lambda_0}\right) + \dots = \frac{t_1' \exp\left(-i \frac{2\pi(n_1 - ik_1)(D-x)}{\cos(\chi)\lambda_0}\right)}{1 - r_1 r_2 \exp\left(-i \frac{4\pi(n_1 - ik_1)D}{\cos(\chi)\lambda_0}\right)}$$
(7.12)

$$K_{a,TF}^- = r_2 t_1' \exp\left(-i \frac{2\pi(n_1 - ik_1)x}{\cos(\chi)\lambda_0}\right) \exp\left(-i \frac{2\pi(n_1 - ik_1)D}{\cos(\chi)\lambda_0}\right) + r_1 r_2^2 t_1' \exp\left(-i \frac{2\pi(n_1 - ik_1)x}{\cos(\chi)\lambda_0}\right) \exp\left(-i \frac{6\pi(n_1 - ik_1)D}{\cos(\chi)\lambda_0}\right) +$$

$$+ r_1^2 r_2^3 t_1' \exp\left(-i \frac{2\pi(n_1 - ik_1)x}{\cos(\chi)\lambda_0}\right) \exp\left(-i \frac{10\pi(n_1 - ik_1)D}{\cos(\chi)\lambda_0}\right) + \dots = \frac{r_2 t_1' \exp\left(-i \frac{2\pi(n_1 - ik_1)x}{\cos(\chi)\lambda_0}\right) \exp\left(-i \frac{2\pi(n_1 - ik_1)D}{\cos(\chi)\lambda_0}\right)}{1 - r_1 r_2 \exp\left(-i \frac{4\pi(n_1 - ik_1)D}{\cos(\chi)\lambda_0}\right)}$$
(7.13)

Thus, the energy flux density leaving the thin film towards the detector after multiple reflections between its two boundaries is:

$$|S_{TF}| = \int_0^D \frac{\bar{n}}{\mu c_0} \left| E_{TF,0} \left[K_{a,TF}^+ + K_{a,TF}^- \right] \right|^2 dx$$
(7.14)

The ratio of the energy flux density after multiple reflections (Eq. 7.14) to the initial energy flux density (Eq. 7.11) gives the scaling factor of the emissivity of the thin film:

$$\begin{aligned}
K_{\varepsilon, \text{TF}} &= 1 - \frac{\int_0^D \frac{\bar{n}}{\mu c_0} \left| E_{\text{TF},0} \exp(-i\omega t) \left[K_{\text{a,TF}}^+ + K_{\text{a,TF}}^- \right] \right|^2 dx}{\int_0^D \frac{\bar{n}}{\mu c_0} \left| 2E_{\text{TF},0} \exp(-i\omega t) \right|^2 dx} = \\
&= 1 - \frac{t_1'^2 \left[\frac{\left(-1 + \exp\left(\frac{-4\pi D k_1}{\cos(\chi)\lambda_0} \right) \right) \left(1 + r_2^2 \cdot \exp\left(\frac{-4\pi D k_1}{\cos(\chi)\lambda_0} \right) \right) \cos(\chi)\lambda_0}{-4\pi k_1} + \frac{r_2 \exp\left(\frac{-4\pi D k_1}{\cos(\chi)\lambda_0} \right) \sin\left(\frac{-4\pi D n_1}{\cos(\chi)\lambda_0} \right) \cos(\chi)\lambda_0}{-2\pi n_1} \right]}{4D \left[1 - 2r_1 r_2 \exp\left(\frac{-4\pi D k_1}{\cos(\chi)\lambda_0} \right) \cos\left(\frac{-4\pi D n_1}{\cos(\chi)\lambda_0} \right) + r_1^2 r_2^2 \exp\left(\frac{-8\pi D k_1}{\cos(\chi)\lambda_0} \right) \right]}
\end{aligned} \tag{7.15}$$

Substrate (Sub)

Similarly, the coefficient of the emissivity of a possibly semitransparent substrate can be derived using the propagation of waves radiated from each volume element of the substrate. In the most general case this must be taken into account. A system consisting of a thin film which is coated on a semitransparent substrate should be considered as a multilayer structure and must be calculated with a matrix theory approach [74] adapted to emitting volume elements with final integration over the thickness. For this work the substrate can be considered opaque and consequently, interference effects within itself can be neglected.

The energy flux density of the radiation from the substrate is given by:

$$|S_{\text{Sub},0}| \equiv \frac{\bar{n}}{\mu c_0} \left| E_{\text{Sub},0} \exp(-i\omega t) \right|^2 \tag{7.16}$$

After undergoing multiple reflections and refractions within the thin film, this wave shows interference effects as well. The according coefficient of emissivity can be written as:

$$\begin{aligned}
K_{\text{a,Sub}} &= t_1' \exp\left(-i \frac{2\pi(n_1 - ik_1)D}{\cos(\chi)\lambda_0}\right) + t_1' r_1 r_2 \exp\left(-i \frac{6\pi(n_1 - ik_1)D}{\cos(\chi)\lambda_0}\right) + \\
&+ t_1' r_1^2 r_2^2 \exp\left(-i \frac{10\pi(n_1 - ik_1)D}{\cos(\chi)\lambda_0}\right) + \dots = \frac{t_1' \exp\left(-i \frac{2\pi(n_1 - ik_1)D}{\cos(\chi)\lambda_0}\right)}{1 - r_1 r_2 \exp\left(-i \frac{4\pi(n_1 - ik_1)D}{\cos(\chi)\lambda_0}\right)}
\end{aligned} \tag{7.17}$$

Thus, the scaling factor for the emissivity of the substrate is:

$$\begin{aligned}
K_{\varepsilon, \text{Sub}} &= 1 - \frac{\frac{\bar{n}}{\mu c_0} \left| E_{\text{Sub},0} \exp(-i\omega t) \left[K_{a, \text{Sub}} \right] \right|^2}{\frac{\bar{n}}{\mu c_0} \left| E_{\text{Sub},0} \exp(-i\omega t) \right|^2} = \\
&= 1 - \frac{t_1^2 \exp\left(\frac{-4\pi D k_1}{\cos(\chi)\lambda_0}\right)}{1 - 2r_1 r_2 \exp\left(\frac{-4\pi D k_1}{\cos(\chi)\lambda_0}\right) \cos\left(\frac{-4\pi D n_1}{\cos(\chi)\lambda_0}\right) + r_1^2 r_2^2 \exp\left(\frac{-8\pi D k_1}{\cos(\chi)\lambda_0}\right)}
\end{aligned} \tag{7.18}$$

Thin film and substrate

By summation of the two scaling factors of emissivity multiplied with the appropriate radiances, the overall radiance of the sample in the case of a semitransparent coating can be written as:

$$\begin{aligned}
L_{\text{Sample}}(T_{\text{Sample}}) &= L_{\text{TF}}(T_{\text{TF}})K_{\varepsilon, \text{TF}} + L_{\text{Sub}}(T_{\text{Sub}})K_{\varepsilon, \text{Sub}} = \\
&= \varepsilon_{\text{TF}}(\lambda, \vartheta, T_{\text{TF}})L_{\text{Planck}}(T_{\text{TF}})K_{\varepsilon, \text{TF}} + \varepsilon_{\text{Sub}}(\lambda, \vartheta, T_{\text{Sub}})L_{\text{Planck}}(T_{\text{Sub}})K_{\varepsilon, \text{Sub}}
\end{aligned} \tag{7.19}$$

Emissivity of thin film materials

Additionally, to the internal interference effect within the sample the measured spectral radiance will depend on interference effect of the sample with the enclosure. Therefore in the case of a thin film sample all terms in the Equations 6.12, 6.13 and 6.14 must be weighted either with the scaling factor of emissivity or with the reflectivity, which considers multiple reflections within the thin film.

Thus, the Equation 6.12 becomes:

$$\varepsilon_{\text{TF}}(\lambda, \vartheta, T_{\text{TF}}) = \frac{p_{\text{TF}}}{t_{\text{TF}}} \tag{7.20}$$

And the two original coefficients p and t are transformed to:

$$\begin{aligned}
\rho_{TF} = & Q \left(\varepsilon_{BB1}(\lambda, 0^\circ, T_{BB1}) L_{\text{Planck}}(T_{BB1}) - [1 - \varepsilon_{\text{Ch}}(\lambda, 45^\circ, T_{\text{Ch}})] \varepsilon_{\text{BB-LN}_2}(\lambda, 0^\circ, T_{\text{BB-LN}_2}) L_{\text{Planck}}(T_{\text{BB-LN}_2}) - \varepsilon_{\text{Ch}}(\lambda, 45^\circ, T_{\text{Ch}}) L_{\text{Planck}}(T_{\text{Ch}}) \right) + \\
& + \rho_{\text{Ch}}(\lambda, 45^\circ, 45^\circ) \varepsilon_{\text{BB-LN}_2}(\lambda, 0^\circ, T_{\text{BB-LN}_2}) L_{\text{Planck}}(T_{\text{BB-LN}_2}) + \varepsilon_{\text{Ch}}(\lambda, 45^\circ, T_{\text{Ch}}) L_{\text{Planck}}(T_{\text{Ch}}) - \\
& - \varepsilon_{\text{Encl}}(\lambda, 0^\circ, T_{\text{Encl}}) L_{\text{Planck}}(T_{\text{Encl}}) \rho_{\text{TF}} F_{\text{Sample-Encl}} \left[1 + \frac{a_{\text{TF}} + a_{\text{TF}}^2}{1-b} \right] - 4 \varepsilon_{\text{Encl}}(\lambda, T_{\text{Encl}}) L_{\text{Planck}}(T_{\text{Encl}}) \rho_{\text{TF}} F_{\text{Entire encl-Encl}} \left[\rho_{\text{Encl}}(\lambda)/\pi \right] F_{\text{Sample-Encl}} \left[\frac{1+a_{\text{TF}}}{1-b} \right] - \\
& - \varepsilon_{\text{Sample}}(\lambda, T_{\text{Sample}}) L_{\text{Planck}}(T_{\text{Sample}}) \left[\int_0^{\pi/2} K_{\varepsilon, \text{TF}} d\chi \right] F_{\text{Encl-Entire sample}} \left[\rho_{\text{Encl}}(\lambda)/\pi \right] \rho_{\text{TF}} F_{\text{Sample-Encl}} \left[\frac{1+a_{\text{TF}}}{1-b} \right] - \\
& - \varepsilon_{\text{Detector}}(\lambda, 0^\circ, T_{\text{Detector}}) L_{\text{Planck}}(T_{\text{Detector}}) \rho_{\text{TF}} F_{\text{Sample-Det}} - \\
& - \varepsilon_{\text{Sub}}(\lambda, \vartheta, T_{\text{Sub}}) L_{\text{Planck}}(T_{\text{Sub}}) K_{\varepsilon, \text{Sub}} - \varepsilon_{\text{Sub}}(\lambda, T_{\text{Sub}}) L_{\text{Planck}}(T_{\text{Sub}}) \left[\int_0^{\pi/2} K_{\varepsilon, \text{Sub}} d\chi \right] F_{\text{Encl-Entire sample}} \left[\rho_{\text{Encl}}(\lambda)/\pi \right] \rho_{\text{TF}} F_{\text{Sample-Encl}} \left[\frac{1+a_{\text{TF}}}{1-b} \right]
\end{aligned} \tag{7.21}$$

$$\begin{aligned}
t_{\text{TF}} = & L_{\text{Planck}}(T_{\text{Sample}}) K_{\varepsilon, \text{TF}} - \varepsilon_{\text{Encl}}(\lambda, 0^\circ, T_{\text{Encl}}) L_{\text{Planck}}(T_{\text{Encl}}) \rho_{\text{TF}} F_{\text{Sample-Encl}} \left[1 + \frac{a_{\text{TF}} + a_{\text{TF}}^2}{1-b} \right] - \\
& - 4 \varepsilon_{\text{Encl}}(\lambda, T_{\text{Encl}}) L_{\text{Planck}}(T_{\text{Encl}}) \rho_{\text{TF}} F_{\text{Entire encl-Encl}} \left[\rho_{\text{Encl}}(\lambda)/\pi \right] F_{\text{Sample-Encl}} \left[\frac{1+a_{\text{TF}}}{1-b} \right] - \\
& - \varepsilon_{\text{Sample}}(\lambda, T_{\text{Sample}}) L_{\text{Planck}}(T_{\text{Sample}}) \left[\int_0^{\pi/2} K_{\varepsilon, \text{TF}} d\chi \right] F_{\text{Encl-Entire sample}} \left[\rho_{\text{Encl}}(\lambda)/\pi \right] \rho_{\text{TF}} F_{\text{Sample-Encl}} \left[\frac{1+a_{\text{TF}}}{1-b} \right] - \\
& - \varepsilon_{\text{Detector}}(\lambda, 0^\circ, T_{\text{Detector}}) L_{\text{Planck}}(T_{\text{Detector}}) \rho_{\text{TF}} F_{\text{Sample-Det}}
\end{aligned} \tag{7.22}$$

where coefficient a must also be changed accordingly:

$$a_{\text{TF}} = \left[1 - \varepsilon_{\text{Sample}}(\lambda, T_{\text{Sample}}) \right] \left[\int_0^{\pi/2} \rho_{\text{TF}} d\chi \right] F_{\text{Entire sample-Encl}} \left[\rho_{\text{Encl}}(\lambda)/\pi \right] F_{\text{Encl-Entire sample}} \tag{7.23}$$

In the case of a hemispherical spectral emissivity, the scaling factor of emissivity must be integrated over all angles.

These equations allow calculating the emissivity of a thin film sample considering the specific geometrical characteristics of the sample structure and measurement conditions and by this deriving the emissivity ε_{TF} . Thus, using this method, various combinations of different materials for the system “substrate and thin film” can be simulated.

7.4.4 Calculation of optical properties of material

In the Equations 7.8, 7.15 and 7.18 the utilized transmission and reflection coefficients can be calculated according to the electromagnetic theory for the two polarizations, using the properties of materials n and k , as well as the angle of refraction χ (or incidence ϑ , Equation 2.41). Thus the values of the index of refraction and the extinction coefficient must be known. They can be taken from literature or calculated separately. Furthermore, the index of refraction and the extinction coefficient are wavelength dependent which requires a spectral calculation. Examples for the calculation of reflectivity and transmissivity are given in Chapter 2.10.4 and in [17, 19].

7.4.5 Emissivity scaling factor calculation of thin films with systematic variation of material properties

Various spectral courses of the scaling factor of emissivity are calculated as follows to illustrate its dependence on the four parameters n_1 , k_1 , D , and the angle of refraction χ of the investigated thin film. The parameters n_1 , D and χ are the arguments of sine and cosine and thus determine the modulation period. The n_1 and k_1 , being the basis for the calculation of transmission and reflection coefficients, mainly affect the amplitude of modulation. The k_1 , D and χ are arguments of the exponent and are responsible for the reduction or increase of the average value of the scaling factor of emissivity (average value, around which the modulation occurs) as well as the amplitude of modulations.

A dependence on the thickness with the other parameters remaining unchanged is shown in Fig. 7.18. The results coincide with the measured emittances of Aeroglaze Z306 (Fig. 7.13), showing an increase in the amplitude and the period of the modulations for thinner layers.

An increase of k_1 for a specific thickness results in a higher opacity of the film, whereas there is only a slight decrease at the long wavelength (Fig. 7.19). A significant reduction of the absorption coefficient k_1 leads to modulations even in the MIR range.

Changes in the scaling factor of emissivity depending on n_1 are shown in the Fig. 7.20, where this parameter affects both the period of the modulation and the average value of the coefficient.

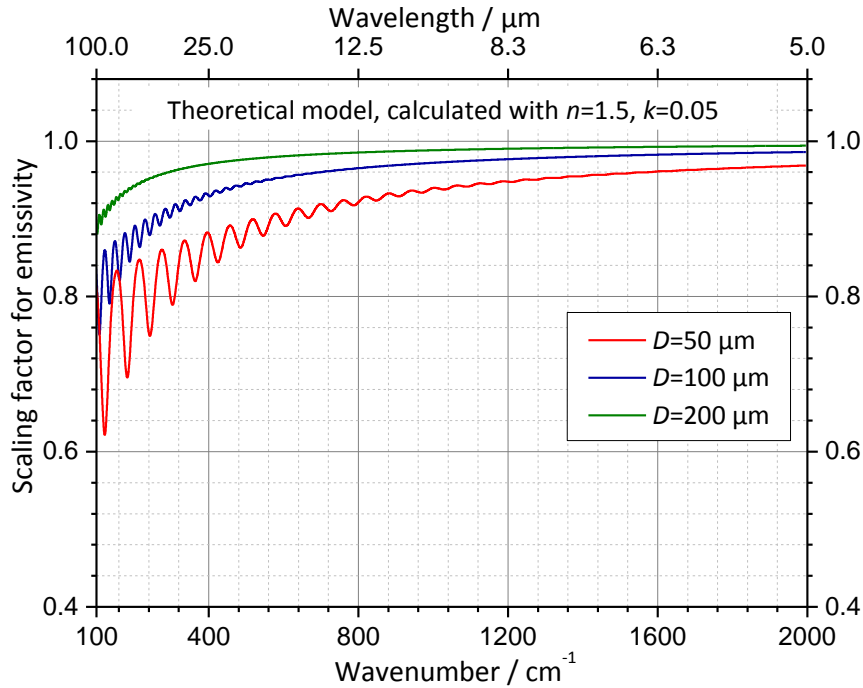


Fig. 7.18: Calculated scaling factors for emissivity of a semitransparent material coated on a high-reflecting substrate. The dependence on three different thicknesses D is shown

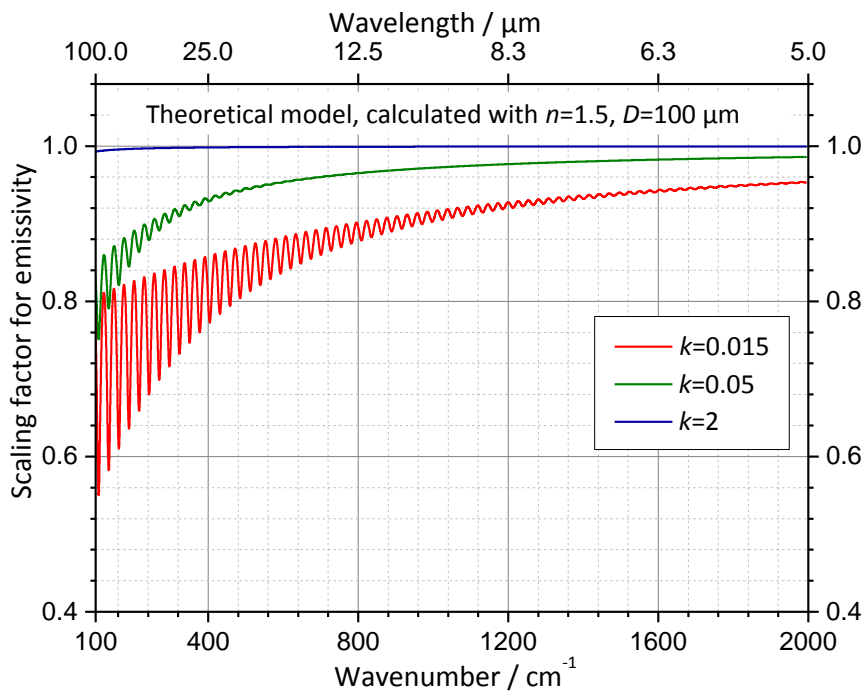


Fig. 7.19: Calculated scaling factor for emissivity of semitransparent material coated on a high-reflecting substrate. The dependence on three different extinction coefficients k is shown.

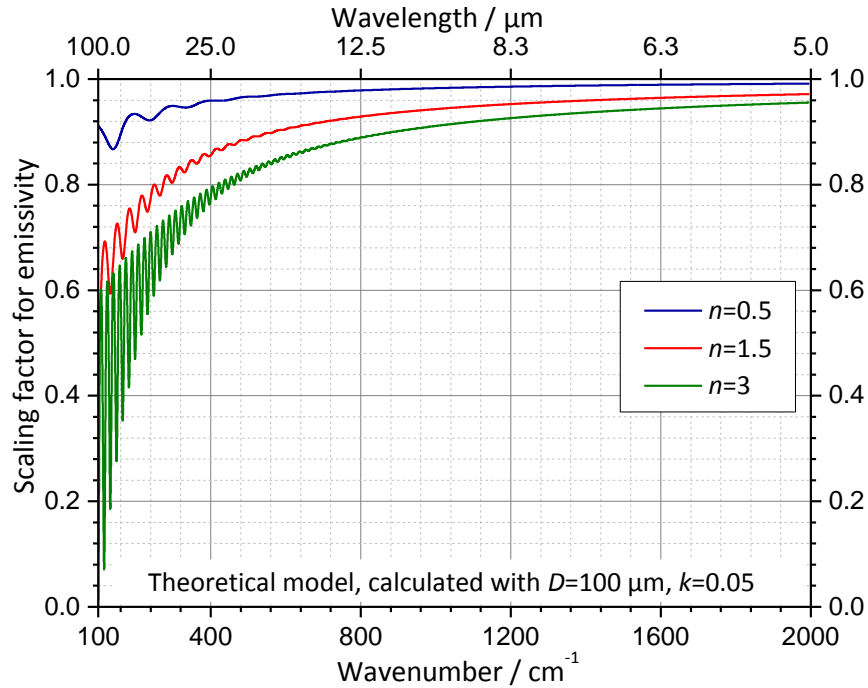


Fig. 7.20: Calculated scaling factor for emissivity of a semitransparent material coated on a high-reflecting substrate. The dependence on three different refractive indexes n is shown

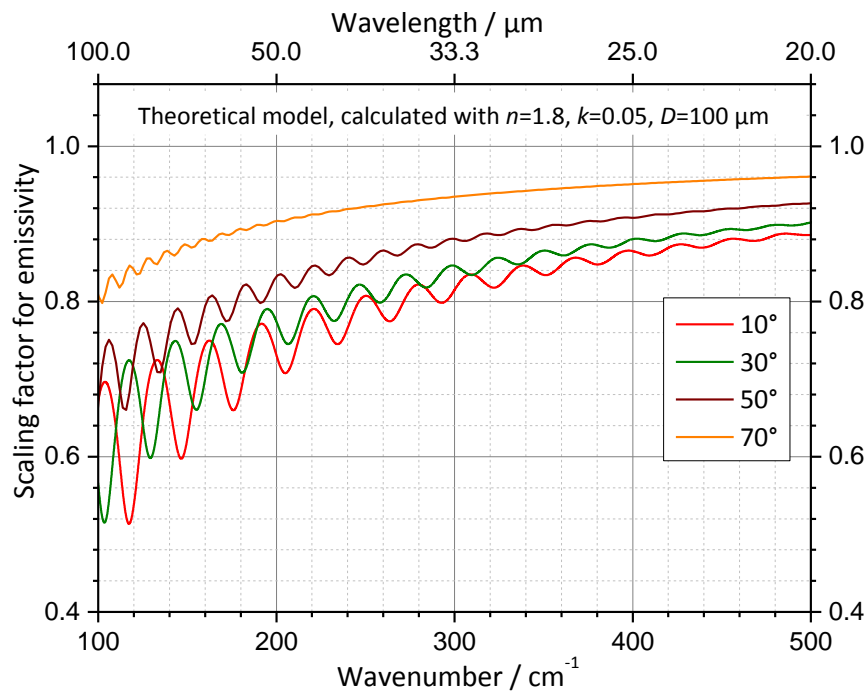


Fig. 7.21: Calculated scaling factors for emissivity of a semitransparent material coated on a high-reflecting substrate. The dependence on different angles of observations ϑ is shown

Finally, the curves at different angles of observation are presented in Fig. 7.21. As seen from the figure, a variation of angle leads not only to a phase difference of the modulation, but

also to a decrease in the amplitude towards larger angles. A noticeable increase in the average level of the coefficient of the angles of 50° and 70° is not a contradiction to the results obtained experimentally (Fig. 7.15). It is necessary to emphasize that the theoretical model represents only the scaling factor of emissivity, while the curves of Aeroglaze Z306 are product of the scaling factor and the emissivity of thin film which, in turn, sharply decreases towards larger angles.

7.4.6 Phase difference between reflectivity and emissivity

Fig. 7.22 illustrates the difference between the spectral reflectivity and the scaling factor of emissivity calculated using the theoretical models according to Equations 7.8 and 7.15, respectively, with identical parameters of n_1 , k_1 and D for both models and the same angle of observation of 10° . The resulting interference, which can be clearly seen, increases toward longer wavelengths, thereby reducing the scaling factor of emissivity and increasing the reflectivity. The amplitude of the reflection modulations is larger than the amplitude of the modulation of the scaling factor of emissivity, and its modulation begins earlier, very similar to the experimentally obtained results (Fig. 7.14). The areas in which the values of curve "1 - reflectivity" lie below the scaling factor of emissivity are also noticeable. These areas can be more or less pronounced for various values of n_1 and k_1 . A phase difference between the reflectivity and the scaling factor of emissivity is also obvious. A variation from the experimental result is that both theoretical models have nearly equal modulation periods, undergoing only slight deviations. The significant difference in modulation periods of the experimental data (Fig. 7.14) can be explained by the optically non-smooth and non-isotropic thin film of the real material. Due to the different fields-of-view of the spectrometer at emissivity and reflectivity measurements, small differences in the average values of n and k are possible, which lead to different results. The integration over all angles, respectively over the whole hemisphere, gives the average value of the scaling factor of emissivity without modulations (Fig. 7.23). For comparison, the corresponding curve of the hemispherical spectral emittance obtained from measurements of Aeroglaze Z306 is shown. This is an important result in understanding the limits of the application of Kirchhoff's law for semitransparent thin films. Due to interference effects, it cannot be applied to the directional spectral emissivity for discrete angles of observation, but has to be restricted to the hemispherical emissivity.

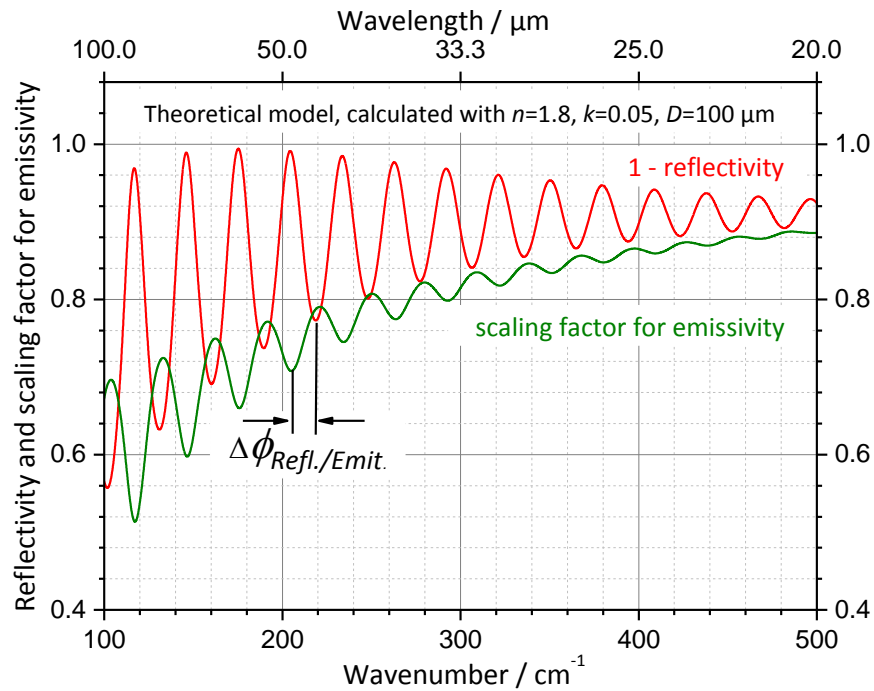


Fig. 7.22: Calculated reflectivity (shown as “1 - reflectivity”) and scaling factor of emissivity of a semitransparent material with wave interference effect using the same parameters

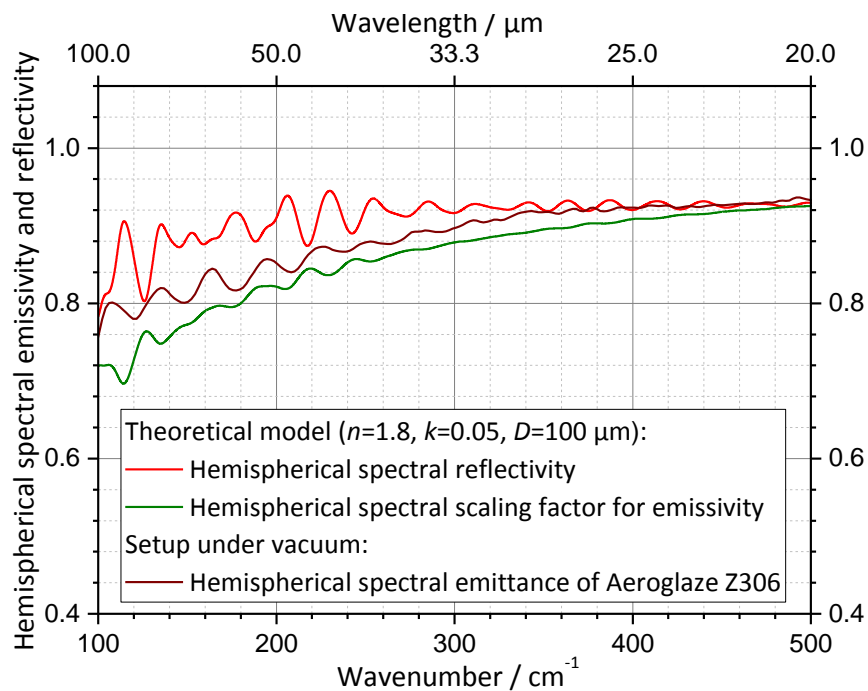


Fig. 7.23: Calculated hemispherical spectral reflectivity and scaling factor of emissivity of a semitransparent material with wave interference effect using the same parameters. The experimentally determined hemispherical spectral emittance of Aeroglaze Z306 is shown for comparison

It must be emphasized that the main objective of this section was not to achieve a perfect agreement between theory and experiment with perfectly adapted coefficients. Rather, the general behavior of the emissivity and reflectivity of thin films is discussed here. It shows, when the calculation of directional spectral reflectivity and emissivity is performed with the same parameters, that a “non-synchronous” onset of the modulation with different amplitudes and periods, phase differences and overlapping areas of two curves can occur. It should also be noted that the green curve shown in Fig. 7.22 represents only the scaling factor of emissivity, which characterizes the changes in emissivity of thin film material. The latter is usually less than 1 and can have a temperature dependence, so the entire curve can also show a slope downward to longer wavelengths, which might eliminate the “crossing-problem” in some areas with the “1 - reflectivity” curve (or not as for Aeroglaze Z306). However, even in this case, the phase difference and different amplitudes and periods of modulations do not allow the application of Kirchhoff’s law correctly.

7.4.7 Validation of Kirchhoff’s law and conclusion

These equations allow calculating the emissivity of a thin film sample considering the specific geometrical characteristics of the sample structure and measurement conditions and by this deriving the emissivity ε_{TF} . Thus, using this method, various combinations of different materials for the system “substrate and thin film” can be simulated.

The analytical procedure proposed in this chapter takes into account the interference effect within the thin film and allows calculating the emissivity of each volume element of the material, considering the specific geometrical characteristics of the sample structure and measurement conditions. It may be necessary in two cases: if it is important to know the characteristics of a “pure” material or if the desired thickness of the coating or the type of material, on which this coating must be applied, are not known beforehand. When these values are obtained, it allows the simulation of various combinations of materials to obtain the desired characteristics.

Certainly, the use of the direct theoretical method has some difficulties, such as the required knowledge of the optical properties of the investigated material. The necessary highly accurate data of the index of refraction and extinction coefficients cannot always be obtained from literature or calculated separately. A spectral dependence of these coefficients in real materials can only be obtained approximately. Furthermore they can be temperature dependent. Another difficulty is the inhomogeneity of real materials, which has been already mentioned above by the comparison of experimental data with the theoretical models. The possible variations of the parameters within the field-of-view of the detector can lead to

changes in the average values of scaling factor and hence, to a change in the structure of the modulation. However, this theory leads to an important conclusion concerning the limitation of Kirchhoff's law for thin films. Different mechanisms of interference by emissivity and reflectivity (and hence absorptivity) can result in variant distribution of the energy flux density carried by the waves within the same optical parameters. On the other hand, according to the law of conservation of energy and theoretical results, the integrated values of emissivity and reflectivity reaffirm Kirchhoff's law (in this case over all angles, Fig. 7.23). Furthermore, by the example of Aeroglaze Z306 we have seen that in the first wavelength range some coatings can remain opaque and be in accordance with Kirchhoff's law but in the semitransparent spectral range of the sample the calculation must be performed based on another principle. Thus, the developed theory leads to the following conclusion concerning the relation between the reflectivity and emissivity of semitransparent thin films: if all of the other parameters, such as the field-of-view of the detector, complex refractive index and thickness are equal, and there is not any temperature dependences of optical properties, the limitation of Kirchhoff's law applies only to the directional quantities of an optically thin material. In this case the indirect calculation of the directional emissivity from the reflectivity is not applicable (Fig. 7.14).

8 In-flight blackbody calibration system of the GLORIA Interferometer

One of the main tasks of research described in this work is the characterization of onboard reference blackbodies for remote sensing missions. These studies are widely used in the European Metrology Research Program (EMRP) MetEOC [85] and MetEOC2 [86]. The project has several considerable aims, however, the main focus is to improve the accuracy and traceability of Earth observation measurements. The measurements are performed with an airborne imaging Fourier Transform Spectrometer GLORIA (Gimballed Limb Observer for Radiance Imaging of the Atmosphere), which has been developed to gain detailed infrared measurements of the Upper Troposphere/Lower Stratosphere (UTLS) region with a three-dimensional resolution. GLORIA has a two-dimensional detector array for observation of atmospheric temperature, trace gas distribution, and aerosols and clouds which is described in detail in [87].

The highly demanding uncertainty requirements and the needed traceability of the measurements to the International Temperature Scale lead to the requirement of an on-board calibration system. It consists of two identical infrared radiators with a large area and high emissivity [88]. During the flight these two GLORIA BlackBodies are operated at two adjustable reference temperatures in a range from $-50\text{ }^{\circ}\text{C}$ to $0\text{ }^{\circ}\text{C}$ (GLORIA Blackbody “Cold” (GBB-C) and GLORIA Blackbody “Hot” (GBB-H), respectively). The regularly repeated observation by the spectrometer is part of the measurement sequence and so the spectrometer is calibrated between the atmospheric measurements.

The development, design, improvement and calibration of the GBBs are a joint work of the Physics Department of the University of Wuppertal, the Karlsruhe Institute of Technology, the Research Centre Juelich and the PTB. The PTB performs the radiometric and thermometric calibration and characterization with a standard uncertainty of less than 100 mK. During the calibration the GBBs are compared with the VLTBB, which is the calibration standard of spectral radiance and radiation temperature, described in detail for this temperature range in Chapter 5. The comparison was performed via VIRST (Chapter 4.4) and via the vacuum FTIR-spectrometer under two conditions: dry nitrogen with a pressure of 100 hPa and high vacuum. The metrological and technical requirements of the GBBs are described in [88]. In the next chapter the dominant design features as well as the spectral and lateral characterization of the emissivity of the two onboard reference blackbodies of the GLORIA instrument will be presented as a primary application of the RBCF in the projects MetEOC and MetEOC2 founded within the European Metrology Research Program.

8.1 GLORIA Blackbodies

Three types of pyramids with different square-shaped bases and different heights, are mounted on the optical surface of a 126 mm x 126 mm cavity (see Fig. 8.1). The array of pyramids, each 7 mm x 7 mm, are used to avoid direct reflections as well as to increase the effective emissivity of the cavity. The pyramids as well as the entire cavity are coated with Nextel Velvet Black 811-21. Each GBB has 16 PRTs for temperature monitoring. Eight PRTs are used for individual temperature control in four sectors: four PRTs located close to the apex of pyramids and four PRTs close to the base of the pyramids. These four chosen pyramids are located in each of the corners of optical surface (see Fig. 8.1). Additionally, the fifth pyramid in the center also has two sensors for temperature monitoring. The Thermo-Electric Coolers provide the required cooling or heating of the GBBs, depending on the necessary operation temperature.

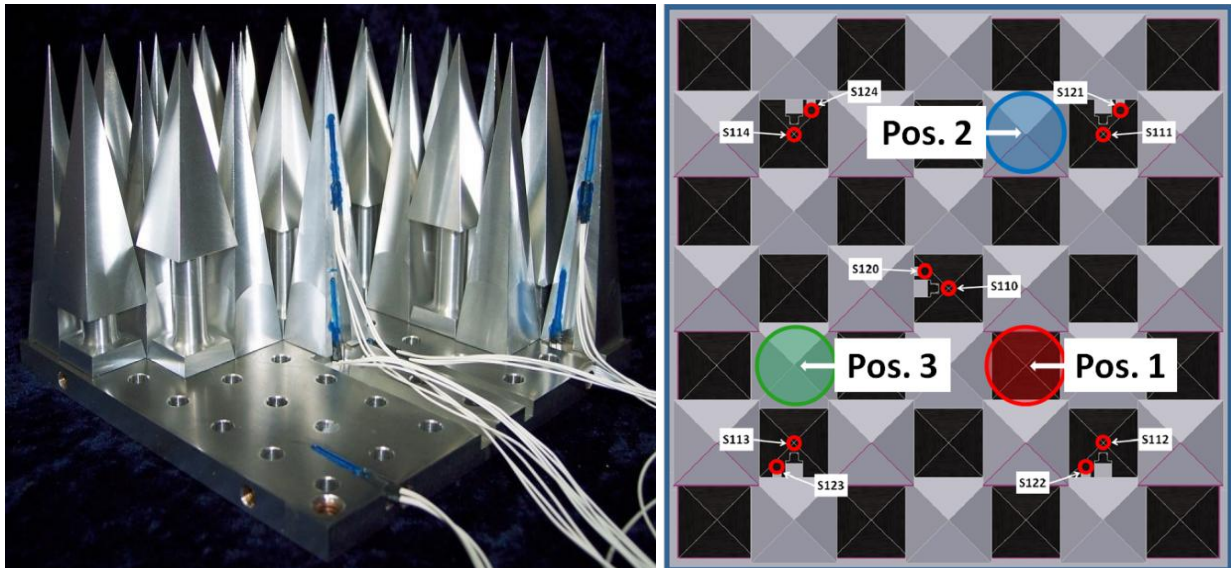


Fig. 8.1: Left: Optical surface of GBBs with partially assembled pyramid field; Right: Schematic representation of radiating optical surface of a GLORIA blackbody with 49 pyramids and 10 PRTs. The circles show the field-of-view of the FTIR-spectrometer at three positions [88]

As discussed above, the additional place in the source chamber of the RBCF is intended not only for the vacuum sample-holder for emissivity measurements, but also for any source to calibrate or to characterize. The source chamber with the installed GLORIA Blackbody for calibration is shown opened in Fig. 8.2. The accurate positioning and measurement of any point of an emitting surface is carried out by using an additional vertical translation stage.

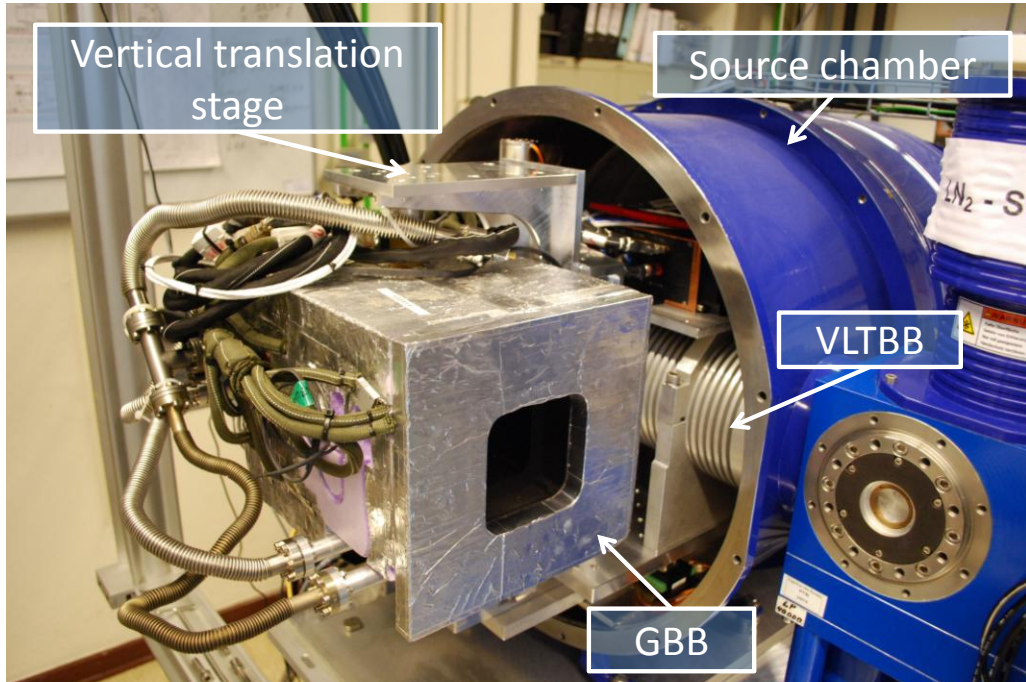


Fig. 8.2: View of the opened source chamber with installed GLORIA Blackbody for calibration. The reference blackbodies of the RBCF, the VLBB and the LN₂-cooled blackbody, can also be seen

Table 8.1: Radiation temperature of 10 positions which correspond to the location of the temperature sensors within the pyramid, measured with VIRST with a combined uncertainty of ($k=2$). Additionally, the respective resistances of the PRTs

Position	$t_s(90)$ GBB-C, °C	R (position), Ohm	U , K
S110	-30.107	88.072	0.086
S120	-30.108	88.139	0.085
S111	-30.101	88.099	0.085
S121	-30.063	88.276	0.086
S112	-30.027	88.090	0.085
S122	-29.986	88.206	0.087
S113	-30.124	88.128	0.085
S123	-30.094	88.216	0.085
S114	-29.957	88.190	0.085
S124	-29.845	88.333	0.085

The measurements of the radiation temperature and the calibration of the PRTs of the GBBs were performed via VIRST from -50 °C to 0 °C in temperature steps of 5 °C. One result measured at -30 °C at 10 positions which correspond to the location of temperature sensors in the pyramid field (see Fig. 8.1) is provided in Table 8.1. Using values of resistance of the PRTs, these measurements allow a calibration of the radiation temperature-resistance relation of the GBBs. Other results can be found in [70].

Because VIRST is a radiation thermometer, it provides the integrated value in the wavelength range from 8 μm to 14 μm which is not sufficient for a complete characterization of the GBBs. Spectrally resolved measurements of the radiation temperature as well as an estimate of the emissivity values of the GBBs are required. These measurements have been performed with the vacuum FTIR-spectrometer in the wavelength range from 7 μm to 16 μm and in the field-of-view of 18 mm.

8.2 Spectral radiance of GBBs

The spectrally resolved radiation temperatures of both GBBs were measured according to the measurement scheme presented in Chapter 5.2.5, in which the VLTBB and the VMTBB were compared. Three positions on the optical surface were chosen to observe three different types of pyramids (see Fig. 8.1). Thus, the field-of-view of the vacuum FTIR-spectrometer was sequentially placed at these three positions and the obtained signals were compared to the reference blackbody VLTBB. Depending on the temperatures and the signal level, the sequence of measurement was repeated between 6 and 10 times for each position. Using Equation 5.18, but solving for GBB-H or GBB-C, the spectral radiance $L_{\text{GBB}}(T_{\text{GBB}})$ can be calculated:

$$L_{\text{GBB}}(T) = \frac{(\tilde{L}_{\text{GBB}}(T_{\text{GBB}}) - \tilde{L}_{\text{BB-LN}_2}(T_{\text{BB-LN}_2})) (L_{\text{VLTBB}}(T_{\text{VLTBB}}) - [1 - \varepsilon_{\text{Ch}}(\lambda, 45^\circ, T_{\text{Ch}})] \varepsilon_{\text{BB-LN}_2}(\lambda, 0^\circ, T_{\text{BB-LN}_2}) L_{\text{Planck}}(T_{\text{BB-LN}_2}) - \varepsilon_{\text{Ch}}(\lambda, 45^\circ, T_{\text{Ch}}) L_{\text{Planck}}(T_{\text{Ch}})}{(\tilde{L}_{\text{VLTBB}}(T) - \tilde{L}_{\text{BB-LN}_2}(T_{\text{BB-LN}_2}))} + \varepsilon_{\text{Ch}}(\lambda, 45^\circ, T_{\text{Ch}}) L_{\text{Planck}}(T_{\text{Ch}}) + [1 - \varepsilon_{\text{Ch}}(\lambda, 45^\circ, T_{\text{Ch}})] \varepsilon_{\text{BB-LN}_2}(\lambda, 0^\circ, T_{\text{BB-LN}_2}) L_{\text{Planck}}(T_{\text{BB-LN}_2}) \quad (8.1)$$

where $\tilde{L}_{\text{GBB}}(T_{\text{GBB}})$ is the measured signal of GBB-H or GBB-C. The corresponding radiation temperature can be found by applying the inverted form of Planck's law.

Table 8.2: Experimental parameters for the measurement of the GBB-H or GBB-C

GBBs	GBB-C	GBB-C	GBB-H	GBB-H
Wavelength range	7.1 μm to 16 μm			
Wavenumber range	1400 cm^{-1} to 625 cm^{-1}			
Detector and beamsplitter	MCT, KBr			
Field-of-view (diameter)	18 mm			
Blackbody	VLTBB, 0.0 $^\circ\text{C}$	VLTBB, -30.0 $^\circ\text{C}$	VLTBB, 0.0 $^\circ\text{C}$	VLTBB, -30.0 $^\circ\text{C}$
LN ₂ -blackbody	-193.4 $^\circ\text{C}$			
GBBs	0.0 $^\circ\text{C}$	-30.0 $^\circ\text{C}$	0.0 $^\circ\text{C}$	-30.0 $^\circ\text{C}$
Spectrometer	27.2 $^\circ\text{C}$			

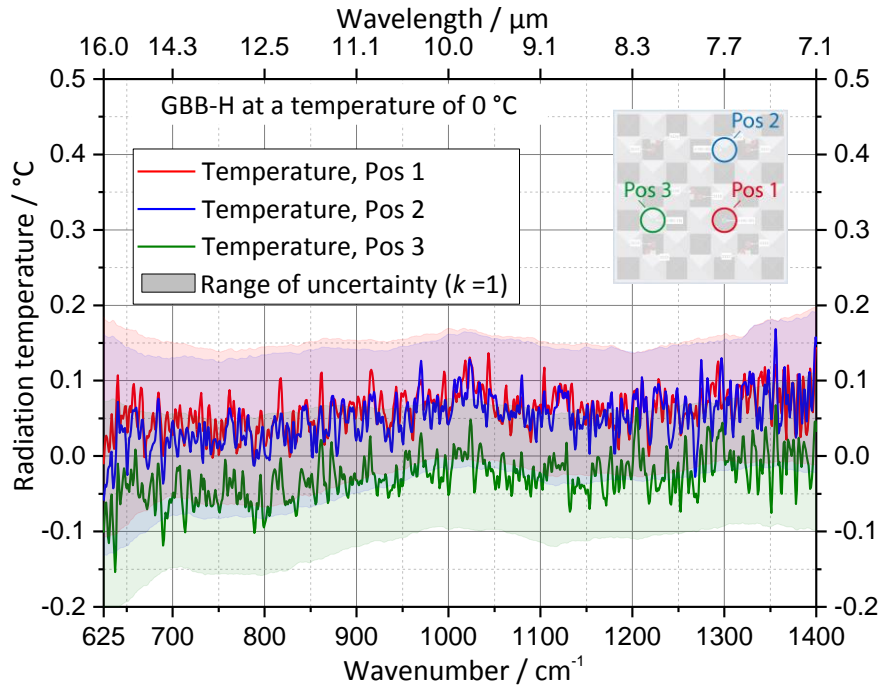


Fig. 8.3: The spectrally resolved radiation temperature of the GBB-H measured at a temperature of 0 °C at three positions on the optical surface (circles in the inset). The measurement was performed with the vacuum FTIR-spectrometer, the ranges of uncertainty are shown as shaded areas

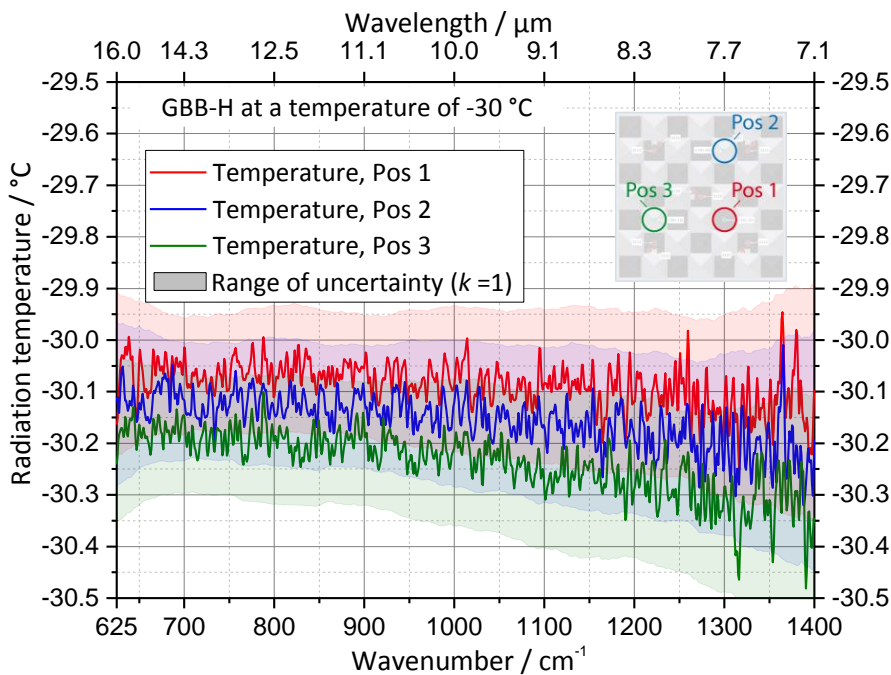


Fig. 8.4: The spectrally resolved radiation temperature of the GBB-H measured at a temperature of -30 °C at three positions on the optical surface (circles in the inset). The measurement was performed with the vacuum FTIR-spectrometer, the ranges of uncertainty are shown as shaded areas

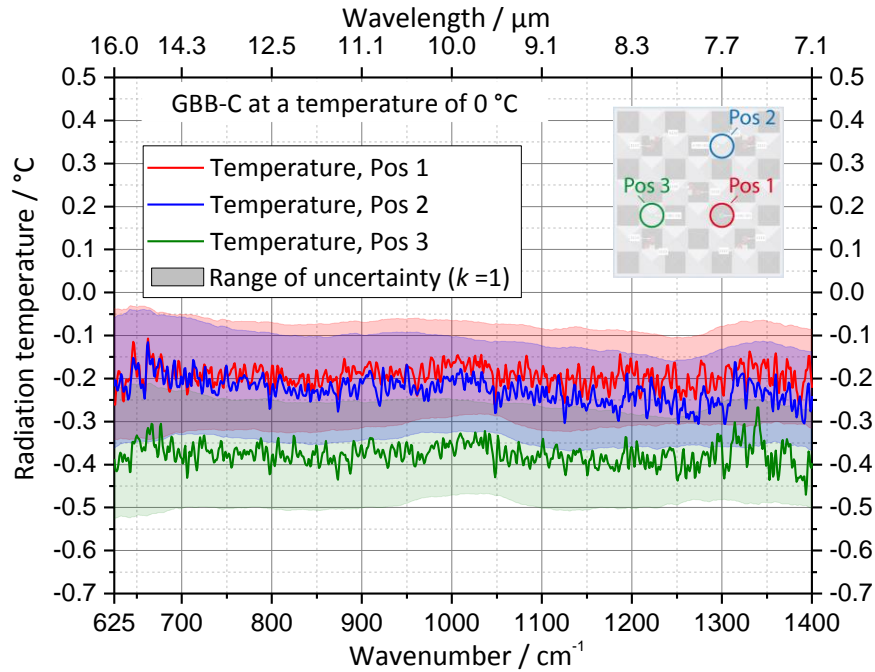


Fig. 8.5: The spectrally resolved radiation temperature of the GBB-C measured at a temperature of 0 °C at three positions on the optical surface (circles in the inset). The measurement was performed with the vacuum FTIR-spectrometer, the ranges of uncertainty are shown as shaded areas

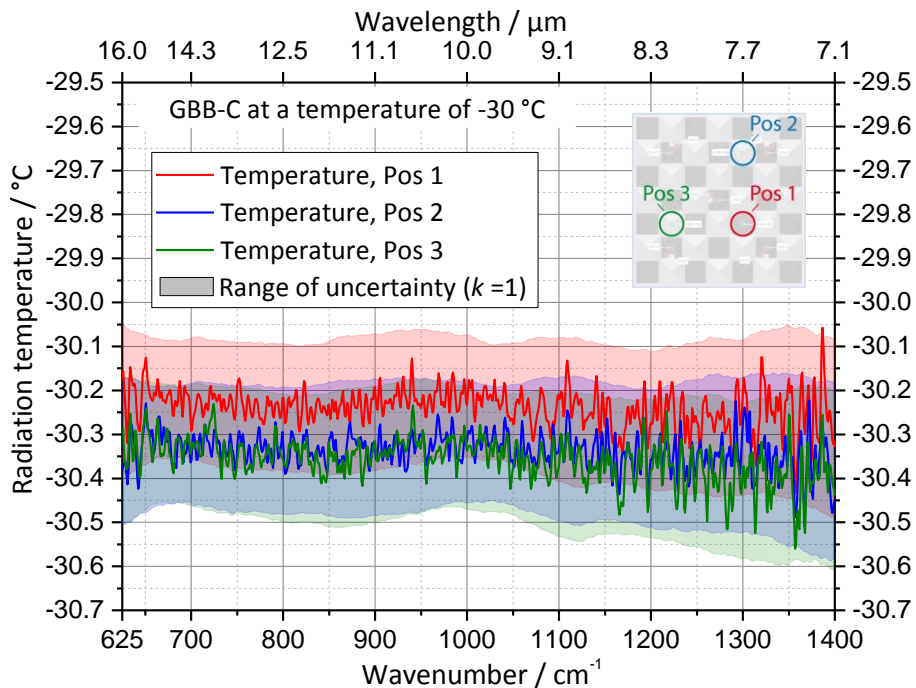


Fig. 8.6: The spectrally resolved radiation temperature of the GBB-C measured at a temperature of -30 °C at three positions on the optical surface (circles in the inset). The measurement was performed with the vacuum FTIR-spectrometer, the ranges of uncertainty are shown as shaded areas

The measurements under vacuum were performed for the GBB-C and GBB-H at two temperatures of $-30\text{ }^{\circ}\text{C}$ and $0\text{ }^{\circ}\text{C}$ by using a combination of the MCT detector and the KBr beamsplitter (Table 8.2). The results are shown in Figures 8.3-8.6. The spectrally resolved radiation temperature is separately plotted for each of the three positions (circles in the inset) with the range of the combined uncertainty ($k=1$) given as semitransparent areas. The results exhibit no significant change in the measured radiation temperatures in the wavelength range of $7\text{ }\mu\text{m}$ to $16\text{ }\mu\text{m}$. The differences in radiation temperature of the three pyramids are also not significant and are equal within the range of combined uncertainty.

The spectrally resolved uncertainty of the radiation temperatures is calculated from four contributions for each of the three positions. The temperature stability of the GBBs results from the readings of the PRTs located at the 18 mm diameter field-of-view shown as circles in the inset of the figures. The homogeneity of the radiation temperature within each of these three areas is calculated from the measurement performed by the scanning of the GBBs with VIRST. The optical surface of both GBBs was measured at the two above-mentioned temperatures with 9 mm step size in two dimensions. The third contribution to the uncertainty budget is the uncertainty of VLTBB, which was considered in detail in Chapter 5.2.4. Finally, the type A uncertainty of the spectrometer measurements results from the repetitive sequences of measurements.

8.3 Emittance of GBBs

Because the temperature of the optical surface is determined by the PRTs, which were calibrated via VIRST in terms of radiation temperature, a direct calculation of the emissivity is not possible. However, for the complete characterization of a blackbody an evaluation of the emissivity is required, as the resulting radiation temperature depends on it. Based on the knowledge that the emittance of Nextel in the desired wavelength range is spectrally nearly constant (see Fig. 7.1) and on the experience of Monte-Carlo calculations of the effective emissivity for such a cavity, which didn't induce any spectral features, a spectrally constant value of the effective emissivity of the cavity from $7\text{ }\mu\text{m}$ to $16\text{ }\mu\text{m}$ can be safely assumed. Substituting three spectrally constant values of the effective emissivity - 1.000, 0.999 and 0.995 - into the calculation of the radiation temperature from the measured spectral radiance via the inverted form of Planck's law, three different spectral distributions of the radiation temperature were obtained (see Fig. 8.7). The calculated radiation temperatures are represented in this figure by the individual points for each wavelength. Furthermore, lines linearly fitted to the three-point clouds are shown. These lines are characterized by significantly different slopes. The spectral distribution of radiation temperatures obtained with the smallest value of 0.995 show the strongest decrease towards longer wavelengths. This

decrease can be caused only by an inhomogeneity of the surface temperature in the observed area (a circle with 18 mm diameter corresponding to the position 1), as the possibility of a spectral change in the effective emissivity by other reasons was excluded. To investigate the temperature homogeneity in the observed area, two-dimensional scans across the optical surface of both GBBs were made using VIRST on a 6 x 6 grid with 4 mm step size, which showed a homogeneity of better than 23 mK (max.-min.) over the diameter of the field-of-view of the spectrometer (Fig. 8.8).

In order to obtain the spectral slopes in radiation temperature shown in Fig. 8.7, the hypothetical temperature inhomogeneity within the field-of-view is required and can be estimated by the following approach: the field-of-view is divided into a grid of four parts. Each part has a different temperature yielding via Planck's law and four different radiances. The mean of these radiances is then calculated and the corresponding radiation temperature is evaluated by the inverted form of Planck's law. To obtain a slope corresponding to the curve calculated for the effective emittance of 0.995, an inhomogeneity of about 12 K (max.-min.) was required, which is much higher than the experimentally found inhomogeneity. Similarly, it can be calculated that the slope of the yellow curve calculated for an assumed emittance of 0.999 would correspond to an inhomogeneity of about 3 K (max.-min.) which also does not correspond to the experimentally found inhomogeneity. Thus, based upon these results, it can be concluded that the value of effective emittance of the GGBs is greater than 0.999.

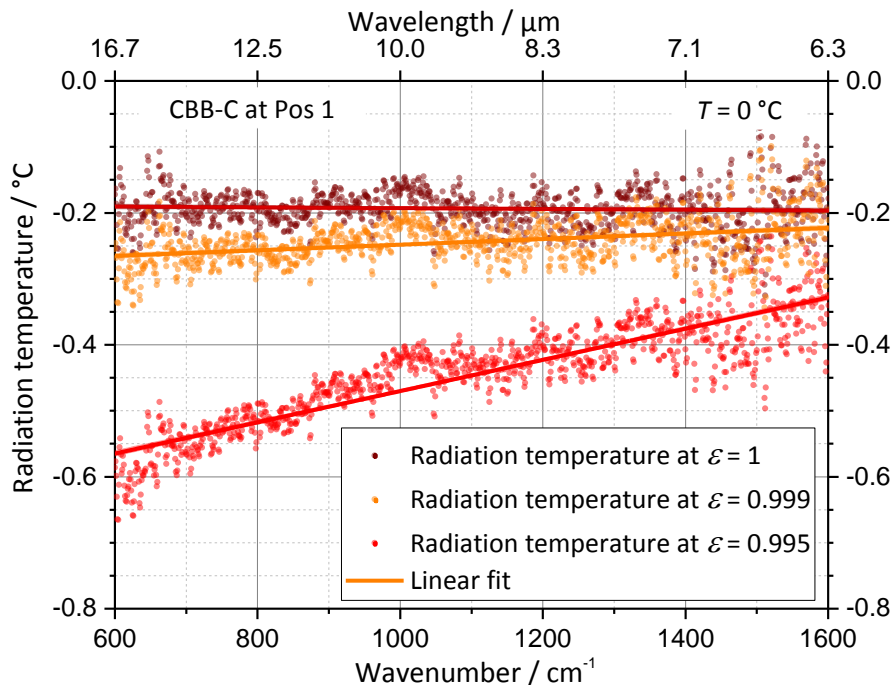


Fig. 8.7: Spectral distribution of radiation temperature for varying emissivities

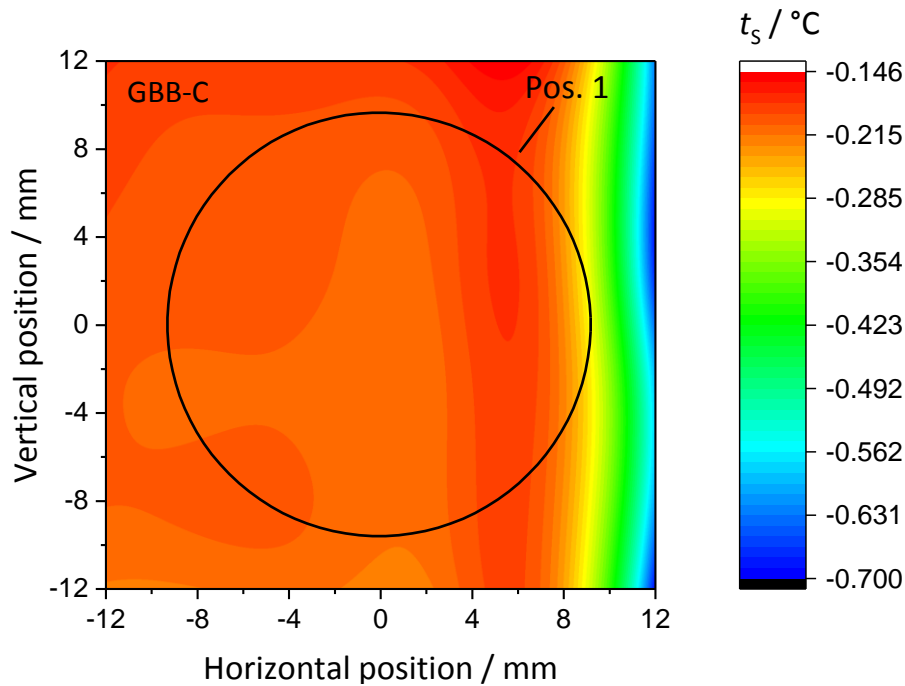


Fig. 8.8: The spatial distribution of the radiation temperature of the GLORIA blackbody GBB-C at a nominal temperature of 0 °C and at the position 1. The field-of-view of spectrometer is shown (circle of diameter of 18 mm). The homogeneity is better than 23 mK (max.-min.)

Thus, the measurement campaigns at the RBCF before and after the flights of the GLORIA instrument provided a radiometric and thermometric calibration of the in-flight calibration system with a low radiometric uncertainty of 100 mK of the GBB reference blackbodies. By investigation of the stability and the calibration of the PRTs, by determining the radiation temperature homogeneity over the full optical surface by the measurement of the spectral radiation temperatures and by the estimation of effective emissivity, a complete characterization of the GBBs is provided and the link of the GLORIA measurements to the ITS-90 is provided and therefore, the traceability of its atmospheric measurements established. This is a very important metrological contribution to remote sensing experiments which hopefully improves the derived climate models and the understanding of the climate of the Earth.

9 Conclusion

The successful realization and validation of a highly accurate method and facility to measure directional spectral, directional total and hemispherical total emissivities under vacuum has been accomplished and presented in this work. The major achievements obtained within this work are the unexampled low uncertainty according to the Guide to Uncertainty of Measurement (GUM) and the operation in unique-broad wavelengths and temperature ranges from 4 μm to 100 μm and from -40 $^{\circ}\text{C}$ to 600 $^{\circ}\text{C}$. Using the direct radiometric method based on the comparison of the spectral radiance of the sample that is located inside of the spherical enclosure, with the two radiation standards- the reference vacuum blackbodies, the measurements are traceable to the International Temperature Scale of 1990 (ITS-90). The method and evaluation scheme developed and described in this work enable the measurement of the radiation properties of a wide range of materials: high and low absorbing samples, various types of coating on different substrates (paints, varnishes, sputtered thin films), a variety of bulk materials- metals, polymers, homogenous, inhomogeneous (i.e. rock) and optical thin films. This capability was illustrated through the investigation of a wide selection of samples. Moreover, the RBCF, being a unique facility within Europe in terms of its versatility and achievable uncertainty, allows performing measurements under vacuum at different pressures as well as under various gases (argon, helium, nitrogen).

The results achieved in this work are validated by a comparison with the two currently established methods providing the validation of measurement. These include full agreement within the ranges of standard uncertainties shown in comparison with the setup for emissivity measurements in air at PTB, successfully aligning with international comparisons to other national metrology institutes, and the comparison with the indirect determination of emissivity (1-reflectivity).

The measurement of directional, spectral and total emissivities for various technological applications can now be offered by PTB using this new facility- the RBCF, which allows to characterize sources under potentially difficult operating conditions. Reference blackbodies for air and space-borne remote sensing missions to study the earth's climate changes can be traceable and characterized with low uncertainties. The proposed evaluation scheme in this work, based on the precisely evaluated radiation balance considering background radiation and drifts, and the high-metrological characterization of the reference blackbodies, has been successfully applied in the European Metrology Research Program (EMRP) MetEOC and MetEOC2. It provided the traceability of the atmospheric measurements of the GLORIA

instrument to the ITS-90 and thereby to an absolute temperature and radiance scale with an uncertainty of less than 100 mK.

The characterization of the vacuum reference blackbodies, which are the essential elements to achieve the required uncertainty and provide the traceability of the measurements, is an important achievement of this work. The successful calculation of the effective emissivity of the reference blackbodies, based on the Monte-Carlo ray-tracing simulations using the emissivity modeling program STEEP3, as well as the compilation of the uncertainty budget are presented in detail.

The development and design of a dedicated vacuum sample holder for emissivity measurements as well as its metrological characterization was the following advancement accomplished in this work. The suitability of its coatings for low temperatures, vacuum conditions and a wavelength range from 4 μm to 100 μm has been verified. The temperature regulation of the sample holder and the enclosure have been adapted and optimized for vacuum conditions.

The general layout and technical description of the several major units of the experimental facility, the vacuum reference blackbodies and the FTIR-spectrometer in particular, are presented with their relevant characteristics. The performance investigation of the FTIR-spectrometer with different sets of detectors (MCT, DLaTGS and Si-composite bolometer) in a wavelength range from 4 μm to 100 μm down to a radiance temperature of $-100\text{ }^\circ\text{C}$ is described.

The developed method and the corresponding software is presented here for the calculation of the emissivity of a sample that is located inside of a temperature-stabilized enclosure with respect to the spectral radiances of the two reference blackbodies at different temperatures. The uncertainty of the emissivity measurements of low-emitting samples can be significantly improved by taking into account multiple reflections between the sample and the enclosure. Eventually, the overall uncertainty budget of the emissivity measurements at RBCF based on the GUM has been compiled and is also discussed in detail.

Examples for emissivity measurements of various materials to illustrate the capability of the facility show the achieved standard uncertainty ($k=1$). It varies from 0.005 or better for samples with high emissivities (black paints Nextel and Aeroglaze Z306 or SiC), better than 0.011 for the low-emitting materials (Gold) and better than 0.025 for measurements of temperatures as low as $-40\text{ }^\circ\text{C}$. It should be noted that the uncertainty of emissivity measurements at the RBCF depends on, among other factors, the temperature of the sample, the type of the detector, the wavelength range and measuring time, and can widely vary depending on these experimental conditions.

The highly accurate metrological characterization of the facility as well as other achievements in this work allow measurements to be performed in very demanding applications. An important example which requires very low uncertainties of measured emissivities is the characterization of absorbers for high-temperature solar thermal energy generation that is close to the operation conditions. The thermal emissivity of absorber coatings, one of the key parameters for the determination of the efficiency of solar thermal systems, is very low in the MIR range, about 0.01 to 0.02. It can be measured at the RBCF with a standard uncertainty of less than 0.005 at a temperature of 600 °C. This improves the accuracy of the available data by a factor of 10, and will allow a systematic improvement of the efficiency of high temperature solar thermal absorbers in the future.

Particular attention is paid to the new method of calculation of emissivity of semitransparent coatings with the consideration of interference effects within the thin film coating. The new analytical procedure is based on the classical thin film model with reflection and refraction of electromagnetic waves. This model was extended by the consideration of the different sources of radiation and the resulting interference schemes for emissivity and reflectivity measurements. It explains in detail the observed phase difference between the directional spectral emissivity and reflectivity measurements of the semitransparent samples. This leads to an important limitation of the applicability of Kirchhoff's law for directional quantities of optically thin materials and of the use of the indirect emissivity calculation from a "1 - reflectivity" measurement in wavelength ranges where the material is semitransparent. In addition, this new method allows the simulation and calculation of the radiation properties of various combinations of composite materials - thin film and substrate - based on the knowledge of the individual optical constants.

Because of its modular and flexible concept and design, the RBCF has great potential of expansion and adaption to future applications and calibration and measurement tasks. As an example, with only a slightly different design of the sample holder and by using the developed evaluation and measurement scheme, the operating temperature range can be extended from -100 °C to 1000 °C. Furthermore, there is the capability to expand the wavelength range to the NIR and to the FIR ranges using suitable detectors and an additional high-temperature blackbody. The development of the facility is ongoing and for the near future the design of a new sample holder for semitransparent bulk materials is planned as well as a further extension of the evaluation procedure for samples that show a large amount of internal scattering. A new source chamber of the RBCF, having more space for various and larger radiation sources, will also be developed in the next years at PTB. Based on experience and knowledge as well as the major achievements and conclusions obtained within this work, more opportunities to

meet challenges posed by modern industrial and remote sensing applications will be made available to radiation thermometry.

References

- [1] **Verein Deutscher Ingenieure**. Richtlinienreihe VDI/VDE 3511 "Technische Temperaturmessung". [Online] https://www.vdi.de/uploads/tx_vdirili/pdf/1566953.pdf, 2010.
- [2] **L. Bartelmeß, C. Monte, A. Adibekyan, O. Sohr, C. Ottermann, T. Korb and J. Hollandt**. Characterization of high temperature solar thermal selective absorber coatings at operation temperature. *Energy Procedia*. 2014, 49, pp. 2070-2079.
- [3] **M. Riese, F. Ploeger, A. Rap, B. Vogel, P. Konopka, M. Dameris and P. Foster**. Impact of uncertainties in atmospheric mixing on simulated UTLS composition and related radiative effects. *J. Geophys. Res.-Atmos.* 2012, Vol. 117, D16305.
- [4] **S. Solomon, K. Rosenlof, R. Portmann, J. Daniel, S. Davis, T. Sanford and G.-K. Plattner**. Contributions of Stratospheric Water Vapor to Decadal Changes in the Rate of Global Warming. *Science*. 2010, Vol. 327, pp. 1219–1223.
- [5] **M. Riese, H. Oelhaf, P. Preusse, J. Blank, M. Ern, F. Friedl-Vallon, H. Fischer, T. Guggenmoser, M. Höpfner, P. Hoor, M. Kaufmann, J. Orphal, F. Plöger, R. Spang, O. Suminska-Ebersoldt, J. Ungermann, B. Vogel and W. Woiwode**. Gimballed Limb Observer for Radiance Imaging of the Atmosphere (GLORIA) scientific objectives. *Atmos. Meas. Tech.* 2014, Vol. 7, pp. 1915-1928.
- [6] **C. Monte, B. Gutschwager, A. Adibekyan and J. Hollandt**. A Terahertz Blackbody Radiation Standard Based on Emissivity Measurements and a Monte-Carlo Simulation. *Journal of Infrared, Millimeter, and Terahertz Waves*. 2014, Vol. 35, Issue 8, pp. 649-658.
- [7] **Joint Committee for Guides in Metrology (JCGM)**. Evaluation of measurement data-Guide to the expression of uncertainty in measurement. [Online] <http://www.bipm.org/en/committees/jc/jcgm/>, 2008.
- [8] **M. Bass**. *Handbook of Optics*. Second Edition. s.l. : The McGraw-Hill Companies, Inc., 2010. Vol. 2.
- [9] **G. Kirchhoff**. Zusammenhang von Emission und Absorption von Licht und Wärme. *Ann. Phys. Chem.* 1860, Vol. 109, pp. 275–301.
- [10] **M. Planck**. Zur Theorie des Gesetzes der Energieverteilung im Normalspektrum. 1900, *VhDPG* 2, pp. 202–204.
- [11] **P.J. Mohr, B.N. Taylor and D.B. Newell**. CODATA recommended values of the fundamental physical constants: 2010. *Rev. Mod. Phys.* 4, 2012, American Physical Society, pp. 1527--1605.
- [12] **W. Wien**. Über die Energievertheilung im Emissionsspektrum eines schwarzen Körpers. *Ann. Phys.* 1896, Vol. 294, pp. 662–669.
- [13] **W. Wien, O. Lummer**. Methode zur Prüfung des Strahlungsgesetzes absolut schwarzer Körper. *Ann. Phys.* 1895, 292, pp. 451–456.
- [14] **Müller-Pouillet**. Lehrbuch der Physik. *Vieweg, Braunschweig*. 1909.
- [15] **J. Hartmann**. High-temperature measurement techniques for the application in photometry, radiometry and thermometry. *Physics Reports* . Vol. 469, pp. 205-269.
- [16] **J. Hollandt**. 125 Jahre Forschung an und mit dem schwarzen Körper. *PTB-Mitteilungen* . 2012, Vol. 122, Heft 3.

- [17] **J.R. Howell, R. Siegel, M.P. Menguc.** *Thermal Radiation Heat Transfer, 5th Edition.* s.l. : Taylor & Francis, 2010.
- [18] **M. Born, E. Wolf.** *Principles of optics.* 4. s.l. : Pergamon Press, London, 1970.
- [19] **S. Kabelac.** *Thermodynamik der Strahlung.* s.l. : Cuvillier Verlag, Göttingen, 1999.
- [20] **L.M. Hanssen and K.A. Snail.** *Integrating Spheres for Mid- and Near-infrared Reflection Spectroscopy.* Chichester : John Wiley & Sons Ltd, 2002.
- [21] **S. Linka.** Untersuchung der Eigenschaften von Schlacken und Schmelzen in technischen Feuerungen. Dissertation, Bochum, 2003.
- [22] **L.M. Hanssen, S. Mekhontsev, J. Zeng, A. Prokhorov.** Evaluation of Blackbody Cavity Emissivity in the Infrared Using Total Integrated Scatter Measurements. *International Journal of Thermophysics.* Vol. 29, 1, pp. 352-369.
- [23] **L.M. Hanssen, C.P. Cagran, A.V. Prokhorov, S.N. Mekhontsev and V.B. Khromchenko.** Use of a High-Temperature Integrating Sphere Reflectometer for Surface-Temperature Measurements. *International Journal of Thermophysics.* 2007, Vol. 28, No. 2.
- [24] **J. Hameury, B. Hay and J.R. Filtz.** Measurement of Infrared Spectral Directional Hemispherical Reflectance and Emissivity at BNM-LNE. *International Journal of Thermophysics.* 2005, Vol. 26, No. 6.
- [25] **W. Smetana and R. Reicher.** A new measuring method to determine material spectral emissivity. *Meas. Sci. Technol.* 1998, Vol. 9, pp. 797–802.
- [26] **C.K. Hsieh and K.C. Su.** Thermal radiative properties of glass from 0.32 to 206 μm . *Sol. Energy.* 1979, Vol. 22, No. 1, pp. 37-43.
- [27] **Cheng Shu Xia, Ge Xin Shi, Yao Cheng Cai, Gao Ju Wen and Zhang Yong Zhong.** Research on the validity of the steady-state calorimeter for measuring the total hemispherical emissivity of solids. *Measurement Science and Technology.* 1993, Vol. 4, No. 7, pp. 721-725.
- [28] **W. Beens, M. Sikkens and J.L. Verster.** An emissometer with high accuracy for determination of the total hemispherical emittance of surfaces. *J. Phys. E: Sci. Instrum.* 1980, Vol. 13, pp. 873-876.
- [29] **J. Hameury, B. Hay and J.R. Filtz.** Measurement of Total Hemispherical Emissivity Using a Calorimetric Technique. *Int J Thermophys.* 2007, Vol. 28, pp. 1607–1620.
- [30] **B.O. Kola, W. Mulwa and P. Mate.** A transient technique for determination of thermophysical properties in an absorption calorimeter. *Meas. Sci. Technol.* 1995, Vol. 6, pp. 888-892.
- [31] **M. Siroux, E. Tang-Kwor, D. Especel.** Emissivity measurements by sine wave thermal modulation: radiometric and calorimetric approaches. *High Temperatures - High Pressures.* 1998, Vol. 30, 2, pp. 217-222.
- [32] **J. Lohrengel.** Temperatur- und Winkelabhängigkeit des Gesamtemissionsgrades schlechter Wärmeleiter im Temperaturbereich von $-60\text{ }^{\circ}\text{C}$ bis $250\text{ }^{\circ}\text{C}$. Dissertation, RWTH Aachen, 1969.
- [33] **C. Monte and J. Hollandt.** The determination of the uncertainties of spectral emissivity measurements in air at the PTB. *Metrologia.* 2010, Vol. 47, pp. 172-181.

- [34] **M. Rydzek, T. Stark, M. Arduini-Schuster and J. Manara.** Newly Designed Apparatus for Measuring the Angular Dependent Surface Emittance in a Wide Wavelength Range and at Elevated Temperatures up to 1400 °C. *Journal of Physics Conference Series*. 2012, Vol. 395, 1.
- [35] **B. Wilthan, L.M. Hanssen, S. Mekhontsev.** Measurements of Infrared Spectral Directional Emittance at NIST. A Status Update. *Temperature: Its Measurement and Control in Science and Industry*. 2012, Vol. 8, pp. 746-751.
- [36] **S. Clausen.** Spectral Emissivity of Surface Blackbody Calibrators. *Int J Thermophys*. 2007, Vol. 28, pp. 2145-2154.
- [37] **L.R. Koirala.** FTIR-Spectroscopic Measurement of Directional Spectral Emissivities of Microstructured Surfaces. Dissertation, Institut für Thermodynamik, Helmut-Schmidt-Universität, Hamburg, 2004.
- [38] **G. Cardone and A. Ianiro.** Measurement of surface temperature and emissivity with stereo dual-wavelength IR thermography. *Journal of Modern Optics*. 2010, Vol. 57, 18, pp. 1708-1715.
- [39] **S. Moghaddam, J. Lawler and J. Currano.** Novel Method for Measurement of Total Hemispherical Emissivity. *Journal of Thermophysics and Heat Transfer*. 2007, Vol. 21, 1.
- [40] **S. Krenek, D. Gilbers, K. Anhalt, D. R. Taubert and J. Hollandt.** A Dynamic Method to Measure Emissivity at High Temperatures. *Int. J. Thermophys*. 2015, Vol. 36, Issue 8, pp. 1713-1725.
- [41] **S. Krenek, K. Anhalt, A. Lindemann, C. Monte, J. Hollandt and J. Hartmann.** A Study on the Feasibility of Measuring the Emissivity with the Laser-Flash Method. *Int. J. Thermophys*. 2010, Vol. 31, p. 998.
- [42] **C. Monte, B. Gutschwager, S.P. Morozova and J. Hollandt.** Radiation Thermometry and Emissivity Measurements Under Vacuum at the PTB. *Int J Thermophys*. 2009, Vol. 30, pp. 203–219.
- [43] The International Temperature Scale of 1990 (ITS-90). *Metrologia* . 1990, Vol. 27, 107.
- [44] **B. Gutschwager, R. Gärtner and J. Hollandt.** An Infrared Precision Radiation Thermometer for the Calibration of Remote Sensing Instrumentations under Vacuum. *Image and Signal Processing for Remote Sensing*. 2009, Vol. 7477.
- [45] **ECSS, European Space Agency.** The application of the black coating Aeroglaze Z306. *ECSS--Q--70--25A*. 1999.
- [46] **T.J. Quinn.** *Temperature*. Second edition. s.l. : Academic Press Limited, 1990.
- [47] **S.P. Morozova, N.A. Parfentiev, B.E. Lisiansky, V.I. Sapritsky, N.L. Dovgilov, U.A. Melenevsky, B. Gutschwager, C. Monte and J. Hollandt.** Vacuum Variable-Temperature Blackbody VTBB100. *Int J Thermophys*. 2008, Vol. 29, pp. 341–351.
- [48] Manual: Low Background Calibration Facility, VNIIOFI, Moscow. 2004.
- [49] **S.P. Morozova, N.A. Parfentiev, B.E. Lisiansky, U.A. Melenevsky, B. Gutschwager, C. Monte and J. Hollandt.** Vacuum Variable Medium Temperature Blackbody. *International Journal of Thermophysics*. 2010, Vol. 31, 8, pp. 1809-1820.
- [50] Manual: Vacuum middle temperature blackbody for PTB medium background facility. *Proforma Offer № MTBB.01-9/2006-Gr*. 2008.
- [51] **W. Herres and J. Gronholz.** Understanding FT-IR Data Processing. *Comp. Appl. Lab*. 1984, Vol. 4.
- [52] **P.R. Griffiths.** *Fourier Transform Infrared Spectrometry*. s.l. : John Wiley & Sons, 1986.

- [53] **A. Rogalski**. HgCdTe infrared detector material: history, status and outlook. *Rep Prog Phys* 2005, Vol. 68, pp. 2267–2336.
- [54] **A.M. Pravilov**. *Radiometry in Modern Scientific Experiments*. s.l. : Springer WienNewYork, 2011.
- [55] **M.D. Aggarwal, A.K. Batra, P. Guggilla and M.E. Edwards**. Pyroelectric Materials for Uncooled Infrared Detectors: Processing, Properties and Applications. *NASA/TM*. 2010, 216373.
- [56] **P.L. Richards**. Bolometers for infrared and millimeter waves. *J. Appl. Phys.* 1994, Vol. 76, 1.
- [57] **Bruker Optik GmbH**. Absolute Reflection Unit, Operating Instructions.
- [58] **A. Adibekyan, C. Monte, M. Kehrt, S.P. Morozova, B. Gutschwager and J. Hollandt**. The development of emissivity measurements under vacuum at the PTB. *Measurement Techniques*. 2012, Vol. 55, pp. 1163-1171.
- [59] **Virial International, LLC**. STEEP320 Manual. [Online] 2011-2013. <http://www.virial.com/steep320.html>.
- [60] **J.V. Nicholas, D.R. White**. *Traceable Temperatures: An Introduction to Temperature Measurement and Calibration*. s.l. : John Wiley & Sons, Ltd, 2002.
- [61] **V.I. Sapritsky and A.V. Prokhorov**. Calculation of the Effective Emissivities of Specular-Diffuse Cavities by the Monte Carlo Method. *Metrologia*. 1992, Vol. 29, pp. 9-14.
- [62] **V.I. Sapritsky and A.V. Prokhorov**. Spectral Effective Emissivities of Nonisothermal Cavities Calculated by the Monte Carlo Method. *App. Opt.* 1995, Vol. 34, pp. 5645-5652.
- [63] **J.R. Mahan**. *Radiation Heat Transfer: A Statistical Approach*. s.l. : Wiley, New York, 2002.
- [64] **A.V. Prokhorov**. Monte Carlo method in optical radiometry. *Metrologia* . 1998, Vol. 35, pp. 465-471.
- [65] **L.M. Hanssen, A. Prokhorov and S. Mekhontsev**. Radiation Properties of IR Calibrators With V-Grooved Surfaces. *SPIE Defense and Security Symposium*. 2006, Proceedings 6205.
- [66] **Physikalisch-Technische Bundesanstalt**. *Calibration Certificate*. 2006. 7.4 -1.10-05-19.
- [67] **C. Monte, B. Gutschwager, A. Adibekyan, M. Kehrt, F. Olschewski and J. Hollandt**. Radiation Thermometry for Remote Sensing at PTB. *AIP Conference Proceedings*. 2013, 1552, pp. 722-727.
- [68] **J. Hollandt, R. Friedrich, B. Gutschwager, D.R. Taubert and J. Hartmann**. High-accuracy radiation thermometry at the National Metrology Institute of Germany, the PTB. *High Temp.–High Press*. 2004, pp. 379-415.
- [69] **B. Gutschwager, E. Theocharous, C. Monte, A. Adibekyan, M. Reiniger, N.P. Fox and J. Hollandt**. Comparison of the radiation temperature scales of the PTB and the NPL in the temperature range from -57 degrees C to 50 degrees C. *Measurement Science and Technology*. 2013, Vol. 24, No. 6.
- [70] **C. Monte, B. Gutschwager, A. Adibekyan, M. Kehrt, A. Ebersoldt, F. Olschewski and J. Hollandt**. Radiometric calibration of the in-flight blackbody calibration system of the GLORIA interferometer. *Atmos. Meas. Tech*. 2014, Vol. 7, pp. 13-27.
- [71] **R.B. Pérez-Sáez, L. Campo and M.J.Tello**. Analysis of the Accuracy of Methods for the Direct Measurement of Emissivity. *International Journal of Thermophysics*. Vol. 29, 3, pp. 1141-1155.

- [72] **A. Adibekyan, C. Monte, M. Kehrt, B. Gutschwager and J. Hollandt.** Emissivity Measurement Under Vacuum from 4 μ m to 100 μ m and from -40 °C to 450 °C at PTB. *International Journal of Thermophysics*. 2015, Vol. 36, pp. 283-289.
- [73] **Key and supplementary comparisons, CCT-S1.** BIPM. [Online] http://kcdb.bipm.org/AppendixB/KCDB_ApB_info.asp?cmp_idy=1224&cmp_cod=CCT1&page=5&search=1&cmp_cod_search=&met_idy=9&bra_idy=0&epo_idy=1&cmt_idy=0&ett_idy_org=16&lab_idy=&cou_cod=.
- [74] **S. Byrnes.** Fesnel manual. [Online] <http://sjbyrnes.com/>.
- [75] **A. Jaffer.** [Online] <http://people.csail.mit.edu/jaffer/FreeSnell/>.
- [76] **S. Byrnes.** [Online] http://sjbyrnes.com/?page_id=12c.
- [77] **H.O. McMahon.** Thermal Radiation from Partially Transparent Reflecting Bodies. *Journal of the Optical Society of America*. 1950, Vol. 40, No. 6.
- [78] **R. Gardon.** The Emissivity of Transparent Materials. *The American Ceramic Society*. 1956, Vol. 39, pp. 278-285.
- [79] **H. Baba and K. Kanayama.** Directional monospectral emittance of dielectric coating on a flat metal substrate. *AIAA*. 1975, No. 75-664.
- [80] **A.K.S. Thakur.** On the Validity of Thin Film Models. *phys. stat. sol.* 1986, Vol. 97, K123.
- [81] **S. Barrat, P. Pigeat, I. Dieguez, E. Bauer-Grosse, B. Weber.** Observation of spectral and normal emissivity as a method of surface control during the growth of diamond films deposited by a microwave plasma-assisted CVD technique. *Thin Solid Films*, 263. 1995, pp. 127-133 .
- [82] **P. Pigeat, D. Rouxel, and B. Weber.** Calculation of thermal emissivity for thin films by a direct method. *Phys. Rev.* 1998, Vol. 57, 9293.
- [83] **P. Pigeat, T. Easwarakhanthan, J.L. Briançon and H. Rinnert.** Optical modelling of photoluminescence emitted by thin doped films. *Thin Solid Films*. 2011, Vol. 519, pp. 8003–8007.
- [84] **G. Zauner and G. Hendorfer.** Optical characterization of growing thin films at high temperatures by analysis of near infrared emissivity variations using CCD thermal imaging. *Proceedings of QIRT*. 2010.
- [85] **European metrology for earth observation and climate, MetEOC.** <http://www.emceoc.org/>. [Online] [https://www.euramet.org/research-innovation/search-researchprojects/details/?eurametCtcp_project_show\[project\]=1121&eurametCtcp_project\[back\]=508&cHash=ee9ad53c59135487ab7a8716c66c1aef](https://www.euramet.org/research-innovation/search-researchprojects/details/?eurametCtcp_project_show[project]=1121&eurametCtcp_project[back]=508&cHash=ee9ad53c59135487ab7a8716c66c1aef).
- [86] **Metrology for earth observation and climate, MetEOC2.** <http://www.emceoc.org/>. [Online] [https://www.euramet.org/research-innovation/search-research-projects/details/?eurametCtcp_project_show\[project\]=1224&eurametCtcp_project\[back\]=508&cHash=f017d01d98142d9b431b36754d78f7d4](https://www.euramet.org/research-innovation/search-research-projects/details/?eurametCtcp_project_show[project]=1224&eurametCtcp_project[back]=508&cHash=f017d01d98142d9b431b36754d78f7d4).
- [87] **F. Friedl-Vallon, T. Gulde, F. Hase, A. Kleinert, T. Kulesa, G. Maucher, T. Neubert, F. Olschewski, C. Piesch, P. Preusse, H. Rongen, C. Sartorius, H. Schneider, A. Schönfeld, V. Tan, N. Bayer, J. Blank, R. Dapp, A. Ebersoldt, H. Fischer, F. Graf, T. Guggenmoser, M. Höpfner, M. Kaufmann, E. Kretschmer, T. Latzko, H. Nordmeyer, H. Oelhaf, J. Orphal, M. Riese, G. Schardt, J. Schillings, M.K. Sha, O. Suminska-Ebersoldt and J. Ungermann.** Instrument concept of the imaging Fourier transform spectrometer GLORIA. *Atmos. Meas. Tech.* 2014, Vol. 7, pp. 3565–3577.

[88] **F. Olschewski, A. Ebersoldt, F. Friedl-Vallon, B. Gutschwager, J. Hollandt, A. Kleinert, C. Monte, C. Piesch, P. Preusse, C. Rolf, P. Steffens and R. Koppmann.** The in-flight blackbody calibration system for the GLORIA interferometer on board an airborne research platform. *Atmos. Meas. Tech.* 2013, pp. 3067-3082.

Acknowledgements

I would first like to thank Professor Ralf Koppmann for the wonderful opportunity to be a PHD-student at the University of Wuppertal, for his willingness to advise and for his thoughtful corrections.

I would like to thank most heartily Jörg Hollandt for giving me such a great opportunity to be a part of the working group “Infrared Radiation Thermometry” at the Physikalisch-Technische Bundesanstalt and for his constant support, guidance and useful discussions.

I would also like to express my most sincere gratitude and appreciation to Christian Monte, not only for his supervision of my work, but also for his helpful advice, daily support, constructive suggestions and valuable teaching.

I also want to thank Friedhelm Olschewski for his support and collaboration on the two metrological projects and for providing me this valuable learning experience.

I would like to give special thanks to my colleagues Mathias Kehrt, Lars Bünger, Marco Schulz, Max Reiniger and Berndt Gutschwager, for their willingness to support me and engage in professional discussions. This was always very helpful and highly productive, thank you very much for that!

I would also like to thank Olga Minaeva and Sergey Anevsky for believing in me while I was a graduate student and for the unique opportunity to gain new professional and work experience in Germany.

Finally, I thank my family for all of their care and support, which I sincerely appreciate.